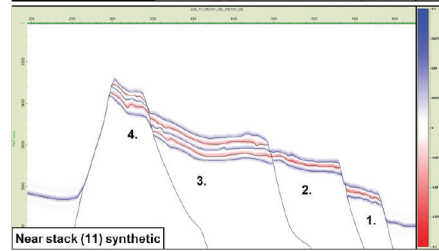
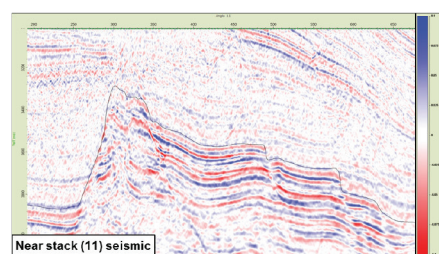
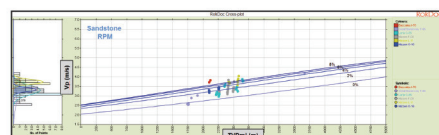
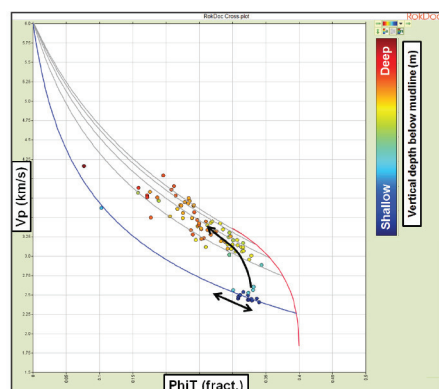
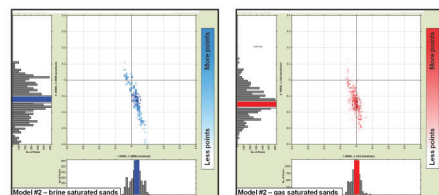


Regional Rock Physics Analysis of Offshore Newfoundland and Labrador: **Unlocking the Shelf-to-Deep-Transition**



Disclaimer

Ikon Science company make no warranty of any kind or character as to the reliability or suitability of this report or the data within for any purpose. The views expressed in this report are based on the best estimates of Ikon Science at the time of publication. Use of these opinions, material and data for any purpose is solely at the risk of the user and should not be used for any purpose other than for which it was intended

Copyright

© Copyright (2016), Ikon Science, Nalcor Energy and their affiliated and subsidiary companies, all rights reserved. All trademarks belong to the respective companies and their affiliated and subsidiary companies, all rights reserved.

Authorship

This report (and the technical analysis within) was undertaken and written by Nick Huntbatch, Neil Whitfield, Alsing Selnes and Alex Edwards, from Ikon Science and underwent technical management, review and guidance by Friso Brouwer, Dr. Jeremy Gallop and Kester Waters and from Ikon Science. The report benefitted from detailed technical and editorial review by Richard Wright, Ian Atkinson, James Carter, Deric Cameron and Nick Montevercchi at Nalcor Energy.

Acknowledgements

Acknowledgements go to Nalcor Energy for the preliminary work done in identifying key wells for the study and generation of certain images shown in the report. All images provided courtesy of Nalcor Energy are referenced accordingly. The authors would like to thank IHS for provision of the well data and TGS & PGS for their seismic contribution.

Table of Contents

1	Introduction	5
1.1	Background to the Study	5
1.2	Project Objectives	6
1.3	Study Area	7
1.4	Study Methodology	9
1.5	Data Sources	11
1.5.1	Data Conditioning.....	11
1.5.2	Analysis and Trends.....	13
1.6	General Introduction to Rock Physics Analysis	14
1.6.1	Methodology	14
1.6.2	Effective Granular Medium Models	15
1.7	Geological Overview of the Newfoundland and Labrador Margin	21
1.7.1	Tectonic History of the Margin	21
1.7.2	Structural Setting	21
1.7.3	Stratigraphy	22
1.7.4	Crystalline Basement	25
1.7.5	Ordovician	25
1.7.6	Jurassic (Basement to J ₁₄₅ Seismic Markers; S1 Sequence)	25
1.7.7	Early Cretaceous (J ₁₄₅ to K ₁₀₀ Seismic Markers; S2 – S4 Sequences)	25
1.7.8	Late Cretaceous (K ₁₀₀ to C ₆₅ Seismic Markers; S5 Sequence)	26
1.7.9	Palaeocene (C ₆₅ to C ₅₄ Seismic Markers; S6 Sequence)	26
1.7.10	Eocene (C ₅₄ to C ₃₄ Seismic Markers; S7 – S8 Sequences).....	26
1.7.11	Eocene-Recent (C ₃₄ to Present; Seismic Markers; S9 – S12 Sequences).....	27
2	Rock Physics Analysis and Seismic Lithofacies	28
2.1	Diagnostic Behaviour of Seismic Lithofacies	29
2.1.1	Lithofacies definitions	30
2.1.2	Lithology-based Up-scaling	34
2.2	Log Data QC and Conditioning.....	37
2.2.1	Identification of erroneous elastic log responses	37
2.2.2	Shelfal Wells.....	39
2.2.3	Flemish-Pass/Orphan Basin (deep-water) Wells	42
2.2.4	Shear Log Data	44
2.2.5	Elastic Log Conditioning.....	47
2.3	Sands	48
2.3.1	Sand Rock Physics Models – A Universal Sand Model.....	50

2.3.2	Shelf Wells (Present-day Shallow-water).....	52
2.3.3	Deep-water Wells	56
2.4	Shales	71
2.4.1	“Normal” Shales	72
2.4.2	“Cemented” Shales	74
2.4.3	Calcareous shales.....	78
2.5	Carbonates	82
2.6	Summary.....	83
3	Multi-well Rock Physics Analysis	84
3.1	Introduction	84
3.1.1	Stratigraphic Intervals.....	84
3.1.2	Trend Summary.....	85
3.1.3	Deep-water and Shallow-water Wells	85
3.2	Pore Pressure and Effective Stress.....	86
3.3	Shale Trends	89
3.3.1	Vp-TVDml.....	92
3.3.2	RhoB-TVDml	95
3.3.3	Vs-TVDml	99
3.3.4	Vs-Vp.....	101
3.3.5	RhoB-VES	103
3.3.6	Vp-VES.....	104
3.4	Sand Trends	106
3.4.1	RhoB-TVDml	108
3.4.2	PhiT-Vp	110
3.4.3	Grain Contact Cement Content – TVDml.....	111
3.4.4	Vs-Vp.....	113
3.4.5	Vp(PhiT)-TVDml	114
3.4.6	RhoB-VES	115
3.5	Summary.....	116
4	Fluid Substitution and Synthetic Seismic Analysis	117
4.1	Introduction	118
4.2	Isotropic Modelling.....	122
4.2.1	Isotropic Synthetic Models	122
4.2.2	Blocky Modelling	137
4.3	Summary.....	148
5	An Integrated Workflow for De-Risking in Frontier Basins	149
5.1	Introduction	149

5.2	Modelling Constraints	149
5.3	AVO Modelling Workflow	152
5.4	Ground Truthing at Mizzen O-16	153
5.4.1	Introduction.....	153
5.4.2	Angle Stack Responses	154
5.4.3	AVO Modelling	156
5.4.4	Model - Well Comparisons	157
5.4.5	Model - Seismic Comparisons	159
5.4.6	Summary and Conclusions	162
5.5	Deploying the Model for AVO Screening.....	163
5.5.1	Absolute Amplitude Calibration	163
5.6	Cretaceous Lead	166
5.6.1	Introduction.....	166
5.6.2	AVO Modelling	167
5.6.3	Cretaceous Lead Seismic Responses	169
5.6.4	Cretaceous Lead Model Responses	170
5.6.5	Cretaceous Lead Model – Seismic Comparison.....	171
5.6.6	Summary & Conclusions	177
5.7	Jurassic Lead.....	178
5.7.1	Introduction.....	178
5.7.2	AVO Modelling	179
5.7.3	Jurassic Lead Seismic Responses	181
5.7.4	Jurassic Lead Model Responses	182
5.7.5	Jurassic Lead Model – Seismic Comparison	183
5.7.6	Jurassic Lead Model-Seismic Comparison – 2D modelling.....	184
5.7.7	Summary & Conclusions	187
5.8	Tertiary Lead.....	188
5.8.1	Introduction.....	188
5.8.2	AVO Modelling	188
5.8.3	Tertiary Lead Seismic Responses	191
5.8.4	Tertiary Lead Model Responses	193
5.8.5	Tertiary Lead Model – Seismic Comparison	194
5.8.6	Recent Analysis with New 3D Seismic Data.....	197
5.8.7	Summary & Conclusions	198
5.9	Summary & Conclusions	199
6	Glossary of Terms	201
7	References.....	212

1 Introduction

1.1 Background to the Study

The Labrador offshore area is a largely unexplored region for hydrocarbons, specifically in the deep-water; although a few significant discoveries have been made on the shelf (Hekja O-71, Snorri J-90, Hopedale E-33, North Bjarni F-06, Bjami H-81 and Gudrid H-55) which have provided confidence in a viable petroleum system. The North Eastern Newfoundland region (Orphan and Flemish Pass basins) has a large areal extent with a proven petroleum system confirmed by recent discoveries in the Mizzen, Harpoon and Bay du Nord wells. The slope and deep-water are relatively under-explored with respect to these tested structural traps, and currently has not tested any stratigraphic traps. The southern margin has encountered only minor occurrences of hydrocarbons in shelf wells drilled in the 80's and earlier. Only recently has attention been given to slope and deep-water regions leaving that portion of the margin relatively un-explored.

In recent years, new deep-water seismic-based exploration work has resulted in the revision of existing basin boundaries and definition of significant sedimentary section in basins of the slope and deep-water along the entire Newfoundland and Labrador margin. The seismic surveys tie some of the earlier discovery wells with extended deep-water Jurassic, Cretaceous and Cenozoic play areas. Furthermore, promising new deep water seismic-based exploration work, initiated by Nalcor Energy, has resulted in redefined basin extents in the deep-water Labrador region, with expanded depocentres in the newly named Henley, Chidley and the Holton basins. The petroleum potential in the area has had confidence built through the identification of slick and seepage locations using 2D seismic data and satellite imagery, the importance being that surface slicks may indicate subsurface hydrocarbon migration from an active petroleum system and the first evidence of a liquids petroleum system for Labrador that has previously been seen as a gas province.

All the recent regional analysis coordinated through Nalcor Energy shows strong evidence for an active petroleum system in the slope and deep-water areas with early seismic interpretation indicating the presence of trapping geometries in regions away from well control. In identifying the potential of these areas, a clear need to understand the controls on deep-water pressure regimes and the experience of drilling similar targets from global analogues was thought to be key to helping de-risk these under explored regions.

The recent regional geopressure study released in 2014 achieved the objective above for the Labrador margin but also raised new opportunities to learn more about the deep-water system. Nalcor Energy identified seismic amplitude anomalies in the deep-water that could be indicative of hydrocarbons but could be simply a function of pressure and/or lithology variation.

With no wells drilled in the deep-water regions of Labrador, and only a few existing in the southern extents and North Eastern Newfoundland, the understanding of elastic properties in the shelf to deep-water environment can prove to be quite a challenge. Calibration points from well log data are often sparse and prospects may be far removed from well control. If the pressure component is taken into account (e.g. overpressure), and the understanding that there is a complex history behind every seismic signal, then one of the key risks in developing the deep-water potential is to understand the intra-relationship between elastic properties and the present day pressure regime.

1.2 Project Objectives

Nalcor engaged Ikon Science to provide an integrated rock physics and geopressure study, looking at 18 wells from offshore Newfoundland and Labrador, Eastern Canada. The objective was to analyse the elastic properties at the wells, using trends and related rock physics models, to help explain seismic anomalies in the area.

A significant challenge in rock physics studies is that the elastic properties of sediments can vary significantly, even within small areas, due to a number of factors, including tectonic history (e.g. exhumation), abnormal pressure (e.g. overpressure) and abnormal temperature. This makes the de-risking of prospects more complex and uncertain.

To overcome some of the challenges related to the aforementioned variables, this study will introduce an integrated methodology for frontier, deep-water exploration purposes. The methodology will make use of (some of the universal) relationships between the elastic logs, via the application of a set of rock physics models, depth trends and elastic property-effective stress relationships, to better understand seismic reflections in the subsurface (Figure 1). The pore pressure component of this report was taken mostly from the regional geopressure report previously commissioned and released by Nalcor Energy in 2014, with some additional pore

pressure interpretations being completed for wells that were not part of the study, including Great Barasway and Baccalieu. The geopressure study was also authored by Ikon Science.

1.3 Study Area

The study area focuses on key wells within the Hopedale and Orphan Basins (HD and OP in Figure 2), offshore Newfoundland and Labrador, Eastern Canada; the newly identified Chidley (CH), Henley (HN) and Holton Basins (HT) in the deep-water are also shown. The Hopedale Basin has been divided into the Nain, Harrison and Hamilton Sub-Basins and the majority of drilling has occurred within these three sub-basins. The deep-water wells, which are important to the trend derivation and prospect AVO modelling in later chapters, are located in the Orphan Basin. The location data used in the project were supplied by Nalcor Energy and are publically available from the BASIN database maintained by Natural Resources Canada (Geological Survey of Canada, Geoscience Data Repository). The locations of the wells are shown in Figure 2. Stratigraphic nomenclature referred to throughout the report and well markers used in this study were provided by Nalcor Energy based on their internal chronostratigraphic naming convention.

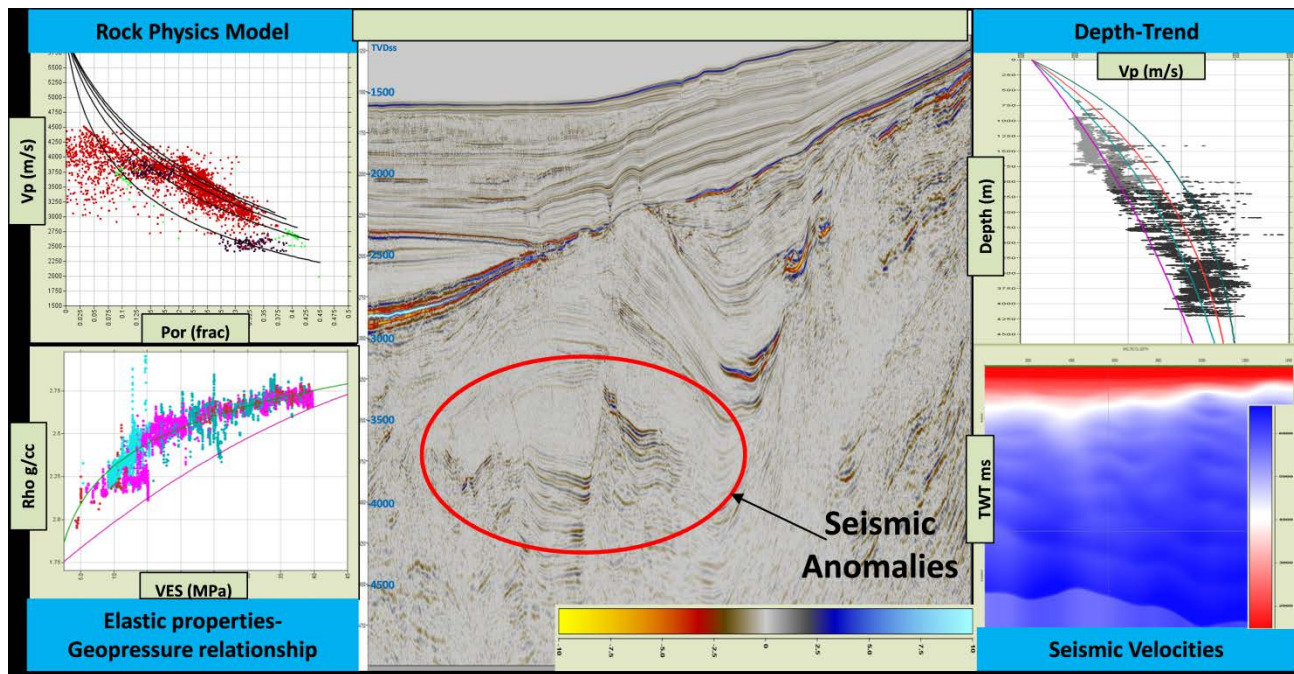


Figure 1. General concept of integrated approach for frontier- and deep water exploration

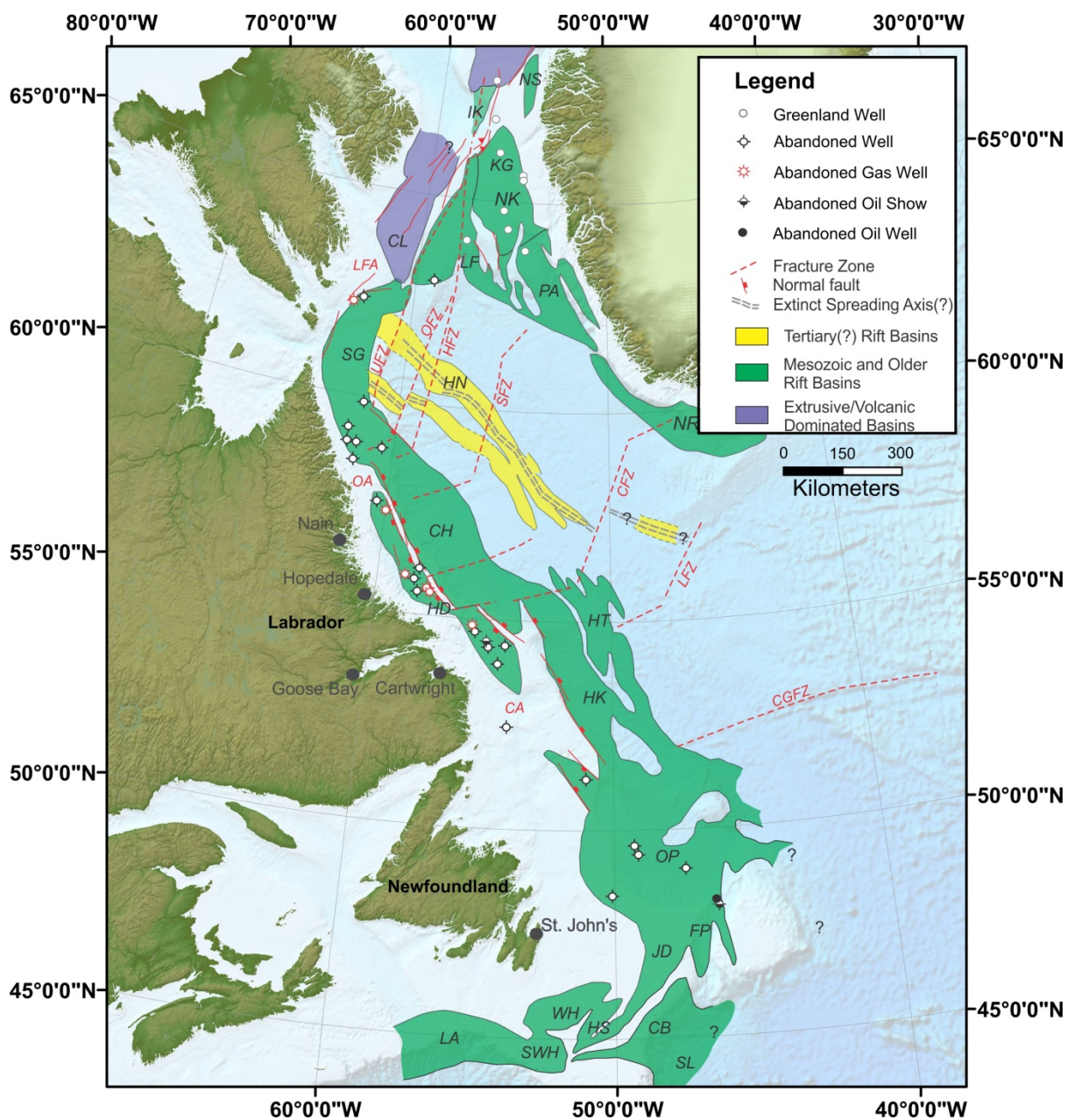


Figure 2. Geographical overview of the study area with basin outlines (adapted by Nalcor Energy) and locations of all wells included in the study.

1.4 Study Methodology

Nalcor Energy and Ikon Science chose 18 wells from offshore Newfoundland and Labrador, Eastern Canada region to be included in the study, covering the area of interest in terms of seismic coverage and expected similarity in rock properties and geopressure.

After petrophysical interpretation had been completed, both single well analysis and multi-well analysis of all the well data using cross-plots was performed. The multi-well approach is good at highlighting any problem wells, such as those that are affected by borehole problems and those with fluid invasion issues. These problems appear as anomalous data offset from any typical trend and require edits before any modelling or quantitative interpretation starts. See Chapter 2 for more information on rock physics analysis and the derivation of seismic lithofacies.

The multi-well approach also included deriving depth trends for Vp, Vs and Rho for sands, shales, silts, calcareous shales and limestones, to understand how AVO signatures can vary with depth. Based on the elastic properties, shale was separated into 4 types: "Normal" shale, cemented shale, Tertiary-Cretaceous calcareous shale and Jurassic calcareous shale. The shale type classifications were used in depth trends analysis and for the derivation of vertical effective stress(VES)-elastic property trends. A Constant Cement rock physics model was fitted to the reservoir sand data, which captured the elastic property behaviour of the sands, across a varying range of cements. See Chapter 3 for more information on trend derivation.

The inputs for the pore pressure and VES (lithostatic pressure minus pore pressure) were imported from the regional geopressure study released by Nalcor Energy in 2014. The geopressure study was authored by Ikon Science and is a 30 well study, incorporating wells from the northern Saglek Basin to the southern Orphan Basin (Figure 2). In the deep-water Orphan Basin, the models for normal compaction and VES were re-evaluated and the original model was validated. Additional seismic lines were available to this study that were not available at the time of the geopressure study, therefore the relationships and geopressure models built in the first study were extended to the new seismic data and the validity of the results were confirmed before being used in this study.

Gassmann fluid substitution (Gassmann, 1951), using Ikon Science's proprietary dry rock modelling techniques, was performed to end-member oil and gas saturations on relatively clean sands. The main reason for using Gassmann is to understand how the seismic amplitude changes with different fluids in the pore system. This can later be utilized in the detection of

hydrocarbons using Amplitude Versus Offset technique (Rutherford and Williams, 1989; Verm and Hiltermann, 1995; Russell, 2002).

Synthetic seismograms were also generated using Zoeppritz equations (Zoeppritz, 1919) for the different fluid states. See Chapter 4 for more information on fluid substitution and synthetic gathers.

The study workflow can be summarised in the flowchart below (Figure 3), with the workflow achieving the following tasks and objectives:

- Provide a regionally consistent deterministic petrophysical interpretation of all key wells.
- Perform a detailed 1D pressure analysis of all the wells (fluid contacts, pressure coupling of reservoirs and non-reservoirs) and produce pore pressure profiles and hence vertical effective stress profiles (VES).
- Perform a multi-well rock physics analysis, incorporating the pore pressure and VES profiles to determine (if applicable) regionally consistent trends.
- Perform a detailed single-well rock physics analysis, modelling fluid end-members.
- Analyse all the data in a regional context to provide a definitive view on the relationships between rock physics and geopressure in the Labrador region and their use as a predictive exploration and appraisal tool.

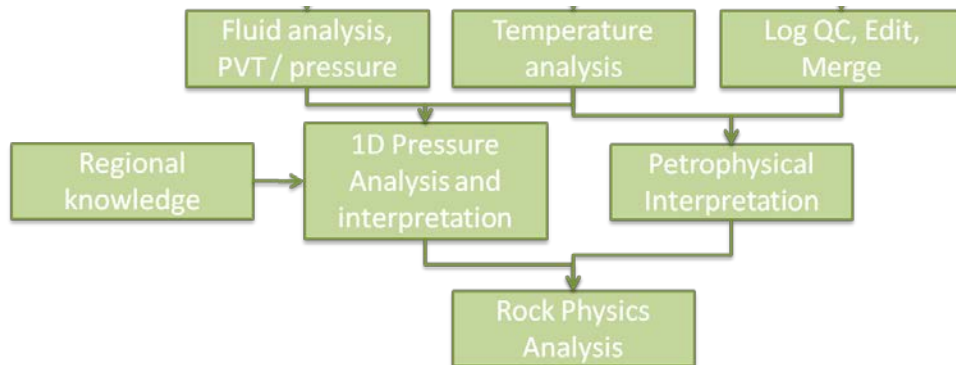


Figure 3. Generalized Project Workflow

1.5 Data Sources

A total of 32 wells were supplied for the study, across various basins. After a screening process, which focused on quality of the raw logs, the final dataset of 18 wells was chosen (Table 1). A total of 7 wells are classified as deep-water wells (present-day water depth >1000 m), while the remaining 11 come from the shelf (present-day water depth <300 m). Out of the 18 wells that founded the basis for our rock physics analysis, 4 were not included in the regional geopressure study: Baccalieu I-78, East Wolverine G-37, Mizzen F-09 and Mizzen O-16.

Name	X Position	Y Position	Water Depth (m)	KB (m)	TVD (m)	Completion Data	Spud Date	Show Type	Mud Type	Log Data						EOWR	Temp Gradient: °C/100m	Core Data	In GeoPressur e Study
										GR	DT	DTS	RHO	RES	Checkshot/ VSP				
North Bjarni F-06	74147.38	6181396	150	12.5	2813	P&A	1980	Gas	Seawater	v	v	-	v	v	-	v	3.6	-	v
Roberval K-92	195708.23	6089510	268.5	12.5	3874	P&A	1978	Dry Hole	-	v	v	-	v	v	-	-	2.92	-	v
Cartier D-70	198534.3	6065962	310	12.3	1927	P&A	1975	Dry Hole	-	v	v	-	v	v	-	-	2.9	-	v
Cumberland B-55	564256.83	5361501	194.8	29.9	4136.4	P&A	1975	Dry Hole	-	v	v	-	v	v	-	-	2.5	-	v
Freydis B-87	256499.37	5982897	176.0	12.3	2314	P&A	1975	Dry Hole	-	v	v	-	v	v	-	-	3.1	-	v
Gudrid H-55	187598.47	6095481	299.3	12.3	2839	P&A	1974	Gas	Lignosulfonate	v	v	-	v	v	-	v	2.57	-	v
Leif M-48	231852.7	6024306	165.2	13	1879	P&A	1973	Dry Hole	Lignosulfonate	v	v	-	v	v	-	-	2.93	-	v
Roberval C-02	194069.41	6088765	276	13.7	2823	P&A	1980	Dry Hole	OBM	v	v	-	v	v	-	v	2.08	-	v
Snorre J-90	-38641.82	6389599	140.8	11.3	3210	P&A	1975	Gas	Lignosulfonate	v	v	-	v	v	-	v	2.86	-	v
Tyrk P-100	43696.89	6173897	117	11.8	1739	P&A	1979	Dry Hole	N/A	v	v	-	v	v	-	-	3.17	-	v
Skolp E-07	-126977	6528167	166.5	12	2992	P&A	1978	Dry Hole	N/A	v	v	-	v	v	-	-	3.13	-	v
Baccalieu I-78	859848	5323359	1093	24	4135	P&A	1985	Dry Hole	OBM	v	v	-	v	v	-	v	2.87	-	-
Mizzen F-09	851006.5	5361180	1065	21.5	3759	P&A	2011	Dry Hole	OBM	v	v	v	v	v	-	v	3.93	v	-
Great Barasway F-66	705883	5478843	2338	25	6750	P&A	2006	Dry Hole	OBM	v	v	v	v	v	v	v	v	v	v
East Wolverine G-37	651768	4959518	1890	31.59	6852	P&A	2009	Dry Hole	OBM	v	v	v	v	v	-	-	Used Regional Trend	-	-
Lona O-55	764112	5442535	2602.4	31.6	5580	P&A	2010	Dry Hole	OBM	v	v	v	v	v	v	v		v	v
Mizzen O-16	849986	5357299	1095	21.15	3758	P&A	2008	Oil	OBM	v	v	v	v	v	v	v		v	-
Mizzen L-11	849896	5346514	1153	23.75	3797	P&A	2003	Dry Hole	OBM	v	v	v	v	v	-	v		v	v

Table 1: Well database for the study (KB: Kelly Bushing in metres and TVD: True Vertical Depth of the well in metres).

2D seismic, in the form of angle stacks, and pre-stack data were supplied by Nalcor Energy for selected lines across the basins, along with seismic velocities. Petrography and thin section analysis were provided for two wells, Mizzen O-16 and Roberval K-92.

1.5.1 Data Conditioning

Any quantitative well-to-seismic analysis has to have good quality input data to give good quality results, meaning there is a crucial need to quality-control both the input seismic and the input well logs before any quantitative decisions are made.

The elastic logs (sonic and density), measured in a wellbore, are affected by borehole quality. Borehole rugosity and wash-outs may lead to errors in measurement due to poor instrument coupling with the borehole wall. This may lead to unreliable density measurements or effects such as cycle skipping, which is due to low S/N ratio on (automated) interpretation of the sonic. In addition, the density log in particular has a shallow depth of investigation, so it can be

severely affected by the drilling mud invading the pore space and replacing the in-situ pore fluid. Hence, the need for standardized techniques that can bring the measured data back to its in-situ state, or replace poor data.

One common and widely used empirical model, which has been adopted by the industry to correct erroneous density data, are the rock physics relationships derived by Gardner (1974). By inverting the equations from the Gardner method, a relationship that outputs compressional velocity (V_p) from density (ρ) can be established. Establishing lithology-based trends by calibrating the Gardner relationships to the study data allows an understanding of the quality of the elastic log data and any poor quality data that falls significantly off the trends can be removed and replaced with model data. Below are the original Gardner equations for various lithologies:

- $\rho_{\text{shales}} = 1.75 * (V_p^{0.265})$
- $\rho_{\text{sands}} = 1.66 * (V_p^{0.261})$
- $\rho_{\text{limestones}} = 1.36 * (V_p^{0.386})$
- $\rho_{\text{dolomites}} = 1.74 * (V_p^{0.252})$
- $\rho_{\text{anhydrites}} = 2.19 * (V_p^{0.160})$

Very often in rock physics studies, there is a lack of measured shear velocity (V_s), which is particularly true for old wells, or the well has a measured shear log where the quality is highly questionable. In wells drilled in the last decade, as oil companies have started to understand the importance of measured shear log and as measurement technology has evolved, wells often now have good quality V_s logs available. Still, there is always the need to double-check the log, and a known approach to predict and calibrate shear data, is the (Linear) method of Greenberg and Castagna (1992). Similar to the Gardner prediction method for ρ and V_p , the coefficients that go in to the Greenberg and Castagna equations have to be calibrated against the locally measured data to give reliable results. Below are the original Greenberg and Castagna equations for various lithologies:

- $VS_{\text{shales}} = 0.7696 * V_p - 0.8673$
- $VS_{\text{sands}} = 0.8041 * V_p - 0.8558$
- $VS_{\text{limestones}} = -0.0550 * V_p^2 + 1.0167 * V_p - 0.990$
- $VS_{\text{dolomites}} = 0.5832 * V_p - 0.077$

Invasion analysis was performed using Gassmann-Biot fluid substitution (Gassmann, 1951; Biot, 1956), one of the cornerstone rock physics theories. Dry rock plots were used throughout

as a means of quality control. This method takes advantage of the way Gassmann works. If an incorrect fluid fill is assumed and inverted to the dry rock, then the resulting $K_{\text{dry}}/K_{\text{min}}$ point will sit in the incorrect space. By modifying the pore fill (and or density) it is possible to qualitatively determine whether the invasion effects are large or small and whether the sonic log should be corrected as well as the density log.

1.5.2 Analysis and Trends

As the general rock physics relationships are already established from the procedure of log conditioning and editing, a study of the depth-dependent properties as a function of burial depth can begin. These rock physics depth trends are very useful and important in exploration for oil and gas for several reasons.

For drilling, it is important to have knowledge of overpressure in the subsurface, commonly derived from well and/or seismic velocities via pore pressure prediction (for a greater discussion of this topic please refer to regional geopressure study), to avoid any hazardous blowouts during drilling.

From a purely exploration point of view, depth trends of sands and shales can significantly increase the understanding of what type of seismic signature to look for in the search of oil and gas. This might be done by empirically fitting a trend (exponential, linear, power law etc.) to the edited Rho, Vp and Vs, separated by relevant lithology cut-offs for sands and shales.

Another, more sophisticated way of deriving depth-dependent Rho, Vp and Vs is by the use of empirical porosity-depth trends for sands and shales (Avseth et al., 2001; Rubey and Hubbert, 1959), which is then one of the important inputs to a rock physics model applicable for the area of interest. Avseth et al. (2008) presented a paper with a good overview of this approach, which has the strength of being both dynamic in nature (as one can change inputs to the rock physics model), and honouring geological processes, such as mechanical compaction and chemical compaction within the model setup. In this study, relationships defining the spatial- and depth-dependent rock property variations are being documented and stored in a database.

1.6 General Introduction to Rock Physics Analysis

Over the course of the last three decades, rock physics has significantly improved the oil and gas industry's ability to use seismic data to analyse, understand and predict fluid and rock properties of hydrocarbon reservoirs. The great efforts of scientists and the continuing research in the development of effective medium models has been, and will continue to be, of great importance for the search and development of hydrocarbon reserves in increasingly challenging environments.

Rock physics provides a link between geologic reservoir parameters such as, porosity, clay content, texture, lithology, cement content and saturation with the seismic properties V_p , V_s and ρ or derivatives of them such as, acoustic impedance, P-wave/S-wave velocity-ratio (V_p/V_s), Poisson's Ratio, bulk density, and elastic moduli. A wide variety of rock physics models can be used to interpret observed sonic and seismic velocities in terms of the reservoir parameters or to extrapolate beyond the available data range to examine certain what-if scenarios, such as plausible fluid or lithology variations. It is important however to recognize that the models have a certain degree of advantages and limitations, and have to be carefully calibrated to local conditions and areas. As Box and Draper (1987) so nicely put it forward; "All models are wrong, but some are useful".

It is along this line that rock physics can "bridge the gap" between qualitative geology and quantitative geophysics and be used to forward model and predict seismic response at the prospect level, given some a priori understanding of the reservoir properties and the overburden properties and conditions.

A more thorough explanation on the various rock physics models commonly used in the industry, whether it be theoretical models, empirical models, heuristic models or bound-filling models, can be found in Avseth et al. (2010).

1.6.1 Methodology

One of the most important things in rock physics is to cross-plot well log data, and look for relationships that exist between various measurable data. The reason for doing this is two-fold: 1) use these relationships to look for bad data and to fix this bad data (alternatively reconstruct if not logged in the wellbore) to get a consistent set of data, and 2) look for intra-relationships

which can be used in forward modelling scenarios and to explain and understand seismic anomalies in the subsurface.

As mentioned in section 1.5.2 (Data Conditioning), empirical models are typically used to repair poor data. Gardner and Greenberg & Castagna relationships are widely used throughout the industry for this purpose, where the former aims to predict Rho (and Vp), and the latter aims to predict Vs logs where these are missing or are of poor quality.

One of the major problems with published empirical models like Gardner and Greenberg & Castagna arises when they are used with unaltered parameterization which will often only work within the basins and stratigraphy where the calibration data originated. This leaves big question marks on the reliability when attempting to extrapolate outside the control areas with these models. One way of addressing this uncertainty is to make these models site-specific; meaning that by adjusting or recalibrating some of the parameterization based on the best possible analogues, the model in question becomes a better fit. But this is still based on the assumption that the same geology and elastic properties exist in the new area where the model is to be applied. However, these are still only empirical functions and there are not many rock physics-based constraints on this approach, nor is it consistent from a geological point of view. Using models based on universally valid geological and physical principles would be a better approach than strictly empirical, and is treated in the next paragraph.

1.6.2 Effective Granular Medium Models

Over more than thirty years, variations of Hertz-Mindlin (Mindlin, 1949) type effective granular medium models have evolved for unconsolidated sediments (Digby, 1981; Walton, 1987; Dvorkin and Nur, 1996; Helgerud, 2001). An advantage of these kind of models is that the physics behind them is understood and theoretically generalized, hence making them a powerful tool for extrapolating outside well control to match seismic amplitudes of interest.

One of the most widely used models is the friable sand model (Dvorkin and Nur, 1996), also referred to as the uncemented sand model or the soft sand model. It is a combination of the heuristic modified Hashin-Shtrikman lower bound (Hashin and Shtrikman, 1963) and Hertz-Mindlin, and in short it essentially describes sediments undergoing mechanical compaction. Mechanical compaction, as the overburden stress increases, causes rotation of grains in the sandstone, slippage of grains, plus the deformation of ductile and brittle grains to cause a loss in porosity with increasing burial depth, while the velocity only slightly increases. The lower

Hashin-Shtrikman bound is theoretically the lowest elastic stiffness possible for a mix of multiple phases.

In the rock physics community the term “*sorting*” has come to be used to refer to sediments that lose porosity as a result of mechanical, non-chemical, compaction. However, in the wider geological community the term “*sorting*” is used to describe grain size distribution (grading) of a sediment as a function of its transport, deposition and provenance. A similar confusion can arise from the definition of the term “*cementation*” used both in the rock physics and geological communities to mean different but similar processes. To avoid confusion in this study the term “*mechanical compaction*” will be used in place of “*sorting*” and “*chemical compaction*” will be used in place of “*cementation*” to describe the compaction-style of a particular sediment.

Ramm and Bjorlykke (1994) and Lander and Walderhaug (1999) also explain the relevance of other factors which cause reduction in porosity, grain size distribution, roundness of the grains, angularity, pore pressure and saturation, but without describing the velocity changes usually observed when a sandstone is subjected to mechanical- and chemical compaction.

A counterpart to the soft sand model is the stiff sand model (Figure 4), which uses the exact same end-members as the soft sand model, zero porosity (e.g. mineral point) and high porosity (e.g. critical porosity (Yin et al., 1993)), except this model connects the two with the modified Hashin-Shtrikman upper bound. This model can be thought of as the stiffest way of mixing load bearing minerals and some pore-filling material, and the use of the model has strong association with rocks that undergo or have undergone chemical compaction processes.

However, adding small amounts of cement to grain contacts is not well-described by this stiff sand model, due to the large stiffening effect on the elastic modulus. Dvorkin and Nur (1996) developed the contact cementation theory as a response for a need for a better model to account for this drastic velocity increase, which takes into account the initial cementation effect with only minor impact on the porosity.

Avseth et al. (2000) introduced a Constant Cement model, trying to describe geological processes like mechanical compaction and chemical compaction in one model, which is more geologically consistent with the rocks that are being buried increasingly deeper, to higher temperatures and pressures. Mathematically, this model is a combination of the contact cement model, where porosity reduces from the initial sand porosity Φ_{critical} to a porosity Φ_{new} due to contact cement deposition, and the friable sand model where porosity reduces from Φ_{new} due to

deposition of the solid phase away from the grain contacts. From a geological perspective, the model essentially describes how the elastic properties of a rock change with both being affected by mechanical compaction and having small amounts of cement added to the pore system (assuming mechanical compaction pre-dominates cementation in the geological time scale).

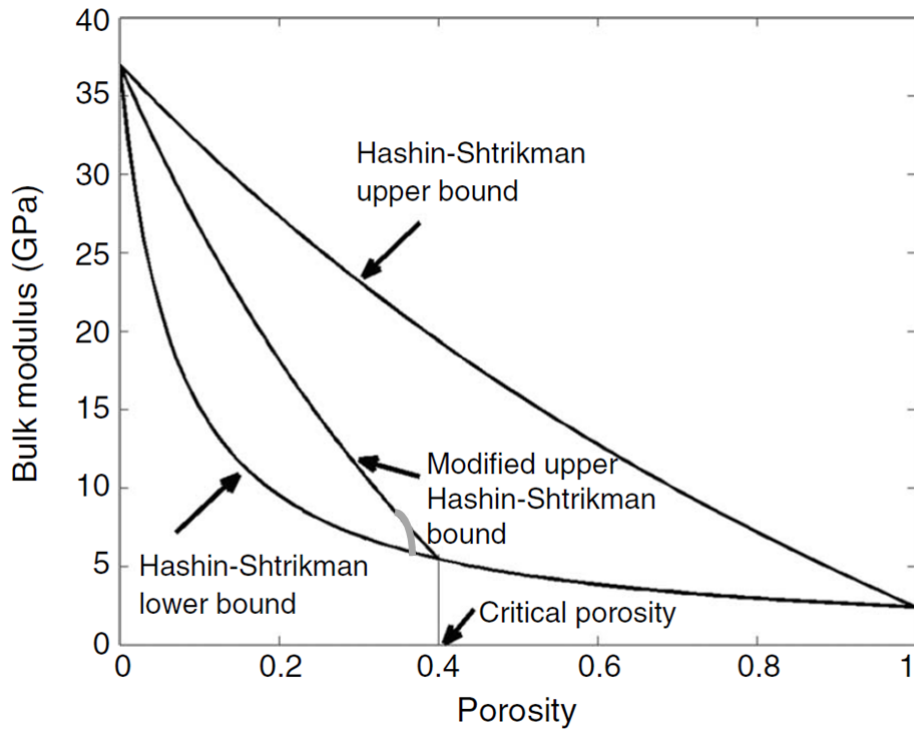


Figure 4. Cross plot of bulk modulus versus porosity: Chemical compaction trends are represented by the steep modified upper Hashin-Shtrikman bound, while mechanical compaction trends are often described well by a lower modified Hashin-Shtrikman bound. Both trends connect the newly deposited sediment on the suspension line, to the mineral point. The contact cement model in grey captures the often observed steep slope with initial mechanical compaction and chemical compaction (After Avseth et al., 2010)).

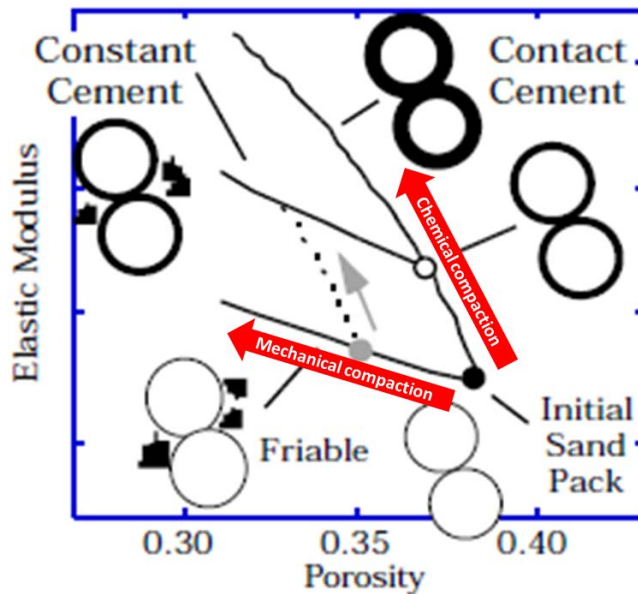


Figure 5. Cartoon showing mechanical- and chemical compaction paths for sands (after Avseth et al, 2000).

1.6.2.1 Diagnosing Rocks Using Site-Specific Effective Medium Models

Dvorkin and Nur (1996) introduced and first published on the topic of rock physics diagnostics. The method tries to infer information about the rock type and the texture from velocity-porosity (alternatively impedance-porosity or velocity-density) relations. Such diagnostic studies work by superimposing a theoretical rock physics model on measured data and working with the assumption that if the data do fall on/close to a theoretical model, it can be related it back to the chosen model (Figure 6). For instance, if the data falls on the relatively flat trend from the soft sand-shale model it is a reasonable assumption that the sediments undergo a process of mechanical compaction, with not much increase in velocity as porosity reduces with increasing burial depth (see Figure 6; The lower trend, marked Troll data). Or, if it falls close to the relatively steep cementing trend, the assumption can be made that the sediments have entered the cementation window (see Figure 6, upper trend, marked Oseberg data), with the consequence of rapid velocity increase with just a few percent reduction in porosity.

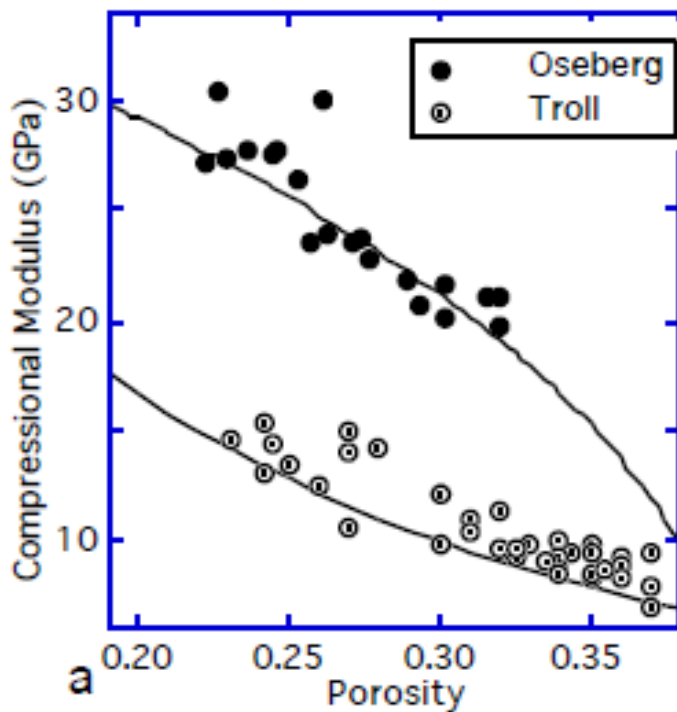


Figure 6. Cross plot of Compressional Modulus versus Porosity for two datasets from the North Sea (after Dvorkin and Nur, 1996).

This process of diagnosing the rock has further implications for understanding the rocks beyond its elasticity; intuitively it is known that cemented rocks will have higher strength than uncemented rocks of same mineralogy and porosity; which will have an impact on production strategies like sanding, but also on permeability and thus the ability to flow hydrocarbons in the reservoir. For example, (slightly) cemented rocks actually tend to have higher permeability than an uncemented counterpart. From a physical point of view it makes sense, as loose material (e.g. variable grains size or non-contact cement) can infill pore space and thus destroy permeability (Dvorkin and Brevik, 1999; Bosl et al., 1998).

The theoretical models explained so far have shown their relevance to the two main factors controlling the elastic properties in the earth; mechanical compaction and chemical compaction. On the basis of these learnings, and the understanding of the relationships between rock physics models and geology and sedimentology, Avseth et al. (2009) showed that by using these models in combination, it should be possible to predict more reliably and constrain the changes in seismic responses as a function of burial depth or depositional environment. In turn, these models should narrow down the expected range of rock properties that give rise to

seismic amplitudes, and hence reduce risk in exploration, especially where well control is sparse.

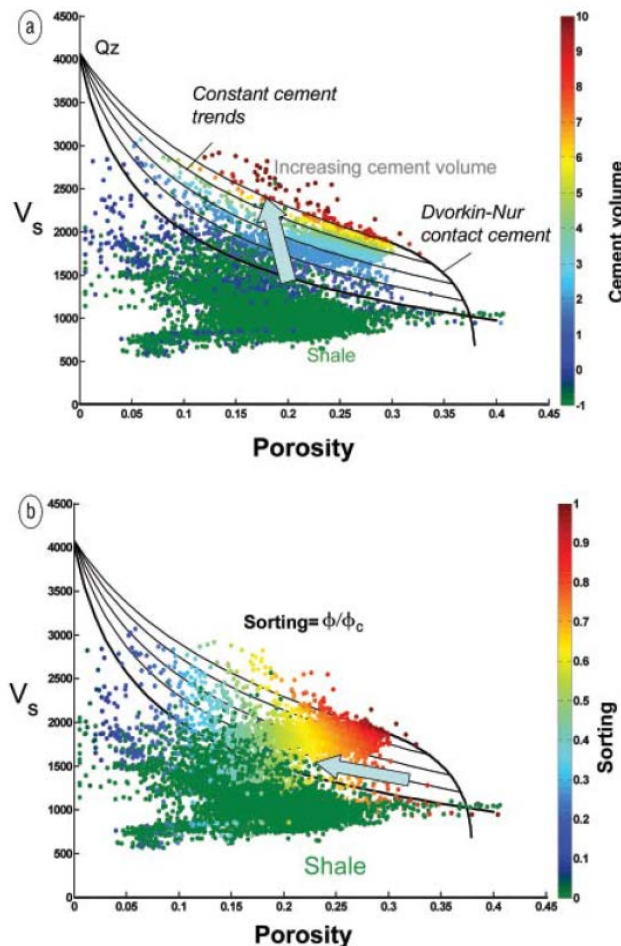


Figure 7. Shear-wave velocity log data versus total porosity and superimposed diagnostic rock physics models. Using the models, (a) the cement volume can be quantified and (b) degree of sorting. (Green points are shale data with high GR values, and are for practical reasons given the value -1 in cement volume and 0 in sorting) (after Avseth et al., 2009).

1.7 Geological Overview of the Newfoundland and Labrador Margin

1.7.1 Tectonic History of the Margin

Starting in the north, the Labrador Sea consists of a series of northwest trending depocentres that developed when the North American and Greenland plates separated. These basins are largely unexplored, specifically in the slope and deep-water (>500 m). To the southern extents of the study area, the Northeastern Newfoundland region, consisting of the Orphan and Flemish Pass basins, had a slightly more complex history.

The formation of the Labrador Sea basins began after an initial period of extension during the Early Cretaceous forming early sedimentary basins now preserved under the continental shelves (the Saglek Basin towards the north and the Hopedale Basin in the central and south of the Labrador Sea) and continuing into slope and deep-water regions (Chidley, Holton and Hawke basins). During the Late Cretaceous this extension ceased, and the basins thermally subsided. Within this period the principal depo-centres are the Saglek Basin and the Hopedale into Chidley basins. The Latest Cretaceous/Early Palaeocene is characterized by renewed extension and ocean floor spreading (McWhae, 1981). This base Cenozoic unconformity (C65 seismic marker) has been clearly defined in the North Eastern Newfoundland and Southern Newfoundland areas as well, making it one of the most significant seismic markers in the region. The development, basin morphology and sedimentary fill of the Flemish Pass and Orphan Basins was connected to the rifting and expansion of the Northern Atlantic Canadian Sea initiated from offshore Newfoundland during the middle to late Jurassic or possibly earlier (Dafoe et al. 2013).

1.7.2 Structural Setting

Faulting in the Flemish and eastern Orphan is remnant of their earliest rifting phase with dominant orientations trending north-northeast to south-southwest. The Labrador basins differ with the extensional direction aligned with Greenland reflective of the latest rifting phase in the region.. The extensional faulting gives rise to typical rifted basin geometry of rotated fault blocks with horsts and grabens (Figure 8), similar to the North Sea, Malay Basin, West of Shetland, and Mid-Norway basins. The horst-graben structures are locally offset by fracture zones oriented orthogonal to the normal faulting and locally creating strike slip offset and inversion

structures. Other features observed are igneous intrusive features (northern Orphan & Hawke) and salt diapirs (Southern and South Eastern Newfoundland regions).

1.7.3 Stratigraphy

The seismic stratigraphy of the Newfoundland margin, as well as a general lithostratigraphy for the area (Grand Banks region shown) is illustrated in Figure 9. The Labrador Sea into the Grand Banks region as defined in this study contains known hydrocarbon accumulations in rocks from Jurassic and Cretaceous age in a variety of trap configurations. To date hydrocarbons are found dominantly in clastic reservoirs (rather than carbonates). The exception being a single gas discovery in sub-cropped Ordovician dolomite found in the Gudrid well.

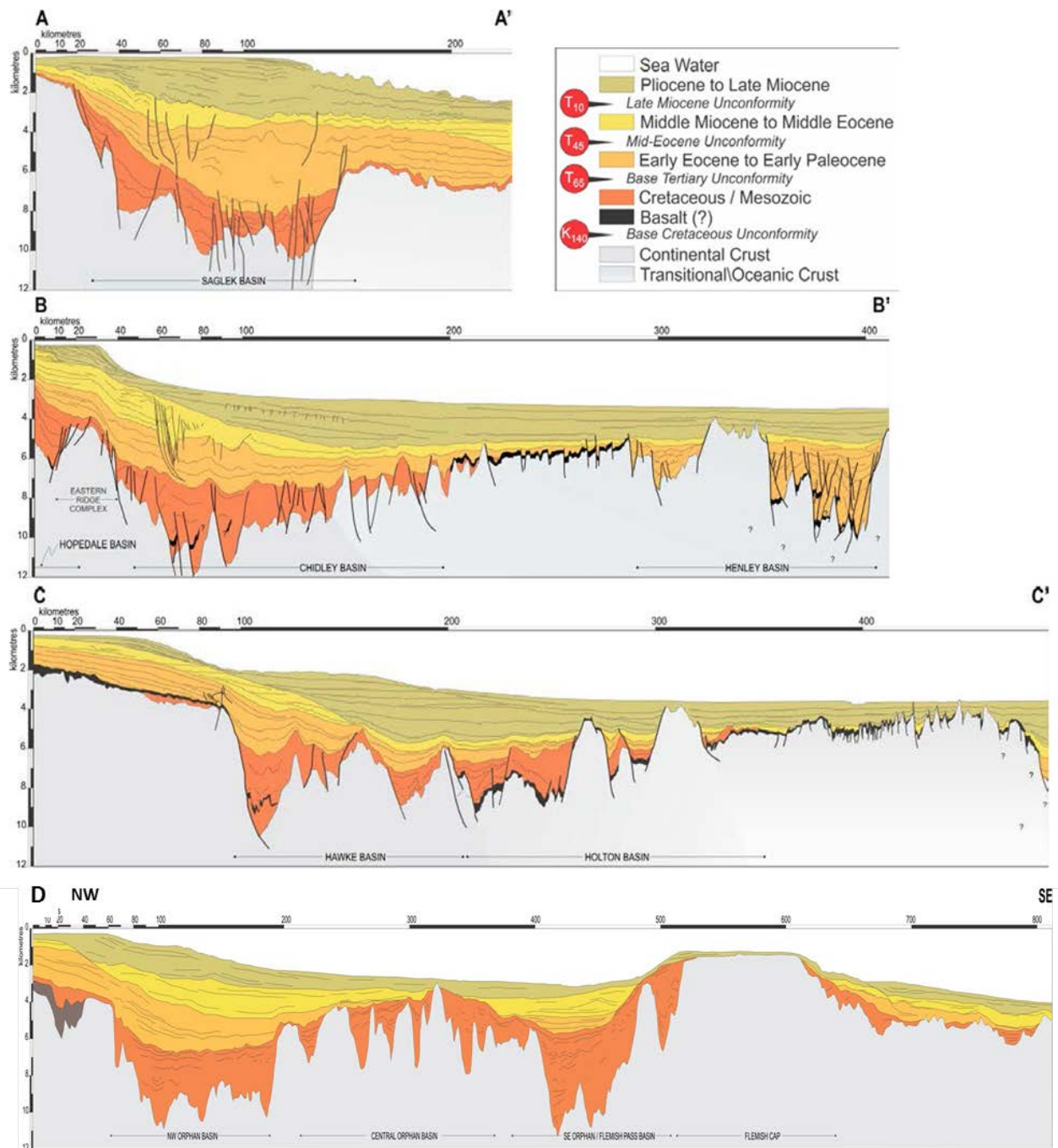
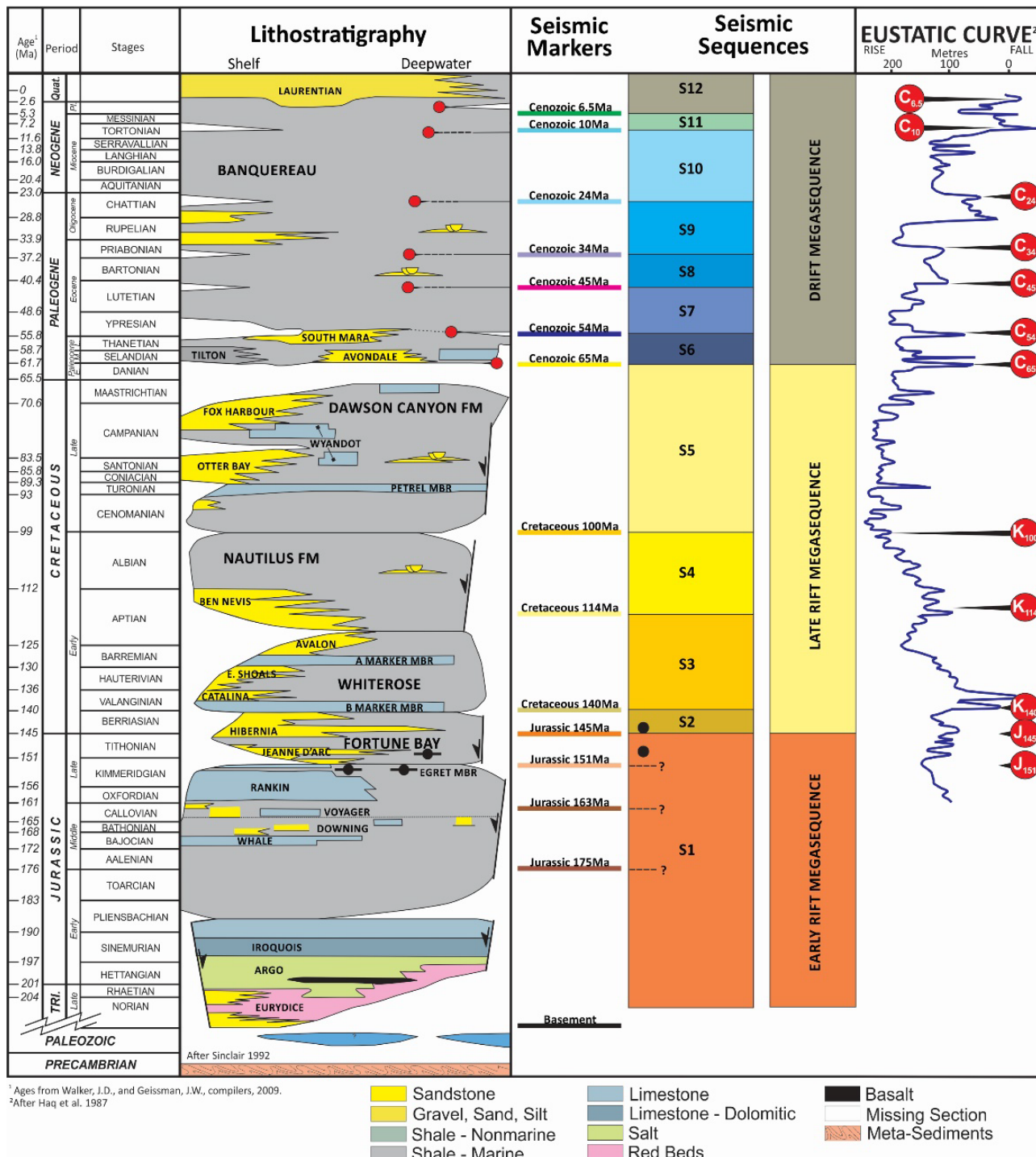


Figure 8. Schematic cross-sections of the Mesozoic Labrador sequence based on a 2D seismic line showing main stratigraphic and structural relationships from shelf to deep-water. Internal framework based on well ties from the shelf. Line A-A' runs from the northern Hopedale Basin into the northern Chidley Basin/southern Saglek Basin (Note thickened Eocene-Paleocene section related to slump features in the region). Line B-B' runs from the southern Hopedale Basin out past the southern extent of the Henley Basin. Line C-C' runs from west of the Hawke Basin to north-east of the Holton Basin. Line D-D' runs from the NW Newfoundland shelf through the Orphan Basin and over the Flemish Cap in a SE orientation. Images courtesy of Nalcor Energy (2013).



¹ Ages from Walker, J.D., and Geissman, J.W., compilers, 2009.

² After Haq et al. 1987

Lithostratigraphy will vary locally and is further addressed in Chapter 3. Image courtesy of Nalcor Energy (2014).

1.7.4 Crystalline Basement

Crystalline basement rocks have been encountered in several wells along the Labrador Shelf and Orphan/Flemish Pass basins. The crystalline rocks are of Pre-Cambrian age (Grenville, Makkovik and Nain orogenies) and consist of weathered and fractured metamorphic and igneous rocks (Ermanovics and Ryan, 1990).

1.7.5 Ordovician

The oldest sediments in the Labrador area are Ordovician in age. These sediments are carbonates that underlie all the Mesozoic-Tertiary successions and are somewhat localized to the north of the Labrador Sea Basin off Baffin Island (Balkwill et al., 1990), although they are encountered at the base of several wells in the Labrador offshore (Schwartz, 2008).

1.7.6 Jurassic (Basement to J_{145} Seismic Markers; S1 Sequence)

Rifting dominated the mid-Jurassic in the Grand Banks region leading to thick mid- to late Jurassic section deposited in the Orphan and Flemish Pass regions of the North Eastern Newfoundland offshore. The Tithonian reservoir and source rock intervals lie just below the J_{145} marker surface, with that horizon occurring as a marked angular unconformity throughout the North Eastern Newfoundland region. Towards the northern end of the Orphan, this Jurassic interval gradually pinches out into the basement with only Cretaceous and younger aged intervals present along most of the Labrador margin. Deposition within this interval marks a mix of marine shales (including Kimmeridgian and Tithonian source rocks) with fluvial to fluvio-estuarine clastic intervals.

1.7.7 Early Cretaceous (J_{145} to K_{100} Seismic Markers; S2 – S4 Sequences)

Rifting dominated the Early Cretaceous leaving sedimentary sequences that are exclusively intra-continental deposits in the central to northern reaches of Labrador, to fluvial through shoreface and marine deposits in the south. Basaltic lava flows and volcanoclastics that form the Alexis Formation were locally generated at this time along the majority of the Labrador margin and reaching as far south as the Hawke-Orphan transition (Dafoe et al., 2015; Nalcor pers. Comm.). In the Hopedale and Chidley basins, these volcanic sequences were largely erupted from a number of extensive fissure systems in the centre of the basin, as identified by linear gravity lows, (Chalmers and Pulvertaft, 2001) into a marine environment. The volcanism

resulted in laterally and vertically overlapping volcanic sequences, with interbedded sequences of fluvial, local lacustrine and marginal marine depositional origin, which together form the Bjarni Formation. The intercalation of sedimentary and igneous material is common in these types of environments as exemplified by the Faroe-Shetland Basin (Naylor et al., 1999; Japsen et al., 2005).

1.7.8 Late Cretaceous (K_{100} to C_{65} Seismic Markers; S5 Sequence)

The Late Cretaceous is dominated by the Markland/Dawson Canyon formation equivalents; a widespread succession of marine shales thought to be Cenomanian to Danian in age (Chalmers et al., 1993), with recent work suggesting a revision to Cenomanian(?) to Late Maastrichtian in age (Ainsworth et al., 2014) with some interbedded clastics (sandstone and dolomite beds). In well penetrations the formation has a sharp to angular unconformable boundary with the Bjarni Formation on the Labrador shelf (no Cenomanian – Turonian has been encountered in Labrador offshore to date; its presence is, however, implied due to thickening of the Upper Cretaceous away from drilled highs, Nalcor pers.comm.). The unit oversteps the Bjarni Formation onto the basement in some areas. The Markland/Dawson Canyon Formation represents the change from rifting to seafloor spreading and is interpreted to have been deposited in accommodation space created by thermally subsiding basins (Chalmers, 1991; Chalmers and Pulvertaft, 2001; Roberts and Bally, 2012). Although not widely encountered in the sparse well control, parts of the Markland Formation contain shallow marine quartzose sandstones that make up the Freydis Member (McWhae and Michel, 1975; McWhae et al. 1980; Bell et al., 1989; Martin, 2007).

1.7.9 Palaeocene (C_{65} to C_{54} Seismic Markers; S6 Sequence)

The Lower Tertiary is characterized by the Cartwright/Banquereau formations, which comprise marine clays and siltstones that unconformably overlie the Markland Formation. The Cartwright Formation is a lateral equivalent to the Gudrid ‘Member’ that is comprised of submarine sandstones. The Gudrid sandstone is interpreted to represent re-deposited eroded material from the Markland delta during a global sea-level low-stand (DeSilva, 1999).

1.7.10 Eocene (C_{54} to C_{34} Seismic Markers; S7 – S8 Sequences)

The Kenamu/Banquereau formations overlie the lower Tertiary intervals and consist of marine shales and siltstones, although clastic input locally along the entire margin creates several unnamed member sandstones within the formation. At the top of the Kenamu Formation on the

Labrador margin lies a fine-grained sandstone interval named the Leif Member (McWhae 1975, 1980). The Leif Member is interpreted as a shallow marine sandstone deposited toward the latter stages of seafloor spreading (DeSilva, 1999; Chalmers and Pulvertaft, 2001; Floistad et al. 2013).

1.7.11 Eocene-Recent (C₃₄ to Present; Seismic Markers; S9 – S12 Sequences)

After the cessation of seafloor spreading a period of basin wide thermal subsidence commenced in the Oligo-Miocene, during which the Mokami Formation and the Pliocene Saglek Formation were deposited along the Labrador margin and the continuation of the Banquereau through Laurentian formations along the Grand Banks. The Mokami Formation is comprised of marine siltstones and shales, while the Saglek Formation consists of fine to coarse-grained conglomerates and sandstones (DeSilva, 1999). These are overlain by un-named glacial beds along the Labrador shelf (Chalmers and Pulvertaft, 2001).

2 Rock Physics Analysis and Seismic Lithofacies

Seismic lithofacies are seismic-scale sedimentary units, each having their own characteristics in terms of petrophysical properties such as clay content, saturation, porosity etc., as well as elastic properties such as velocity and density. Normally, seismic-scale units are referred to as packages that are observed and easily mapped from seismic data, however this depends on wavelet length, signal to noise ratio (S/N), etc. These are commonly on the metre to tens of metre scale, which is in stark contrast to petrophysical properties that are measured on the centimetre scale and subject to wide spreads in ranges of the property values.

To bring these measurements into comparable scales, lithology ‘flags’ derived from conservative log-based cut-offs isolate the petrophysical properties to the true values for the rock type, and filter out the outlier values. For example, when transitioning from shale into sandstone, log responses will commonly show a hybrid response merging the effects of the two rock types and creating a subpopulation of petrophysical data that is not representative. This is especially critical in areas of interbedded stratigraphy (thin bed effects). This leads to anomalous data included on cross-plots and can lower confidence in any correlation if those zones are not filtered. By eliminating these points from the distribution, seismic lithofacies and petrophysical rock properties can be compared at similar scales without the spurious data impacting the relationship.

The direction and analysis of this chapter essentially shows how the rock physics diagnostics procedure identifies the various seismic lithofacies. In other words, how to detect seismic lithofacies and how each can be differentiated by the use of rock physics analysis and theories. It will be shown how the rock physics diagnostic procedure helps in explaining how various lithologies manifest themselves in various cross-plot domains, such as V_p versus porosity, V_p versus V_s . The purpose is to constrain what is observed using proper rock physics models that allow extrapolation beyond well control for forward modelling and de-risking of AVO anomalies elsewhere. In the sections that follow, it will be shown that the selected constant-cement models properly describe the various seismic lithofacies, which confirms the strength of the models. The better understanding of the various seismic lithofacies provides a starting point for deriving the depth trends and will be used extensively in the case studies presented in Chapter 4.

2.1 Diagnostic Behaviour of Seismic Lithofacies

A petrophysical interpretation on the entire well bore was performed, not just on the sand intervals. The sole purpose of petrophysical interpretation is to establish reliable estimates of shale volume, porosity and water saturation that serve as a description of the geology and are linked to the elastic properties as measured by the elastic logs (Vp, Vs and RhoB logs). Typically, sands show low gamma ray (GR) readings due to low radioactive content and high GR readings in the surrounding shales; but this may not always be the case, for example, when the sands are slightly micaceous or feldspathic (containing potassium) or when they may contain small amounts of uranium or thorium then the sands demonstrate high GR readings. In those cases, it might be worthwhile to use a combination of GR and Density-Neutron to secure the most accurate clay content in sands.

Porosity was calculated from density using the following equation:

$$\Phi = \frac{Rho_matrix - Rho_measured}{Rho_matrix - Rho_fluid}$$

where;

- Rho_matrix is the Hill's harmonic average of the mineral constituents present in the sands, calibrated against core densities if available
- Rho_measured is the measured density log in the well (corrected for mud filtrate invasion effects if invaded)
- Rho_fluid is the density of the fluids present in the sands

If the well in question encountered hydrocarbons, the equation was corrected for the hydrocarbon effect to give the best match with the core porosities where available (Figure 11).

Saturation was calculated by the Indonesia equation (Poupon, 1971), which is the same as the original Archie equation (Archie, 1942) in clean sandstones, but takes into account the conductivity of the shales for more accurate water saturation profiles in shaly sediments. The formation brine resistivity was estimated from water samples, if collected, or from nearby wells believed to have the same salinity or from a clean water zone (Pickett, 1966) in the well under investigation.

A cross-plot of any combination of Rho, Vp and Vs (or any derivative of these) is usually the starting point for identifying the clusters of data that are to be scrutinized. These clusters of data will then be classified according to the petrophysical interpretation and rock properties, which are representative of each lithological unit and its mineral constituents.

Depending on how many lithofacies are present, there might be a very clear separation between facies, as for instance between a soft shale and a cemented sand, which helps seismic reflection analysis. But, as often is seen, overlapping properties between facies result in more complex reflections. The spread of responses and amount of overlap between facies is a function of lithology, porosity, fluid fill, pressure and burial depth. The aim of this study is to understand the effect of each of these variables on the seismic and acoustic/elastic response of the facies.

2.1.1 Lithofacies definitions

Based on the petrophysical interpretation and elastic log response, a set of lithofacies is defined at log scale. These facies are subsequently used in the interpretation of the elastic log response across the well dataset, to determine the elastic responses as a function of lithology, burial depth and saturation (in the reservoir facies). The defined facies, petrophysical cut-offs used and symbols per facies are shown in Figure 10.

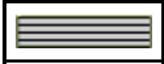
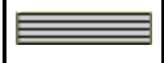
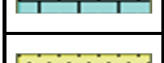
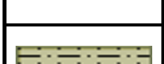
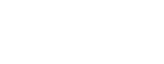
Facies name	Cut-offs	Comments	Symbol	
Normal shale	>75% Vshale	Normal shales in Tertiary, Cretaceous and Jurassic sections		Here normal and cemented shales are both shown with the same symbol. The distinction between the two is made in the Vp-TVDml plots in terms of velocity.
Jurassic cemented shale.	>75% Vshale	Low calcite content shales with faster velocities, predominantly identified in the Jurassic.		
Calcareous shale	>20% Vshale >20% Vcalcite	Shale with significant calcite content in the Tertiary, Cretaceous and Jurassic.		
Limestone	>80% Vcalcite	Limestone stringers, predominantly encountered in the Jurassic.		
Sandstone	>75% Vsand	Clean sandstones, certain reworked carbonate clastic intervals removed due to (i.e. TiO in Mizzen O-16).		
Siltstone	<75% Vsand, <75% Vshale <80% Vcalcite	Any data points that do not fall into the other end-member facies. Predominantly silty sands.		
Dolostone	>50% Vdolomite	Thicker dolomite sections encountered in some wells.		

Figure 10: Facies definitions, petrophysical cut-offs and symbols.

The cemented shale facies is distinguished from the normal shale based on its Vp-TVDml behaviour.

The facies logs are also used in the lithology-based up-scaling technique, this aims to identify log responses that are representative of the facies while avoiding mixed facies log responses where facies are rapidly varying due to fine layering. This technique will be explained in detail later in this report.

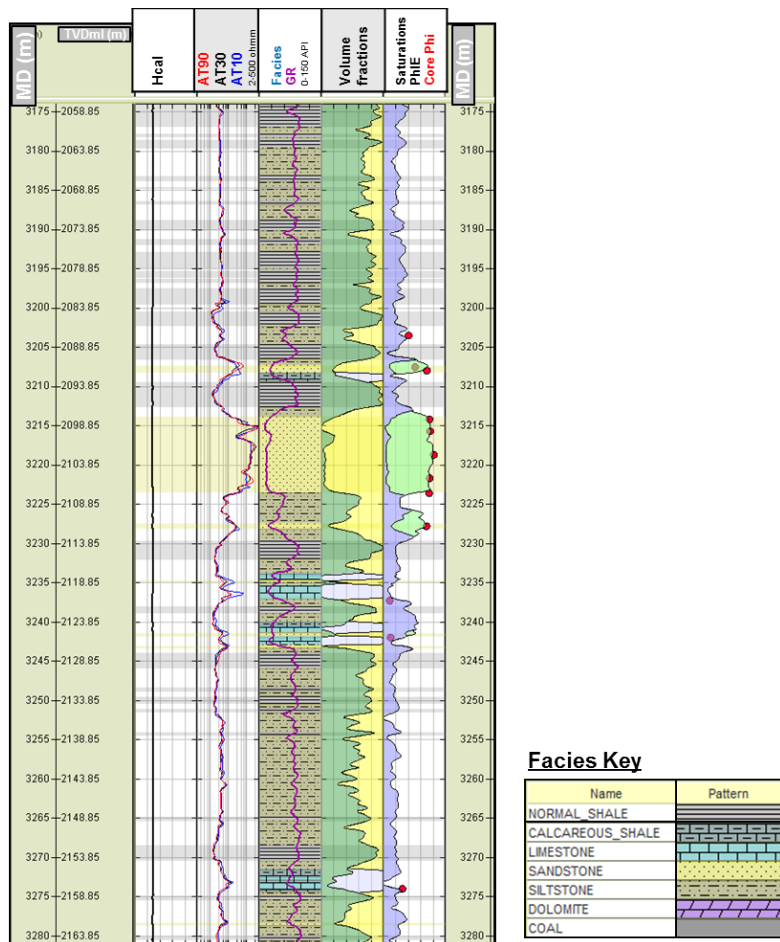


Figure 11: CPI plot for Mizzen O-16.

In this study six major lithofacies were defined from well log analysis, they are:

1. Normal Shales,
2. Calcareous Shales,
3. Cemented Shales,
4. Sandstone
5. Limestones
6. Dolostones

The sandstone facies was further divided into a brine sand, oil sand and gas sand for use in subsequent parts of the study, to make eight facies in total. For the initial analysis the cemented shales and normal shales are combined, as the cemented shales are distinguished in terms of their velocity response and not their petrophysical response. Only sands and shales were considered as end-member lithologies for trend-fitting in Chapter 3. An example of the facies logs is shown in Figure 12, here the facies log is shown in the left hand track for each well, with the symbols used shown in Figure 10. For simplicity, the study has neglected micro-details in the rocks used in defining clastics, such as grain size and bedding orientation in sands and bedding orientation in shales, but a quantitative distinction between uncemented sands and (slightly) cemented sands has been made.

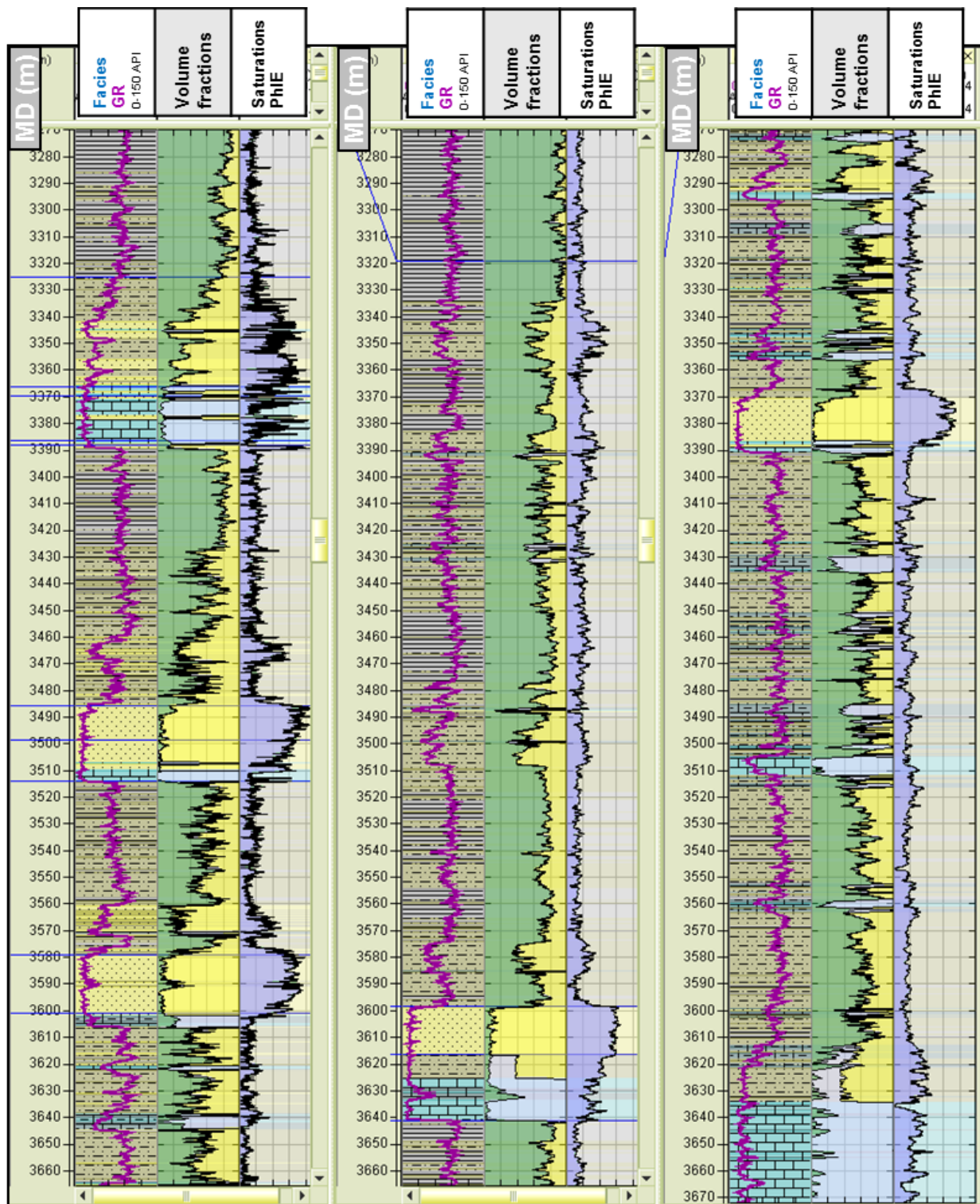


Figure 12: Facies and petrophysical interpretation for the three Mizzen area wells, left to right: Mizzen F-09, Mizzen L-11, Mizzen O-16.

2.1.2 Lithology-based Up-scaling

In order to investigate the elastic response of each lithofacies at appropriate scales up-scaling is performed. The facies log defined in the last section is used to perform lithology based up-scaling. This technique uses the facies log to extract discrete points from the continuous elastic log curves from the centre of thick lithology packages and avoid intervals of high variation in facies relative to the log measurement scale. The aim is to avoid shoulder-bed effects and log responses from mixed facies where there is fine layering. A coefficient of variation is specified that determines at which point the extraction is made. Figure 13 shows an example of the lithology-based up-scaling technique at the Mizzen O-16 well. Here points are extracted from the Vp, Vs and RhoB logs within thick (relative to log measurement scale) facies units.

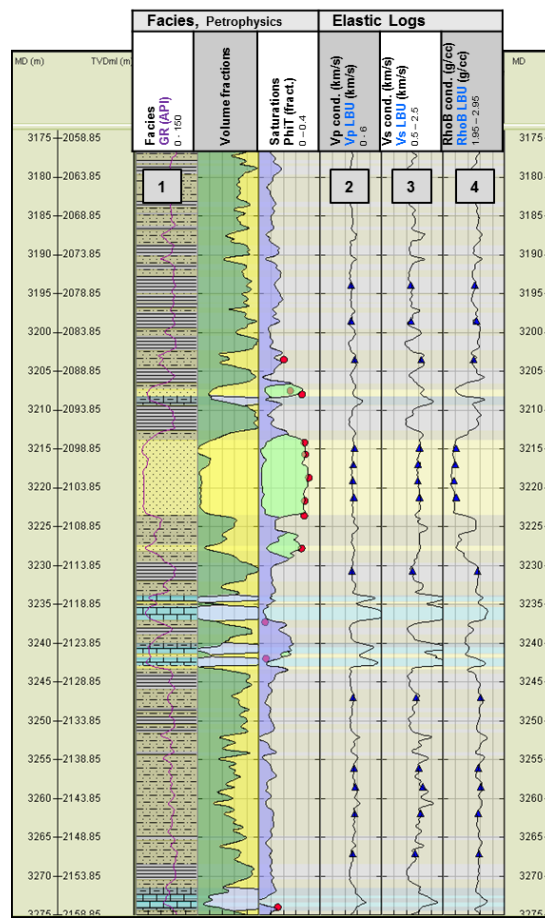


Figure 13: Discrete points are extracted from the continues elastic log curves (tracks 2, 3, 4) based on the facies log and the vertical variation in that facie slog (track 1). The blue points are the discrete, up-scaled points.

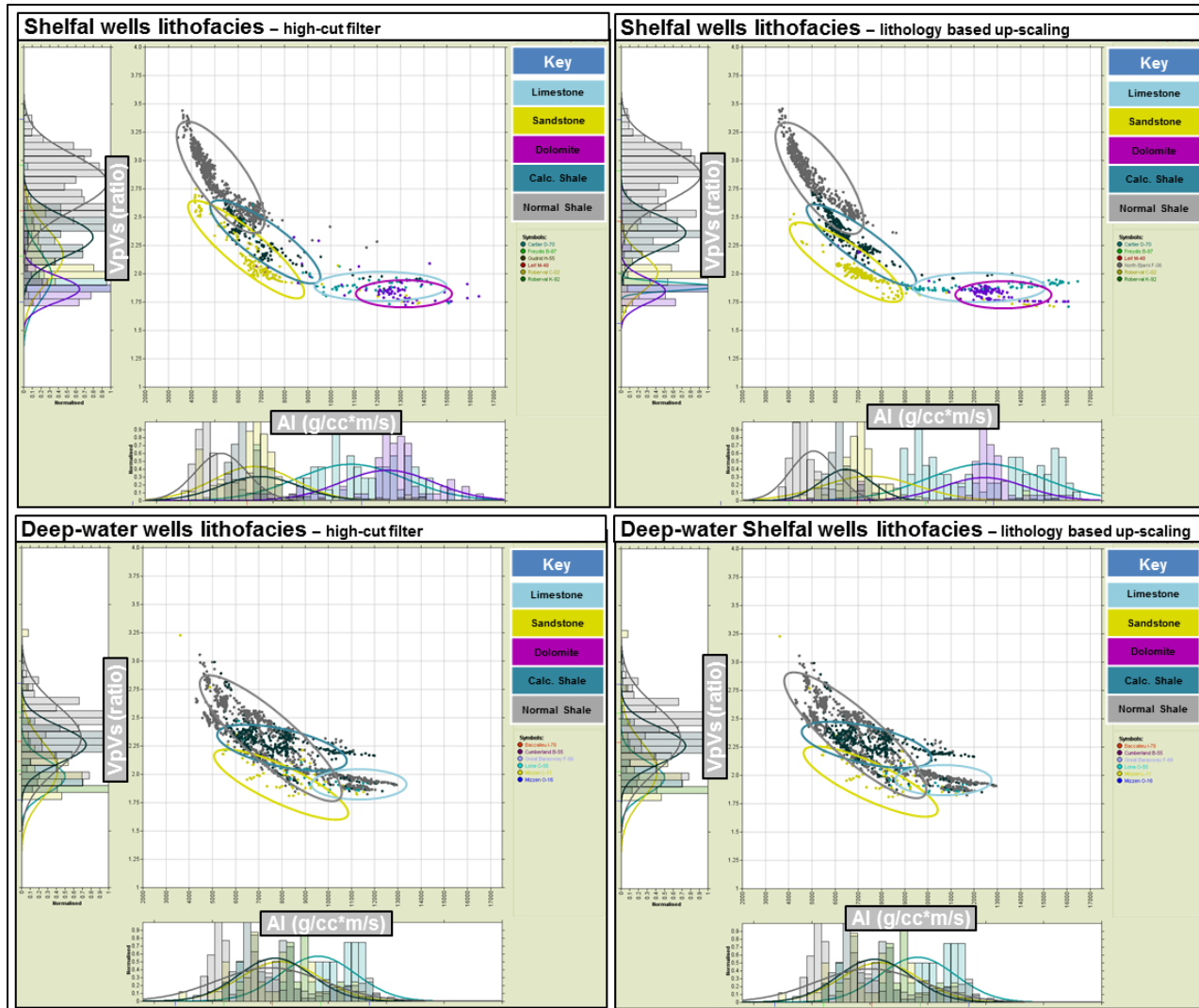


Figure 14: Up-scaled AI versus VpVs log data for the deep-water and shelfal wells. Yellow ellipse captures sands, grey ellipse normal shales, dark turquoise ellipse calcareous shales, light turquoise limestone and purple dolomite. These plots illustrate the differences between each of the identified facies in elastic response. While the shallower intervals encountered by the shelfal wells is generally larger, deeper formations in the deep-water wells shown more overlap.

The AI-VpVs cross-plots in Figure 14 display both shelf wells and deep-water wells and is coloured by facies. The upper two plots are for the shallow water shelfal wells (Cartier D-79, Freydis B-87, Gudrid H-55, Leif M-48, Roberval C-02, Roberval K-92), and the lower plots for the deeper wells (Baccaieu I-78, Cumberland B-66, Great Barasway F-66 and the Mizzen wells). The points here have been up-scaled, the left-hand plots have a high-cut filter applied to remove high frequencies not likely recorded by the seismic, the right-hand plots are points from the lithology-based up-scaling method

The data here has been conditioned (the log conditioning step is described later in this report) and up-scaled. These serve to illustrate the elastic response of the facies in the study well database.

As can be seen, the separation between facies is different for the shelf compared to the deep-water, this is a function of lithology (shale lithology and sand porosity and consolidation), saturation and burial depth. In the shelfal wells the sands are generally acoustically harder than the shales, with the shales having higher VpVs ratio values. The carbonates have lower VpVs ratio values than the sands and shales, and are significantly acoustically harder than the clastic sediments. In the deep-water wells the sands and shales have reduced separation in elastic response, this is due to the differential effect of compaction, both mechanical and chemical, in the sands and shales.

Capturing the change in elastic response of each facies with depth, lithology and saturation is therefore key to understanding the behaviour of each facies at a given lead or prospect.

If the area of interest comprises mostly a clastic environment, then most of the reflections will be associated with sand and shale boundaries and the contrast in impedances over these. During shallow burial, the sands will be relatively hard as compared to the surrounding shales, while the sands tend to be harder after increased burial depth and following onset of cementation.

Seismic lithofacies may also occur in very predictable patterns, both in terms of lateral and vertical distribution. This distribution is described and analysed in the field of (seismic) sequence stratigraphy. Combining these modes of analysis can help tremendously in seismic reservoir characterization and hence link sedimentary units and processes to depositional environments. Furthermore, as an AVO reconnaissance tool, the seismic lithofacies can also be used as blocks of averages to model blocky AVO responses for various combinations of cap rock properties and potential reservoir properties, and in probabilistic facies prediction via statistical rock physics (Mukerji et al., 2000).

2.2 Log Data QC and Conditioning

The log data QC and conditioning stage aims to investigate the quality, availability and consistency of the available log database. The aim is to ensure a reliable set of input curves for use in the rock physics, trend definition and modelling. This work is a key prerequisite to any rock physics analysis, as the log database is the foundation of the models and trends that are used to investigate and understand the seismic response.

2.2.1 Identification of erroneous elastic log responses

A set of QC logs is defined in order to assist the inspection of the elastic logs. These QC logs are:

- the dCal log (calliper minus bit-size), indicating where the hole is over (caving) or under (mud-cake build-up) gauge.
- dRho (correction applied to the bulk density log), high positive or negative corrections indicate reduced confidence in the measurement.
- the resistivity logs, used to indicate any mud filtrate invasion effects.
- compensated neutron log (CNL), indicates where sand/shale intervals are, and can be compared to the elastic log response.
- Poisson's ratio log (calculated based on the measured Vp and Vs log where available), indicates reasonable or otherwise relationships between the measured Vp and Vs logs, compared to the petrophysical interpretation (e.g. do we expect high PR in sands?).

The philosophy behind the log conditioning stage is to identify the best measurements in the study wells for each facies, and correct spurious measurements based on these. This is generally done via the use of lithology specific, end-member, empirical elastic trends between the p-wave velocity (Vp) and bulk density (RhoB) logs and the p-wave velocity (Vp) and s-wave velocity (Vs) logs. Care is taken to preserve genuine lithology effects, while removing spurious log data (a common example is the identification of coal responses as against washed out shale responses).

All the raw Vp and RhoB data is plotted in Figure 15, coloured by well (top left), burial depth (top right), facies (bottom left) and dCal (bottom right). As can be seen from these plots a lot of scatter is evident, with significant spread of data away from the main trend. A lot of this scatter is associated with high dCal values, indicating overgauge hole, and with shallow burial depth.

High scatter is expected when comparing well data across such a large geographic area (shelf to deep-water) and temporal range.

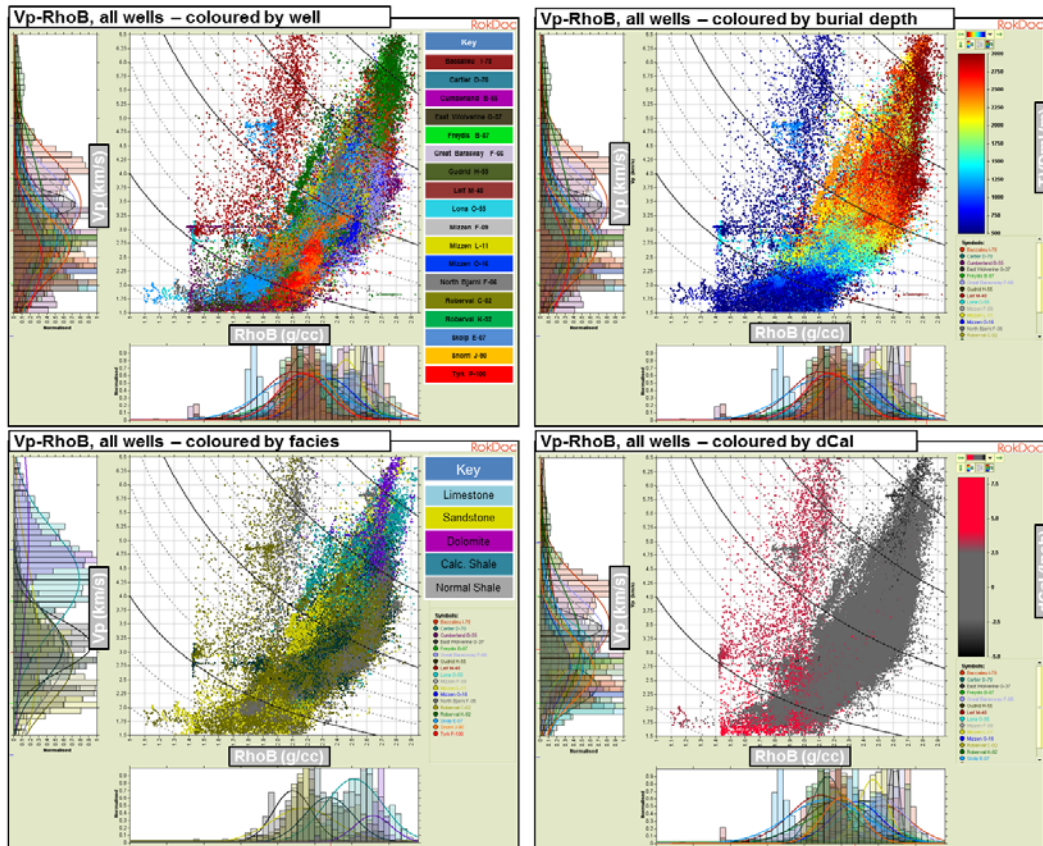


Figure 15: Raw Vp-RhoB data for all study wells, coloured by well (top left), burial depth (top right), facies (bottom left) and dCal (bottom right). The data is highly scattered, as might be expected when such high geographic and temporal spread of data is plotted. Clearly some data is effected by bore-hole conditions. The data is broken down into two subsets in order to further investigate the quality of the log responses.

To investigate further the wells are separated into those in the deep-water and those on the shelf. The shelfal wells are generally older, with most logs being acquired in the 1970s and 1980s. These wells also generally reach rocks at shallow burial depth. The deep-water wells were all drilled in the 2000s, with the exception of the Baccalieu I-78 well which was drilled in 1985 and the Cumberland B-55 well which was drilled in 1975. These wells generally encounter deeper formations. The aim is to investigate the quality of the well data by looking at those wells in a similar geographic location.

2.2.2 Shelfal Wells

The general quality of the Vp and RhoB data in the shallow-water wells was of lower quality, showing higher influence of borehole environment effects (predominantly bore-hole washouts and cavings) and of sections that were clearly logged through casing on the QC logs. This is primarily due to the vintage of the wells, with the data being acquired in the mid-70's through early 80's. This is specifically true for the Freydis B-87 well, where the entire Tertiary interval has a shift. In reviewing the shifted interval, it was found that the problem was not constrained to a specific hole section (i.e. it extended between and through multiple casing points). Nor did it appear to be related to drilling fluid composition or other sources of contamination. While this may be attributed to provenance changes relative to the other wells, without further information, the data from the Tertiary in Freydis was removed from the model dataset as it has low confidence associated. The Cretaceous interval in the Freydis well did appear to be consistent with the adjacent wells, and while lower confidence is associated with the data, it was included in this study.

Overall, the shale data were especially susceptible to bad borehole conditions, leading to multiple erroneous elastic log measurements where the log is wholly or partly reading the mud. Any sections that are identified as having been logged through casing are replaced. Figure 16 shows the raw Vp and RhoB log responses for the shelfal wells, these plots are coloured by well, facies, depth (below mudline) and dCal. As can be seen there is a significant scatter in this plot, with data from the Leif M-48 well clearly plotting away from the other well points. Many points here plot parallel to the RhoB axis (highly variable RhoB values for a consistent Vp), which raises suspicions about the RhoB log, these points are associated with high positive dCal values which indicate overgauge hole.

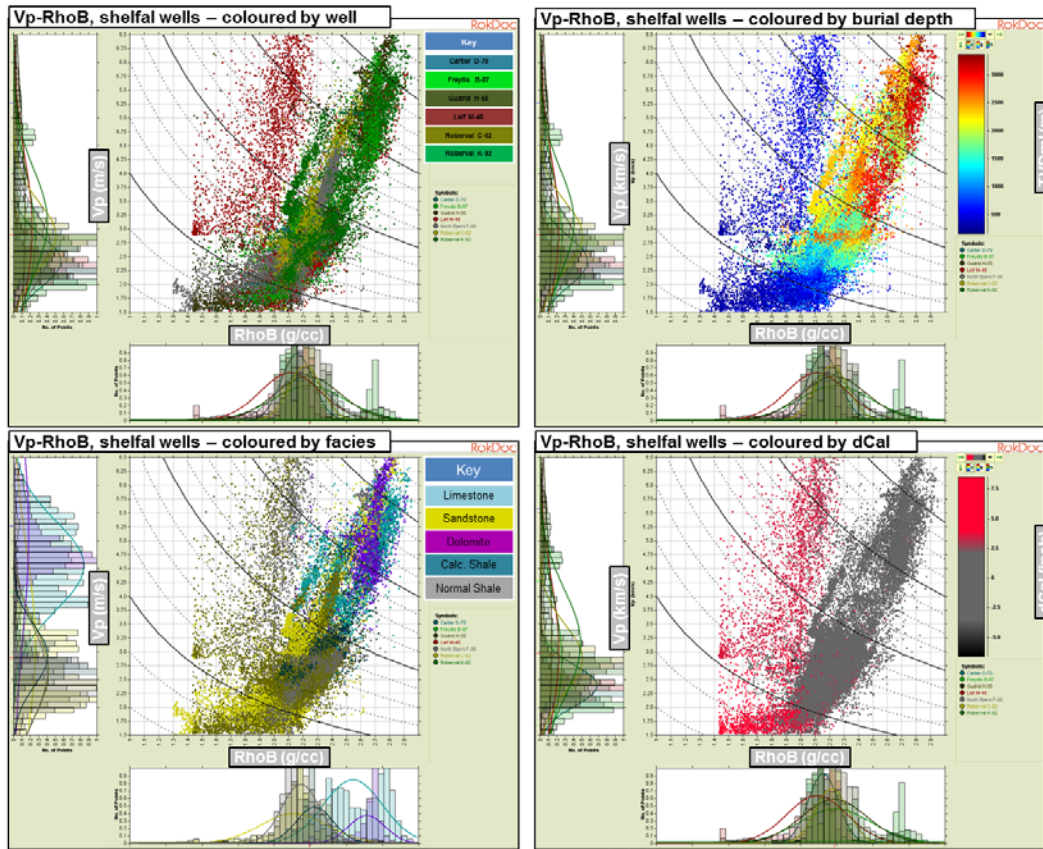


Figure 16: Raw Vp-RhoB data for the shelfal wells, coloured by well (top left), burial depth (top right), facies (bottom left) and dCal (bottom right). High scatter is noted, with a lot of data (particularly in the shallow section) associated with high dCal values indicating borehole washouts and cavings. The contours on this image indicate lines of constant AI, with the solid black contours ranging from 4000 g/cc*m/s in the lower left of the plot, and 20000 g/cc*m/s in the upper right of the plot.

The plots in Figure 16 indicate that much of the scatter in Figure 16 is associated with the shale facies (grey points in the lower left plot of Figure 16), and with shallow data. The indication being that the logs in the shallow sections of the wells are less robust than at depth (which might be expected due to the consolidation of the rocks, drilling parameters, logging through casing, hole size, etc.). It is also clear that a lot of the scatter comes from the Leif M-48 well.

More details of the parts of the log identified as being erroneous can be seen in Figure 17. Here two sections of the cross-plot are highlighted for the data at two of the wells. The central section of the Freydis B-87 well, drilled in 1975, shows highly varying dCal readings that indicate high borehole rugosity. The RhoB can be particularly sensitive to the smoothness of the borehole wall, as where the wall is highly rugose, the tool pad can lose coupling with the wall, allowing mud between the tool and bore hole wall. The result is that the density measurement does not solely respond to the formation, but is influenced by the mud density. Here points that plot

parallel to the Vp axis (i.e. formations with varying Vp measurements for constant RhoB measurements) indicate potential mis-readings in the density log. The density measurements in this section of the Freydis B-37 well have high correlation with the dCal log, are parallel to the RhoB axis in the Vp-RhoB plot, and are therefore replaced with a prediction from the Vp log. Another example of bad data in the shallow wells can be seen in the upper portion of the Leif M-48 well, this well was drilled in 1973. This well again has highly variable dCal values in the upper section, and lower than expected RhoB responses, there are also unrealistically high Vp responses which result in extreme acoustic impedance responses. It is evident that the measurements here are incorrect and should be replaced.

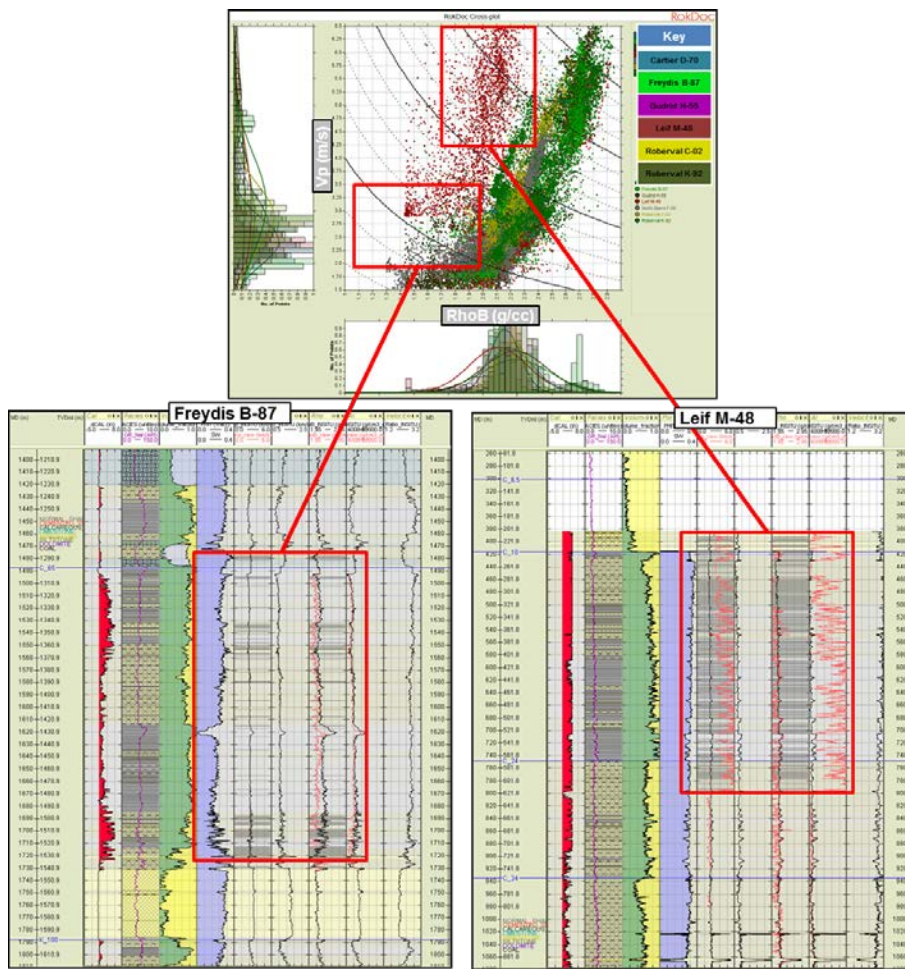


Figure 17: Shelfal well Vp-RhoB raw data is plotted in the cross-plot, with detail from Freydis B-87 and Leif M-48 shown below. These serve as examples as to where data is identified as being effected by bore-hole issues. The data in Freydis B-87 in the central interval of the well shows high dCal readings in the shale section, this is correlated to low RhoB values. The upper section of Leif M-48 shows very high Vp readings that are inconsistent with the shales immediately below, this section is identified as having been logged through casing, and is removed and replaced.

2.2.3 Flemish-Pass/Orphan Basin (deep-water) Wells

The general quality of the Vp and RhoB data in the deep-water wells was good, this is in no small part related to the fact that these wells are on average more recently drilled than the majority of the shelfal wells. With significant advances in both drilling and logging technology over 30 or so intervening years between when the shelfal wells were drilled and when the deep-water wells were drilled, improvements in log data quality are to be expected.

The raw log data for the deep-water wells are shown in Figure 18. Initial inspection reveals less scatter in the plot than for the shelfal wells, with a generally tighter cluster of data points. Some outliers are seen with very low bulk density measurements, and these are associated with high dCal readings in the Lona O-55 well.

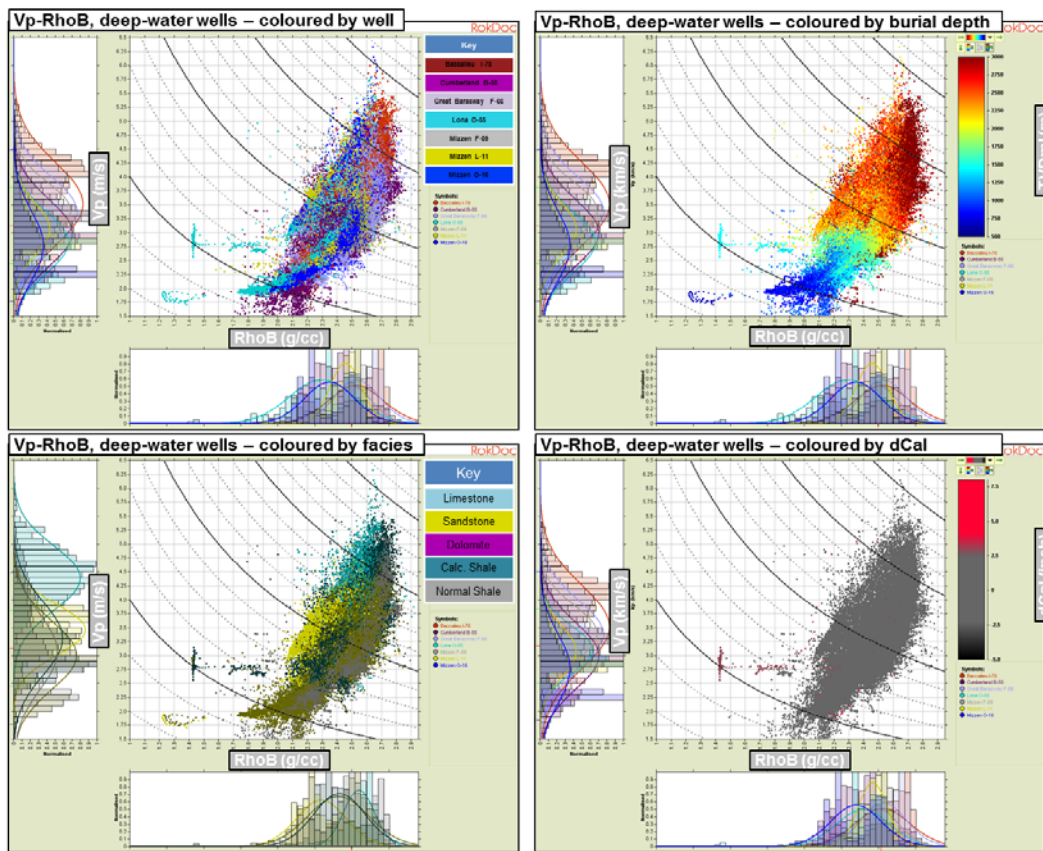


Figure 18: Vp-RhoB raw data is shown for the deep-water wells, coloured by well (top left), burial depth (top right), facies (bottom left) and dCal (bottom right). The data generally shows less scatter than for the shelfal wells, and is generally seen to be of better quality, this is probably a result of the fact that most of these wells are a lot more recently logged. The contours on this image indicate lines of constant AI, with the solid black contours ranging from 4000 g/cc*m/s in the lower left of the plot, and 20000 g/cc*m/s in the upper right of the plot.

Figure 19 highlights some of these areas at two wells (Lona O-55 and Cumberland I-78), and the data points are seen to be related to casing changes in each well.

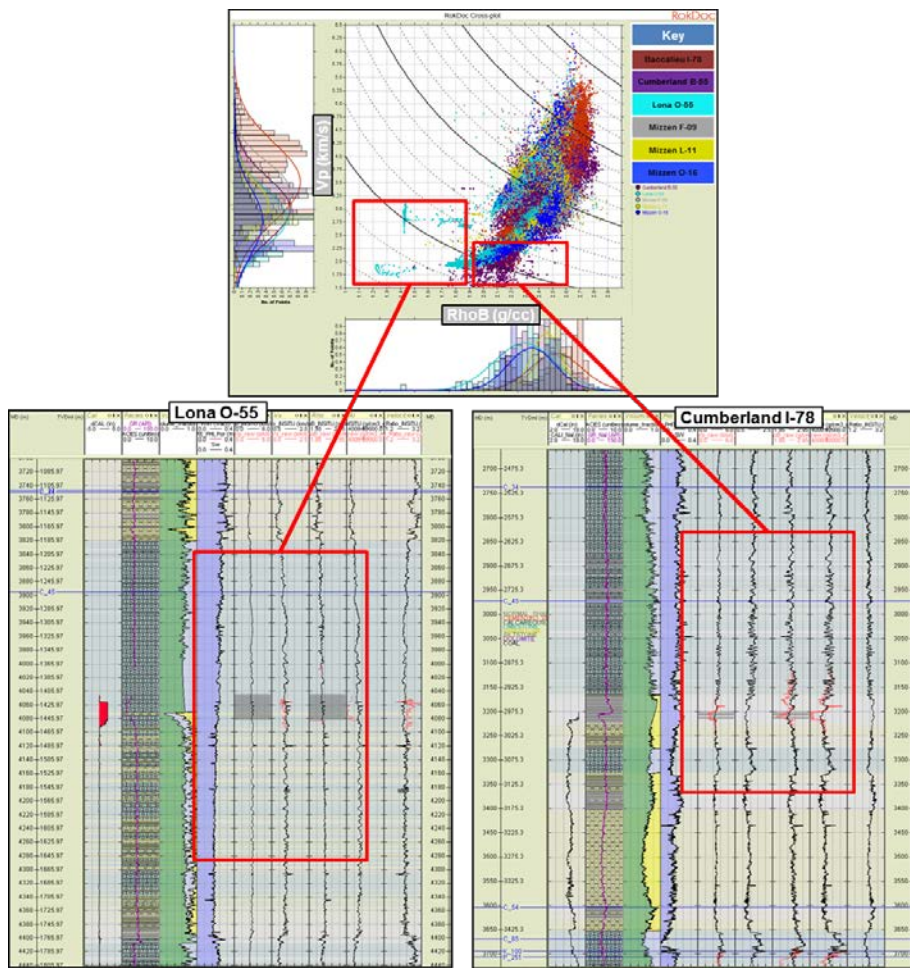


Figure 19: Raw Vp-RhoB data from deep-water wells is plotted in the cross-plot, with detail from Lona O-55 and Cumberland I-78 wells. Here data that plots in unexpected regions of the plot (e.g. lower than expected RhoB for a given Vp) is highlighted. In both of these wells these intervals are at casing points as indicated by the calliper logs. These sections are therefore flagged for removal and replacement.

2.2.4 Shear Log Data

In an study of the elastic properties of rocks shear information is key. This data provides information on the seismic response of the rocks away from zero-offset, and is therefore key in order to model the AVO response. An understanding of the shear behaviour of the facies to be includes in the study is therefore required, this is based on the available data.

Limited shear log was available in the study well database, and as might be expected based on the vintage of the wells this was in the deep-water only. Data was available from the Mizzen F-09, Mizzen O-16 and Lona O-55 wells.

The raw Vp-Vs data is plotted in Figure 20 coloured by well (top left), volume of shale (top right), facies (bottom left) and dCal (bottom right), the contour lines are lines of constant VpVs ratio (with the upper dashed line a VpVs ratio of 1.2 and the lower dashed line a VpVs ratio of 2.8). Vp-Vs trends from published data are plotted for reference (these are Greenberg and Castagnas sand and shale lines (pink and yellow), and the Murphy/Simm clean quartz line (red)). On initial inspection the data can be said to be overall of fair quality, with implied VpVs ratio values within reasonable bounds. However there are sections that require a closer look. In particular some shale points fall away from the main trend of shale points, with a cloud of shale data sitting on the expected sand trend.

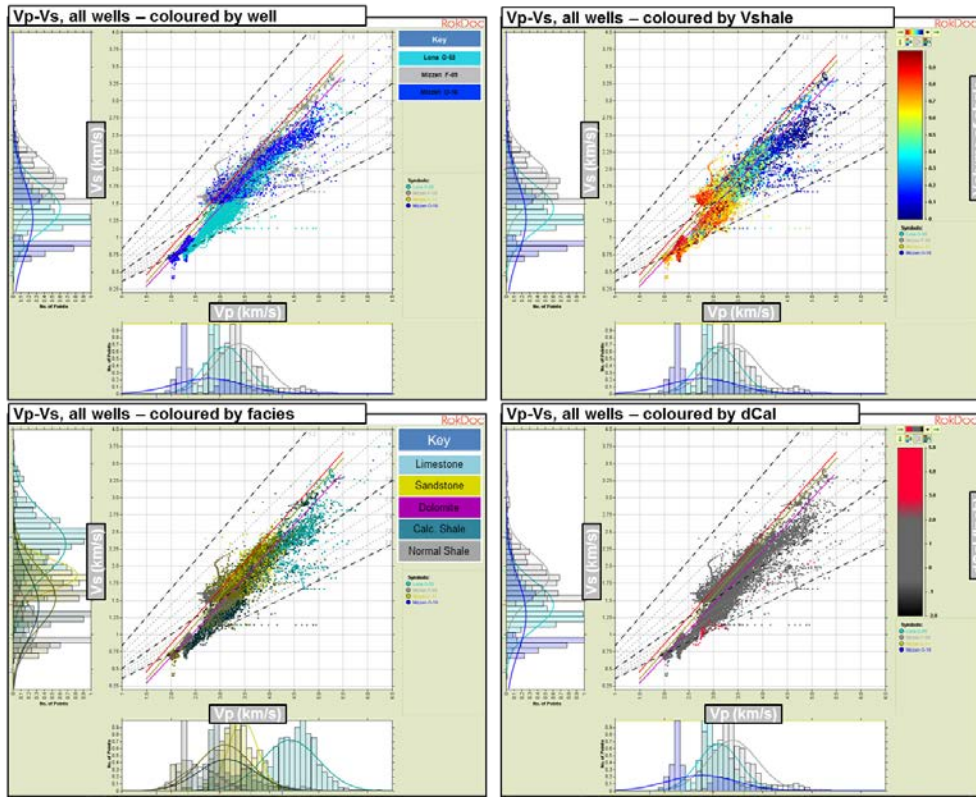


Figure 20: The raw Vp-Vs data is plotted here. This data is from the Mizzen O-16, Mizzen F-09 and Lona O-55 wells. These are deep-water recently drilled wells. The plots are coloured by well (top left), volume of shale (top right), facies (bottom left) and dCal (bottom right). Grey, dashed contours represent lines of constant VpVs ratio, and reference trends are plotted (red = Murphy/Simm pure quartz line, yellow and pink = Greenberg-Castagna sand and shale lines. The data is generally of fair quality, plotting within reasonable VpVs bounds. However some points require further investigation, with highly variable trends noted in the shales in particular.

As an example, highlighting these points on the well view (Figure 21) reveals issues with the shear log in Lona O-55. Throughout the Jurassic section in this well the raw shear log is seen to consist of multiple interpolated and linear segments through sparse data points. This data is therefore not representative of the geology of interest through this section, and including it in the study could result in false conclusions being drawn regarding the elastic response of these rocks.

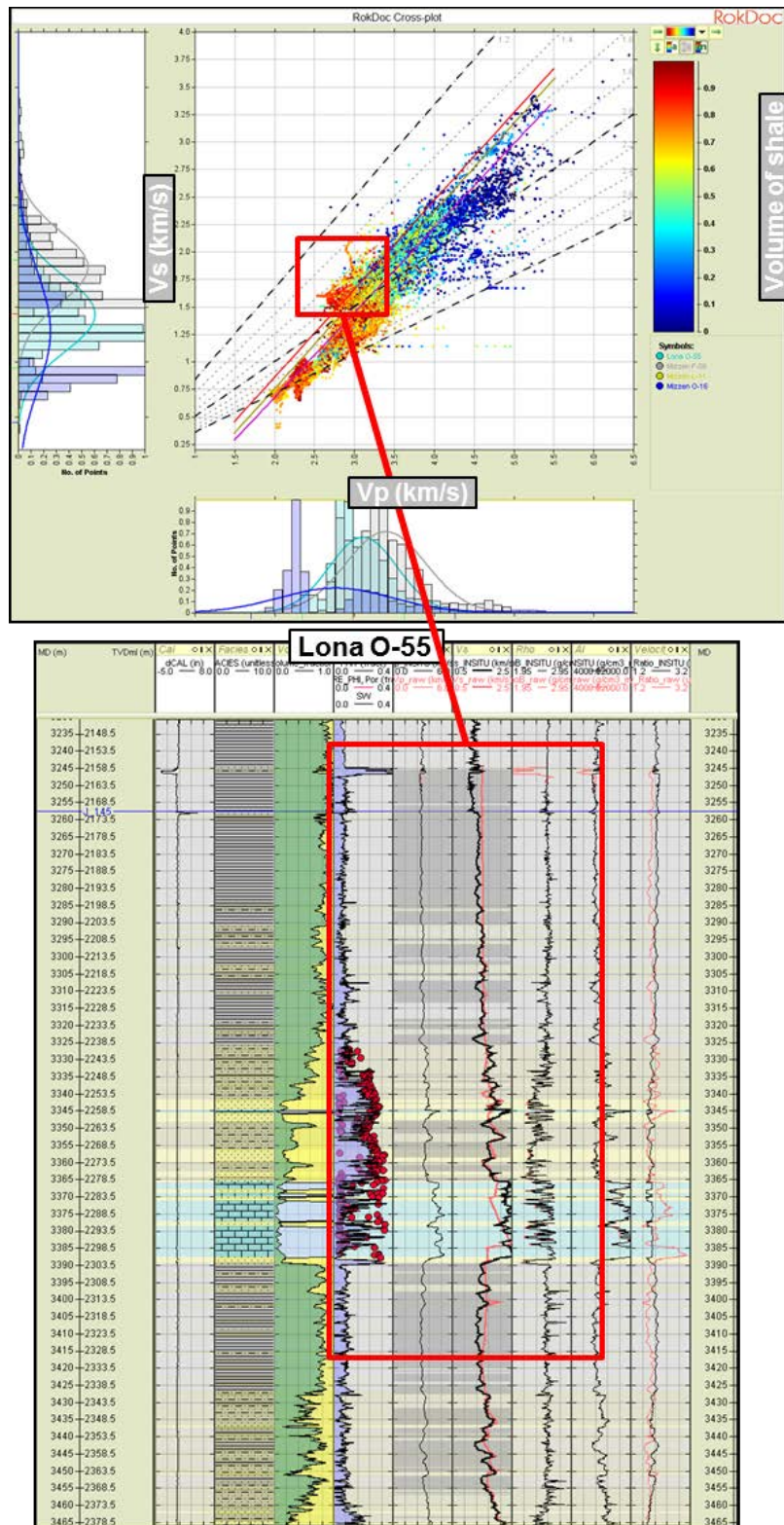


Figure 21: The available raw V_p - V_s data is plotted in the cross-plot, with detail from Lona O-5. Here data that plots in unexpected regions of the plot (here some shale points plot on the expected sand trend) is highlighted. The V_s log in this section of the well is seen to be highly erratic, not consistent with the V_p log, and has obvious linear interpolations and splines. This data is removed and replaced.

2.2.5 Elastic Log Conditioning

Once the log data of suspect quality is identified, it is removed and replaced using empirical trends defined based on the best quality data points.

The Vp-RhoB transforms shown in Figure 22 (upper plot) serves as a regional template for shallow-water settings and were used for calculating RhoB if Vp was known, and Vp if RhoB was known in the shallow water wells. The Vp-RhoB transforms shown in Figure 22 (lower plot) serves as a regional template for deep-water settings and were used for calculating RhoB if Vp was known, and Vp if RhoB was known in the deep-water wells.

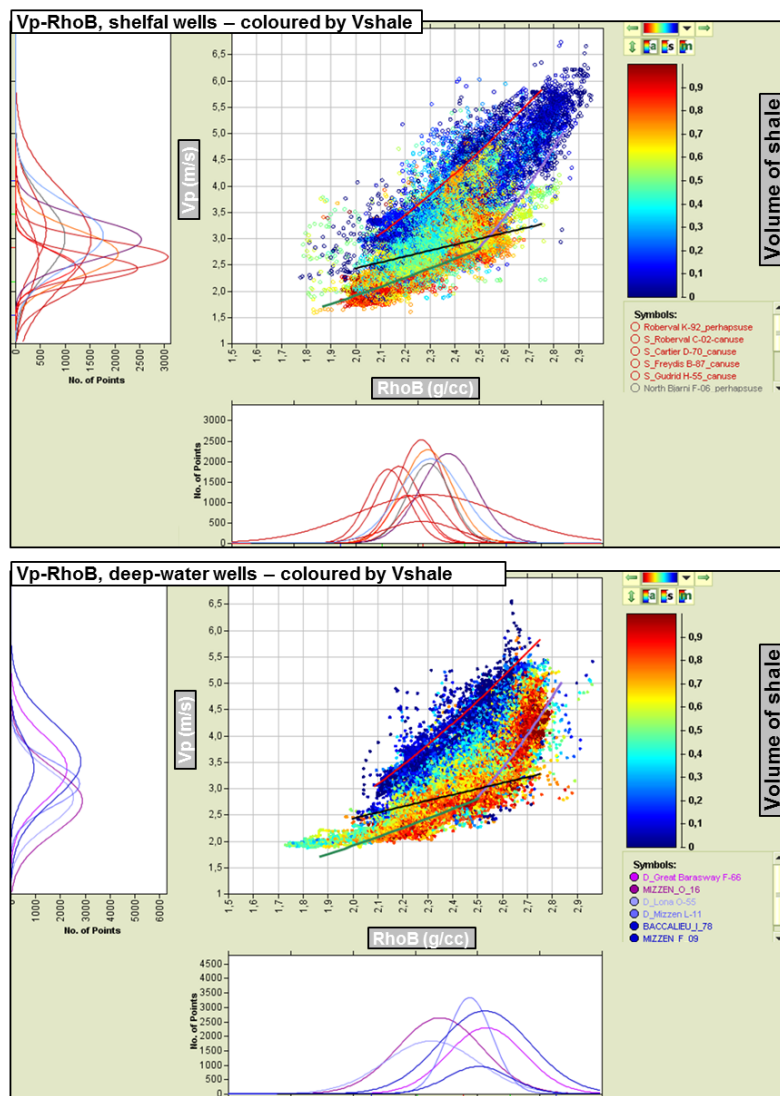


Figure 22: Empirical Vp-RhoB sand and shale transforms, the upper plot is for shelfal wells, the lower for deep-water wells (red line = slightly cemented sands, black = uncemented sands, purple = cemented shales, green = normal shales).

Two example well panels are shown in Figure 23, these show the wells pre- and post-conditioning.

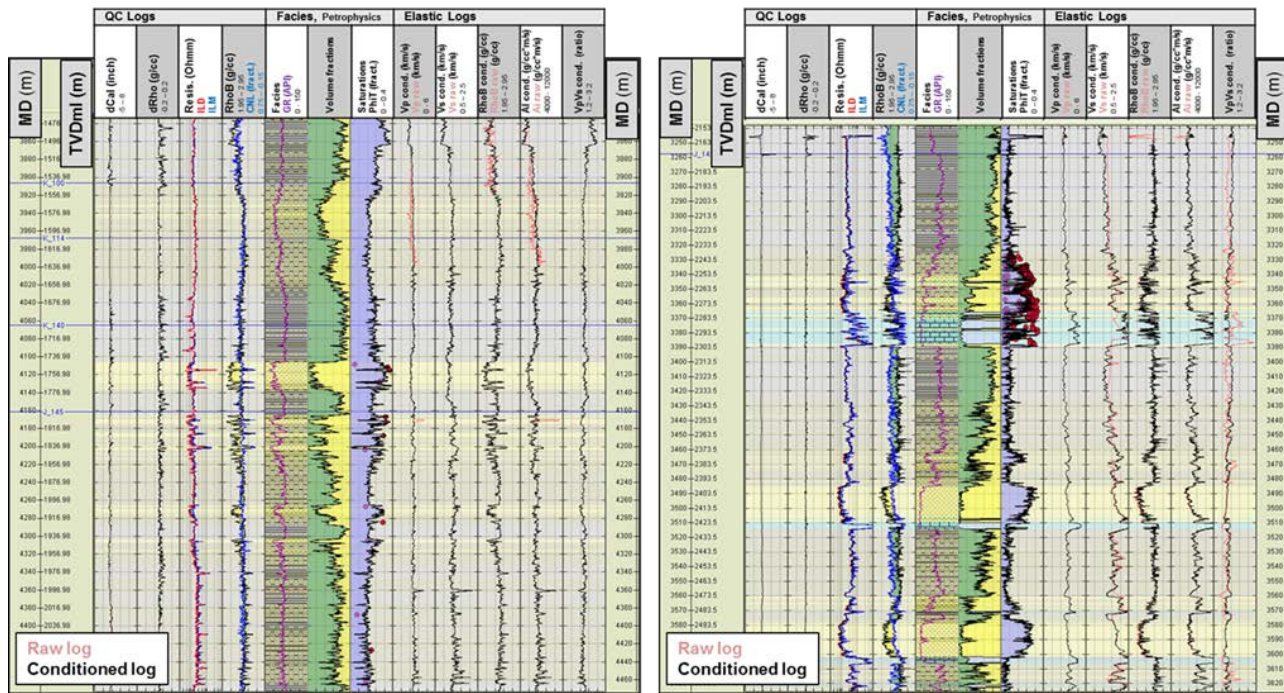


Figure 23: Example well panels (Great Barasway F-66 on the left, and Mizzen F-09 on the right) showing the elastic log data pre and post conditioning. The pink logs are the raw logs, and the black the conditioned.

2.3 Sands

Sands and sandstones can be comprised of many mineral constituent combinations (e.g. quartz, calcite, feldspar, dolomite, clay).

Folk (1974) gave a good overview of how to classify sandstones according to varying degree of feldspar and rock fragments (Figure 26), but does not include much discussion on how clay interacts with the load supporting grains in the rock. Clay content plays a vital role on the reservoir properties, but equally/more important is how the clay particles are distributed in the pore system as that can have a devastating effect on reservoir properties and performance.

Thomas and Stieber (1975) developed a model to calculate porosity in thinly bedded sands and shales, with the assumption that a mixture of clean, high porosity sands, and low porosity shales can construct the rock in the interval of interest. These configurations of sand-shales mixes will

impact the elastic properties as well (Marion et al., 1992; Dvorkin and Gutierrez, 2001; Katahara, 2004; Skelt, 2004).

The offshore Newfoundland region as a whole has a significant amount of wells drilled on the shelf, but one major problem with these is that they were drilled thirty to forty years ago, and hence the quality of the log data is highly variable. One of the wells used for characterisation of the sands located on the present-day shelf (Roberval C-02) had petrography performed and thus may act as a calibration point for the other wells in that region and their associated rock properties. However, no core data were available for final calibration of density-derived porosities.

For the wells drilled in the deeper waters of the Orphan Basin, Mizzen O-16 had special core analysis performed (thin-section analysis, core porosity, permeability etc.), while Lona O-55, Great Barasway, Mizzen L-11 and Mizzen F-09 had analysis performed on sidewall cores. As there was good agreement between sidewall and conventional core-based porosity, and the wells are recently drilled (i.e. modern sidewall coring techniques applied), it was concluded that the sidewall cores represented reliable porosity data for use in calibrating the log derived porosity. The shelfal wells typically consist of clastic environments, with occasional formations prone to calcareous shales, limestones and dolostones (diagenetic and in situ).

Targeted reservoir sands in the wells used for this study range from Tertiary to Cretaceous in the shelf wells and Tertiary to Jurassic in the deep-water wells. Four wells from the shelfal area were selected (Roberval C-02, Gudrid H-55, Freydis B-87 and Cartier D-70) while six wells from the deep-water regions were selected (Great Barasway F-66, Lona O-55, Mizzen L-11, Mizzen F-09, Mizzen O-16 and Baccalieu I-78) to represent the best available sand reservoir intervals. The wells represent the sands, both in terms of clay content and related reservoir quality, but also from a log quality point of view. At this time it is worth mentioning that all sands that contain hydrocarbons were brought back to brine (only Mizzen O-16 here), and that potential mud filtrate invasion effects have been corrected for, before proceeding with more detailed analysis of the sand properties.

2.3.1 Sand Rock Physics Models – A Universal Sand Model

The behaviour of sandstone elastic response as a function of mechanical and chemical compaction can be captured using theoretical and heuristic contact models (e.g. Avseth et al., 2005). These models aim to capture the effect of different geological processes in terms of their effect on the elastic behaviour of the sands. In particular, these processes are sorting and diagenetic changes.

Previous studies have recognised that the slope of sandstone velocity-porosity trends is variable and depends on the nature of the processes controlling porosity loss (e.g. Dvorkin and Nur, 1996).

Mechanical compaction trends can be captured by modified lower Hashin-Shtrikman bounds, and chemical compaction trends can be captured by modified upper bounds. Figure 24 shows the typical elastic moduli – porosity pathways for mechanical and chemical compaction in sands.

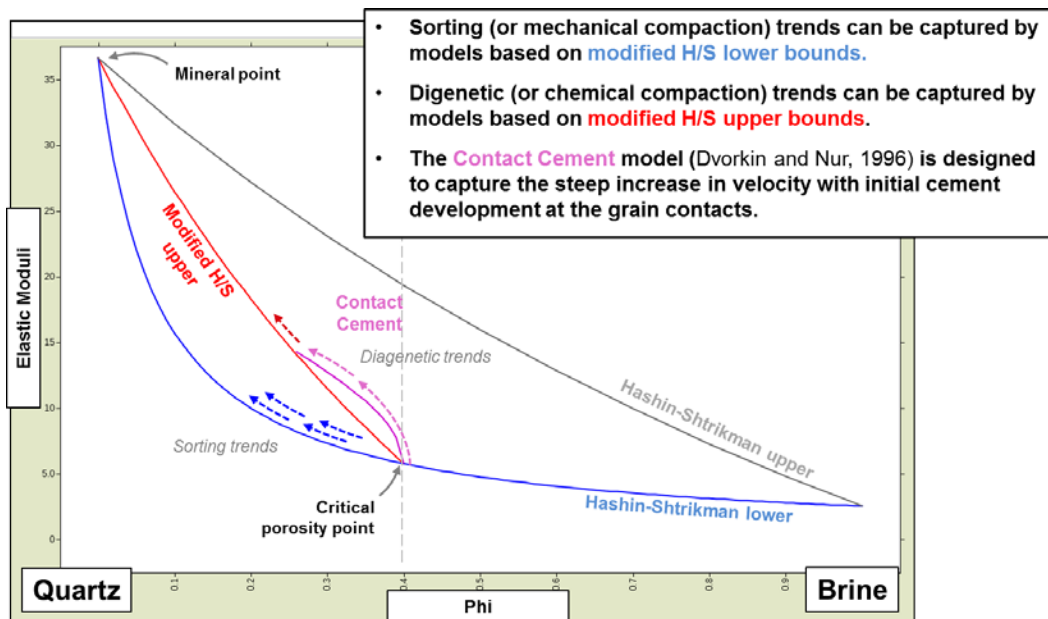


Figure 24: Sandstone compaction pathways. Mechanical compaction pathways can be captured using lower Hashin-Shtrikman lower bounds (blue), chemical compaction pathways can be captured using modified upper Hashin-Shtrikman pathways. The sand points (in elastic moduli – phi space) move between the critical (or depositional) porosity point and the mineral point. The Contact Cement model captures the behaviour of sands with initial cementation at the grain contacts.

Rock physics models can be developed that capture the porosity-elastic moduli (hence referred to as poro-elastic) behaviour of sandstones as a function of mechanical compaction and grain

contact cement content. The Contact Cement model (Dvorkin and Nur, 1996) shown in Figure 24 is a theoretical upper limit for initial grain contact cementation in perfectly sorted sands.

Another, more useful model, is known as the Constant Cement model (Avseth, 2000), this is shown in the schematic shown in Figure 25. This combines the effect of cement at the grain contacts (using the cementation theory of Dvorkin et al. (1994)) and the effect of sorting via the use of modified lower Hashin-Shtrikman bounds. Lines of constant grain contact cement content are generated, against which the measured data can be compared. In this chapter the data in the study wells are compared against these types of bounds and models in order to investigate the poro-elastic effects seen in the dataset. In subsequent chapters these models will be used to predict the poro-elastic response away from well control. It is important at this stage that any references to sandstone cement content are referring to grain contact cement only, and not pore filling (or occluding) cement.

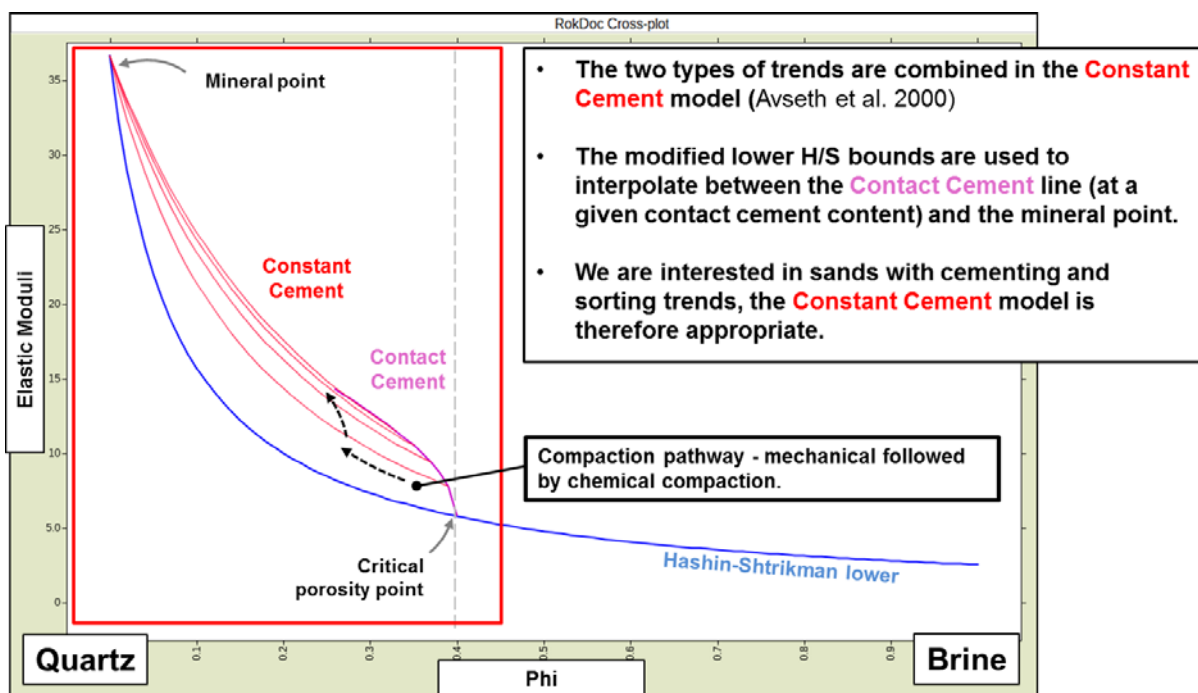


Figure 25: The Constant Cement model captures the behaviour of sands with defined constant cement at the grain contacts, and captures both the mechanical and chemical compaction pathways.

The model is calibrated to the available elastic log data and petrophysical interpretation, and used to investigate the responses seen in the study wells in this chapter. Available petrographic core analysis can then be used in conjunction with the model to further interrogate the log responses the study wells.

2.3.2 Shelf Wells (Present-day Shallow-water)

An investigation of four wells in the Tertiary and Cretaceous are shown here to illustrate how the rock properties of the sands might affect seismic amplitude. Figure 27, show the log views for Cartier D-70, Freydis B-87, Roberval C-02 and Gudrid H-55 (from left to right), and show GR and Vp over zones where GR both is low, to capture non-clay clastics, and high, to capture the surrounding clay-rich shales. The orange bars in Figure 27 correspond to intervals of high net-to-gross, with multiple clean sandstone beds, while the green bars correspond to cemented and lower porosity zones. The orange bar in Freydis B-87 shows a very heterogeneous interval, with some cleaner sand beds toward the base. These sands are separated out by the petrophysical interpretation and facies definitions (see section 1.1.1). The orange bar in Cartier D-70 corresponds to what appears to be a relatively clean interval, intercalated with shale stringers. Common to all wells are that the sands appear to have a higher velocity than the shales above and below, and that cemented sand velocities exceed both sands and shales.

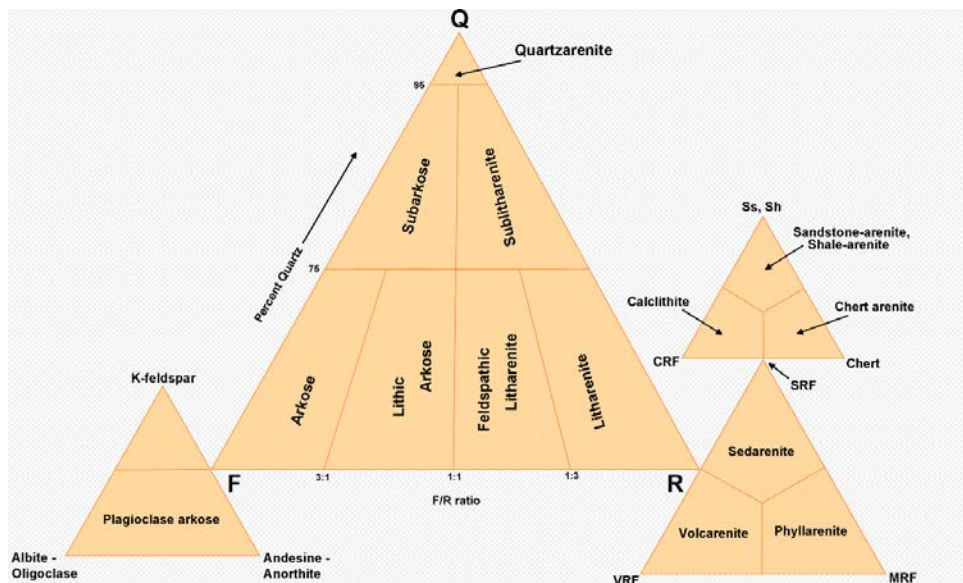


Figure 26. Folk's classification of sandstones

Three of the wells belong to the same stratigraphic unit in the Tertiary, age-equivalent to the Cartwright Formation (T54-T65 Ma), while the Freydis B-87 is Cretaceous in age and belongs to the T65-C114 Ma interval (age-equivalent to the Markland/Bjarni formations). Assuming a temperature gradient of 30 degrees Celsius per kilometre will give an onset of quartz

cementation (Bjorlykke et al., 1999) in the range of 2000-2500 TVDmsl in the area it seems that only Roberval C-02 has been buried deep enough to generate quartz-cement. The other three wells seem to be buried too shallow for any quartz cementation at the present day. Another complicating factor relating to cementation in sands is that the area has in places, been subjected to uplift, with the consequence that the sediments might have been buried below the onset of quartz cementation and hence be cemented despite not currently being buried deep enough. Also calcite/dolomite cementation (Dutta et al., 2008) may be present, which is not temperature dependent.

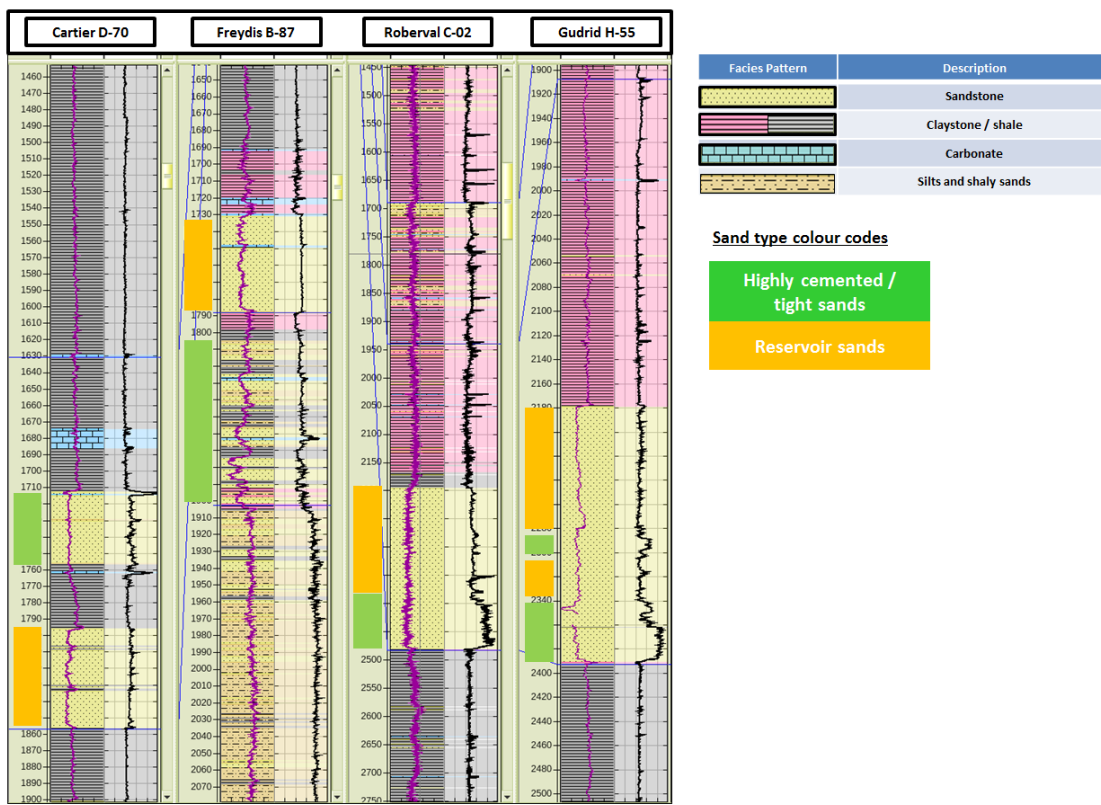


Figure 27. Log views of GR and Vp for Cartier D-70, Freydis B-87, Roberval C-02 and Gudrid H-55 (left to right). Orange bars indicate reservoir sands, and intervals of high net-to-gross, blue bars indicate highly cemented and low porosity sands.

Figure 28 shows cross-plots of Vp versus PhiT for the wells shown in Figure 27 (the colours in this plot correspond to those in the well tracks, Figure 27), and to understand better the processes behind the observed patterns, various rock physics models are superimposed on top of the data, the contours here are the slightly cemented model (Constant Cement model), and a friable shale model (shown in green). The lower green line is the friable shale trend, the steep red line is the Contact Cement model, the other black lines are the Constant Cement line for

pure quartz (various grain contact cement contents represented by contour lines). Initial sand porosity is set to 40% (though it might be lower/higher, depending on initial sorting/packing arrangement), while cementing porosity is 38% for the quartz (it is then assumed that contact cement occupies 2% of the pore space in the initial sand).

The intervals represented by the orange bars in Figure 27, for all four wells, seem to fall in between the uncemented line and the slightly cemented line, which is likely indicative of slight cementation – see Figure 29. Thinking about quartz cement, and assuming that the wells are at maximum burial today, only Roberval C-02 may be in the right depth range to exhibit the effects of grain contact cement, if temperature is the crucial part for onset of quartz cementation. Indeed, Roberval C-02, which is buried the deepest at present time, is actually slightly cemented (mostly dolomite cement, but also calcite cement and to a lesser degree, quartz cementation as quartz overgrowths), and this is confirmed by scanning electron microscope data (Figure 29).

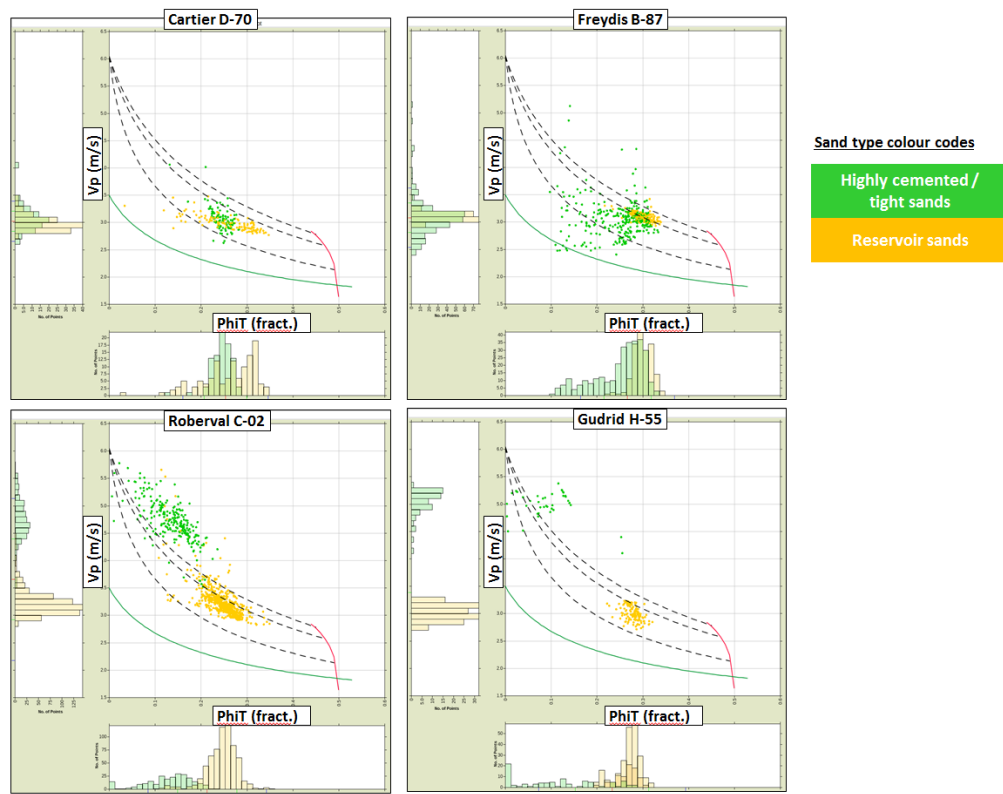


Figure 28. V_p versus Φ_{IT} ; upper left is Cartier D-70, upper right is Freydis B-87, lower left is Roberval C-02 and lower right is Gudrid H-55. The colours here correspond to the intervals in Figure 27. The black contours are the Constant Cement model (introduced earlier) representing slightly cemented sands, the Friable shale model is shown in green, representing the shale trend. The red line represents the theoretical initial cementation trend for a random pack of spheres.

Unfortunately, no firm values on the actual amounts of cement in the pores in Roberval C-02 were available, neither was this kind of analysis available for the other shelf wells, but it does show that the cementation theory allows for a proper understanding of how the velocities change with changing compaction regime (mechanical to chemical).

PLATE 3

Scanning electron micrographs showing diagenetic characteristics of Gudrid sandstones from depths of 2235m (A and B) and 2295m (C and D).

- A. Dissolution microporosity in detrital grain of potassic feldspar. (230X)
- B. Pitted quartz overgrowths (Q) in rock fragment composed of quartz and degraded feldspar. (790X)
- C. Dolomite cement (D) with dissolution pores developed along cleavage surfaces. Overgrowth surfaces are visible on quartz grain (Q) that passes beneath the dolomite. The upper surface of the dolomite bears the imprint of two or more detrital grains that have been broken away from the chip sample. Kaolinite (K) occurs in a secondary pore and is shown at higher magnification in D. (400X)
- D. Degraded kaolinite booklet (K). Authigenic dolomite (D) occurs in lower left quadrant and possibly also in upper centre. (2000X)

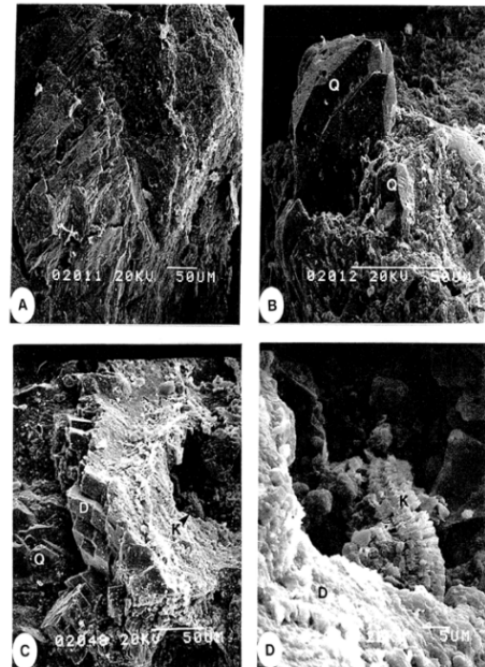


Figure 29: Description of results from Scanning Electron Microscope study taken from Roberval C-02 Report – Petrography of Tertiary Sandstones.

After a closer look at the intervals represented by the green bars (in Figure 27 and Figure 28), it is immediately clear that the high velocities and low porosities in Roberval C-02 and Gudrid H-55 are associated with highly cemented intervals. However, the trend in Cartier D-70 has a relatively flat behaviour and it seems more like a trend characteristic of poor sorting/poor sand quality. Jizba (1991) looked into the details of how clay content impacts cementation in sands, and concluded that increasing clay content means decreasing cement volume (and vice versa). Therefore, the flat trend might also be due to a reduction of the cement content in the pores, with an increase in clay content simultaneously, thus counteracting the cementation in this zone.

In Freydis B-87, the interval belonging to the green bar is indicated in the petrophysics as a very heterogeneous interval, which is confirmed by the cross-plot, where the data points cover clean shales and clean sands, and everything in between the rock end points.

2.3.3 Deep-water Wells

For the purpose of diagnosing the sediments (the sands first and foremost) the models superimposed on the cross-plots are the same as for the shelfal wells, except for the quartz maximum constant cement line having been increased to better match the data.

Panels for four wells from the deep-water bathymetry in the Mizzen area are shown in Figure 30, zones where GR is low, to capture non-clay clastics, and high, to capture some of the surrounding clay-rich shales and interbedded sand and shale sequences, are highlighted.

Within these packages different sequences are identified based on the petrophysical interpretation, these sequences are now investigated in terms of Vp-PhiT response, with comparison to rock physics models. The sequences are indicated in the well panels (Figure 10) with coloured bars, the Vp-PhiT points from these intervals are then plotted in Figure 31 using the same colour scheme. Here interbedded, blocky and fining upwards sand/shale sequences are identified within the sand facies based on the petrophysical interpretation.

In Baccalieu I-78 a sand at 3180m MD shows an interbedded nature with layering of sands and shales within the interval, this is indicated by a green bar in Figure 30. Deeper in this well an apparent fining upward sequence is noted at around 3720m MD (marked with a red bar in Figure 30), which is usually found in fluvial environments with depositional energy varying laterally.

The other wells, Mizzen F-09, Mizzen O-16 and Mizzen L-11, all have blocky GR signatures, and are clean sands, these are marked by orange bars in Figure 30. At 3320m MD in Mizzen F-09 an apparent fining upward sequence is noted, and is marked by a red bar in Figure 30.

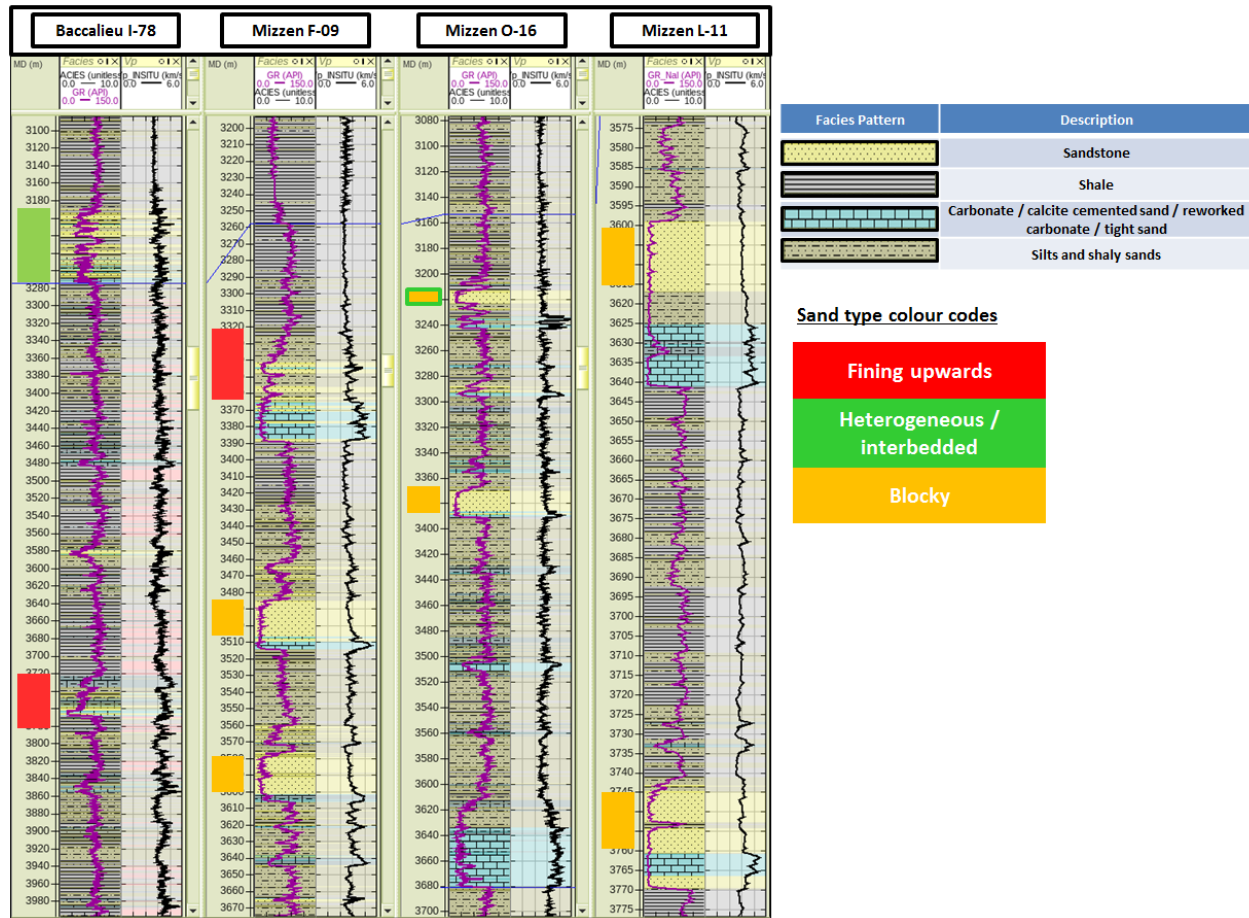


Figure 30: Well log panels for deep-water wells in the Mizzen area. From left to right: Baccalieu I-78, Mizzen F-09, Mizzen O-16 and Mizzen L-11. The facies logs show sands, shales and silts. Carbonates, re-worked carbonates and cemented sandstones are all included in a single facies. Blocky, interbedded and fining upwards sequences in the sands are represented by orange, green and red bars respectively. The Vp-PhiT data highlighted by these bars are plotted in Figure 31.

Reviewing the Vp-PhiT cross-plot for Baccalieu I-78 (upper left in Figure 31), the data points from the fining upward and interbedded sequences (red and green bars in Figure 30 respectively) seem to show a V-shaped trend, this pattern is also observed in the Vp-PhiT data from Mizzen F-09 (upper right plot in Figure 31).

This V-shaped pattern has been extensively studied during the last decade (e.g. Dvorkin and Gutierrez, 2002; Dutta et al., 2009; Dejtrakulwong, 2012), and indicates the effect of dispersed clay or shale in the system (Figure 33 and Figure 34). Arrows connecting the clean sand point with the clean shale point are shown in the cross-plot, the intersection between these arrows (the point of the V) is the point at which the sand porosity is filled with dispersed clay (see Figure 33 and Figure 34). The clean sand points seem to follow the slightly cemented sand

lines, so it is anticipated that the model works for these sands, even without corroborating cement volume from thin-section analysis.

In Figure 31 the upper right cross-plot shows the Vp-PhiT data from Mizzen F-09, and as can be observed there is a large variation in the data. The blocky GR signatures, indicated by orange bars in Figure 30, capture clean sands, and it can be seen that these points plot consistently across the four wells included in this analysis (see orange coloured points in all four cross-plots in Figure 31).

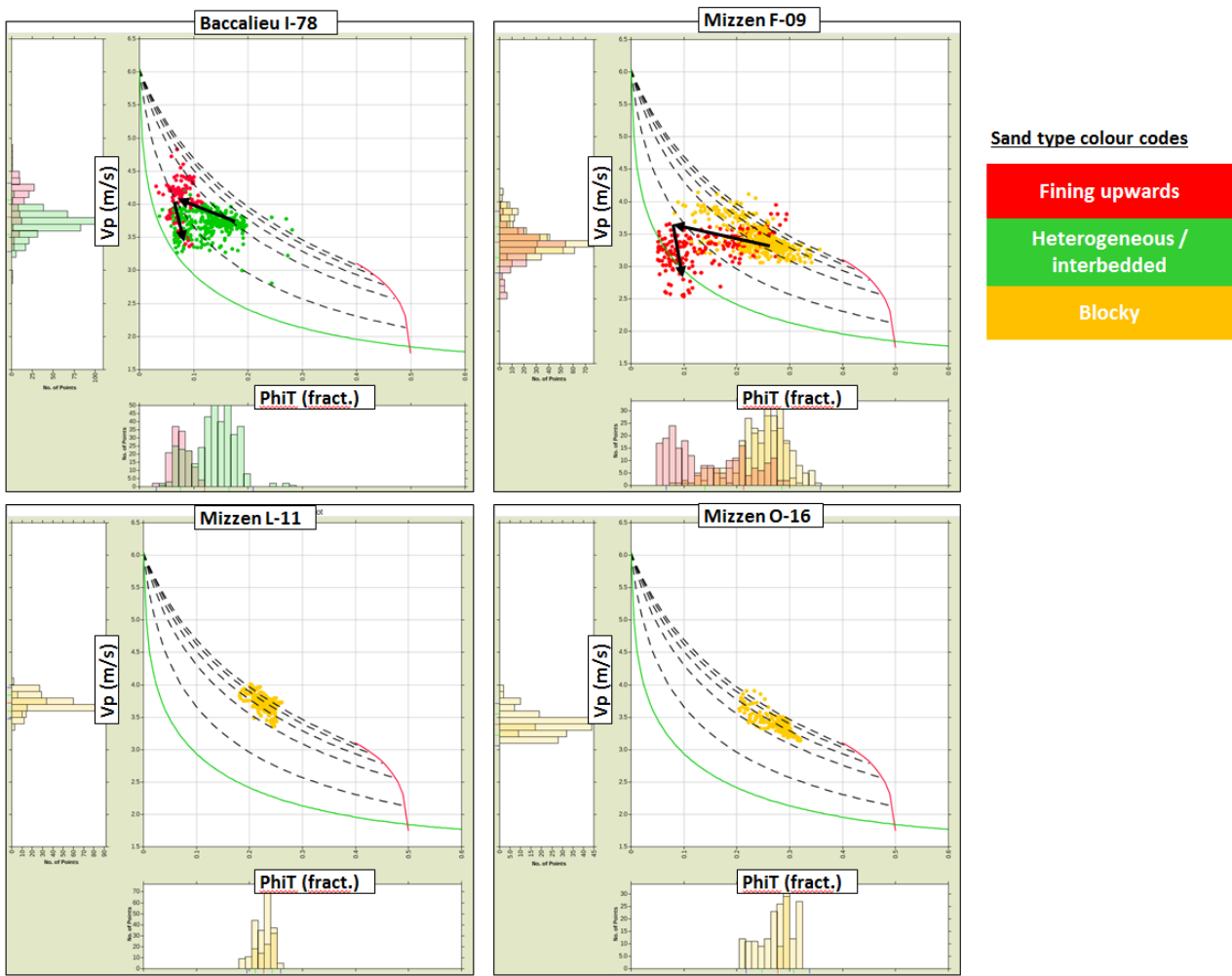


Figure 31: Vp versus PhiT for deep-water wells in the Mizzen area. Clockwise from top left: Baccalieu I-78, Mizzen F-09, Mizzen L-11 and Mizzen O-16. The green line is the shale line, the dashed lines are sandstone trends for varying contact cement content, and the red line is an increasing contact cement line. The intervals plotted here are indicated in Figure 30 where the same colour scheme is used.

The red points represent a fining upwards sequence, where the V shape pattern previously mentioned is observed.

The lower right cross-plot in Figure 31 shows Vp-PhiT data from Mizzen O-16, one of four deep-water wells with hydrocarbons in-situ oil (Bay du Nord C-78 & C-78z and Harpoon O-85 – log data was not available for these additional wells at the time of this study). In Figure 30, the oil column resides in the clean blocky Tithonian sand represented by the orange bar with the green outline, below this at 3360m MD another clean blocky Tithonian sand is present with brine saturation.

As previously mentioned, the quartz constant cement line had to be increased to capture the sands better for the Flemish Pass region, and this is confirmed quantitatively by thin section analysis on sands in Mizzen O-16 (Figure 32). Other cement types, as dolomite cement and calcite cement are also present, most in the form of occluding cement. It is important to emphasize that even though the cementation theory have been successfully applied to the data, and to some extent confirmed by thin section analysis, there might be contacts that haven't been cemented yet (see Section 2.2.1.2.1), hence leaving behind a patchy cement scenario (Avseth et al., 2012). The last well from the Mizzen area, Mizzen L-11, is in the lower left of Figure 31 and has clean blocky sands in the zones represented by the orange bars shown in Figure 30.

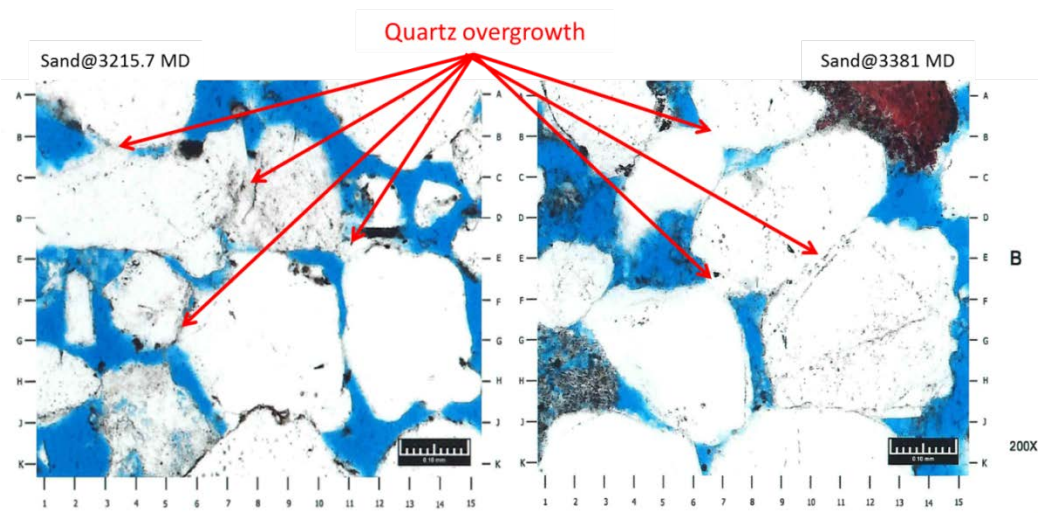


Figure 32: Detailed thin section analysis from the Core Analysis Report for Mizzen O-16 (Core Analysis Report – StatoilHydro Canada Limited. CA Mizzen O-16 Well, Mizzen Field, Offshore, Newfoundland, Final Report, Rotary Sidewall Core. Weatherford Laboratories).

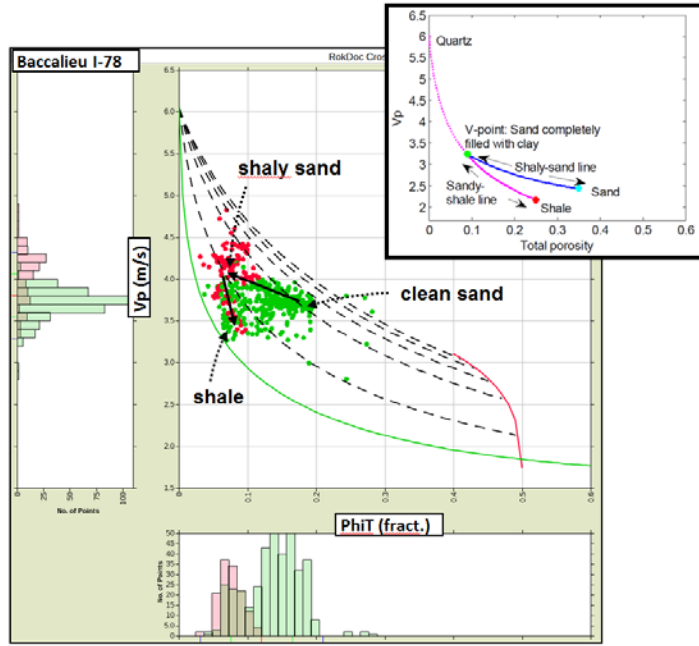


Figure 33: V_p versus Φ_{IT} for Baccalieu I-78, with a schematic model (model after Dvorkin and Gutierrez, 2002). The data plotted here is from the intervals indicated by corresponding colours in Figure 30. The V-shape in the V_p - Φ_{IT} data is interpreted to be due to the presence of dispersed shale. The green line is the shale line, the dashed lines are sandstone trends for varying contact cement content, and the red line is an increasing contact cement line.

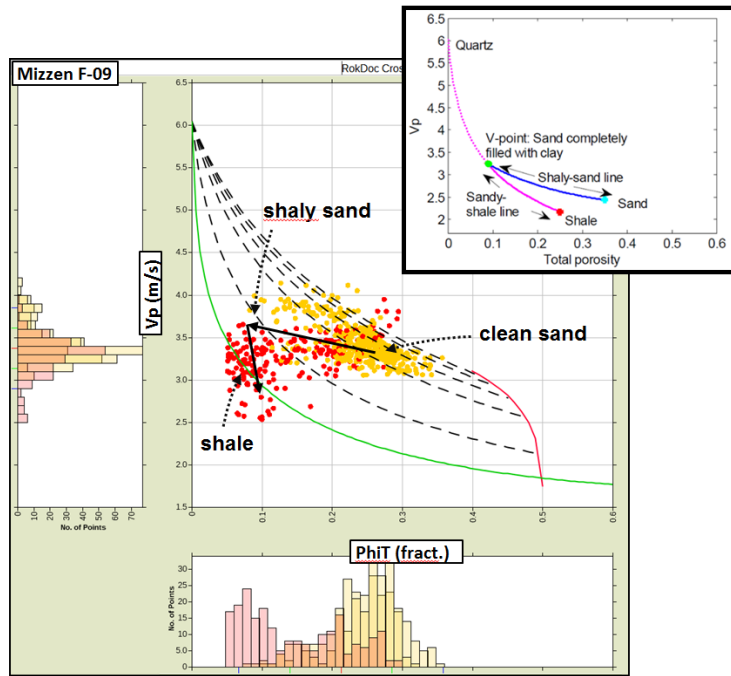


Figure 34: V_p versus Φ_{IT} for Mizzen F-09, with a schematic model (model after Dvorkin and Gutierrez, 2002). The data plotted here is from the intervals indicated by corresponding colours in . The V-shape in the V_p - Φ_{IT} data is interpreted to be due to the presence of dispersed shale. The green line is the shale line, the dashed lines are sandstone trends for varying contact cement content, and the red line is an increasing contact cement line.

Figure 35 shows two wells from the Orphan Basin, Great Barasway F-66 and Lona O-55, here various intervals that have low GR readings are highlighted with orange and green bars. The orange bars indicate sands that have a blocky nature, the green bars indicate intervals that have a heterogeneous or interbedded nature.

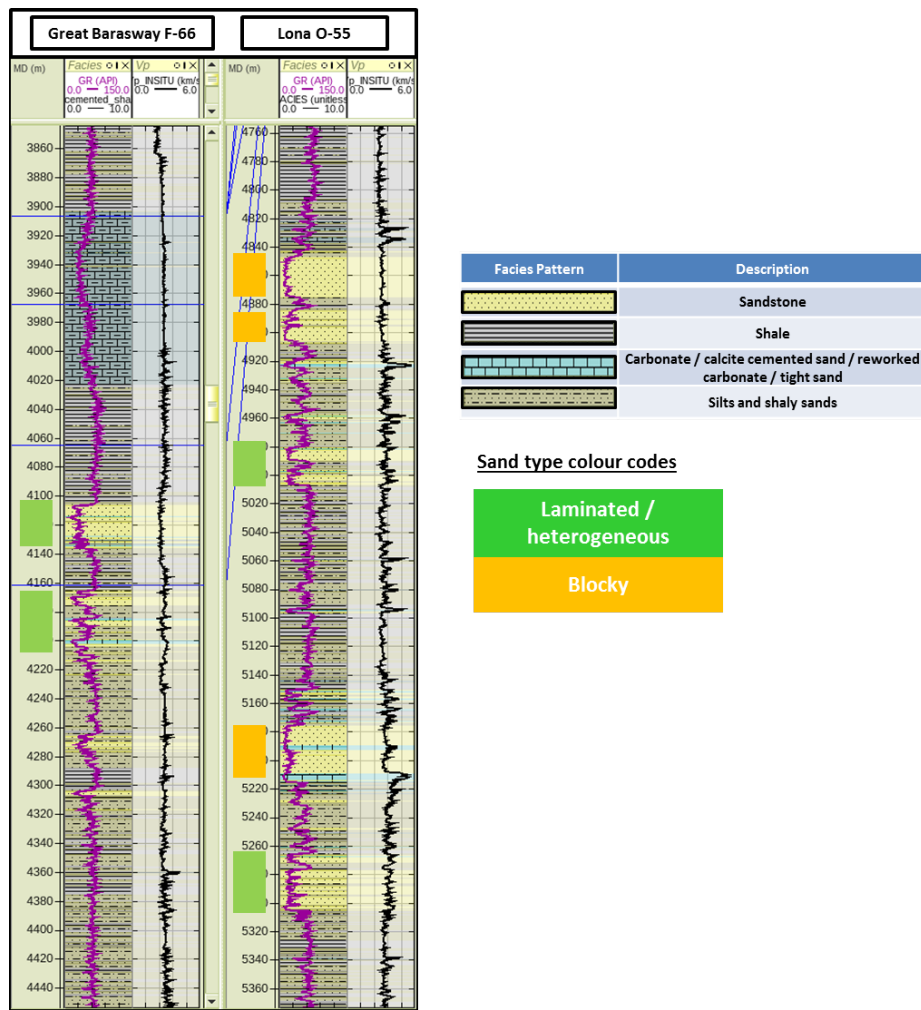


Figure 35: Well log panel for Great Barasway F-66 and Lona O-55, located in the Orphan Basin, Vp-PhiT for the intervals indicated are plotted in figure 25. The intervals highlighted in orange correspond to blocky sands, the intervals highlighted in green correspond to interbedded and heterogeneous intervals.

Vp-PhiT cross-plots that correspond to these intervals are shown in Figure 36. The intervals highlighted by the green bars in Great Barasway F-66 (Figure 35) are indicated to have low net-to-gross by the petrophysical interpretation (i.e. there are numerous sand/shale interbeds in the interval). The Vp-PhiT behaviour for the clean sands in this interval fall close to the uncemented sand line, with flat Vp-PhiT trends noted between the sands and shaly sands / shales. Flat

trends between sands and shales are indicative of a laminated shale system, where the transition from clean sand to shale is via an increase in the number of shale laminae.

The sands in Lona O-55 range from clean and blocky as indicated by the orange bars in Figure 35, to laminated and heterogeneous, where porosity is low and velocity is erratic as indicated by the green bars. The Vp-PhiT data for these intervals is shown in Figure 36, right hand cross-plot. The clean sand data in this well conforms to the slightly cemented sand contours.

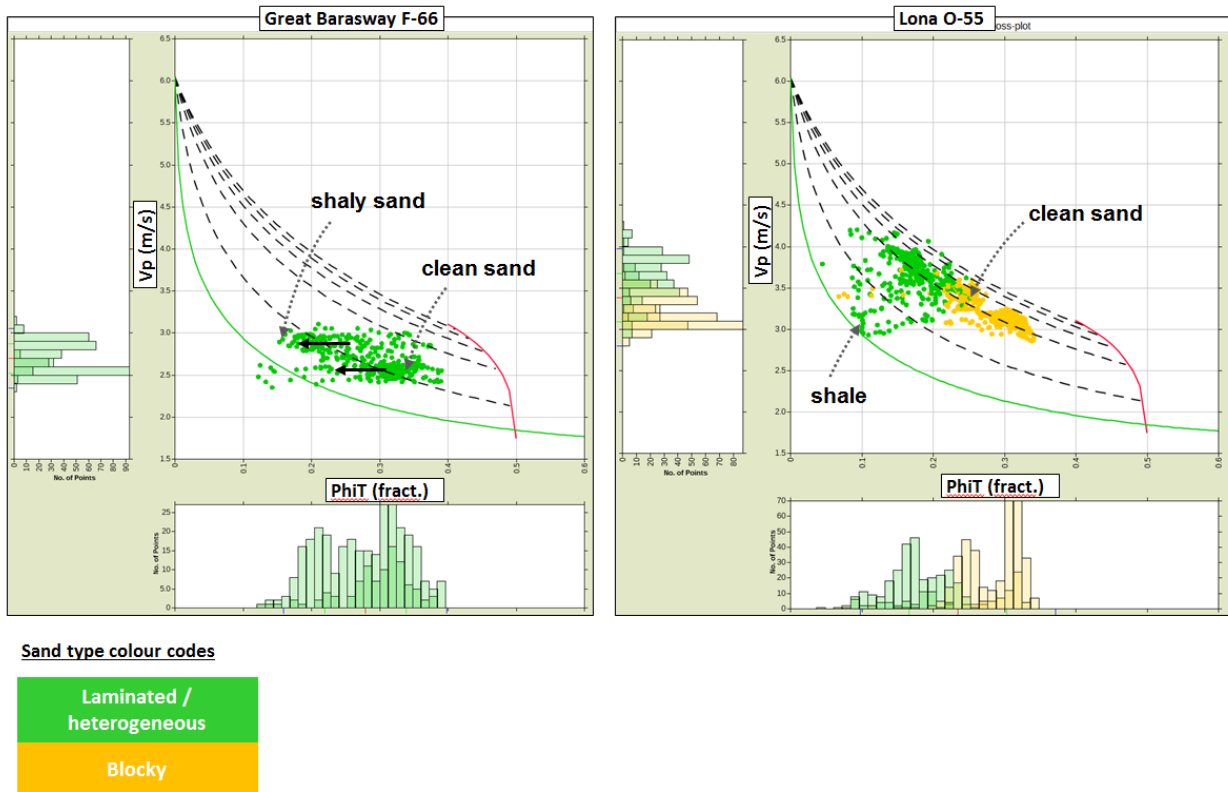


Figure 36: Vp versus PhiT for Great Barasway F-66 (left-hand plot) and Lona O-55 (right-hand plot). The data plotted is indicated by colour in Figure 35. The green line is the shale line, the dashed lines are sandstone trends for varying contact cement content, and the red line is an increasing contact cement line.

2.3.3.1.1 Diagnosing microstructure of well data – an example from Mizzen O-16

This section provides an example of how a rock physics model of the type described in section 2.3.1 can be used to investigate the rock microstructure. Here the Constant Cement model is calibrated to the available elastic log data in the study wells. A closer look is then taken at the implications of the calibrated model based on the available core analysis at the Mizzen O-16 well in the Jurassic Tithonian sands.

The following section will outline in detail how microstructure impacts velocity and subsequently reveals something about reservoir quality in Mizzen O-16. The sands in question are of Jurassic age (J145), are classified in a Folk classification as being sublitharenite (Figure 37). This means they are relatively quartz-rich, in this case, between 80 and 95% of the supporting grains are quartz in the intervals of interest.

The aim is to provide an insight into the model-data match, the interpretations of well log behaviour that can be made with reference to these types of rock physics models, and the implications for the use of these models in a predictive manner.

After applying a cut off of $VSH < 0.2$ to sand intervals, Table 2 and Table 3 were investigated in more detail to look for confirmation of cementation, sand quality and other relationships that might help explain cross-plot behaviour.

Tithonian 3 sand (3212m – 3228m MD)

This sand interval is relatively clean and homogenous (Figure 38). Most of the samples are described as having good reservoir properties, even though total cement volume from the core analysis can be as high 14.3%, with an average of approximately 11%. The quartz overgrowth is around 4-5 %, and is mostly concentrated around the grain contacts (Figure 32), which will contribute to the velocity increase usually seen when adding cement to grain contacts. This then confirms the results of applying the selected rock physics model for slightly cemented sands.

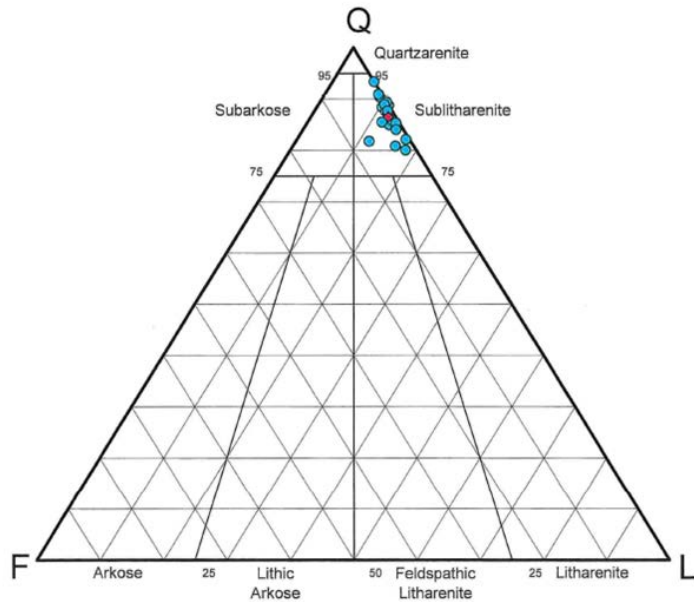


Figure 37: Sandstone composition for Mizzen O-16 (Report: Mizzen Core Analysis).

Name	Sample Depth	Core Porosity	Core Permeability
Sand 1	3227.8 m	0.276	158.0 mD
	3221.7 m	0.297	2020.0 mD
	3218.7 m	0.324	5310 mD
	3215.7 m	0.299	3250 mD
	3214.2 m	0.295	417 mD
Sand 2	3381 m	0.252	2640 mD
	3378 m	0.27	3170 mD

Table 2: Sample depth, core porosity and core permeability for thin section analysis for Mizzen O-16 (from Mizzen O-16 Core Analysis Report).

Sample Depth	Quartz Overgrowth	Total Cement	Sorting	Average Grain Size	Grain Size Range	Porosity (NCS) %
3227.8 m	4.66%	14.3%	Moderately	0.09 mm	0.01-0.24 mm	27.6
3221.7 m	6.05%	13.7%	Moderately	0.20 mm	0.02-0.6 mm	29.7
3218.7 m	4%	5.98%	Moderately	0.22 mm	0.02-0.61 mm	32.4
3215.7 m	3.33%	8.63%	Moderately	0.17 mm	0.02-0.56 mm	29.9
3214.2 m	6%	12.98%	Poorly	0.12 mm	<0.01-0.43 mm	29.5
3381 m	4.66%	11.31%	Moderately	0.29 mm	0.02-0.95 mm	25.2
3378 m	4.66%	11.97%	Moderately	0.25 mm	0.03-0.68 mm	27

Table 3: Sample depth, cement volume, sorting description, average grain size and grain size range (from Mizzen O-16 Core Analysis Report).

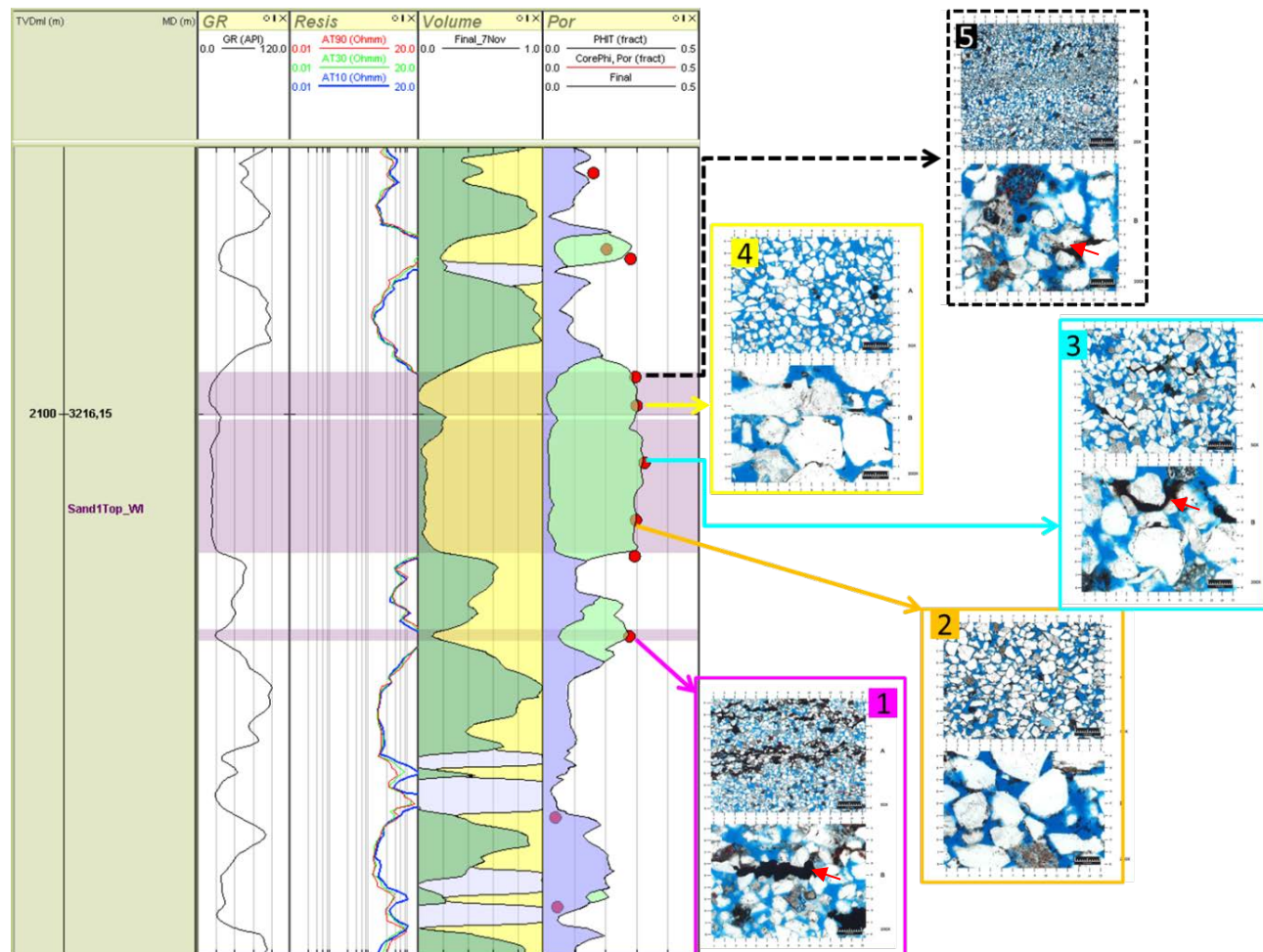


Figure 38: Well log panel for Sand 1 in Mizzen O-16, also showing thin sections of five samples (Mizzen O-16 Rotary Sidewall Core Analysis, Weatherford Laboratories, performed for StatoilHydro). Pseudo-matrix (red arrows) contributes to lower permeability in the poorest sorted intervals. Floating grains in figure 4 illustrate the friable nature of these reservoir units, and are likely indicative of grain 'plucking' during sample preparation.

Looking at the five samples taken from the Tithonian 3 sand (Figure 38), it can be seen that samples 2, 3 and 4 have the best reservoir qualities and are moderately sorted, angular to sub-rounded quartzose sandstones. Note in image 4 that there are floating grains suggesting grain 'plucking' during sample preparation. Samples 5 and 1 still have good porosity, but significantly lower permeability. As illustrated in Figure 38, images 1, 3 and 5, the moderate- to poorly sorted intervals include the presence of interstitial clay clasts 'squeezed' into the pore spaces (pseudo-matrix) is contributing to this lower permeability. Florez (2005) showed that permeability is highly linked to grain size distribution, and hence sorting.

If quantitative analysis like deriving the standard deviation of the grain size distribution was performed on the samples, a good parameter of sorting, (S), which is defined as the standard deviation of grain size (σ) normalized to the mean grain size (M), $S = \sigma/M$, and its impact on rock properties could have been studied in more detail.

From this equation, it follows that when S is relatively large, the sands are relatively poorly sorted, but if this value is small, then the sands are interpreted as well sorted. These relationships were studied in detail by Avseth et al. (2001) (Figure 39), and could perhaps have helped in explaining different sand porosity trends as a function of sorting, and hence reflecting reservoir quality (see section 4.2.2).

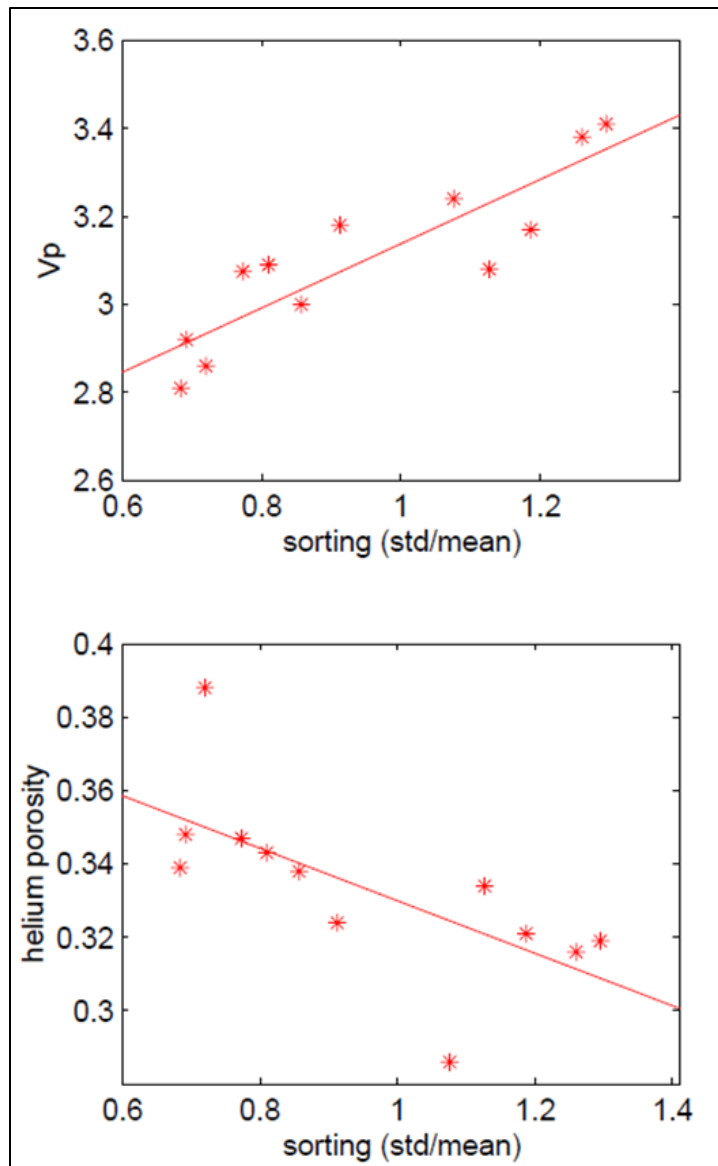


Figure 39: The derived sorting factor shows good correlation to Vp and porosity (after Avseth et al., 2001).

Looking at the cross-plot in Figure 40, most of the data from samples 2, 3 and 4 conforms to the 4.5% quartz cement line, and slightly above, which is in line what thin section analysis show. As these samples have pretty much the same grain sizes and ranges, it probably means that the (small) porosity decrease is more attributed to compaction effects rather than sorting alone. The sample at depth 3214.2m MD corresponds to the start of a fining upwards sequence as seen from GR behaviour (Figure 38). Fining upwards sequences are known to contain increasing amounts of dispersed clay (Dvorkin and Gutierrez, 2001), and as these clay particles fill up the pore space, the porosity tends to decrease while velocity, a bit counter intuitively, increases.

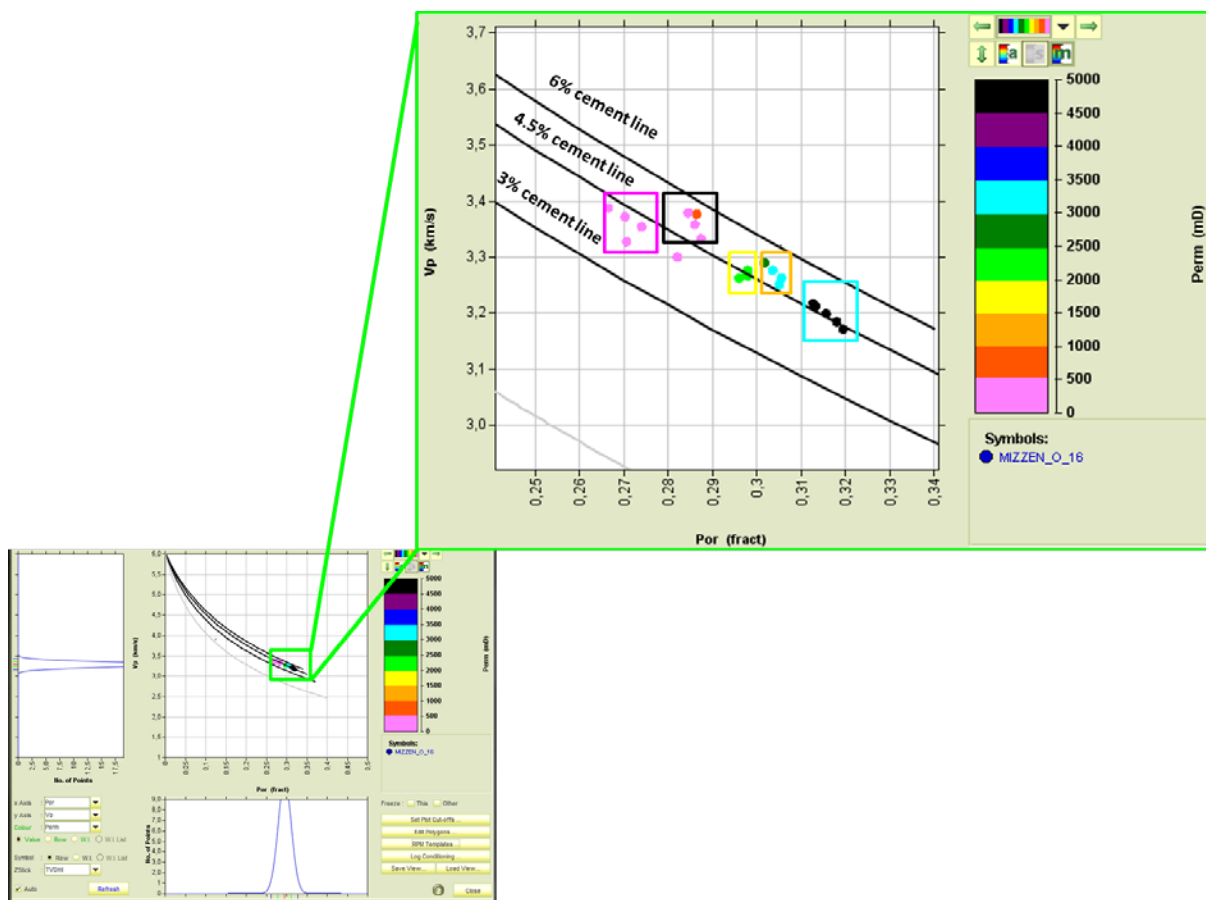


Figure 40: V_p versus porosity for log data in the sample depth range, color-coded by permeability. The zoomed in data highlighted in the light cyan box refers to sample depth around 3218.7m MD, the orange box to sample depth around 3217m MD, the yellow box to sample depth around 3215.7m MD, the black box to sample depth around 3214.2m MD and the pink to sample depth around 3227.8m MD.

Tithonian 2 sand (3378m – 3381m MD)

This sand interval is relatively clean and homogenous (Figure 41). The two samples are described as having good reservoir properties, even though total cement volume averages 11% in the core analysis report. The quartz overgrowth (cement at the grain contacts) is around 4.66% in Sand 2, and is mostly concentrated around the grain contacts (Figure 32), which will contribute to the velocity increase usually seen when cement is concentrated around grain contacts. As was the case for the previous sand at depth between 3212m – 3228m MD, this then also confirms the results of applying the selected rock physics model for slightly cemented sands with varying cement volume.

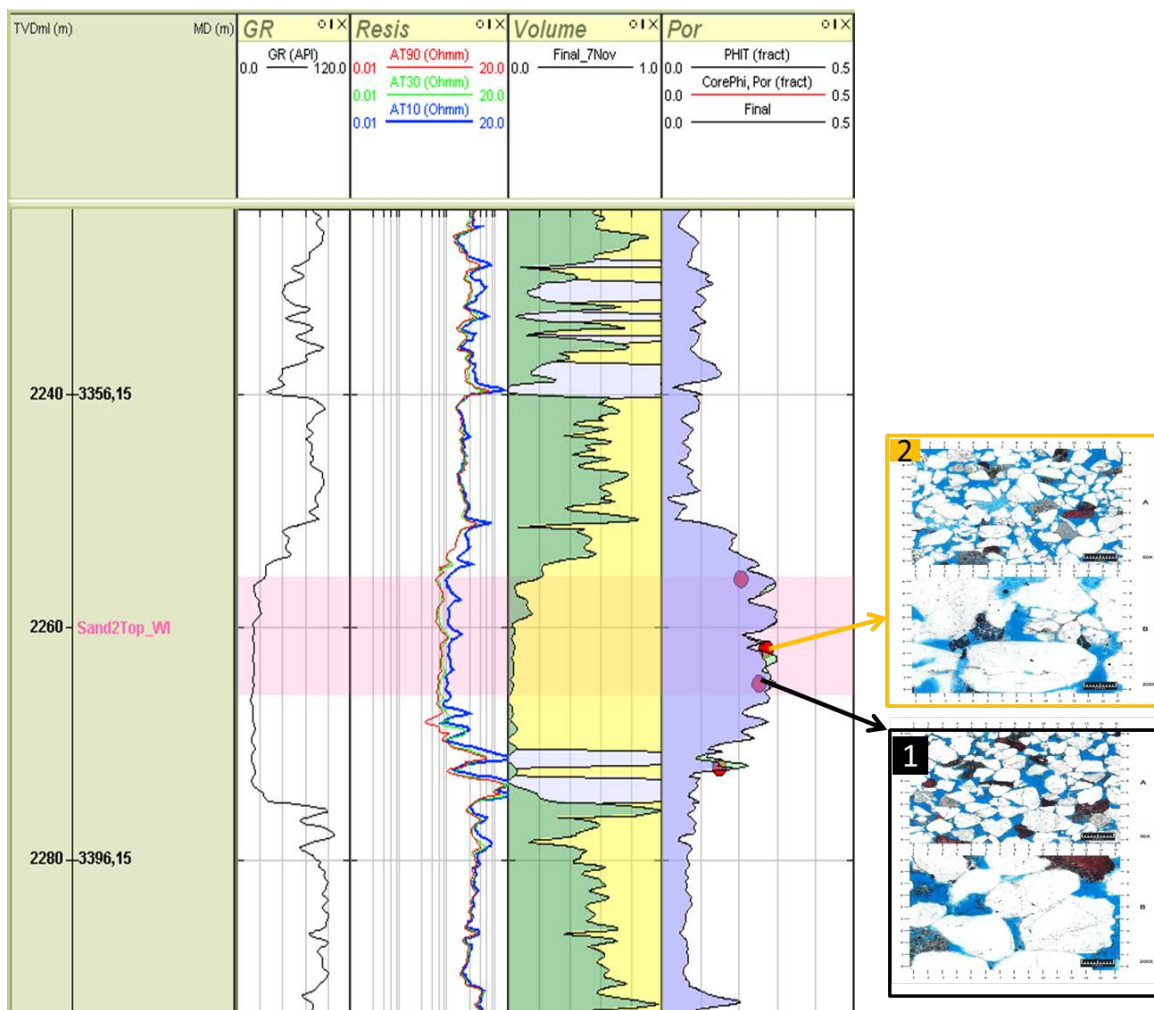


Figure 41: Well log panel for Sand 2 in Mizzen O-16, also showing thin sections of 2 samples. (Mizzen O-16 Rotary Sidewall Core Analysis, Weatherford Laboratories, performed for StatoilHydro).

Looking at the cross-plot in Figure 42, the data from sample 2, which has 4.66% quartz overgrowth in the pore system (taken from the Mizzen O-16 Rotary Sidewall Core Analysis, Weatherford Laboratories, performed for StatoilHydro), seem to lie closer to the 6% quartz cement line than the 4.5% cement line. The reason for this slight mismatch between the model and the data is not totally understood, but different packing might give an extra increase in velocity (Florez, 2005; Zimmer et al., 2007) that is not totally captured by the slightly cemented model that has been selected.

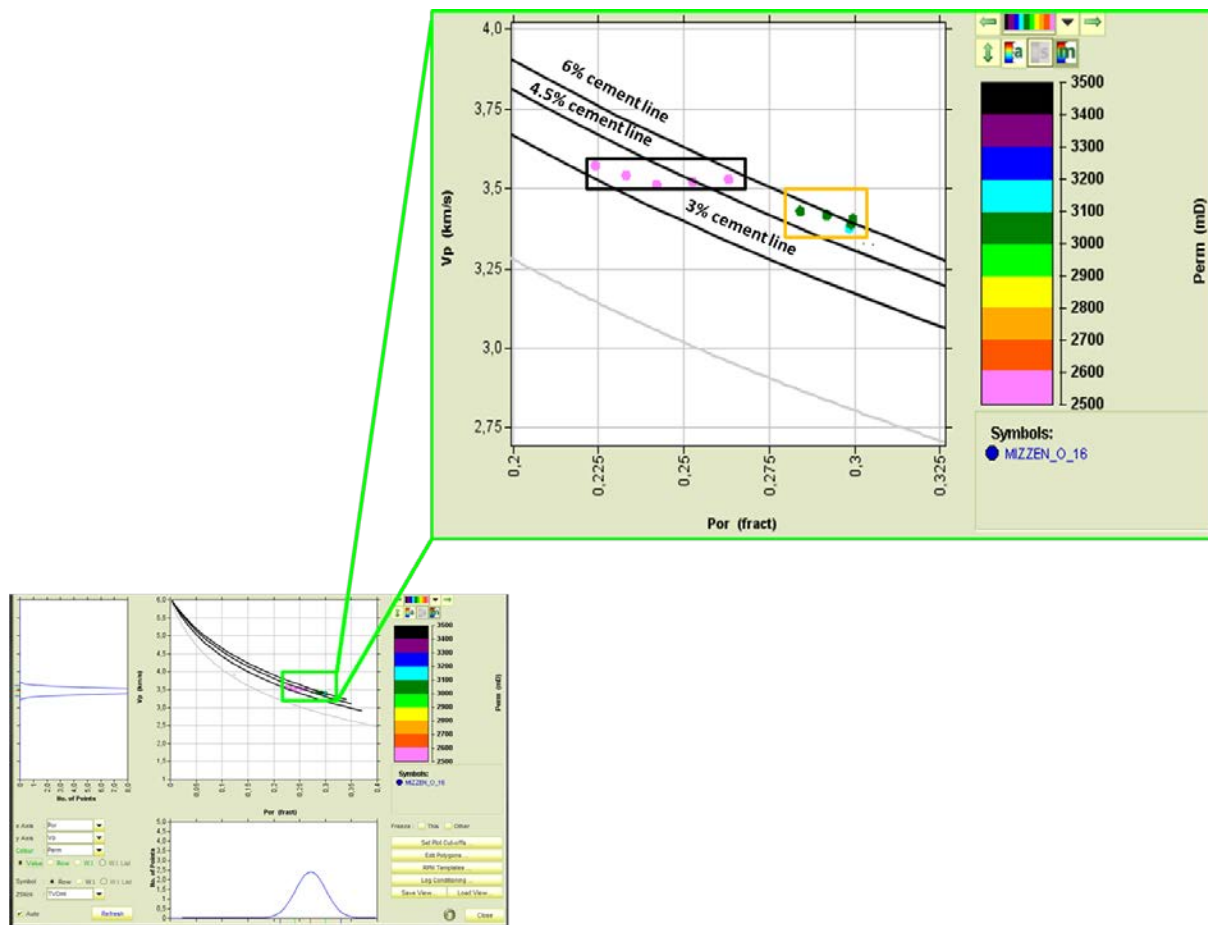


Figure 42: V_p versus porosity for log data in the sample depth range, color-coded by permeability. The zoomed in data highlighted in the black box refers to sample depth around 3378m MD, and the orange box to sample depth around 3381m MD. The data in the plot is from logs, and a detailed comparison to the calibrated rock physics model is shown.

This potential implication of different packing affects the coordination number (average number of contacts each grain has with surrounding grains), which again affects velocity; if the number of contacts per grain decreases, then so does the velocity, and vice versa.

2.4 Shales

Shales comprise most of the sediments in sedimentary basins around the world. Shales also form the seal and source rocks for many hydrocarbon reservoirs and may, in some cases, act as both the source rock and reservoir. Normally, shales are classified based on grain size (Wentworth, 1922), and most shales consist of clay minerals and clay- and silt-sized feldspar, quartz, calcite, dolomite and siderite minerals. However, it is important to differentiate between two different meanings of the word “clay”, commonly occurring in the literature: 1) as mentioned above, related to grain size, and 2) typically an indicator of mineralogy in the shales, whether it is smectite, illite, chlorite or kaolinite.

For the purposes of rock physics workflow the terms shale and claystone can be used interchangeably, they simply describe a rock with high contents of clay minerals and low effective porosity (dry clay mineral plus clay-bound water), the fractions of these rocks are normally identified from the GR log response. The rock physics modelling assigns properties to the identified fractions, and this is done on a per depth basis. So if a claystone has different properties to a shale then these properties are assigned accordingly.

Up until a decade ago, geophysicists didn't pay much attention to shales, as they only formed the potential cap rock over a reservoir, but more knowledge about the complexity of these sediments have resulted in a more detailed understanding of how shales have a very key effect on the seismic-wave propagation in the stratigraphic column. As the wave propagates within the earth, seismic reflectivities, due to differences in impedances between adjacent layers, can be used in AVO analysis on pre-stack data in the search for hydrocarbons. However, the complexity and layered nature of shales make them highly anisotropic (Vernik and Liu, 1997; Sayers, 1999; Brevik et al., 2007; Sondergeld and Rai, 2011; Holt et al., 2011), which causes problems both in processing, but also in the aforementioned AVO analysis and related quantitative seismic interpretation. Also, the mechanical to chemical compaction transformation zone alters the clay minerals into other minerals, which complicates any further seismic interpretation.

Shales in offshore Newfoundland and Labrador vary both in composition and origin, and may give rise to seismic signatures that are anomalous to what is expected in the area and/or zone of interest in the sub-surface. There is not much information available on shale intervals from thin-section analysis (e.g. x-ray diffraction (XRD)) or core data to assist with the description of the shale intervals. Therefore, the procedure of rock physics diagnostics might prove valuable in

order to better constrain the mineral composition such as calcite content (i.e. calcareous shales) and quartz content (i.e. silt) and their impact on the acoustic properties of the shales. The rock physics analysis may also show how these shales can be differentiated from other lithologies like sandstones, limestones and dolostones. A better understanding of the variety of shales also affects other exploration-related disciplines such as pore pressure prediction (Edwards et al., 2015) and AVO analysis (Rauch and Collins, 1998).

2.4.1 “Normal” Shales

At initial deposition, shales usually have very high porosities, ranging from 0.5 to 0.8, depending on the mineral constituents present in the shale. During burial, the clay platelets break down, and re-orientate into a preferential arrangement for compaction (Figure 43). This process is responsible for the rapid loss of porosity and permeability in shales, and may cause overpressured intervals, as the sediments cannot dewater effectively during burial. Because of the platy nature of clays, and therefore being more prone to compaction than sands (due to a preferred grain shape of the clays), they form the basis for pore pressure prediction methods.

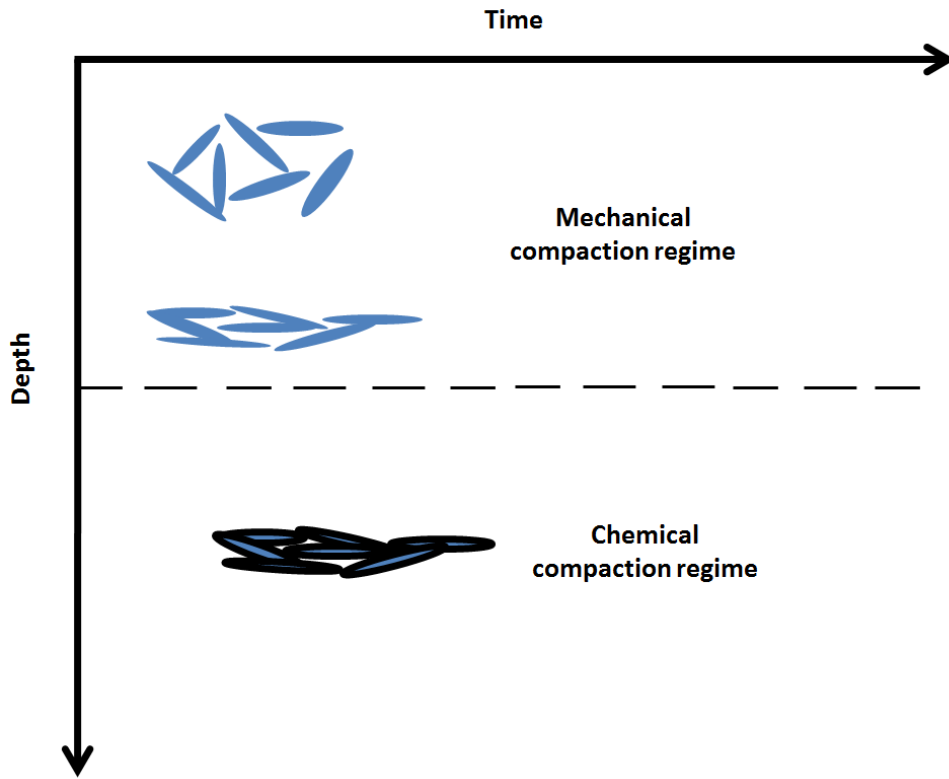


Figure 43: At deposition the clay minerals are oriented randomly, but reorient themselves and almost align parallel/subparallel with increasing burial depth. Within this first mechanical compaction regime, the shales loose most of their porosity. Entering the chemical compaction regime, allows for further reduction in porosity via cementation or mineral transformations (redrawn after Draege et al., 2006).

In Figure 44, data from the Tertiary (T45-T65 Ma; age-equivalent to the Lower Kenamu and Cartwright formations) and the Upper Cretaceous (T65-C100 Ma; age-equivalent to the Markland Formation) are cross-plotted in the V_p versus total porosity domain. These formations are interpreted to be very clay-rich, based on high GR readings as compared to clean sands, a large separation between RhoB and Neutron (Katahara, 2006), and cuttings descriptions from mud loggers. Superimposed on the cross-plot is the diagnostic friable shale line in dark green (lower line), and a good correlation can be seen between the two. The reason that most of the shales are plotting slightly above the shale line may indicate that the shales are not 100% clay. The exact amount of clay will not be known unless XRD analysis is performed on cores in these intervals. The clay content seems to vary between the 100% clay line and the silty shale line in light green (upper line; containing 50% clay and 50% quartz). After all, silt is just a lithology, consisting of clay particles and clay- and silt-sized quartz, as well as calcite, dolomite etc. A rule

of thumb is that clay-rich shales normally consist of 80-90% clay particles (Dvorkin, personal communication), unless kaolinite-rich shales are present that can exceed those percentages.

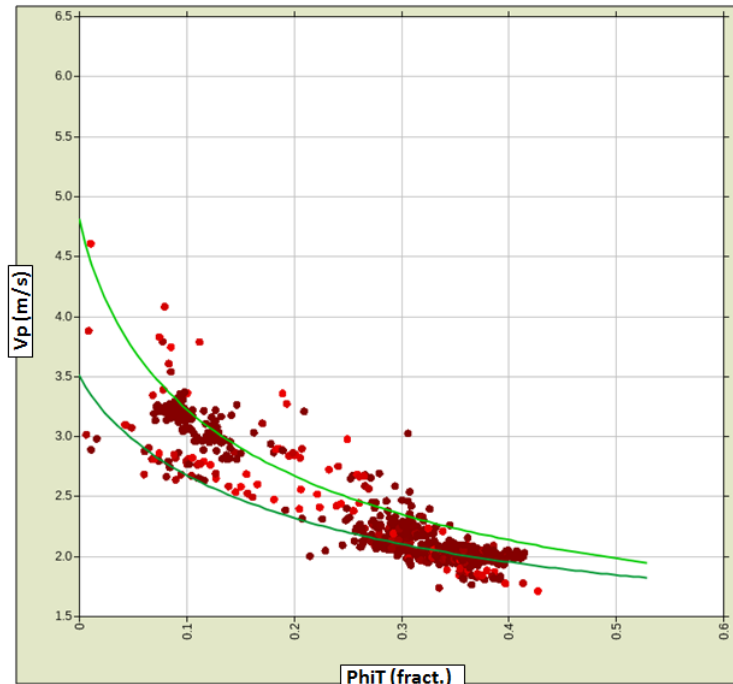


Figure 44: V_p versus Φ_{iT} for known clay-rich shales, the data is coloured by GR, with all points having GR values of 100 or more. The lower line is the friable shale line, while the light green is the silty shale line.

2.4.2 “Cemented” Shales

During burial, shales undergo various geochemical processes that alter both the mineral composition of the original deposited shales, but also the elastic properties. The smectite to Illite transformation (Peltonen et al., 2009; Small, 1994; Van der Kamp, 2008) is such a scenario, where shales are becoming stiffer, faster, denser and higher resistivity due to mineral changes related to the process of increased overburden stress and temperature. This process is highly dependent on temperature and changes the composition, texture and the elastic properties of the shales. Thyberg et al. (2009) showed that micro-quartz cementation in shales changes the elastic properties, while the mineral composition remained fairly un-altered during the cementation process.

Figure 45 shows the clay-rich shales shown in Figure 44, but also plotted are fast shales, interpreted here as being quartz-cemented. The upper cross-plot in Figure 45 shows the same

data as the lower cross-plot, but the lower cross-plot is colour coded by wells; the wells that are interpreted to have penetrated cemented shales. The blue arrow indicates cemented shale trend, and it is noted that velocities increase in the range of 400–600 m/s in a 500m interval; the shales go from normally compacting shales to cemented shales, while porosity remains approximately the same/ slight decrease during the process. The fact that porosity remains the same/ slight decrease is strongly indicative of quartz cementation (and not, for instance, calcite cementation), assuming a clay density of 2.67 g/cc and a quartz density of 2.65 g/cc. The lower cross-plot reveals that the cyan well and the light blue, Baccalieu I-78 and Mizzen L-11 respectively, show the most distinct cementation trend, while Mizzen O-16 show scattered data indicative of both normal shales and small cemented shale intervals.

Considering Baccalieu I-78 (Figure 46) in more detail, the high GR readings in the Jurassic interval would be interpreted as shales, however looking back at Figure 45 it is clear that the high velocity shales diverges from the friable shale line. Observing how resistivity also changes within stable high GR reading intervals while density stays the same indicates quartz cementation in adjacent layers. Looking at the whole interval, starting in the lower Cretaceous and older, it seems like the general background shale resistivity is elevated compared to Tertiary and rest of the Cretaceous, which will have implications for CSEM interpretations in the area of interest (Gist et al., 2013).

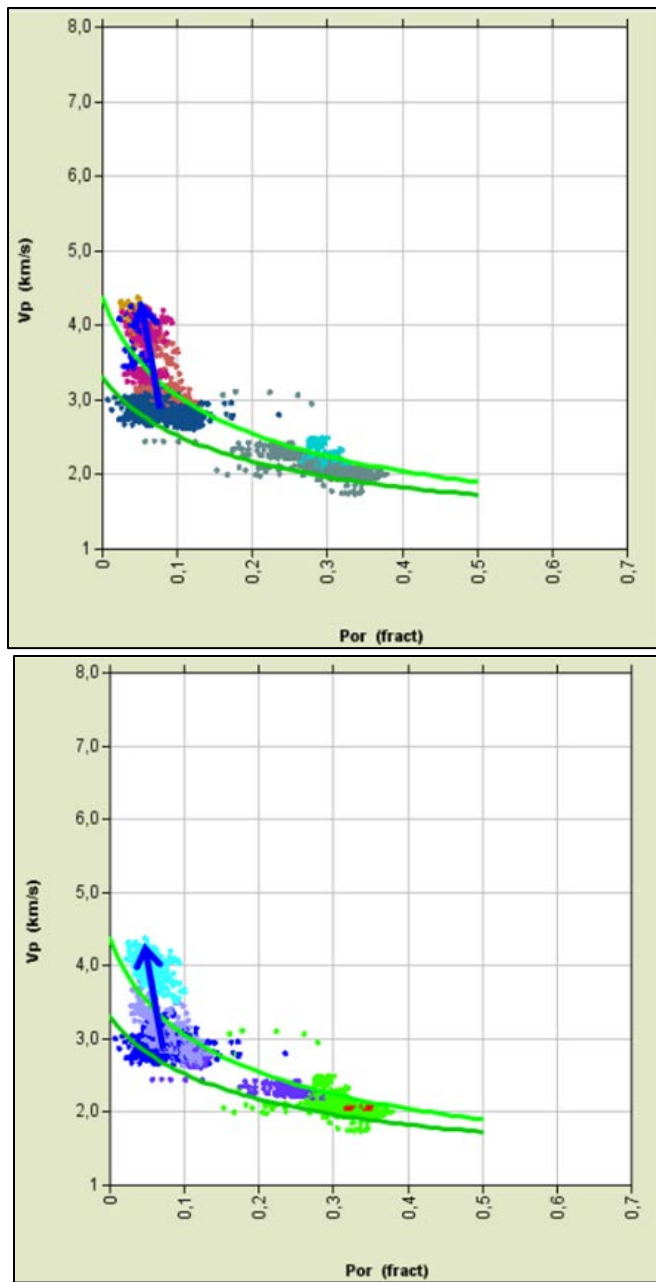


Figure 45: V_p versus Φ_T for known clay-rich shales, and intervals of cemented shales. Upper plot is colour-coded by lithofacies, while the lower plot is colour coded by wells. Again, for reference, the lower trend line is the friable shale line, while the upper light green is the silty shale line. Cyan: Baccalieu I-78; light blue: Mizzen L-11; purple: Mizzen O-16.

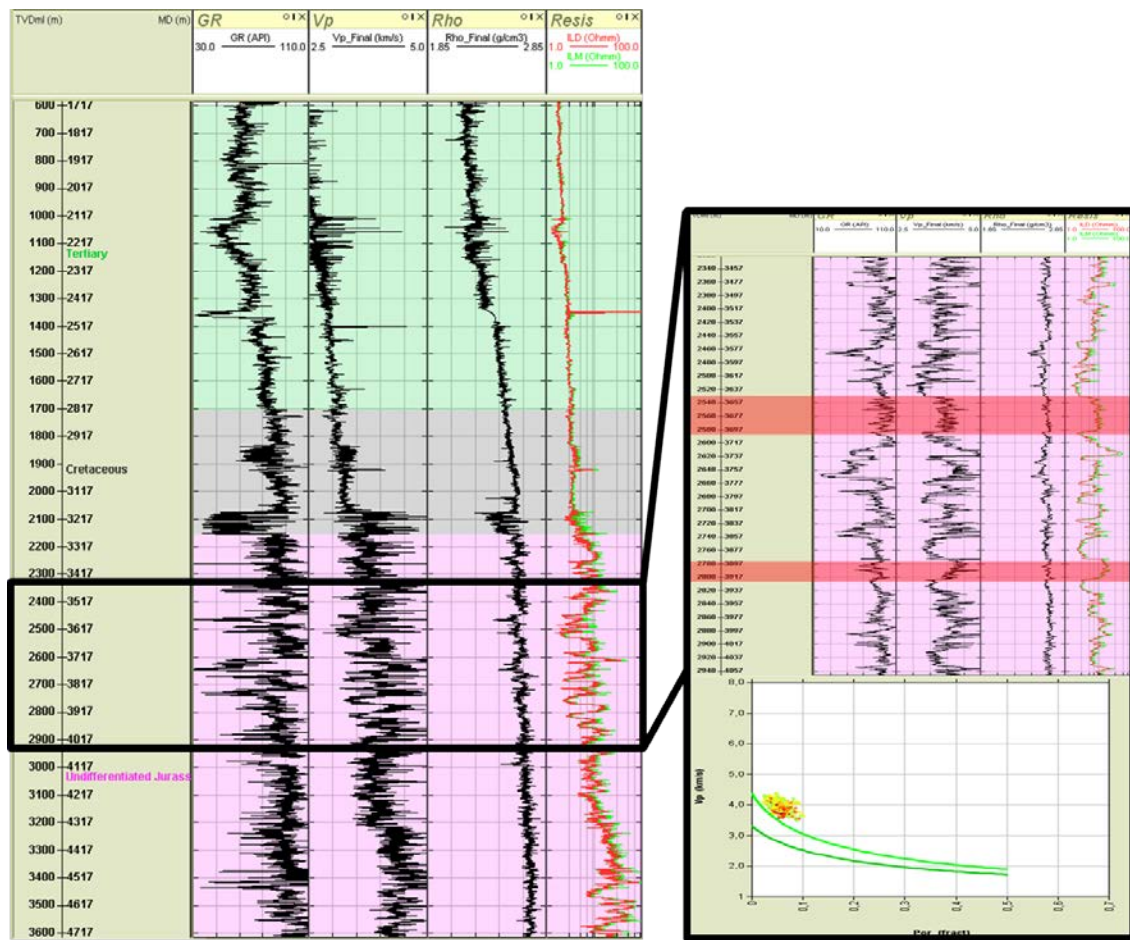


Figure 46: Baccalieu I-78, showing cemented shales in an interval within the Jurassic.

Figure 47 shows a cross-plot of Vp versus Vs for Lona O-55, Mizzen O-16 and Mizzen F-09, is annotated with a light cyan dashed line (the slightly cemented sand line from Figure 31) and the dark green line (the friable shale line). The red data on Figure 47 are cemented shales, blue data are slightly cemented sands and green data are normal shales. It is observed that the cemented shales lie on the same trend as the slightly cemented sands, while the normal shales follow the shale line. The green arrows indicate a rotation of Vp versus Vs behaviour for the these shales, a similar type of rotated behaviour as seen when organic-rich shales are plotted (Edwards et al., 2014). The excessive increase in both Vp and Vs responses for quartz-cemented shales will ultimately yield a change in Vp/Vs and Poisson's Ratio that might create false positives due to AVO character that can be associated with hydrocarbons.

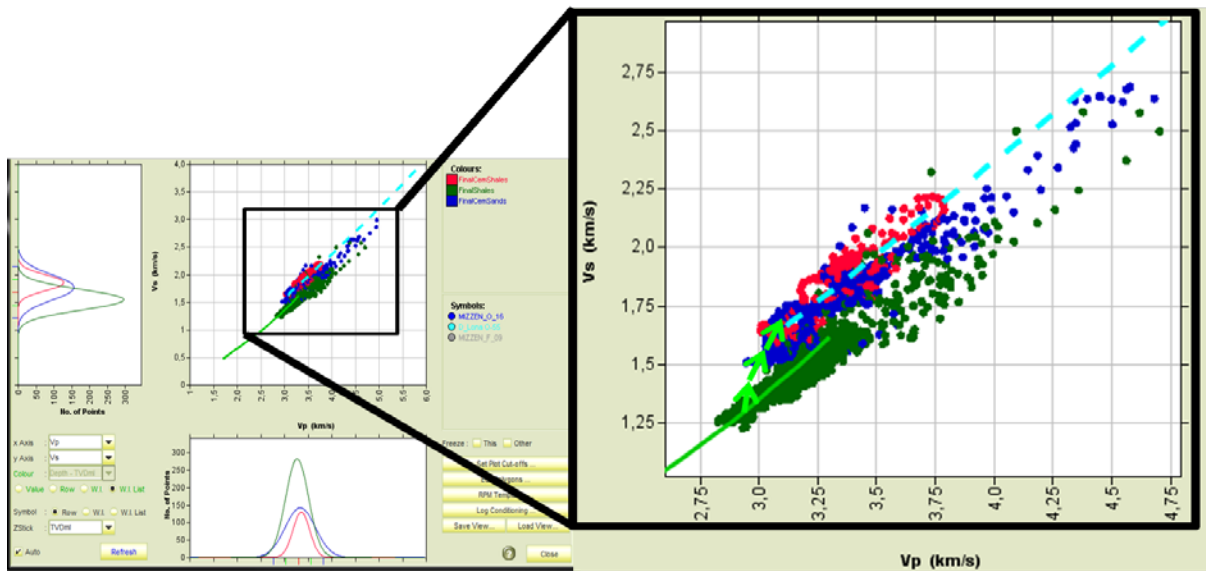


Figure 47: V_p versus V_s for Lona O-55, Mizzen O-16 and Mizzen F-09, coloured by shale type. Red: cemented shales; blue: slightly cemented sands; green: normal shales.

2.4.3 Calcareous shales

Shaly sediments containing different amounts of calcite may be called several different names, depending on the calcite:clay ratio (Figure 48), but to avoid any misunderstandings within this study, all shales containing some calcite will be called calcareous shales. Calcareous sediments are usually deposited in shallow water near land, since the carbonate component is precipitated by marine organisms that need terrestrial-derived nutrients. Generally speaking, the further from land that sediments are deposited, the less calcareous they are. Some areas can have interbedded calcareous sediments due to storms, or changes in ocean currents.

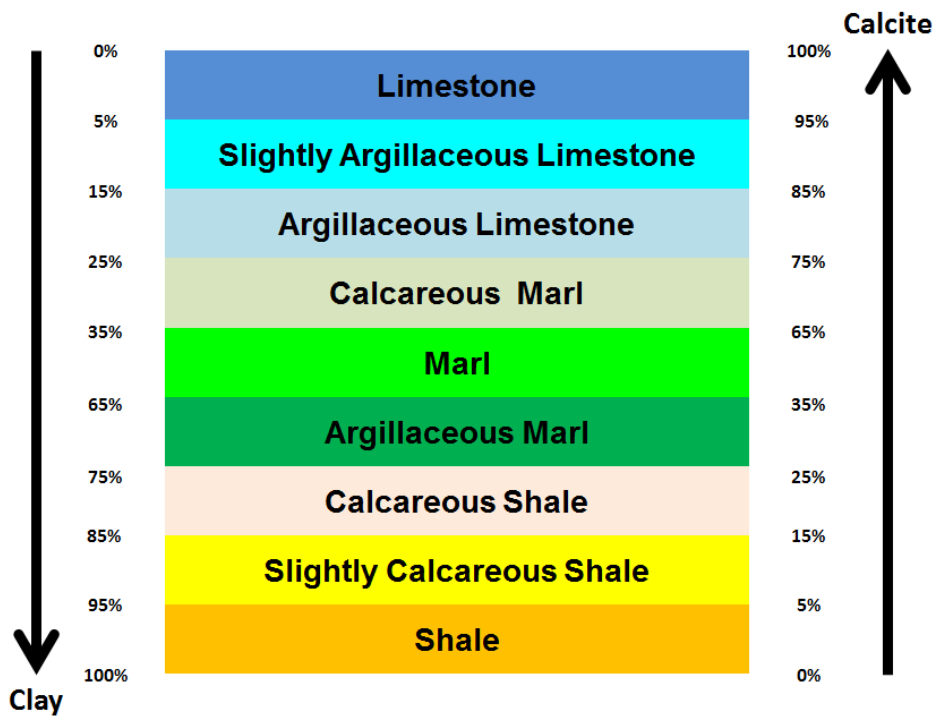


Figure 48: Scheme of the transitional lithotypes from mud (or mudstone) to lime (or limestone), illustrating the definition of marl (marlstone) as a mix of calcium carbonate and clay (redrawn after Wikipedia).

A lot of detailed work has been carried out over the last two decades on the impact of calcite occurrence in clastic reservoirs (Bjorkum and Walderhaug, 1990; Dutta et al., 2008; Vanorio et al., 2008), for better predictions of reservoir quality in sandstones. However, even though their relatively common presence in the sub-surface all over the world, there has not been very much detailed rock physics analysis on calcareous shales.

Calcareous shales differ from quartz-cemented shales in that they have varying calcite content in the matrix. Both cements usually mean higher velocity in the host rock, but, as opposed to quartz which has a density close to the clay in shales and hence no increase in bulk density, calcite has higher density (2.71 g/cc) and thus increases bulk density as well as the velocity, in calcareous shales. One of the wells showing the best diagnostic behaviour of normal shales versus calcareous shales in terms of velocity increase and density increase is Cumberland B-55 (Figure 49). Although the GR is relatively high in middle and lower Tertiary, there is a clear increase in velocity, and to a lesser degree, density, at around 1650m MD. Resistivity is still high throughout the section, but gets significantly lower in the early Tertiary sequence at around 3125m MD which coincides with a significant drop in velocity (the resistivity log is shown in the

left-hand track in Figure 49). Some uncertainty is associated with the log measurements at this interval, although clear issues with the log data (included casing changes) were identified and rectified during the log conditioning stage. At this stage of analysis, it may be premature to classify the shale as calcareous shale, as no measured shear velocity was available. Therefore, other ways of constraining the petrophysical interpretation, in terms of its mineral constituents, need to be investigated.

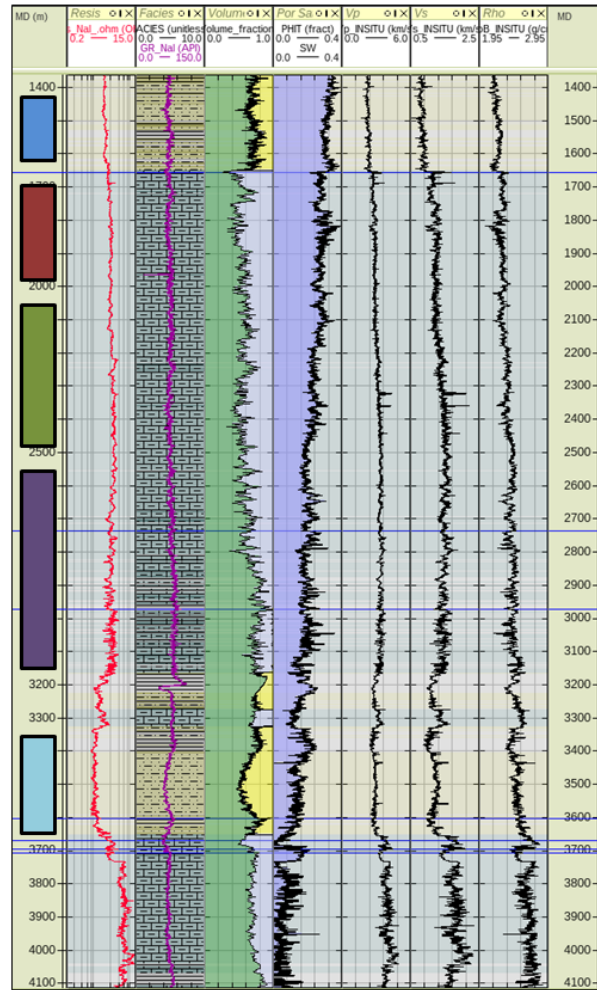


Figure 49: Well log panel for Cumberland B-55. Sections of the well log PhiT – Vp response are highlighted, and plotted in Figure 50. These show different shale behaviours, between calcareous and non-calcareous shale. The red, green and purple intervals are calcareous shales, the light and dark blue are non-calcareous shales. Refer to figure 40 for Vp-PhiT cross-plot responses for these intervals.

Normally shales lose porosity during compaction in a very predictable manner, which serves as one of the foundations of pore pressure prediction, but because of higher calcite content, the trend will deviate from the normal trend when burial depth increases. This deviation can easily

be seen in Figure 50, which shows the expected compaction trends for normal shales (black arrows) and calcareous shales (red arrows). For diagnostics, the green line is friable shale line, while dark purple is 100 % calcite line.

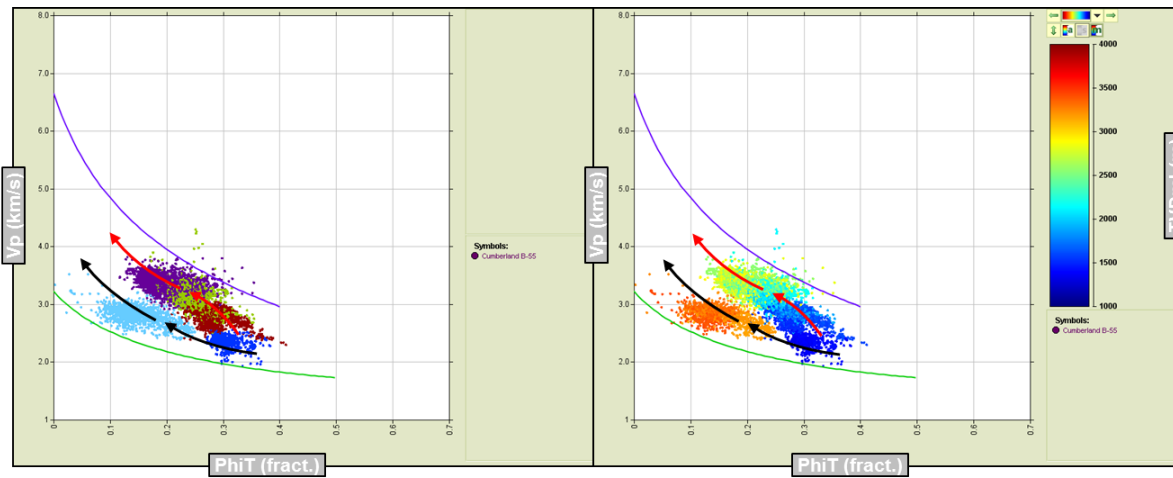


Figure 50: Cross-plot of V_p versus Φ_{IT} for Cumberland B-55. Left-hand plot coloured by interval indicated in Figure 49 for the Cumberland B-55 well, right-hand plot coloured by burial depth. The black arrows indicate the compaction trend for normal shales and the red arrows indicate the compaction for calcareous shales. The green line is the friable shale line and the purple line is a 100% calcite line.

2.5 Carbonates

Limestones and dolostones, are present in both the wells drilled on the shelf and drilled in the deep-water. On the shelf, the depositional environments associated with carbonates were predominantly shallow water and appear as thick successions, while the wells drilled in present day deep-water show both deep water carbonates that appear as stringers as well as thicker successions (Lona O-55, Mizzen O-16) that appear to be shallow water deposits. Large ranges in the log response of the interpreted carbonates are seen, but most of the data is bounded by the Modified Lower Hashin-Shtrikman Bound (MLHS) and the Modified Upper Hashin-Shtrikman bound (MUHS), using pure calcite as the effective density and moduli to mimic the carbonate environment. The range in data most likely reflects local conditions on diagenetic effects and other depositional processes that might have been controlling the elastic properties during burial (e.g. texture and clay content).

Inclusion-based models, like the Self Consistent Model (Berrymann, 1985) and the Differential Effective Medium Model (Norris, 1985), can, in many cases, better describe biogenic carbonates than shown here; but for understanding and describing carbonate-facies, the MLHS and MUHS are sufficient for this study. Generally, carbonates exhibit higher velocity, higher resistivity and higher density than the clastic counterparts of sands and shales. Thus, because of the high moduli of the carbonates, the common perception is that different fluids (i.e. brine, oil, gas) have no or little effect on the carbonate properties and cannot be approached with a traditional AVO like in clastics. Cases exist however (Li and Downton, 2000; Fabricius, 2003) where AVO fluid effects can be separable even in a carbonate environment. The study of biogenic carbonates is beyond the scope of this study. The reworked carbonates, and sands with high calcite cement contents (both at the contacts and within the pore space) in the lower Tithonian (Ti-0) intervals are separated from the overlaying quartzose sandstones for use in the rock physics analysis.

2.6 Summary

A petrophysical interpretation has been performed on the log data in the 18 wells from the shelf and deep-water. This interpretation is then used to guide a litho-facies definition, where the major facies encountered by the wells were identified and classified. The elastic logs were then conditioned in order to remove any erroneous log measurements relating to casing points, bore-hole cavings, or mud filtrate invasion effects. The elastic log data was replaced where required based on lithology-specific empirical elastic trends (V_p - V_s and V_p - ρ_B), these are applied based on the interpreted volume fractions of each rock type. The result of the conditioning stage is a database of log responses that are consistent in terms of quality across the wells, with less reliable data in the older predominantly shelfal wells being conditioned to be consistent with generally more recent data in the deep-water wells.

Once the log data points that fall into each facies have been identified a further investigation of the sands and shales was made based on established rock physics models, and rock physics diagnostics methodologies. This was made with reference to petrographic analysis where this was available. The result is confirmation that the behaviour of the facies in the deep-water can be captured via sensible calibration of published models, which in turn will allow the modelling of rock elastic properties away from well control in subsequent analysis.

It has been shown that the use of established trends and rock physics models can give insight into the poro-elastic behaviour of sediments, and the use of these models should allow the prediction of elastic properties away from well control.

3 Multi-well Rock Physics Analysis

3.1 Introduction

The aim of the rock physics analysis is to define elastic property trends based on the well log responses from the study database. These defined trends will become the basis of a modelling framework that predicts the elastic response of each identified facies (see Chapter 2) as a function of depth, sandstone porosity, saturation, consolidation (in terms of grain contact cement), and pore pressure (vertical effective stress). A prerequisite for this stage of the workflow is the petrophysical interpretation and elastic log conditioning documented in Chapter 2.

The focus of this chapter will be to analyse elastic property cross-plots in a multi-well sense, in order to understand and calibrate facies dependant trends and models for the two end-member lithologies - sand and shale.

It is important to note that only 100% brine-bearing log data was used in the multi-well analysis (i.e. elastic log data has been fluid substituted to 100% brine conditions where in situ hydrocarbons were encountered), removing the effect of any hydrocarbon effects on the regional trends – the trends and rock physics models shown here are therefore valid for brine conditioning.

3.1.1 Stratigraphic Intervals

The stratigraphy was separated into three intervals for multi-well analysis – Tertiary, Cretaceous and Jurassic. Depth trends were calibrated across all intervals, to ensure they were as robust as possible for AVO modelling. Based on the results of the depth trend analysis, several properties required unique trends over specific intervals, using cut-offs to define end members.

The petrophysical cut-offs used to identify the end-member lithologies are listed in Table 4.

End-member	Cut-offs
Sand	Shale Volume (V_{sh}) < 0.2, Saturation (SwT) = 1, Sand Flag = 1
Normal Shale	$V_{sh} > 0.9$
Cemented Shale	$V_{sh} > 0.9$; trend fitted to high velocity data
Calcareous Shale	Calcareous Shale Flag = 1 , Porosity (Φ_{iT}) < 0.05.

Table 4: End-member cut-offs. The Calcareous Shale facies was defined using cut-offs of volume of shale >0.4 and volume of lime >0, and the Sand facies was defined using cut-offs of volume of shale < 0.2 and volume of lime = 0. Both facies were manually adjusted in some parts to match the elastic log response.

Limestone, though encountered in some of the wells, was not an end-member lithology for the study, so these data were excluded from the trend analysis.

3.1.2 Trend Summary

The following elastic property trends have been derived for shale:

- V_p -TVDml
- ρ_B -TVDml
- V_s -TVDml
- V_s - V_p
- ρ_B -VES
- V_p -VES

The following elastic property trends have been derived for sand:

- ρ_B -TVDml
- Φ_{iT} - V_p (captured by a calibrated rock physics model)
- V_s - V_p
- ρ_B -VES

3.1.3 Deep-water and Shallow-water Wells

Given that Nalcor wishes to understand deep-water prospectivity, the multi-well trends in this study are derived from the 6 deep-water wells: Baccalieu I-78, Great Barasway F-66, Lona O-55, Mizzen F-09, Mizzen L-11 and Mizzen O-16.

3.2 Pore Pressure and Effective Stress

Vertical effective stress (vertical confining pressure minus pore pressure) is predominantly used to predict pressures in the subsurface for the purposes of well planning. However, if integrated with elastic properties, one can create a rock velocity and density profile from elastic property-VES transforms which can then be used in a forward modelling sense for the de-risking of seismic amplitudes. Figure 53 shows an example of how the VES trends can be used to model elastic responses at the wells. Here elastic properties are predicted directly from the VES profiles documented in Sections 1.3 and 1.4; this method assumes that the dominant controlling factor on elastic properties is VES. For the purposes of this study, the defined normal compaction depth trends will be used as the primary method of elastic property prediction, with elevated overpressure being modelled away from the normal compaction trend via the use of the VES trends.

Beyond the scope of this project, a more advanced analysis of elastic properties versus stress is possible. Important points to consider include the direction of the stress (e.g. including tectonic stresses), the effect of mineral composition and the effect of cementation state. Bakulin et al., 2008 shows that the stress path is also anisotropic, which can vary the elastic properties according to main stress directions. Eberhart-Phillips (1989) gave a set of empirical equations in her PhD, based on V_p and V_s that produces good results, and is widely used in the industry today. These equations do not only rely on effective stress, but also clay content and porosity as contributing factors to estimate velocities. It has been industry practice to assume that cemented sands are stress insensitive, and cannot be used for 4D seismic feasibility studies, but work by Duffaut et al., 2011 showed that even cemented sandstones can show stress sensitivity.

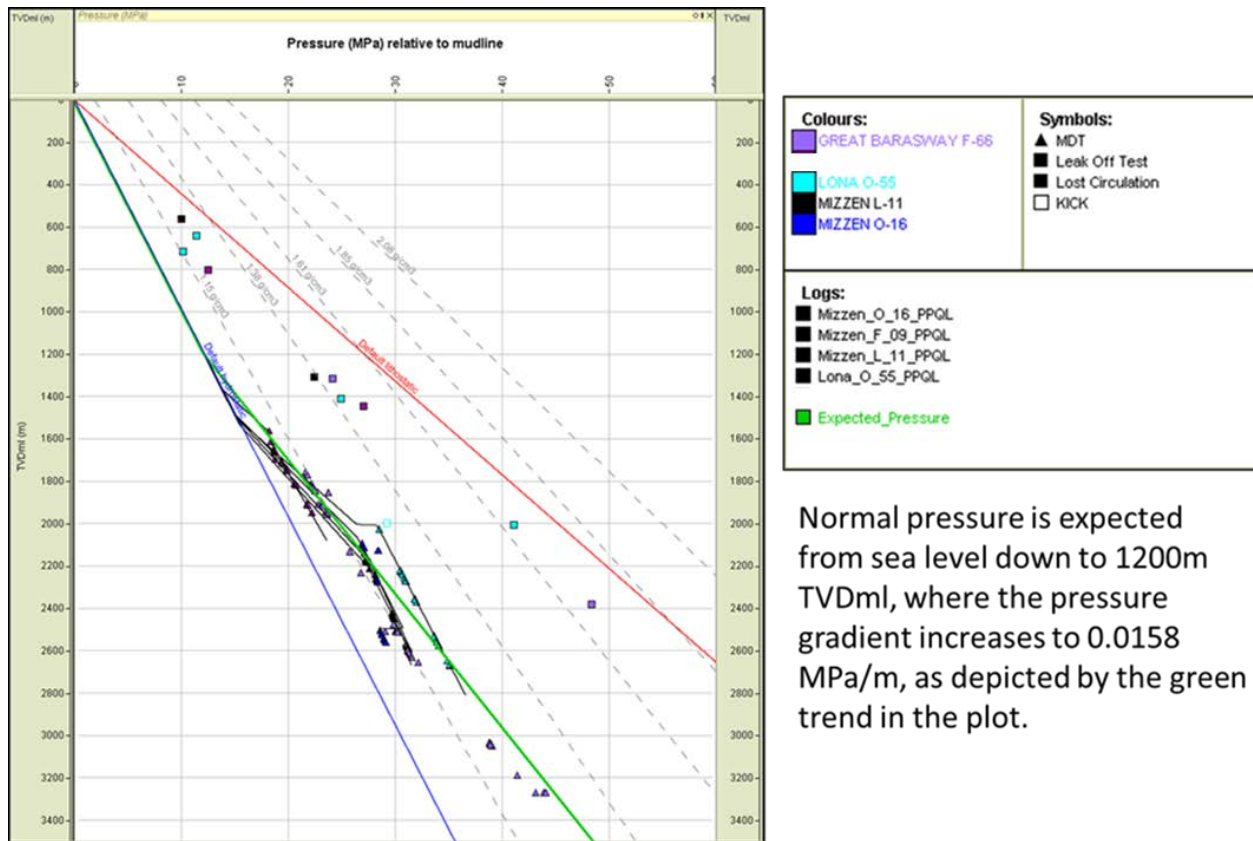


Figure 51: The expected pore pressure profile derived from the direct pressure measurements in the study wells. This trend is assumed to represent the in situ conditions for the elastic logs.

The expected case pore pressure profile is hydrostatic pressure until 1200m TVDmi, then overpressured at 0.7 psi/ft.

The high case pore pressure profile is hydrostatic pressure until 1200m TVDmi, then overpressured at 0.95 psi/ft. This is the proposed pressure profile for the pressure perturbation in the AVO modelling. The overburden gradient is set at 0.95 psi/ft, the gradient was estimated based on the 2014 regional pressure study (Nalcor Energy and Ikon Science, 2014). Figure 51 shows the direct pressure measurements available in the study wells, and the expected pressure profile in green. The expected pressure profile is assumed to correspond to the in situ pressures for the elastic log measurements in the study wells.

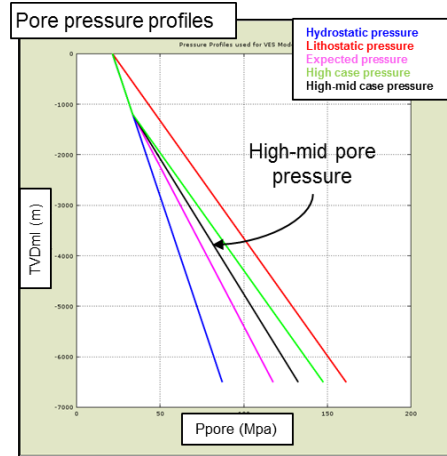


Figure 52: A high pore pressure case is used to model the low VES case within the modelling framework. The high-mid case is used to model overpressures at the Cretaceous lead.

In Figure 52 the pressure profiles used in the VES modelling are shown. These models are the expected profile (the same as Figure 51), high profile, and high-mid profile (pink, green and black respectively in Figure 52). The high profile is taken from the regional pore pressure study that accompanies this work, and the high-mid case is half way between the high and expected cases. The high-mid case is introduced for use in the lead and prospect modelling to represent a slightly overpressured case.

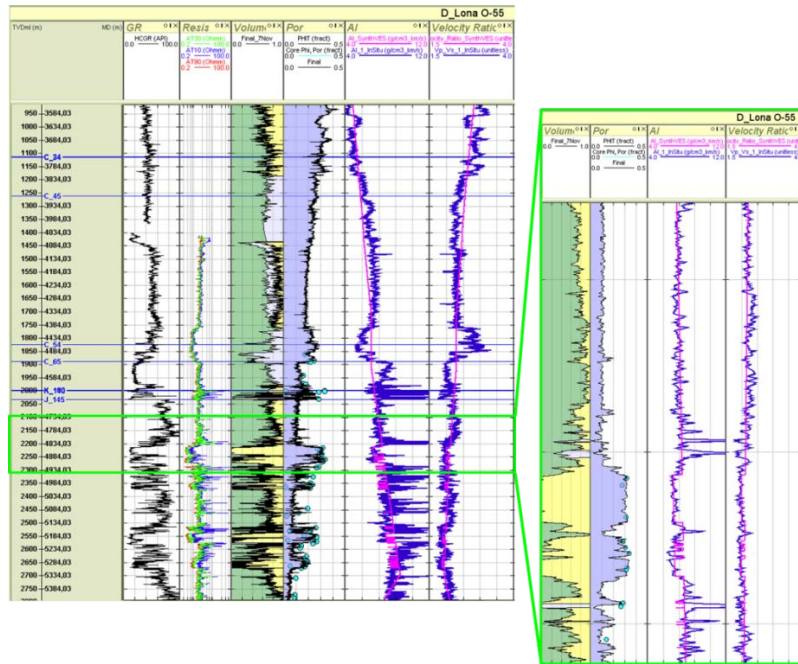


Figure 53: Example of VES transforms for Lona O-55. First and second in from right show V_p/V_s and AI respectively. The dark blue logs are the in-situ data and the pink logs are the modelled from VES transforms. The zoomed in area shows good correlation between the measured data and the synthetic generated from VES transform. Any mismatch observed can be attributed to the effect of calcite cement on the computed VES when a geological model is not used.

3.3 Shale Trends

Shale depth-dependency is captured by empirical V_p , V_s and ρ_{B} – TVDml trends. The identified shale facies, determined from the petrophysical interpretation (facies definition documented in Chapter 2) and elastic log behaviour, were divided into a ‘normal’ shale, a ‘calcareous’ shale and a ‘cemented’ shale. Depth trends provide both an understanding of how the elastic properties vary with increasing depth and aid in the identification of bad data (Figure 54). A complicating factor for deriving depth trends is the presence of uplift. In the case of uplifted strata, rocks will appear to be over-compacted for their depth. In addition to uplift effects, complex processes occur in the pores, which are heavily dependent on fluid-fill. No attempt was made in this study to correct the depth trends for the effects of uplift due to the belief that the study area has generally undergone only a small amount of uplift.

The normal shale trends (pink line; Figure 55 (V_p -TVDml), Figure 58 (V_s -TVDml) and Figure 61 (ρ_{B} -TVDml)) were fitted through the bulk of the shale data, identified using a cut-off volume of shale > 0.9 . It was found that normal shales from all intervals (Tertiary, Cretaceous and Jurassic) could be characterised with one depth trend.

Chapter 2 revealed in more detail how both velocity and density for calcareous shales, identified from the petrophysical interpretation, (light and dark blue lines; Figure 57, Figure 59 and Figure 62) follow a slightly different trend to normal shales in the cross-plot domain, i.e. calcareous shales have higher velocity but also higher density than the surrounding normal shales.

The non-calcareous shale in the deeper sections shows two distinct velocity-depth trends. The faster trend has been labelled a cemented shale trend (red line; Figure 55, Figure 58 and Figure 61) and is fitted through the higher velocity data, again identified using a cut-off of volume of shale > 0.9 . The shale data for this trend were taken from deeper and hotter zones, so the shale is interpreted to have undergone additional diagenesis, e.g. smectite to illite transformation and cementation. Diagenetic processes are generally temperature dependent (and therefore depth dependent), so it is reasonable to assume that deep Cretaceous shales may follow a similar trend, although the only observed cemented shales are found in the Jurassic in this study. The 100°C isotherm (~3300m TVDms in this study) is generally understood to be a temperature at which smectite to illite transformation starts to have a significant effect on a shale's elastic properties.

Additional detail in Chapter 2 shows how the velocity and density behaviour in cemented shales differs from the normal shales (and the potential impact on AVO signatures).

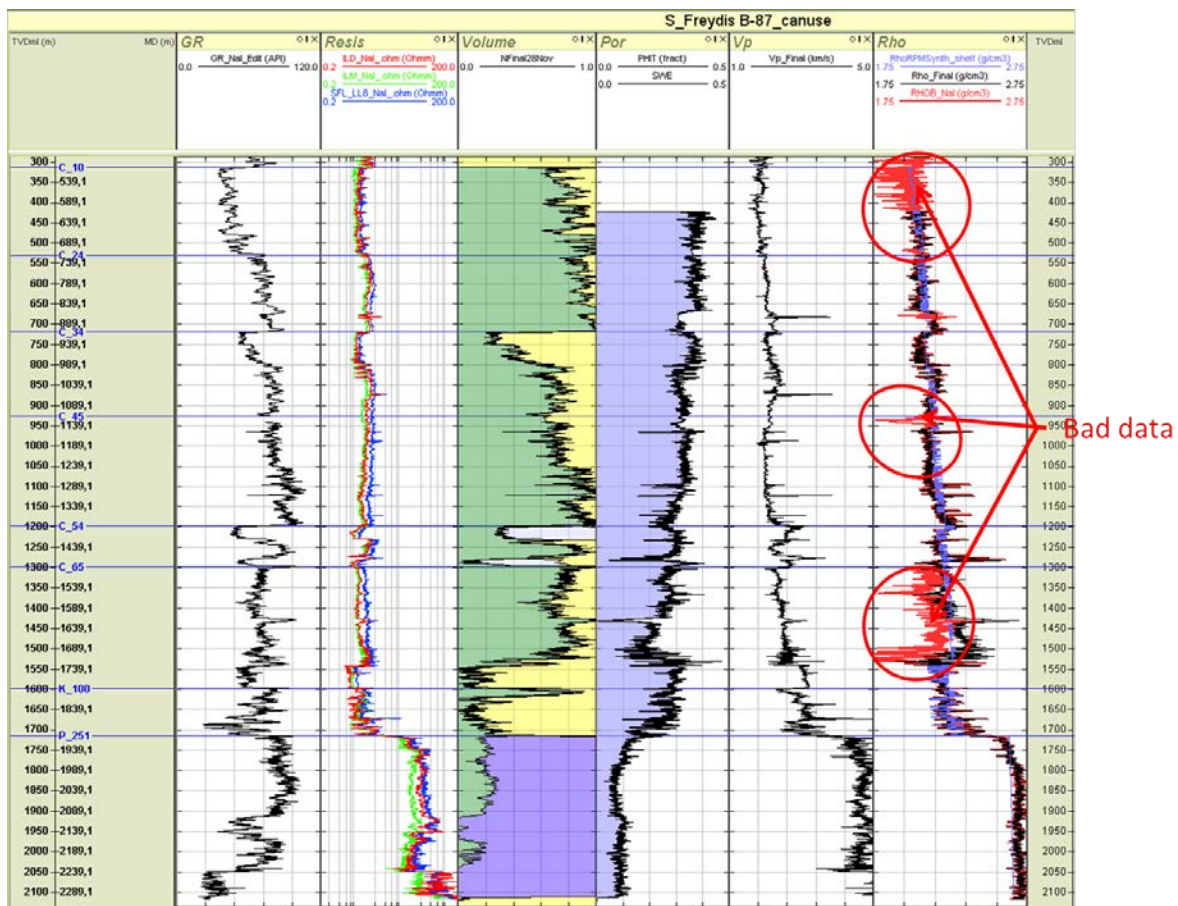


Figure 54: Well log panel for Freydis B-87. The track on the far right (track 6) shows the raw measured density log (red) and the edited density log (black). The blue log is a modelled density log, derived using the trends and arithmetic averaging. This modelled log is observed to match most of the log data and shows the location of questionable data (circled in).

3.3.1 Vp-TVDml

Significant variation in Vp-TVDml space is observed for the shale data. The difference is partly due to variations in the shale mineralogy, but there is also a systematic shift to higher velocities in the deep section.

The normal shale trend (pink line, Figure 55) lacks calibration at depth because the shales are interpreted to undergo diagenesis and become cemented shales at depths below 2.5 to 3km burial depth; the cemented shale trend (red line, Figure 55) lacks calibration in the shallow section for the same reason. The points used to define the normal and cemented shale trends are indicated in Figure 56, with the normal shales in grey and the cemented shales in red. Separating the data points into the two shale facies is a somewhat subjective exercise, as the two trends are defined based on a general shift to higher velocities below 2.5 to 3 km burial, and represent two end-member shale types. When modelling AVO anomalies the two end-member shale types could be mixed to provide further options of overburden lithology, this process could be guided by the use of single interface models.

The Jurassic calcareous shales (dark green line, Figure 57) are observed to be much faster than their Tertiary-Cretaceous counterparts (light green line, Figure 57), so a separate trend was necessary. A summary of the shale Vp-Depth trends is located in Table 5 and the trends are of the following form:

$$Vp = Vp_{matrix} - (Vp_{matrix} - Vp_{top}) * \exp(-b * TVDml)$$

Where Vp_{top} = velocity at mudline; b = compaction coefficient; Vp_{matrix} = velocity asymptote at depth.

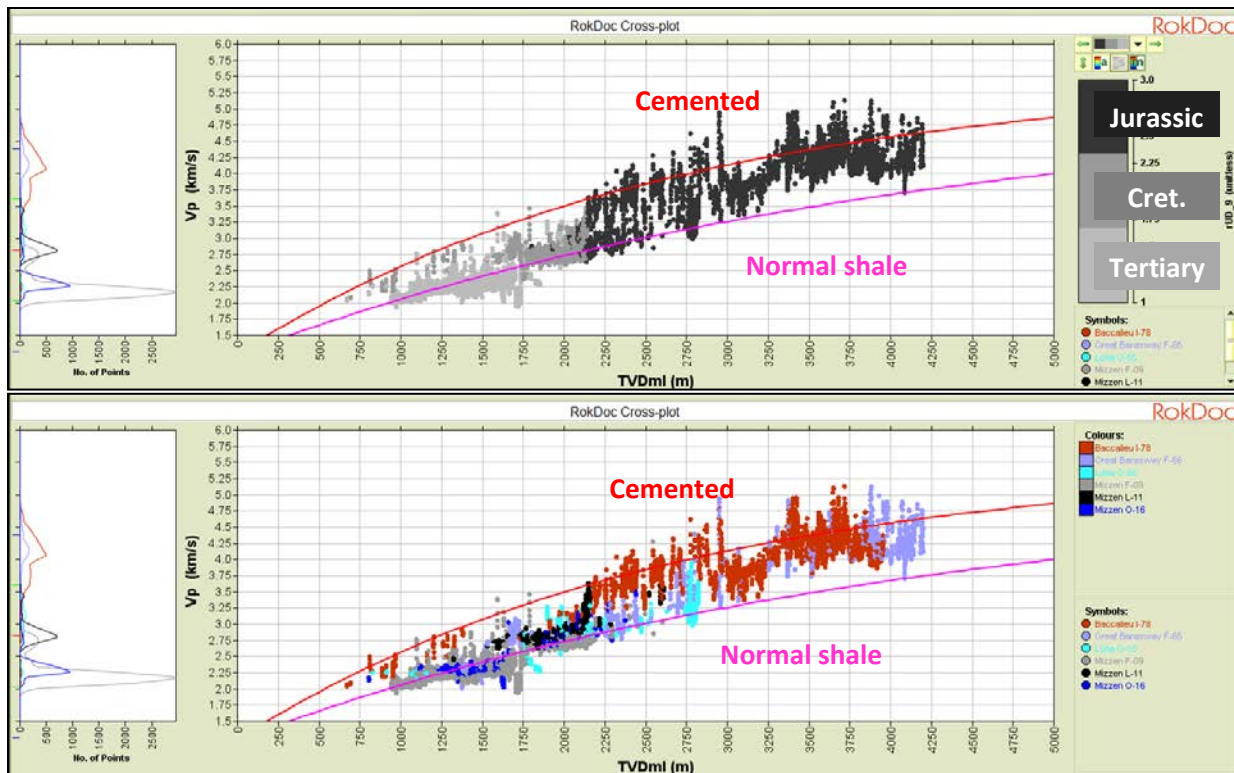


Figure 55: Vp-Depth (TVDmi) for shale data, showing Normal and Cemented shale. Upper plot: coloured by interval; Lower plot: coloured by well.

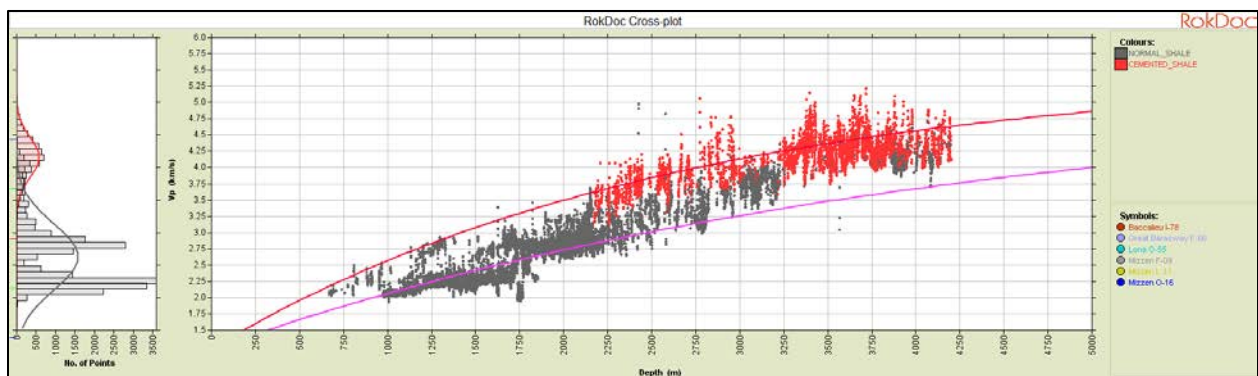


Figure 56: Vp-Depth (TVDmi) for shale data, showing Normal and Cemented shale. The points here are coloured by shale type, with shales interpreted to be cemented shown in red.

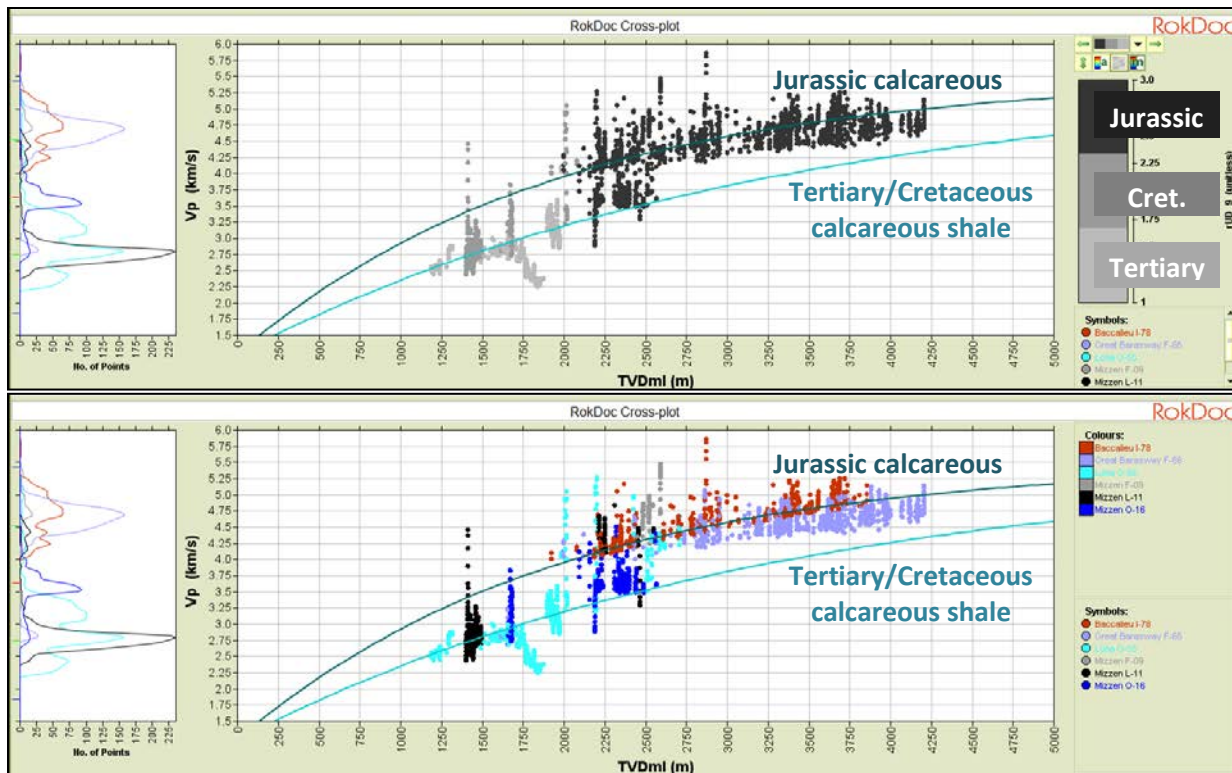


Figure 57: Vp-Depth (TVDml) for shale data, showing Calcareous shale. Upper plot: coloured by interval; Lower plot: coloured by well.

Lithology/Facies	Working Interval	Empirical Trend	Calibration Range (m TVDml)
Normal shale	Tertiary - Jurassic	$V_p = 5200 - (5200 - 1200) * e^{-2.4E-4 * TVDml(m)}$	= 900 – 4200
Cemented shale	Jurassic	$V_p = 5500 - (5500 - 1200) * e^{-3.8E-4 * TVDml(m)}$	= 2150 – 4200
Calcareous shale	Tertiary – Cretaceous	$V_p = 5500 - (5500 - 1200) * e^{-3.1E-4 * TVDml(m)}$	= 900 – 4200
Calcareous shale	Jurassic	$V_p = 5500 - (5500 - 1200) * e^{-5.1E-4 * TVDml(m)}$	= 2150 – 4200

Table 5: Summary of Shale Vp-TVDml regressions.

3.3.2 RhoB-TVDml

The bulk density of the shales is consistent between the normal and cemented shales, with a general increase in the deep section where the shales are interpreted to be cemented (Figure 58). It is to be expected that the effect of cementation will be more pronounced in the velocity domain. At depth, for the cemented shale (red line, Figure 58), the RhoB-TVDml behaviour is consistent between the two deep wells, Baccalieu I-78 and Great Barasway F-66. The difference between Tertiary-Cretaceous calcareous shales (light blue line, Figure 59) and Jurassic calcareous shales (dark blue line, Figure 59) is also not as pronounced as it is in Vp-TVDml. Low-density shale data are observed between 1600-1800m TVDml (Figure 60), these points are associated with low velocities (as per Figure 55 and Figure 57 and appear to be related to a marl or soft shale lithology at this depth. A summary of the shale RhoB-Depth trends is located in Table 6. The trends are of the following form:

$$RhoB = RhoB_{matrix} - (RhoB_{matrix} - RhoB_{top}) * \exp(-b * TVDml)$$

Where $RhoB_{top}$ = density at mudline; b = compaction coefficient; $RhoB_{matrix}$ = density asymptote at depth.

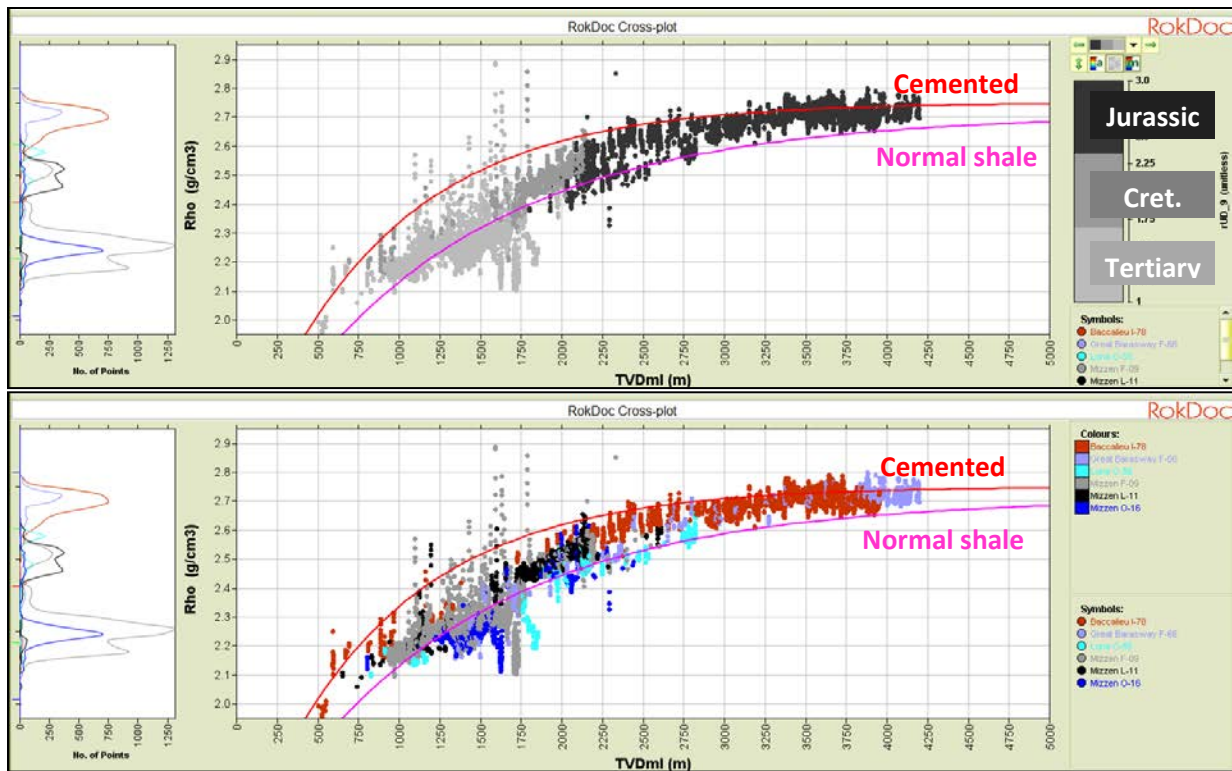


Figure 58: RhoB-Depth (TVDmi) for shale data, showing Normal and Cemented shale. Upper plot: coloured by interval; Lower plot: coloured by well.

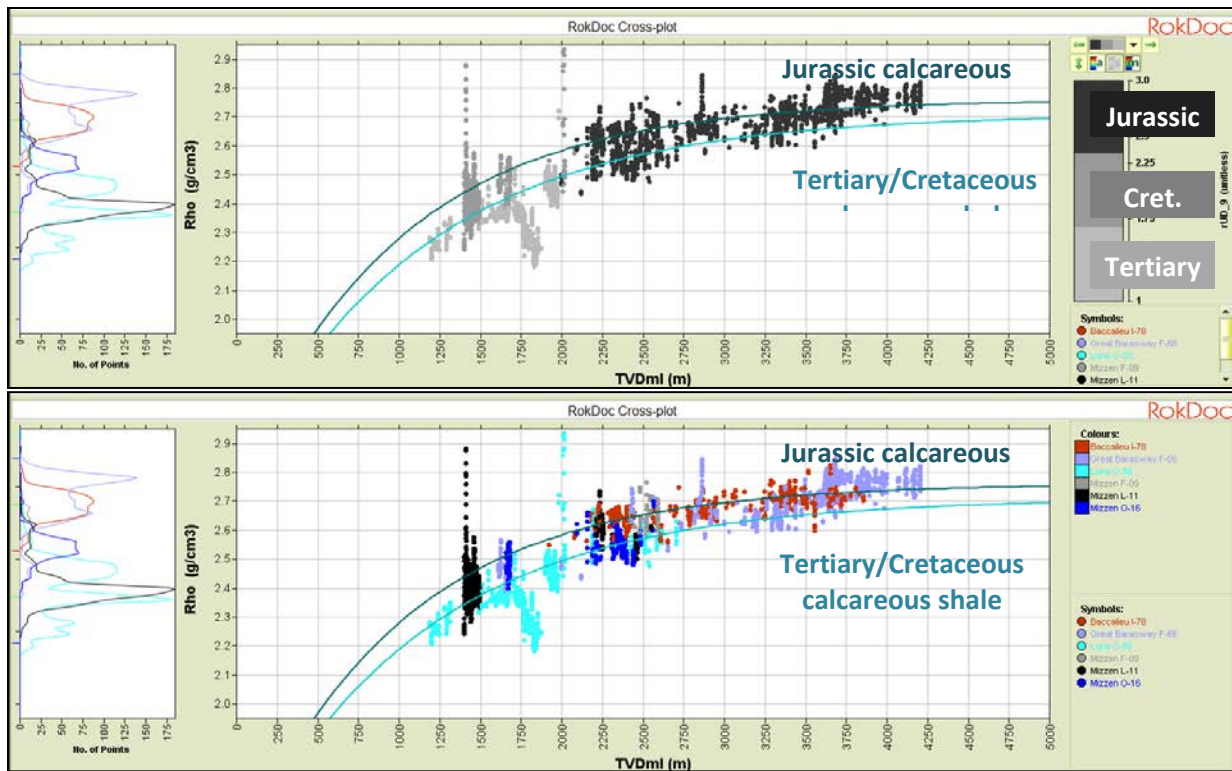


Figure 59: RhoB-Depth (TVDml) for shale data, showing Calcareous shale. Upper plot: coloured by interval; Lower plot: coloured by well.

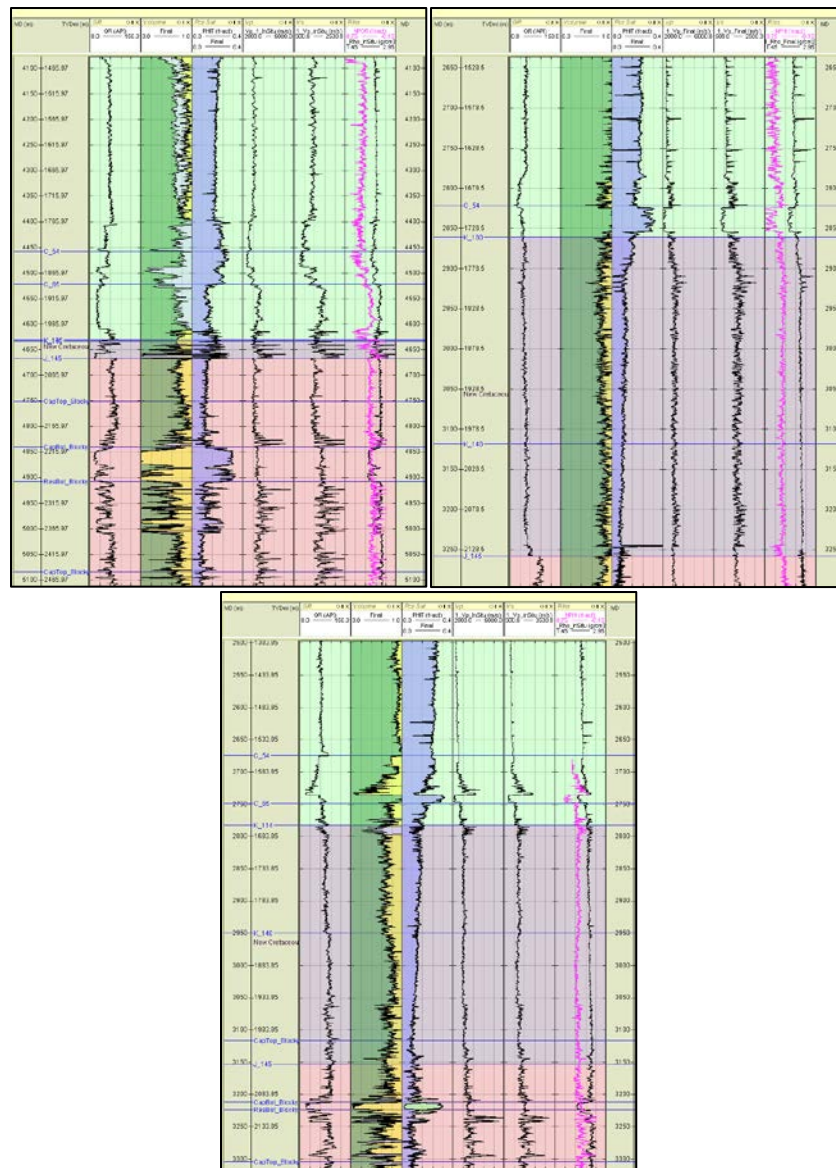


Figure 60: Well log panels showing the slow, low density shale lithology in Lona O-55 (left; 4400-4520m MD), Mizzen F-09 (middle; 2820-2855m MD) and Mizzen O-16 (right; 2735-2747m MD).

Lithology/Facies	Working Interval	Empirical Trend	Calibration Range (m TVDml)
Normal shale	Tertiary - Jurassic	RhoB(g/cc) 2.71 – (2.71 – 1.45) * e ^{(-7.75E-4 * TVDml(m))}	= 900 – 4200
Cemented shale	Jurassic	RhoB (g/cc) 2.75 – (2.75 – 1.45) * e ^{(-11.4E-4 * TVDml(m))}	= 2150 – 4200
Calcareous shale	Tertiary – Cretaceous	RhoB(g/cc) 2.71 – (2.71 – 1.45) * e ^{(-8.8E-4 * TVDml(m))}	= 900 – 4200
Calcareous shale	Jurassic	RhoB(g/cc) 2.76 – (2.76 – 1.45) * e ^{(-10E-4 * TVDml(m))}	= 2150 – 4200

Table 6: Summary of Shale RhoB-Depth trends.

3.3.3 Vs-TVDml

The shale data in the Baccalieu I-78 and Great Barasway F-66 wells trend between the normal shales in the shallower section and cemented shales in the deeper section (red and pink lines respectively, Figure 61). This intermediate trend is interpreted to be related to changes in the nature of the shales at depth, being consistent with the smectite to illite transformation as per the interpretation of the Vp-TVDml data. Measured Vs data were only available in three deep-water wells – Mizzen F-09, Mizzen O-16 and Lona O-55, the Vs in the other wells is modelled based on the relationships observed in these well penetrations. Due to the Vs being modelled from the Vp, the Jurassic calcareous shales (dark blue line, Figure 62) are observed to be much faster than their Tertiary-Cretaceous counterparts (light blue line, Figure 62). A summary of the shale Vs-Depth trends is located in Table 7 and the trends are of the following form:

$$Vs = Vs_{matrix} - (Vs_{matrix} - Vs_{top}) * \exp(-b * TVDml)$$

Where Vs_{top} = Vs at mudline; b = compaction coefficient; Vs_{matrix} = Vs asymptote at depth.

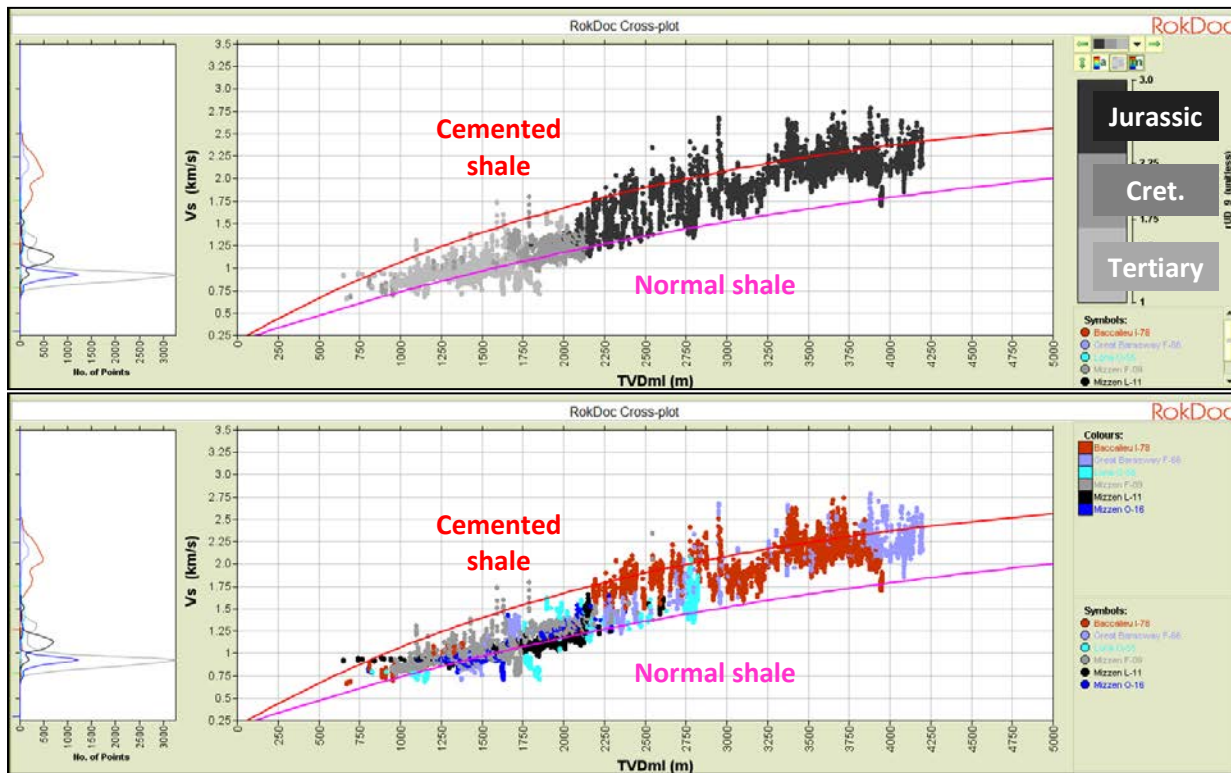


Figure 61: Vs-Depth (TVDml) for shale data, showing Normal and Cemented shale. Upper plot: coloured by interval; Lower plot: coloured by well. Measured and modelled Vs shown.

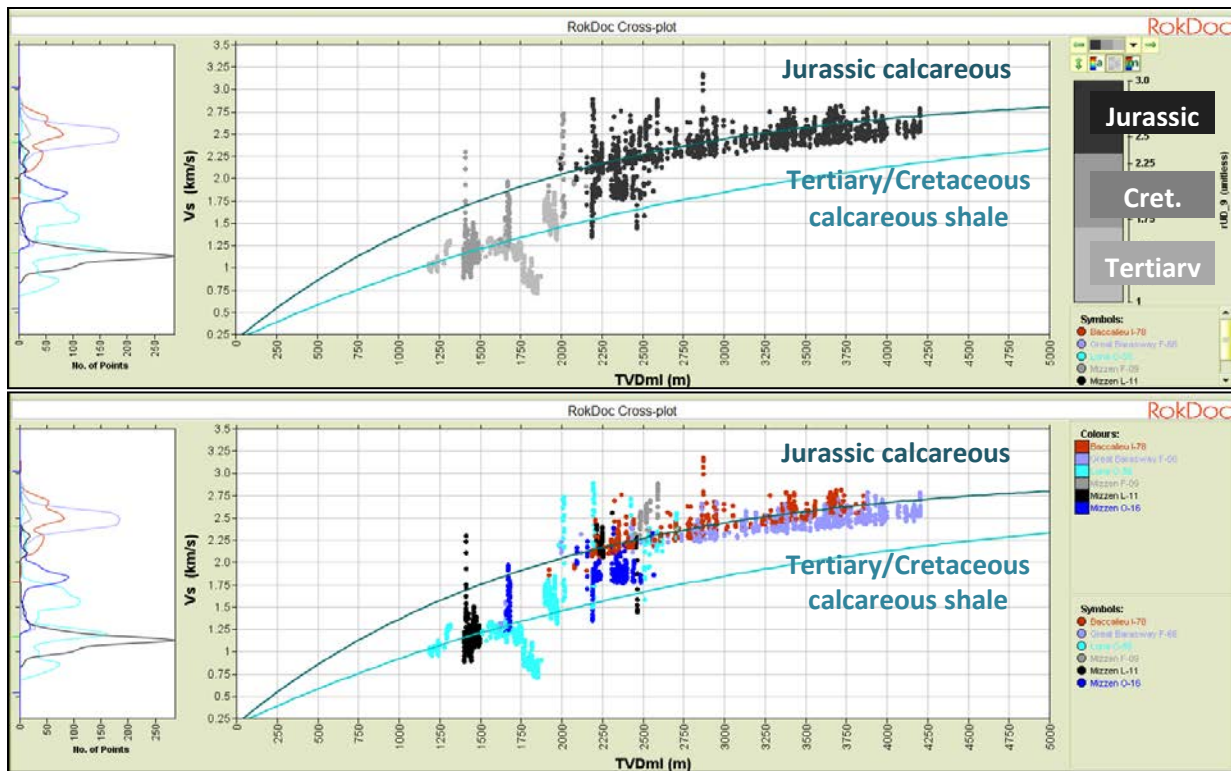


Figure 62: Vs-Depth (TVDml) for shale data, showing Calcareous shale. Upper plot: coloured by interval; Lower plot: coloured by well. Measured and modelled Vs shown.

Lithology/Facies	Working Interval	Empirical Trend	Calibration Range (m TVDml)
Normal shale	Tertiary - Jurassic	$V_s \text{ (m/s)} = 2783 - (2783 - 175) * e^{-2.4E-4 * \text{TVDml(m)}}$	900 – 2800
Cemented shale	Jurassic	$V_s \text{ (m/s)} = 2979 - (2979 - 175) * e^{-3.8E-4 * \text{TVDml(m)}}$	No measured Vs available for this lithology.
Calcareous shale	Tertiary – Cretaceous	$V_s \text{ (m/s)} = 2878 - (2878 - 175) * e^{-3.3E-4 * \text{TVDml(m)}}$	900 – 2600
Calcareous shale	Jurassic	$V_s \text{ (m/s)} = 2978 - (2978 - 175) * e^{-5.5E-4 * \text{TVDml(m)}}$	2150 – 2600

Table 7: Summary of Shale Vs-Depth trends.

3.3.4 Vs-Vp

Measured Vs data were only available in three deep-water wells – Mizzen F-09, Mizzen O-16 and Lona O-55 – the overall quality was reasonable. Several sections of poor quality data were identified (Figure 63) and noisy data were removed to give realistic values of Vp/Vs and Poisson's Ratio. Unfortunately, a lot of the poor quality and noisy Vs data were in the shales so the Vs-Vp trend has a relatively high uncertainty in calibration, although it generally agrees with published trends. After the analysis, a linear trend was fitted to the shale data for Lona O-55 only (Figure 64), and used to predict Vs in the other wells. A summary of the shale Vs-Vp trend is located in Table 8 and the trend is of the following form:

$$Vs = m * Vp + c$$

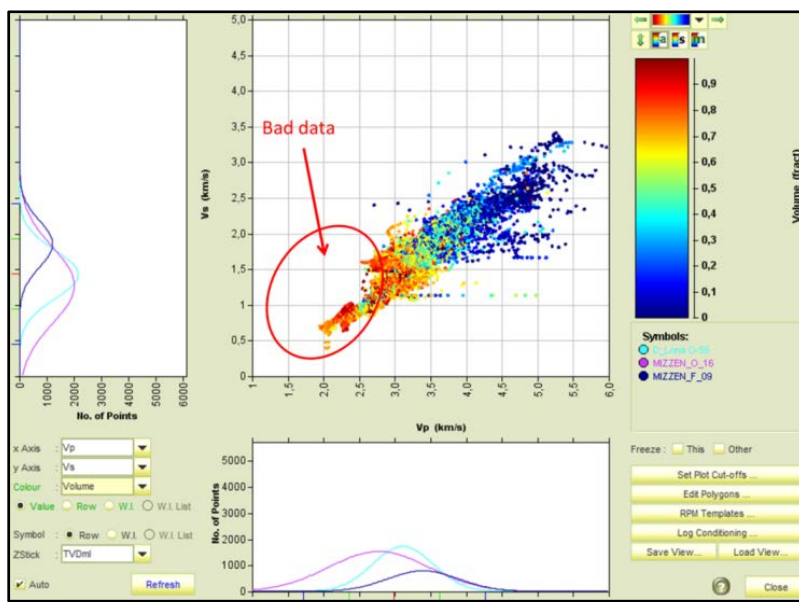


Figure 63: Vs-Vp for the 3 wells that had measured shear data (Lona O-55, Mizzen O-16 and Mizzen F-09). All lithologies shown.

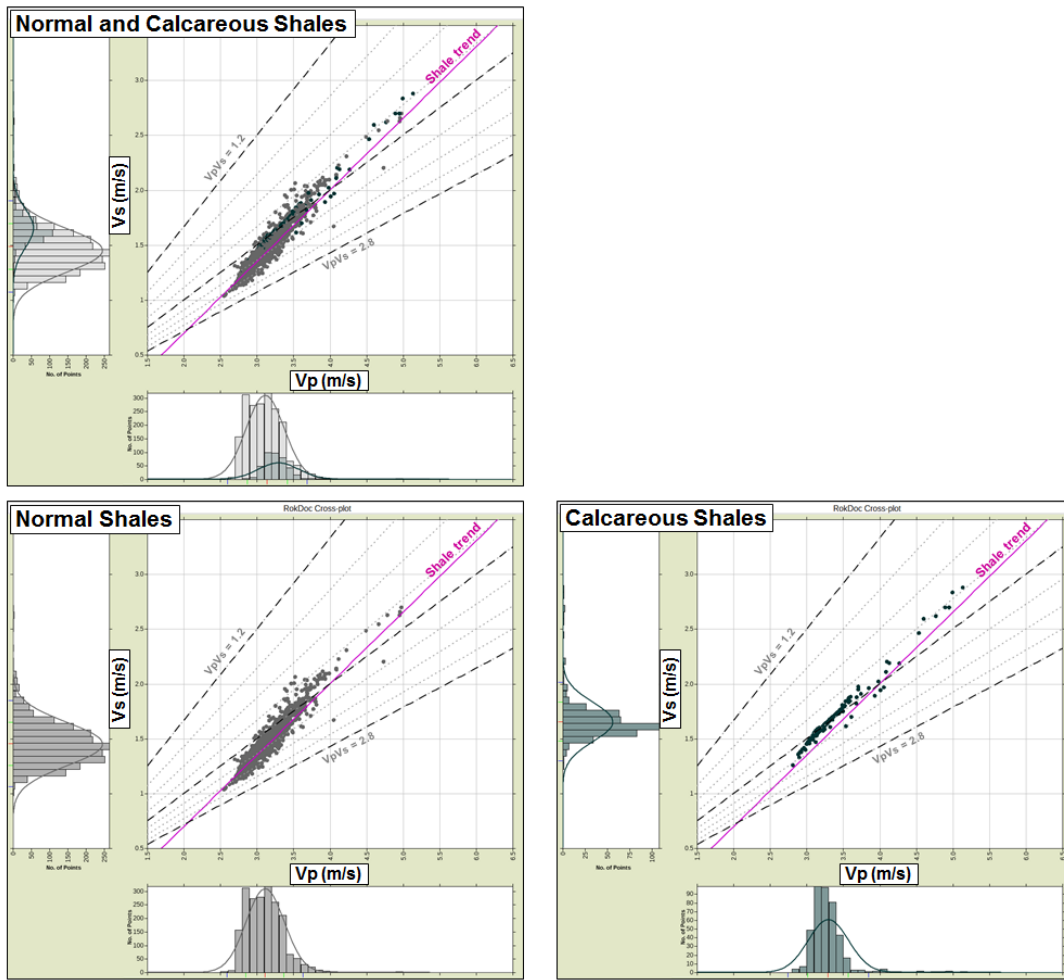


Figure 64: The Vp-Vs trend is defined based on the data shown above. This is taken from the shales in Lona O-55, where normal and calcareous shales are encountered. The upper plot shows both shale facies, while the lower plots show each shale facies individually. The shale Vp-Vs trend used in the modelling is shown in pink, and lines of constant Vp/Vs ratio are shown as grey dashed lines, from a Vp/Vs of 1.2 to a Vp/Vs of 2.8.

As can be seen in Figure 64, the trend is a good fit to the bulk of the shale data (which comes from the normal shale facies), but predicts slightly higher Vp/Vs ratio values for the calcareous shale data (per measured Vp value). Although the differences are considered small, the Vp-Vs trend should have higher uncertainty attached in the calcareous shale facies versus the normal shale facies.

Lithology/Facies	Working Interval	Empirical Trend	Calibration Range (m TVDmi)
All Shale	Tertiary - Jurassic	$Vs(m/s) = 0.652 * Vp(m/s) - 607$	All Shale

Table 8: Summary of Shale Vp-Vs trends.

3.3.5 RhoB-VES

All shale RhoB-VES data is shown in Figure 65. A power law was fitted to this data to capture the change in RhoB as a function of vertical effective stress. As observed the effect of VES on RhoB is greatest at low stresses, where pore pressure is able to maintain porosity. RhoB can vary substantially depending on the amount of overpressure present in the system which is consistent with what is expected in overpressured rocks since overpressure acts to preserve porosity.

The trend shows a good match to the data and follows reasonable start and end (mineral) points, there is no obvious separation in RhoB-VES trend between shale types. For the purposes of this study, there is more interest in the higher overpressure end of the trend, which is observed to fit the data well. A summary of the VES trends is located in Table 9.

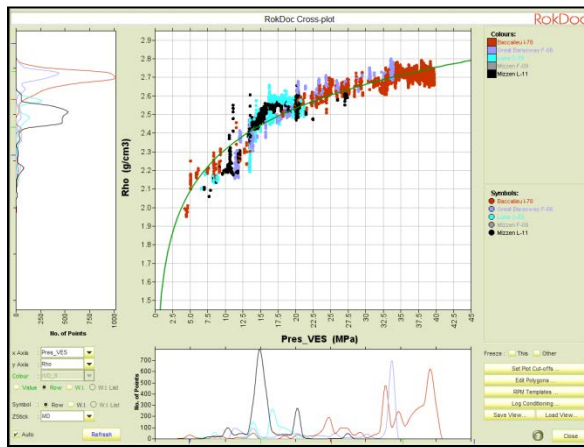


Figure 65: RhoB-VES for shale data, showing all shale, coloured by well.

3.3.6 Vp-VES

Unlike the RhoB-VES trend, a correlation was observed between shale type and Vp-VES behaviour, so different Vp-VES trends were derived for each shale type (Figure 66 to Figure 69).

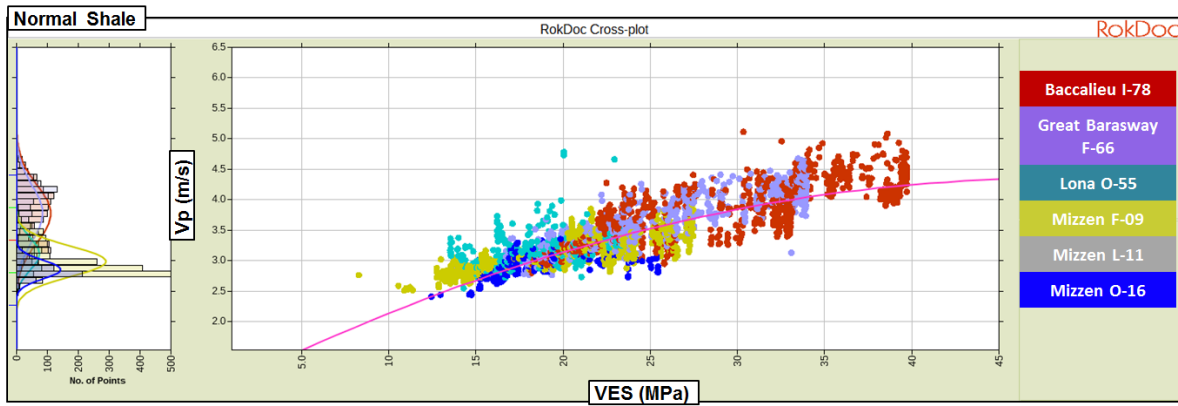


Figure 66: Vp-VES for shale data, showing normal shale, coloured by well.

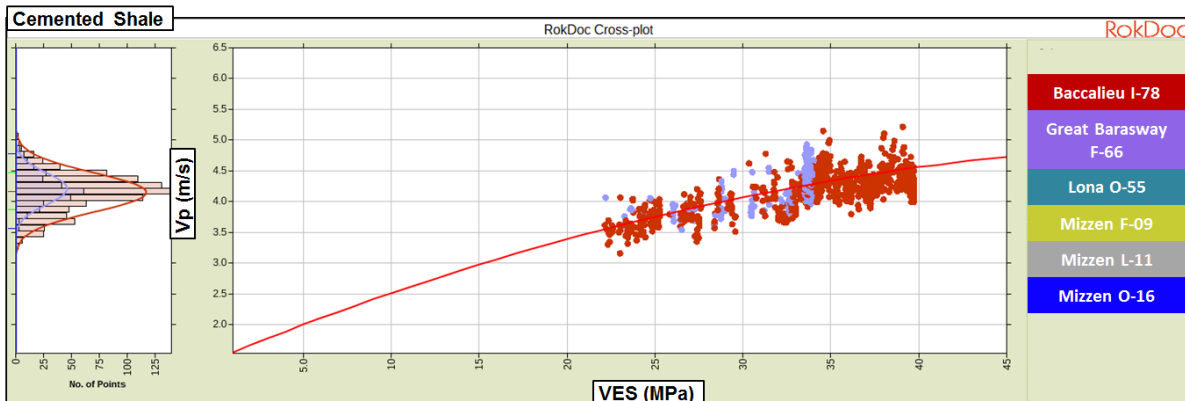


Figure 67: Vp-VES for shale data, showing cemented shale, coloured by well.

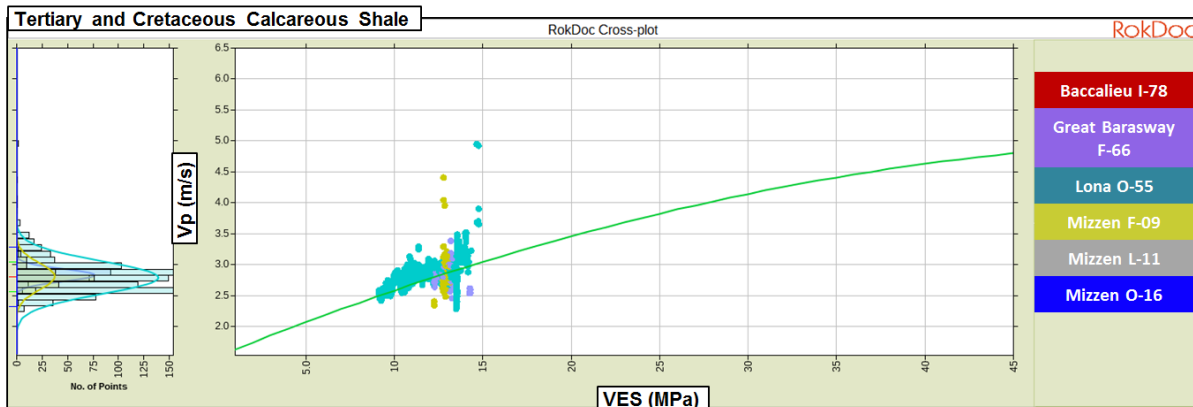


Figure 68: Vp-VES for shale data, showing Tertiary-Cretaceous calcareous shale, coloured by well.

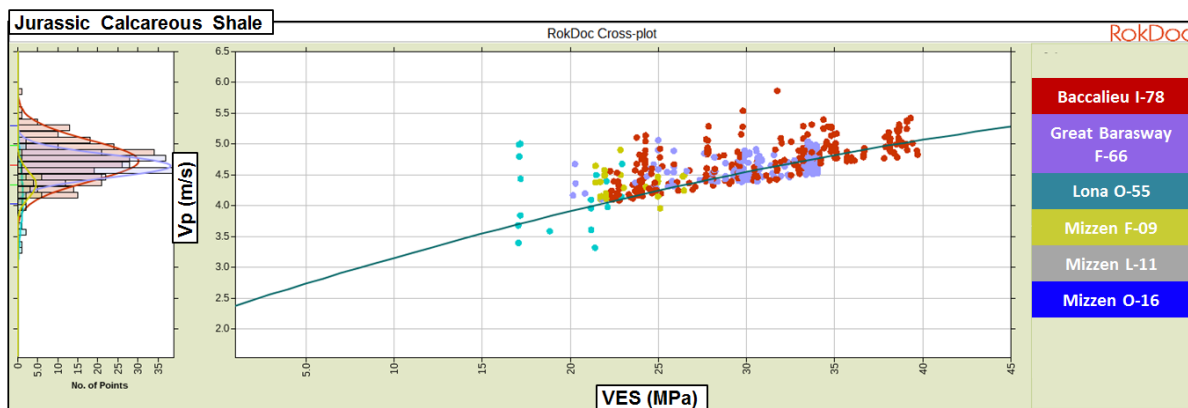


Figure 69: Vp-VES for shale data, showing Jurassic calcareous shale, coloured by well.

Trend Type	Lithology/Facies	Working Interval	Description	Calibration Range (m TVDml)
RhoB-VES	All Shale	Tertiary - Jurassic	$\text{RhoB (g/cc)} = -82.418 * (\text{VES (MPa)} ^ {-3.914E-3} + 83.989)$	VES: 5 – 40 MPa
Vp-VES	Normal Shale	Tertiary - Jurassic	$\text{Vp (km/s)} = (-1.493E-3 * \text{VES (MPa)} ^ 2) + (0.145 * \text{VES(MPa)}) + 0.827$	VES: 5 – 40 MPa
Vp-VES	Cemented Shale	Tertiary - Jurassic	$\text{Vp (km/s)} = (-9.734E-4 * \text{VES (MPa)} ^ 2) + (0.117 * \text{VES(MPa)}) + 1.429$	VES: 5 – 40 Mpa
Vp-VES	Calcareous Shale	Tertiary-Cretaceous	$\text{Vp (km/s)} = (-9.734E-4 * \text{VES (MPa)} ^ 2) + (0.117 * \text{VES(MPa)}) + 1.429$	VES: 8 – 15 MPa
Vp-VES	Calcareous Shale	Jurassic	$\text{Vp (km/s)} = (-5.790E-4 * \text{VES (MPa)} ^ 2) + (9.266E-2 * \text{VES(MPa)}) + 2.280$	VES: 17 – 40 MPa
RhoB-VES	All Sand	Tertiary - Jurassic	$\text{Rho(g/cc)} = (-2.163E-4 * \text{VES (MPa)} ^ 2) + (3.320E-2 * \text{VES(MPa)}) + 1.672$	VES: 12.5 – 30 MPa

Table 9: Summary of VES Trends.

3.4 Sand Trends

The sand data is sparse compared to the shale data, as might be expected, and the sands are generally encountered as thin packages. Therefore, up-scaling of the log data is a required step before trend fitting. This up-scaling ensures that the clean sand elastic response is extracted, while avoiding shoulder bed and hybrid log responses (where there is fine geological layering relative to log measurement scale). The up-scaling is a lithology based technique that uses the derived facies log (cut-offs applied to the petrophysical interpretation) and a coefficient of variation (maximum allowed level of facies variation within a window). The workflow extracts discrete points from thick facies packets encountered by the continuous elastic log data and is described in Chapter 2.

A single RhoB-depth trend was derived for all sands (Figure 70) in the study and the RMS error of 0.126 g cm⁻³ was taken to capture the high and low density (low and high porosity) cases. This was converted to a porosity-depth trend (Figure 71) using a matrix density of 2.65g cm⁻³ and a fluid density of 1g cm⁻³. The matrix density is guided by matching the core porosities in Lona O-55, Mizzen F-09 and Mizzen L-11.

The log responses indicate that the grain contact cement content is variable across the study wells (as a general rule p-wave velocities above 3km/s are normally indicative of some grain contact cement, and the well logs show values greater and less than this value), so a rock physics model is required to capture the effects of both cementation and sorting for these reservoir rocks.

The Constant Cement (Avseth, et al. 2000) rock physics model (Figure 73) was fitted to the well data in PhiT-Vp space. As described in Chapter 2, this model captures the influence of mechanical and chemical compaction, the effect of chemical compaction on the bulk rock elastic properties is implied to be the result of increasing grain contact cement by the model. Cement is added at the grain contacts using the Cementation theory of Dvorkin et al (1994), and sorting trends at a given grain contact cement level captured via the use of modified lower Hashin-Strikman lower bound (these bounds are used to interpolate between the cemented grain pack at critical porosity (at the defined grain contact cement level) and the mineral point at zero porosity).

A calibrated Greenberg-Castagna trend was used to derive Vs (Figure 75) from the Vp predicted by the Constant Cement model.

The PhiT-depth trend was used as an input for the Constant Cement model to derive Vp-depth trends (Figure 76) for 0% - 8% cement.

A RhoB-VES (Vertical Effective Stress) trend was derived for all sands (Figure 77), which will allow the effect of overpressure on sandstone porosity, and therefore elastic properties, to be investigated during the AVO modelling phase in a quantitative manner.

The Vp(Por-TVDml) and RhoB-TVDml trends for sands are of the following form (shown for RhoB-TVDml):

$$\frac{1}{RhoB} = \frac{1}{RhoB_{matrix}} - \left(\frac{1}{RhoB_{matrix}} - \frac{1}{RhoB_{top}} \right) * \exp(-b * TVDml)$$

Where $RhoB_{top}$ = density at mudline; b = compaction coefficient; $RhoB_{matrix}$ = density asymptote at depth. A summary of the sand trends is located below in Table 10.

Trend Type	Lithology/Facies	Working Interval	Description	Calibration Range
RhoB-TVDml	All sand	Tertiary Jurassic	$RhoB(g/cc) = 1/ ((1/2.66) - ((1/2.66) - (1/1.765)) * e^{(-4.52E-4 * TVDml(m)))}$	1750 – 2700m TVDml
Vp(PhiT-TVDml)	Friable sand	Tertiary Jurassic	$Vp(km/s) = 1/ ((1/9.650) - ((1/9.650) - (1/2.035)) * e^{(-1.944E-4 * TVDml(m)))}$	
	Cemented sand (2%)	Tertiary Jurassic	$Vp(km/s) = 1/ ((1/7.432) - ((1/7.432) - (1/2.329)) * e^{(-2.429E-4 * TVDml(m)))}$	
	Cemented sand (4%)	Tertiary Jurassic	$Vp(km/s) = 1/ ((1/6.930) - ((1/6.930) - (1/2.423)) * e^{(-2.747E-4 * TVDml(m)))}$	
	Cemented sand (6%)	Tertiary Jurassic	$Vp(km/s) = 1/ ((1/6.791) - ((1/6.791) - (1/2.495)) * e^{(-2.847E-4 * TVDml(m)))}$	
	Cemented sand (8%)	Tertiary Jurassic	$Vp(km/s) = 1/ ((1/6.656) - ((1/6.656) - (1/2.518)) * e^{(-2.990E-4 * TVDml(m)))}$	
Vs-Vp	All sand	Tertiary Jurassic	$Vs(km/s) = 0.724 * Vp (km/s) - 0.674$	Vp: 3 – 4 km/s
RhoB-VES	All sand	Tertiary Jurassic	$RhoB(g/cc) = (-2.163E-4 * VES ^ 2) + (3.320E-2 * VES) + 1.672$	VES: 12.5 – 30 MPa

Table 10: Summary of sand trends.

3.4.1 RhoB-TVDml

The RhoB-TVDml sand trend was defined based on clean reservoir sand points using the up-scaled RhoB data. Calcareous cemented sand, and reworked carbonates were removed from the data used to define the trend as they are not considered a reservoir sand facies in this study.

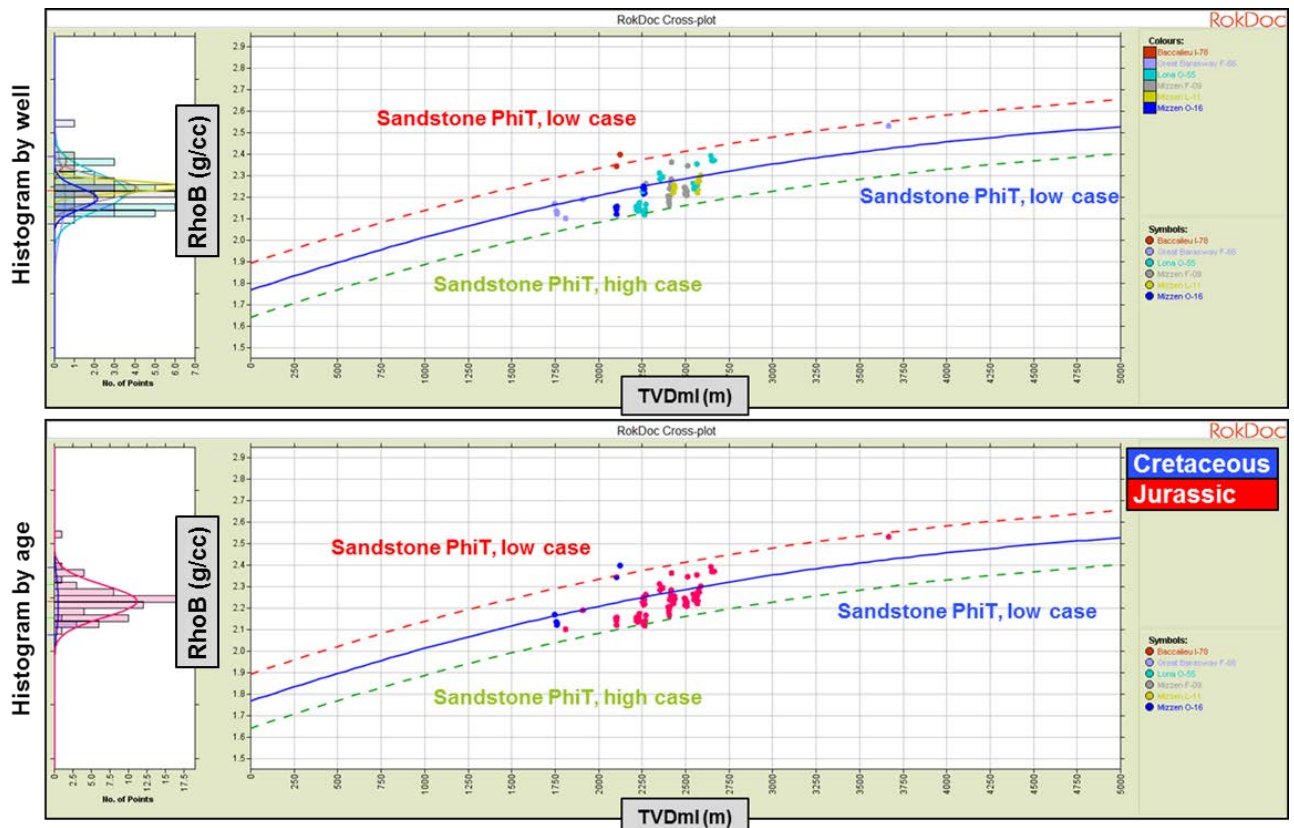


Figure 70: RhoB-TVDml for sand data, showing all reservoir-quality sand. Upper plot: coloured by well; Lower plot: coloured by age interval. The data here has been up-scaled using a lithology-based technique as described in chapter 2. The aim is to extract log data points avoid areas of fine facies layering relative to log scale.

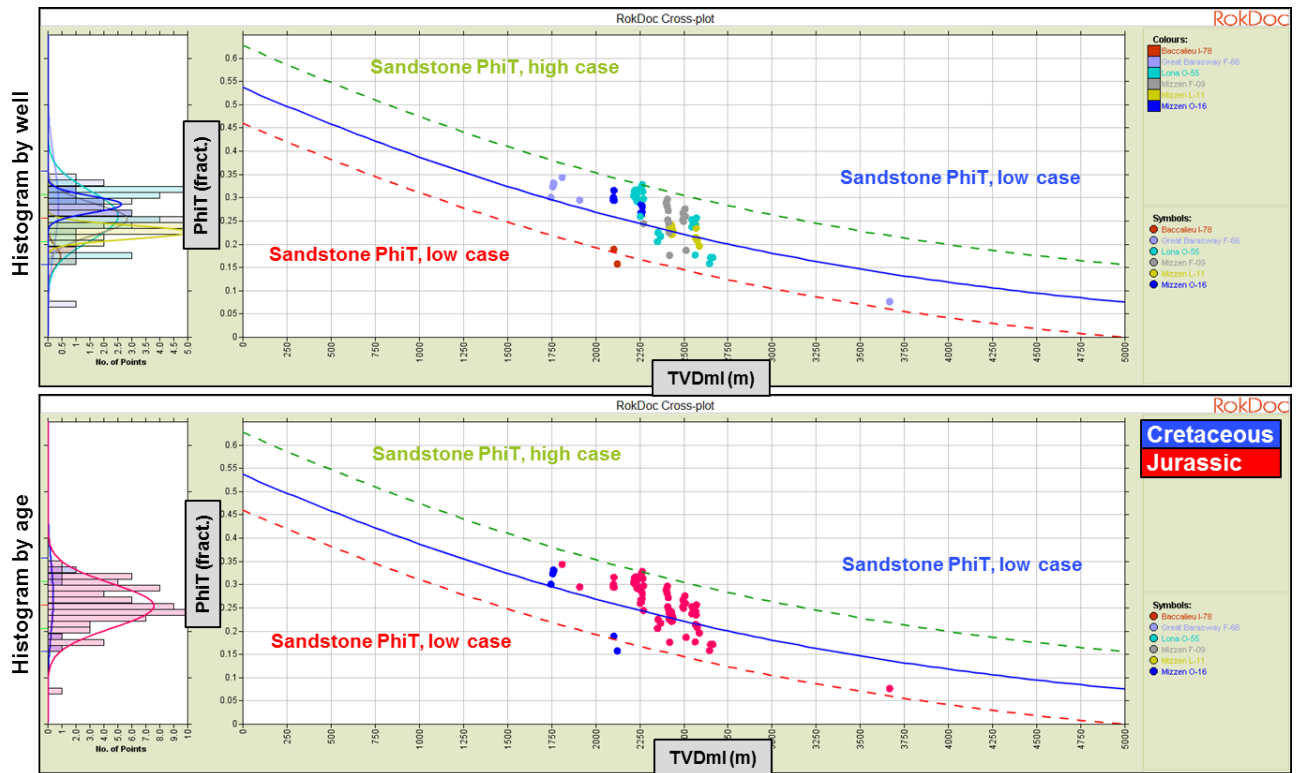


Figure 71: Por(PhiT)-TVDml for sand data, showing all reservoir-quality sand. Calculated from RhoB-TVDml. Upper plot: coloured by well; Lower plot: coloured by age interval. The data here has been up-scaled using a lithology-based technique as described in chapter 2. The aim is to extract log data points avoid areas of fine facies layering relative to log scale.

The porosity-depth data from the study were compared to analogue data from the Norwegian continental shelf (shown in Figure 72) and all trends show a reasonable match.

There are points in the Norwegian data that plot on the low case porosity-depth trend but no effort has been made to exclude highly cemented sand points from the analogues, which may partly explain this. There are also several clusters of data points from the Norwegian wells that show porosity at depth that is far beyond that observed in the Orphan Basin/Flemish Pass wells. The reason for this is postulated to be porosity maintenance via very high overpressure (several of the Norwegian wells have overpressure that is significantly above that observed in the study dataset), which validates the use of VES modelling in later chapters.

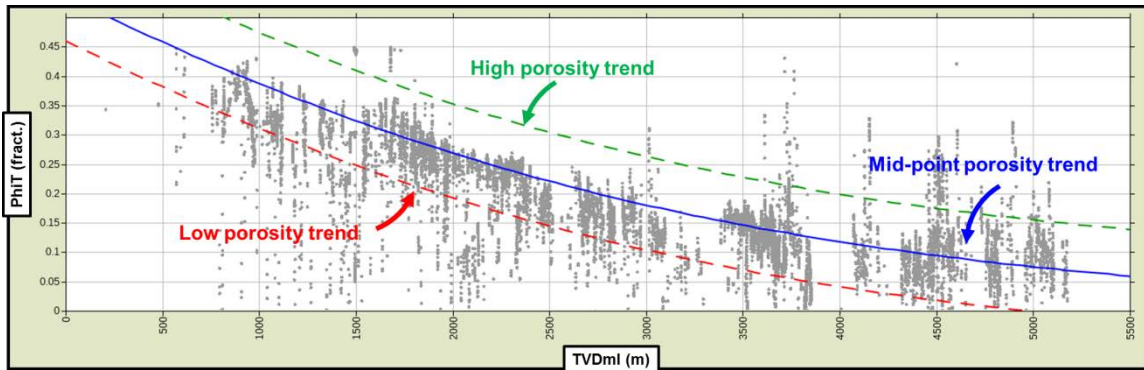


Figure 72: PhiT-depth data from analogue well data from mid Norway. The PhiT-TVDml trends (blue = mid-point, green = high, red = low). High porosities of up to 30% are noted in the deeper stratigraphy of the Norwegian wells (around 4.5 km to 5 km).

3.4.2 PhiT-Vp

The PhiT-Vp trends are captured via the use of the Constant Cement Rock Physics Model (RPM) to the reservoir sand data. The model is described in more detail in Chapter 2. The model is calibrated to the study well responses, assuming the matrix is quartz and that the grain contact cement is quartz. The model is fit to the spread of data via a variable grain contact cement content, here between 0% (unconsolidated rock) and 8% for the most cemented sands. Some verification is provided by the petrographic analysis at the Mizzen O-16 well, where an estimate of quartz overgrowth is made from the analysis (where the quartz overgrowth values are assumed to represent grain contact cement). The PhiT-TVDml trend defined in the last section forms the input into the RPM, generating sand Vp-TVDml trends for a range of cements from 0% (friable; uncemented) to 8%.

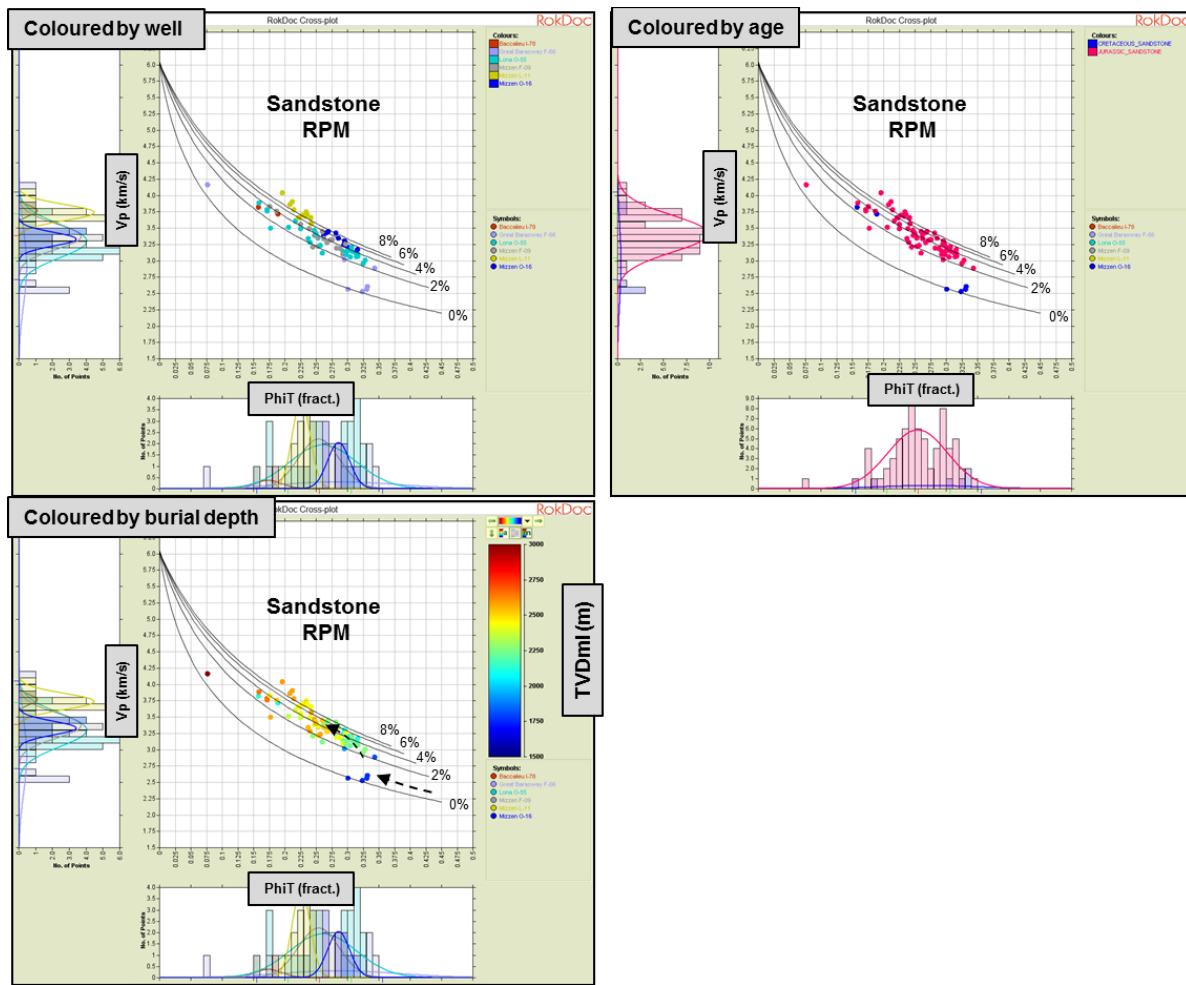


Figure 73: Por-Vp for sand data, showing all reservoir-quality sand. Top left plot: coloured by well; top right plot: coloured by age interval (blue = Cretaceous, red = Jurassic), lower left plot: coloured by burial depth (TVDml). As the sands undergo mechanical compaction the points move along the contours, as the sands undergo chemical compaction the points move across contours (arrows, lower left).

3.4.3 Grain Contact Cement Content – TVDml

An estimate of grain contact cement at each lead depth is required as the second input into the rock physics model. Knowing that the burial depth has exceeded the expected onset of quartz cementation, several scenarios in the rock physics model for the sands have been generated according to varying degree grain contact cement content. As previously discussed (in Chapter 2) the model is fit to the elastic log measurements of the sand facies in the study wells, and compared to the available petrographic analysis of quartz overgrowth. Cases for 0%, 2%, 4% 6% and 8% cement are generated via the Constant Cement model.

The estimate of grain contact cement content for a given depth is based on the available data points. These are constrained at 2km, the onset depth at which grain contact cementation is generally expected , and at 4km with a maximum grain contact cement of 8%. The data points shown in Figure 74 are taken from the petrographic core analysis for the Mizzen O-16 well. These are estimates of quartz overgrowth taken from thin section analysis, and give us an estimate of the expected grain contact cement content as a function of depth (assuming that quartz overgrowth is grain contact cement and not pore occluding cement).

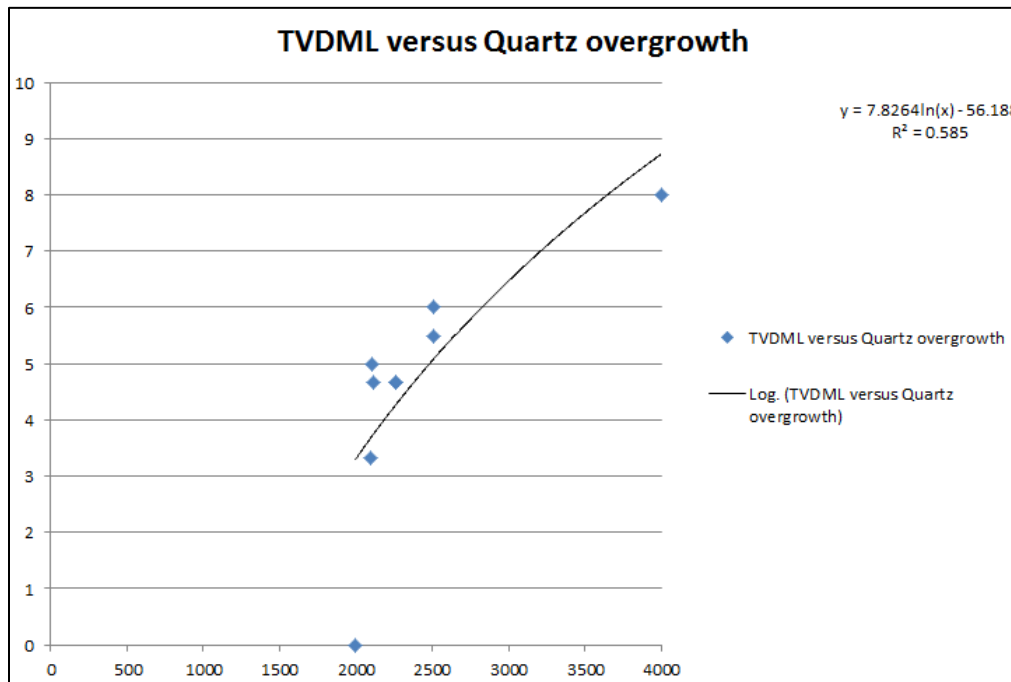


Figure 74: Quartz overgrowth versus burial depth from the petrographic analysis of the sandstones in the Mizzen O-16 well. (Core Analysis Report – StatoilHydro Canada Limited. CA Mizzen O-16 Well, Mizzen Field, Offshore, Newfoundland, Final Report, Rotary Sidewall Core. Weatherford Laboratories).

The fit to this data is used to give an estimate of grain contact cement at a given depth. When estimating cementation rates for prospect and lead analysis it is important to consider alternate cementation trend scenarios. The only cementation data made available for this study were for Jurassic sands at Mizzen O-16. This is an important consideration for several reasons. Firstly, in this region the Jurassic has presumably undergone extensive uplift and erosion that likely would alter the true cementation depth trends in the area. Secondly, the established trend is data limited to only one well. Thirdly, other well data and descriptions indicate that lower cementation values may be present at depth. It is evident from previous work in the report that the cross-plot analysis shows consistency with the estimated cementation ranges at Mizzen O-16. Using only cross-plot analysis at Lona O-55, the reservoir quality sands in the Jurassic plot at lower

cementation values (~2.5%) than what has been recorded at Mizzen O-16 even though they are located at TVDmI values that are at greater depths (2600-2700 m TVDmI). In addition, thin Tertiary sands intersected in Baie Verte at 3700 TVDmI are described as well sorted and unconsolidated in the well reports.

3.4.4 Vs-Vp

A single Vs-Vp trend was derived for reservoir sand data using the measured Vs data from Lona O-55, Mizzen F-09 and Mizzen O-16. As might be expected Vs was recorded in these later wells drilled in the deep-water. A previously discussed, these wells encountered consolidated sands in the Jurassic. Therefore, the available measured Vs data in the sands (Figure 75) do not cover the range of grain contact cement contents encountered by the wells without measured Vs data (i.e. both consolidated and unconsolidated sands are encountered by the study wells). There is potential for a change in Vp-Vs relationship with a change in consolidation.

The use of the Vs-Vp trend in unconsolidated sands is therefore more uncertain than the other trends.

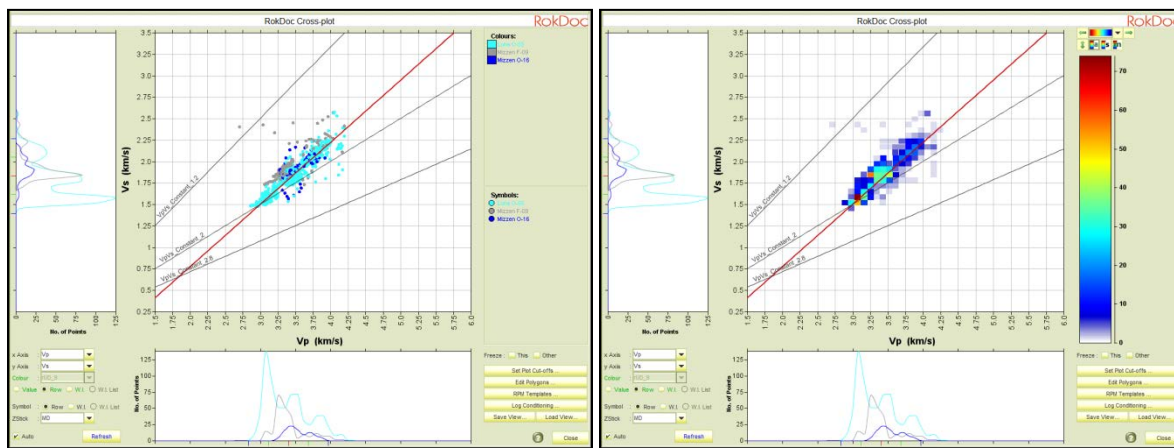


Figure 75: Vs-Vp for sand data, showing all reservoir-quality sand. Left plot: coloured by well; right plot: coloured by point density.

3.4.5 Vp(PhiT)-TVDml

Figure 76 shows the Vp-TVDml trends resulting from inputting the PhiT-TVDml trends into the Constant Cement model (shown in Figure 73), each line represents a constant grain contact cement content (from 0% to 8%). Empirical fits were then made to the outputs of the rock physics model to provide simple and straightforward relationships for use in the AVO modelling workflow.

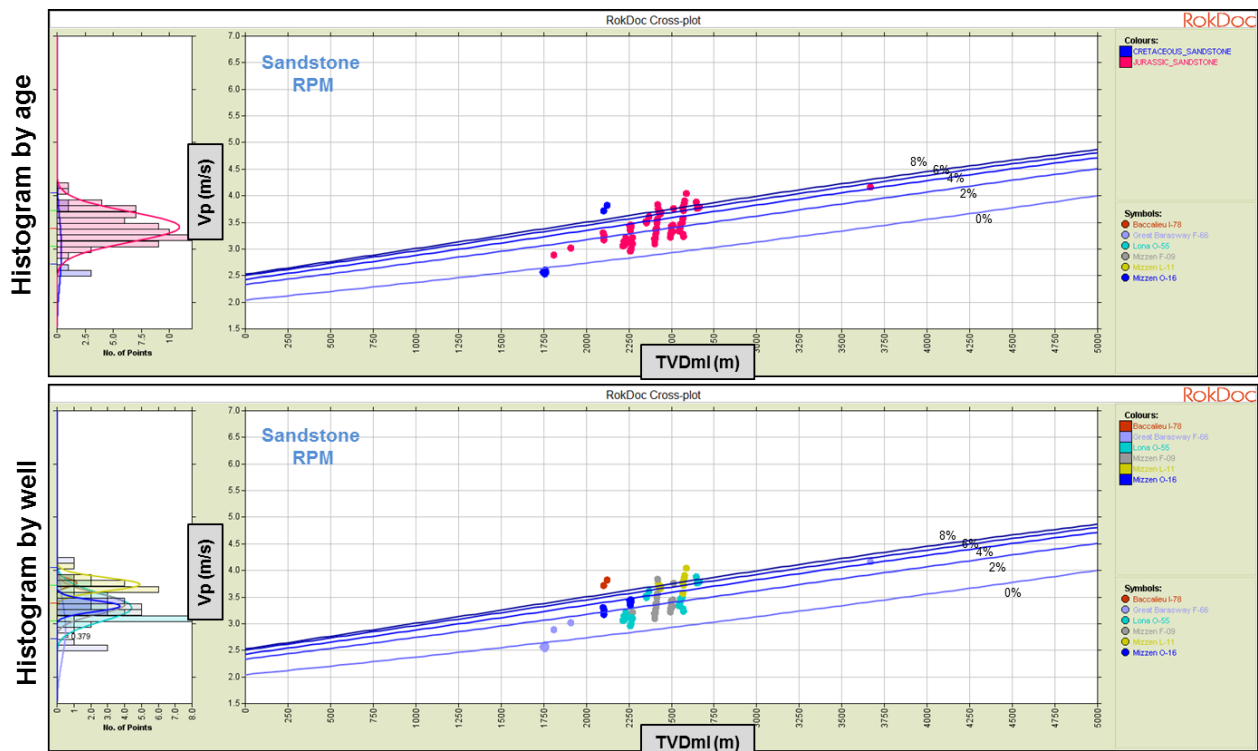


Figure 76: Vp-TVDml for sand data, showing all reservoir-quality sand. Calculated from PhiT-TVDml and Constant Cement model. Upper plot: coloured by age; lower plot: coloured by well. The data here has been up-scaled using a lithology-based technique as described in Chapter 2.

3.4.6 RhoB-VES

A RhoB-VES trend was derived in the sands to understand the effect of changing VES on sandstone RhoB, these are shown in Figure 77. While there is clear scatter in the data, the trends capture the behaviour of decreasing VES (increasing pore pressure).

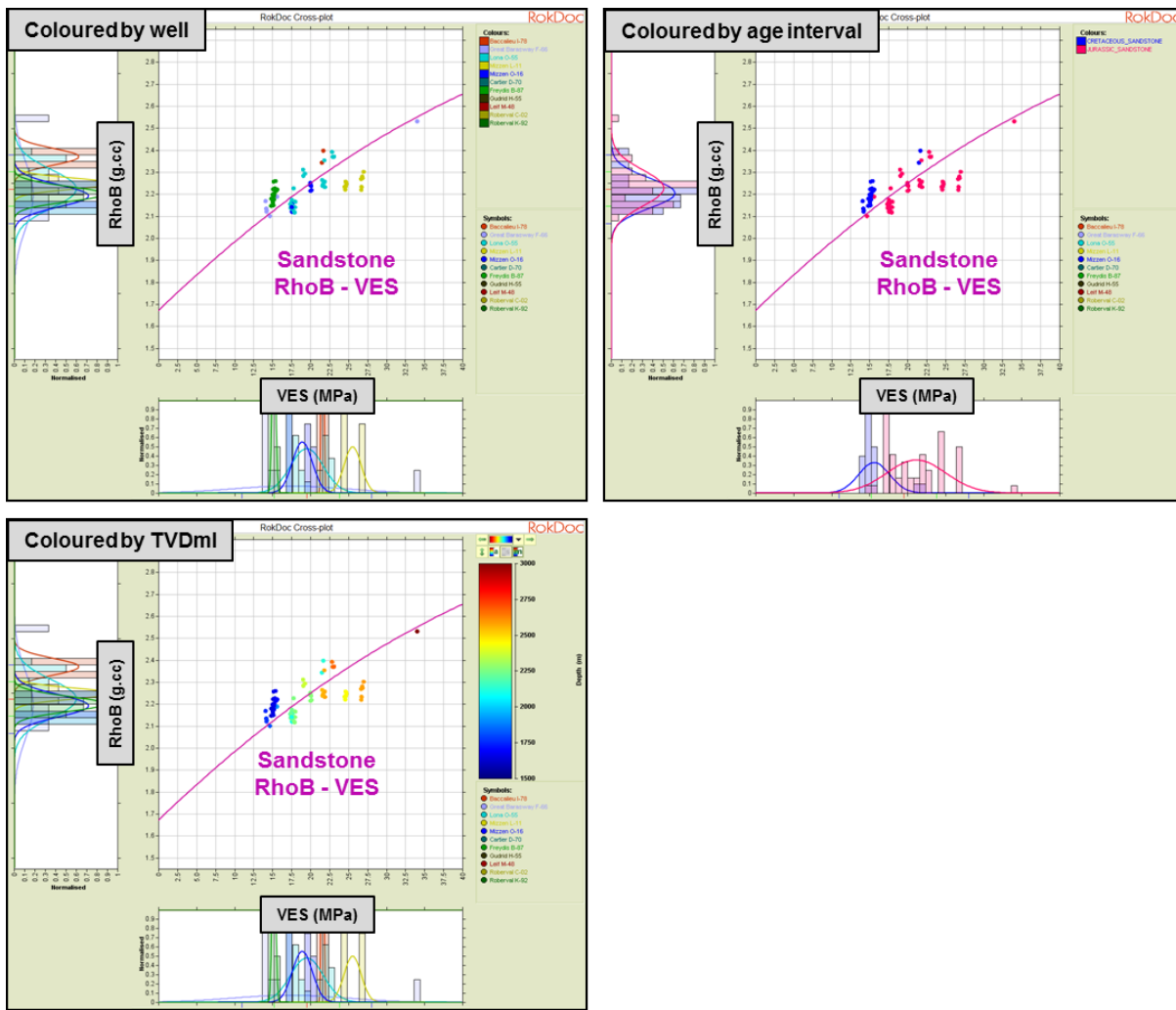


Figure 77: RhoB-VES for sand data, showing reservoir-quality sand. Left plot: coloured by well; right plot: coloured by point density. The data here has been up-scaled using a lithology-based technique as described in chapter 2. The aim is to extract log data points avoid areas of fine facies layering relative to log scale.

These trends allow the modelling of the effect of overpressure in the sands away from those pressures encountered by the study wells.

The modelling will be based around the assumption that the effect of pore pressure in the sands is to preserve porosity. No effect of pressure on the sandstone framework elastic moduli is modelled, as separating the combined effect of both pore pressure and cementation is not clear.

3.5 Summary

Multi-well trends have been generated per facies, the aim of these trends is to capture the depth dependency of each facies of interest. The sand log data has been up-scaled, to remove the effect of hybrid and shoulder bed effects in the log responses, as the sands are relatively thin compared to the log measurement scale.

The depth dependency of the shales has been captured via the use of V_p , V_s and ρ_B – TVDml trends. The depth dependency of the sand facies is captured as a function of porosity and grain contact cement content via a calibrated rock physics model; the Constant Cement model.

The trends and models form the framework used to generate AVO half-space models for a series of leads in Chapter 5.

Non-reservoir depth trends match the measured data from the study wells, giving reasonable values down to 5km burial depth and have sensible surface values.

A sand ρ_B , Φ_iT - TVDml trend has been established and captures the high, low and expected porosities from the study wells. Analogue data from the Norwegian continental shelf have been compared to the derived $\rho_B(\Phi_iT)$ -TVDml trends, and shows a good match.

The rock physics model for the sands was calibrated to the log measurements in the study database, and verified with the available petrographic analysis at the Mizzen O-16 well. This model will be used in conjunction with the ρ_B , Φ_iT – TVDml trend and a prediction of grain contact cement content to model the elastic response of the sand facies with depth.

In addition, empirical elastic property -VES trends have been derived and will allow the perturbation of the elastic properties to higher overpressures in the AVO modelling of Chapter 5.

4 Fluid Substitution and Synthetic Seismic Analysis

One of the most fundamental challenges in quantitative geophysics is to understand what drives the seismic signal recorded in the sub-surface. Rock physics analyses on wells drilled in similar environments and analogue settings are some of the most important methods available to try to understand what the fluid fill is at the prospect level. One of the cornerstone theories in rock physics, the Gassmann fluid substitution recipe, allows the geoscientist to predict the elastic response of rock as a function of saturating fluid type. The substituted logs can be used to investigate the changes in seismic response due to variable fluid fills. This analysis can help in predictive exercises by quantifying seismic responses away from well control.

In this section elastic log data from regional offset wells, along with Gassmann fluid substitution, is used to generate synthetic seismic and AVO half-space models, with the aim of understanding the likely lithology and fluid responses in the seismic data.

4.1 Introduction

Among the most important problems in rock physics analysis of log data, core data and seismic data is using elastic properties of rocks saturated with one fluid to predict those of rocks saturated with a second fluid, or equivalently, predicting saturated-rock velocities from dry-rock velocities, and vice versa; this is the fluid substitution problem.

The low-frequency Gassmann theory (Gassmann, 1951) predicts the resulting increase in effective bulk modulus, K_{sat} , of a saturated rock using the following equation:

$$\frac{K_{sat}}{K_0 - K_{sat}} = \frac{K_{dry}}{K_0 - K_{dry}} + \frac{K_{fl}}{\Phi(K_0 - K_{fl})}, \quad \mu_{sat} = \mu_{dry}$$

where K_{dry} is the effective bulk modulus of the dry rock; K_{sat} is the effective bulk modulus of the rock with pore fluid; K_0 is the bulk modulus of the mineral material making up the rock; K_{fl} is the effective bulk modulus of the pore fluid; Φ is the porosity; μ_{dry} is the effective dry shear modulus of the dry rock; and μ_{sat} is the effective shear modulus of the rock with pore fluid.

Gassmann's equation assumes a homogenous mineral modulus and statistical isotropy of the pore space, but is free of assumptions about the pore geometry. Most importantly, it is valid only at sufficiently low frequencies, such that the induced pore pressures are equilibrated throughout the pore space (i.e. there is sufficient time for the pore fluid to flow and eliminate wave-induced pore pressure gradients).

Table 11 shows the wells of interest and their corresponding ages and markers used for fluid substitution. The petrophysical cut-offs used for defining a reservoir sand were VSH < 0.2 and PHIE > 0.1. Table 12 shows the fluid properties, along with temperatures and pore pressures at the target level.

Wells	Age	Marker Name
Cartier D-70	Tertiary	C54
Freydis B-87	Cretaceous	K100
Roberval C-02	Tertiary	C54
Gudrid H-55	Tertiary	C54
Great Barasway F-66	Cretaceous	K140
Lona O-55	Jurassic	J145
Mizzen O-16	Jurassic	J145
Mizzen F-09	Jurassic	J145
Mizzen L-11	Cretaceous	K140
Bacalieu I-78	Cretaceous	K140

Table 11: Summary of wells, age and markers for fluid substitution.

Wells	Salinity (kppm)	GOR (L/L)	Oil API	Gas gravity	Temp @ZOI (celsius)	Pore Pressure @ZOI (MPa)
Cartier D-70	43	65	26	0.65	~45	~25.70
Freydis B-87	55	65	26	0.65	~48	~27.10
Roberval C-02	95	65	26	0.65	~60	~31.80
Gudrid H-55	47	65	26	0.65	~57	~29.70
Great Barasway F-66	53	5	22	0.65	~52	~46.60
Lona O-55	83	5	22	0.65	~66	~62.00
Mizzen O-16	51	5	22	0.65	~91	~38.11
Mizzen F-09	84	5	22	0.65	~70	~35.00
Mizzen L-11	71	5	22	0.65	~72	~44.88
Bacalieu I-78	25	5	22	0.65	~85	~32.99

Table 12: Summary of fluid properties, along with associated temperatures and pore pressures.

Seismic data are commonly used to interpret structural and stratigraphic features in the subsurface. The physical properties of pore fluids have an effect on the seismic response of a porous rock containing those fluids. It is necessary to have an understanding of the changes in P-wave (compressional) velocity, S-wave (shear) velocity and density as fluid or rock properties change to recognise or predict the effect of changes in seismic amplitudes and travel times.

Evaluation of fluid properties aids in determining the usefulness of time-lapse seismic, in predicting and inverting seismic AVO and amplitude responses, and in making production and reservoir engineering decisions and forecasting. Basic input values for modelling a field or area of interest are determined by testing a sample or using analogue information from a nearby area. Based on these input values, the fluid properties of the reservoir may be calculated using the FLAG (FLuid Application of Geophysics, University of Houston) model.

The Gassmann recipe can then be used to determine the elastic response of a bulk rock as a function of saturating fluid. The P- and S- wave velocities and density for the fluid saturated reservoir rock may then be used along with the overburden rock property information (determined from logs or estimated) for AVO modelling, to compare a calculated response to seismic observations.

Synthetic seismograms are created using a standard approach, which consists of a Ricker wavelet with a 20 Hz central frequency, being convolved with the reflectivity derived from the well logs; the reflectivity coefficients were calculated from the log data using the Zoeppritz (1919) equations. Besides in-situ seismograms, additional seismograms were constructed for all fluid cases (100% brine saturated, 80% oil-saturated and 90% gas-saturated), generated using the Gassmann approach described above. The seismograms were produced to understand how the seismic response changes between the different fluid phases.

One major goal for this exercise was to analyse AVO responses for the various fluids. These can then be compared to pre-stack seismic data (NMO-corrected gathers and/or angle stacks), to understand seismic anomalies at a prospect level. However, one major problem is that rocks are not always blocky and homogeneous, thus interfaces between caprock and reservoir maybe be gradual, or irregular. In these configurations, picking the right seismic signature can prove difficult, if not impossible in many instances.

The general experience is that due to heterogenous cap rocks and/or heterogeneous reservoirs, there is disagreement between the blocky AVO modelling and the AVO response extracted from synthetic gathers. A general explanation of the various AVO classes is given in Table 13, and will be used to describe AVO character of sands with brine, oil and gas, respectively.

AVO CLASS	Near reflectivity	Far reflectivity	Comments following SEG polarity convention (increase in acoustic impedance is peak)
CLASS I	Positive	Positive	Positive on nears, dims with angle/offset.
CLASS IIP	Low positive	Negative	Positive on nears, changes phase with angle/offset.
CLASS II	Slight negative	Negative	Transparent on nears, brightens negatively with angle/offset.
CLASS III	Negative	Negative	Negative on nears, brightens negatively with angle/offset.
CLASS IV	Negative	Positive	Negative on nears, dims with angle/offset.

Table 13: A summary of AVO classes.

4.2 Isotropic Modelling

Referring to rocks as isotropic means that velocity is constant at various angles of incidence and azimuth of the wave front, meaning that the vertical and horizontal velocities are the same. The description above might be correct for sandstones but shales are often anisotropic, due to layering of the clay platelets, (Voltolini et al., 2008) so the results of isotropic synthetic modelling should be treated with caution.

4.2.1 Isotropic Synthetic Models

Synthetic seismograms were calculated by convolving a 20 Hz Ricker wavelet (Figure 78) with the reflectivity from the well logs, in all fluid cases. Up-scaled logs were calculated using a band-pass filter and used as the inputs for the reflectivity logs. Up-scaled logs have a similar frequency content to the seismic data, so they more correctly replicate what the seismic data resolves as the seismic pulse traverses the earth, creating reflections at various impedance contrasts.

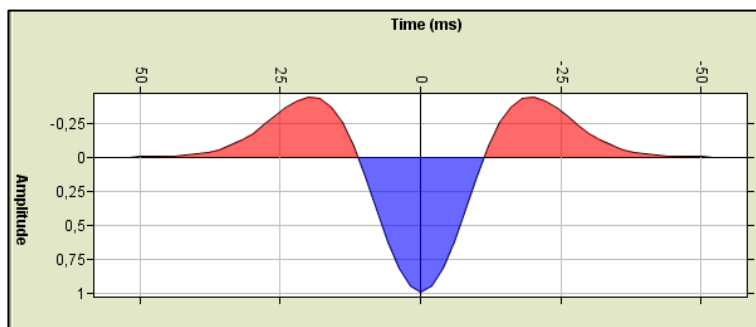


Figure 78: 20 Hz Ricker wavelet used in the synthetic seismic modelling.

The fluid substitutions in Lona O-55 were performed in Jurassic sands (Table 14). Figure 79 and Figure 80 show the synthetic gathers for Lona O-55, the whole well and the zone of interest (ZOI), respectively. Both extractions (red and blue) in Figure 80 are affected by side lobe effects and general interference of heterogenous layers above the sands, so the AVO response would most likely be different if there had been a homogeneous cap rock and sand.

Depth (MD)	AVO Class – Brine	AVO Class - Oil	AVO Class - Gas
4842 – 4905 m	Class IV	Class IV	Class IV
5176 – 5208 m	Class IV	Class IV	Class IV

Table 14: AVO classes from isotropic synthetic seismic for the Jurassic sands in Lona O-55

The fluid substitutions in Great Barasway F-66 were performed in Cretaceous sands (Table 15).

Figure 81 and

Figure 82 show the synthetic gathers for Great Barasway F-66, the whole well and the zone of interest (ZOI), respectively.

Depth (MD)	AVO Class – Brine	AVO Class - Oil	AVO Class - Gas
4106 – 4127 m	Class IV	Class III	Class III

Table 15: AVO classes from isotropic synthetic seismic for the Cretaceous sands in Great Barasway F-66.

The fluid substitutions in Mizzen O-16 were performed in Jurassic sands (Table 16). Figure 83 and Figure 84 show the synthetic gathers for Mizzen O-16, the whole well and the zone of interest (ZOI), respectively.

Depth (MD)	AVO Class – Brine	AVO Class - Oil	AVO Class - Gas
3213 – 3223 m	Class IV	Class IV	Class III
3369 – 3386 m	Class II	Class III	Class III

Table 16: AVO classes from isotropic synthetic seismic for the Jurassic sands in Mizzen O-16.

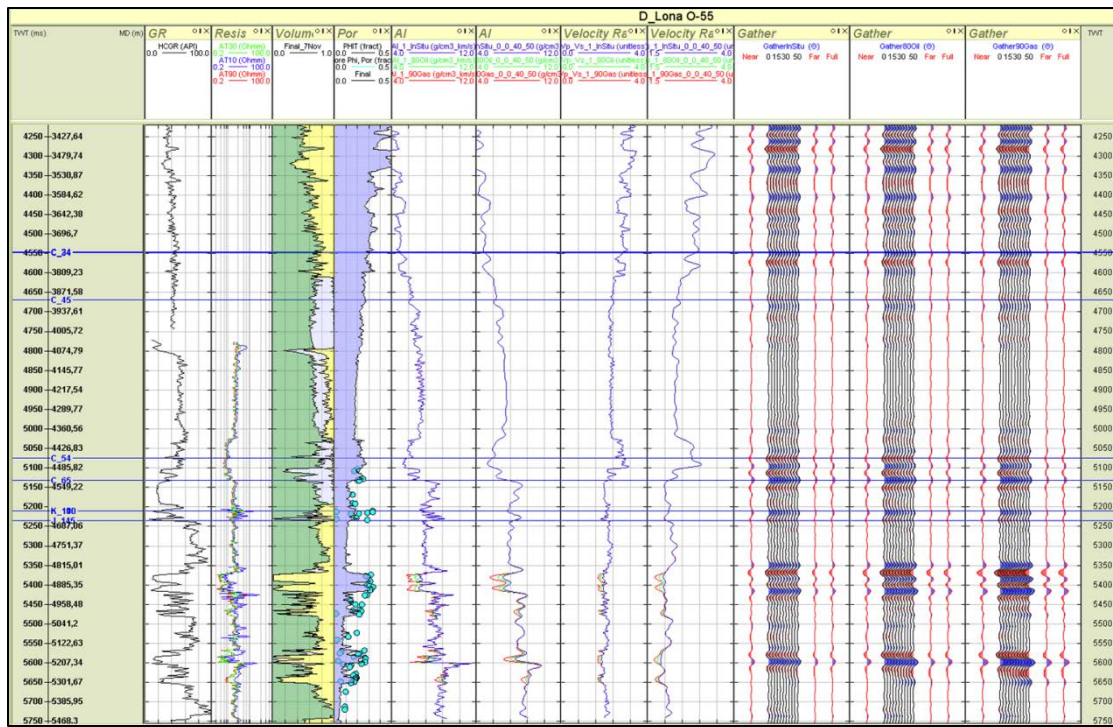


Figure 79: Isotropic synthetic seismic for Lona O-55, showing the whole well. In-situ case is brine. Tracks from left to right: GR, resistivity, lithology, porosity, acoustic impedance (coloured by fluid case; blue: brine, green: oil, red: gas), up-scaled acoustic impedance (coloured by fluid case), VpVs (coloured by fluid case), up-scaled VpVs (coloured by fluid case), gather for in-situ case (brine), gather for oil case and gather for gas case.

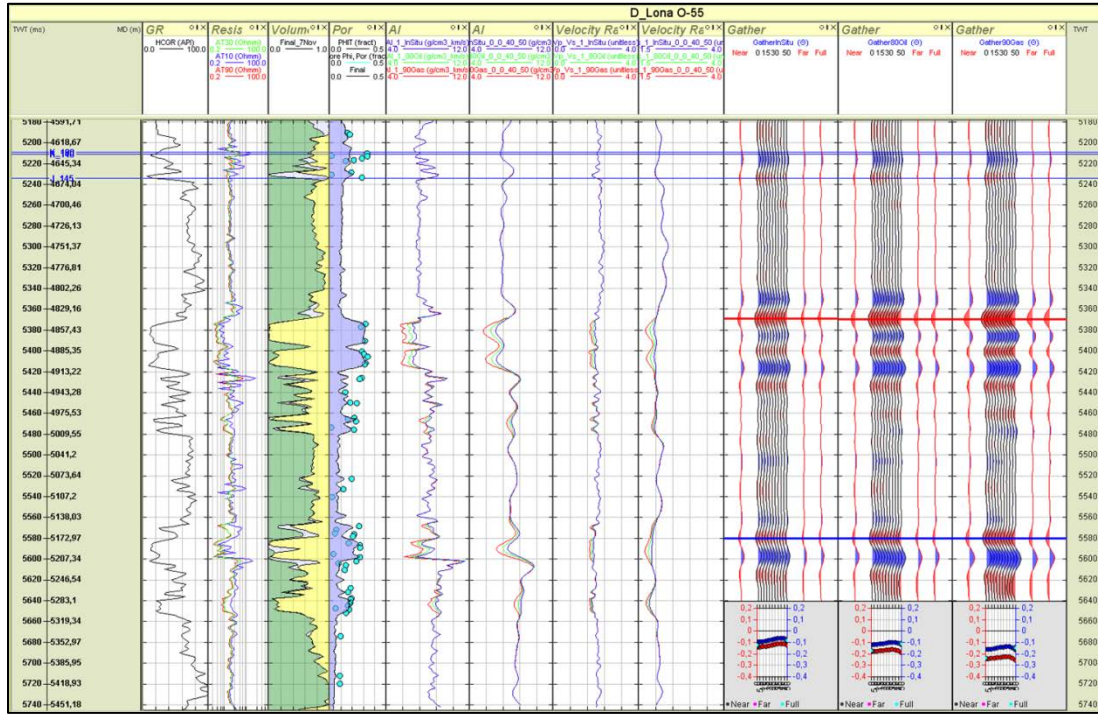


Figure 80: Isotropic synthetic seismic for Lona O-55, showing the ZOI only. In-situ case is brine. Tracks from left to right: GR, resistivity, lithology, porosity, acoustic impedance (coloured by fluid case; blue: brine, green: oil, red: gas), up-scaled acoustic impedance (coloured by fluid case), VpVs (coloured by fluid case), up-scaled VpVs (coloured by fluid case), gather for in-situ case (brine), gather for oil case and gather for gas case. The plots below the synthetic seismic show the amplitude, extracted along the red and blue markers, vs. angle.

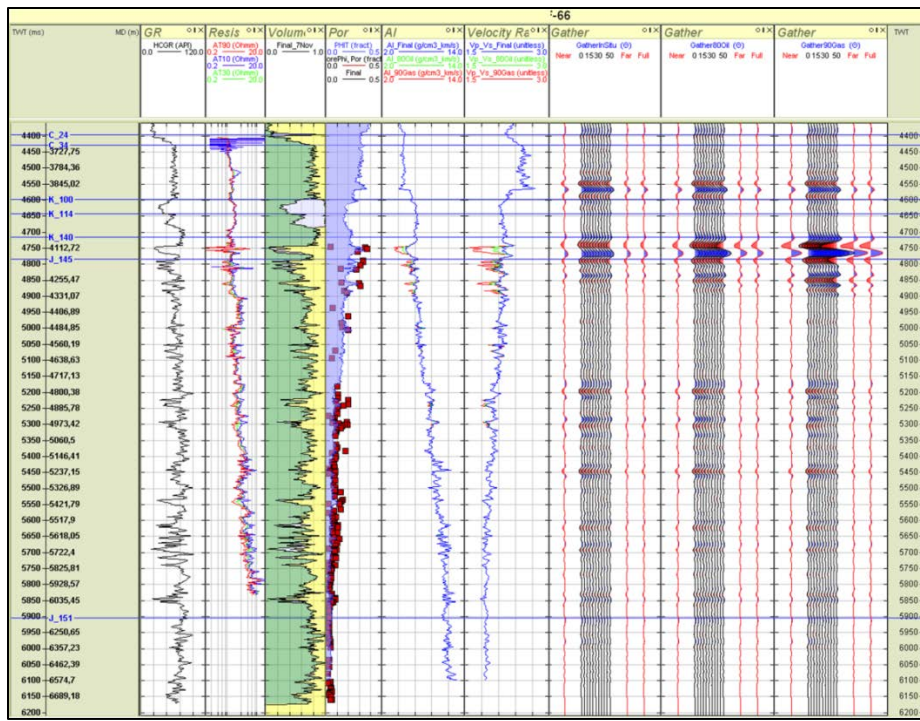


Figure 81: Isotropic synthetic seismic for Great Barasway F-66, showing the whole well. In-situ case is brine. Tracks from left to right: GR, resistivity, lithology, porosity, acoustic impedance (coloured by fluid case; blue: brine, green: oil, red: gas), up-scaled acoustic impedance (coloured by fluid case), VpVs (coloured by fluid case), up-scaled VpVs (coloured by fluid case), gather for in-situ case (brine), gather for oil case and gather for gas case.

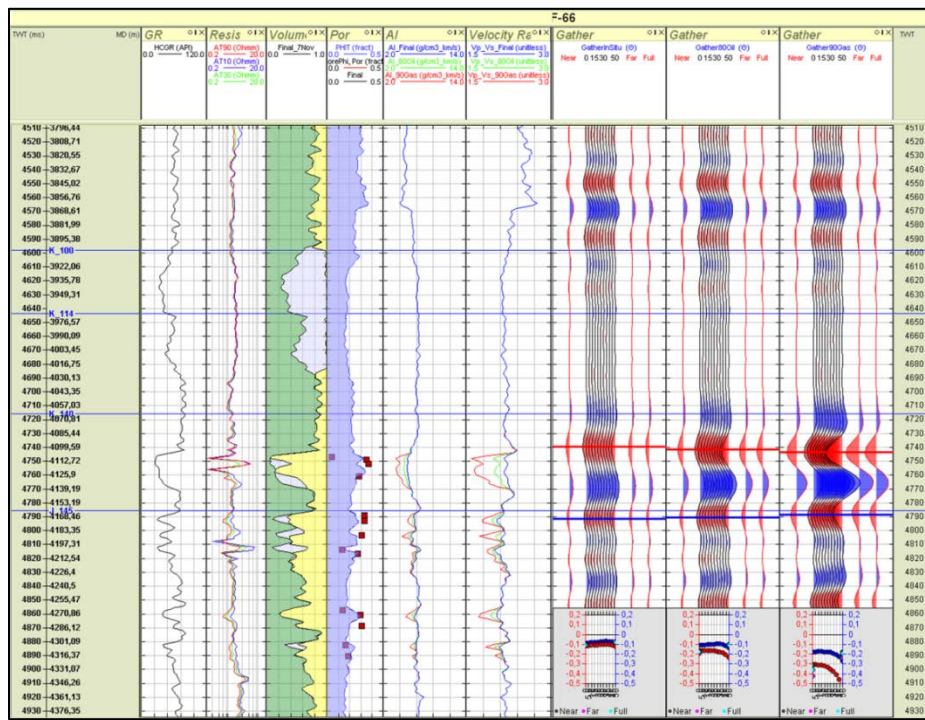


Figure 82: Isotropic synthetic seismic for Great Barasway F-66, showing the ZOI only. In-situ case is brine. Tracks from left to right: GR, resistivity, lithology, porosity, acoustic impedance (coloured by fluid case; blue: brine, green: oil, red: gas), up-scaled acoustic impedance (coloured by fluid case), VpVs (coloured by fluid case), up-scaled VpVs (coloured by fluid case), gather for in-situ case (brine), gather for oil case and gather for gas case. The plots below the synthetic seismic show the amplitude, extracted along the red and blue markers, vs. angle.

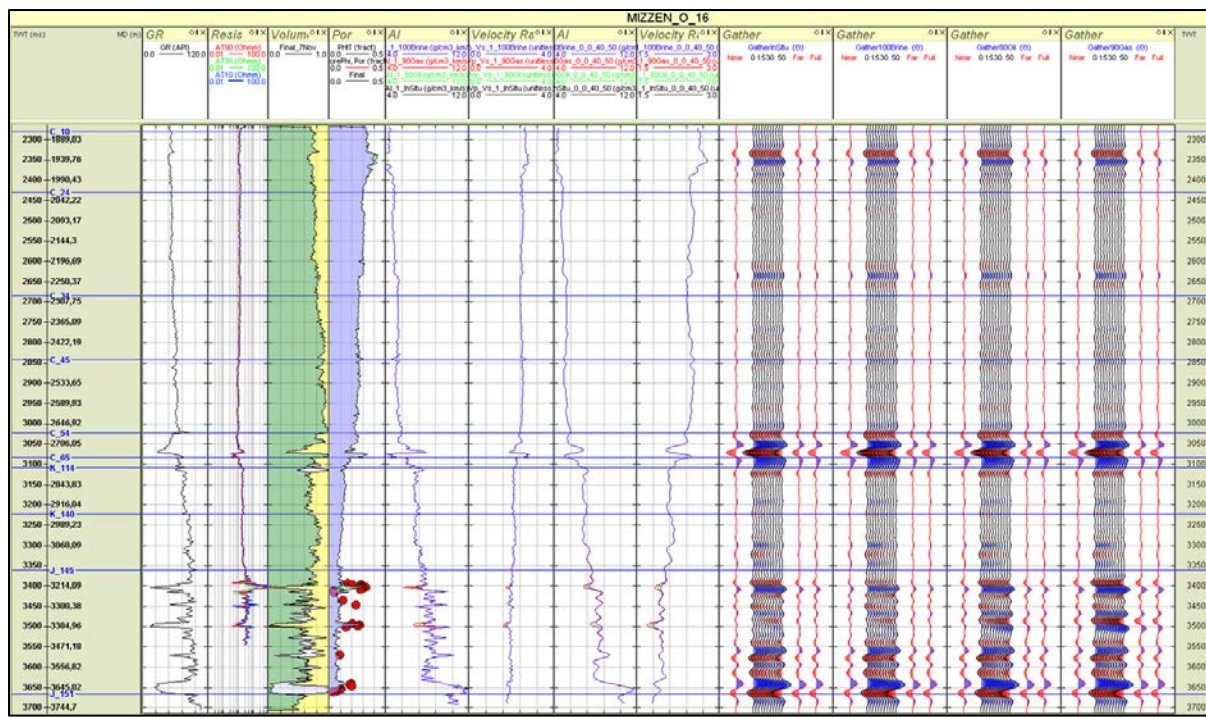


Figure 83: Isotropic synthetic seismic for Mizzen O-16, showing the whole well. In-situ case is oil-bearing. Tracks from left to right: GR, resistivity, lithology, porosity, acoustic impedance (coloured by fluid case; in-situ: black, blue: brine, green: oil, red: gas), up-scaled acoustic impedance (coloured by fluid case), VpVs (coloured by fluid case), up-scaled VpVs (coloured by fluid case), gather for in-situ case (brine), gather for oil case and gather for gas case.

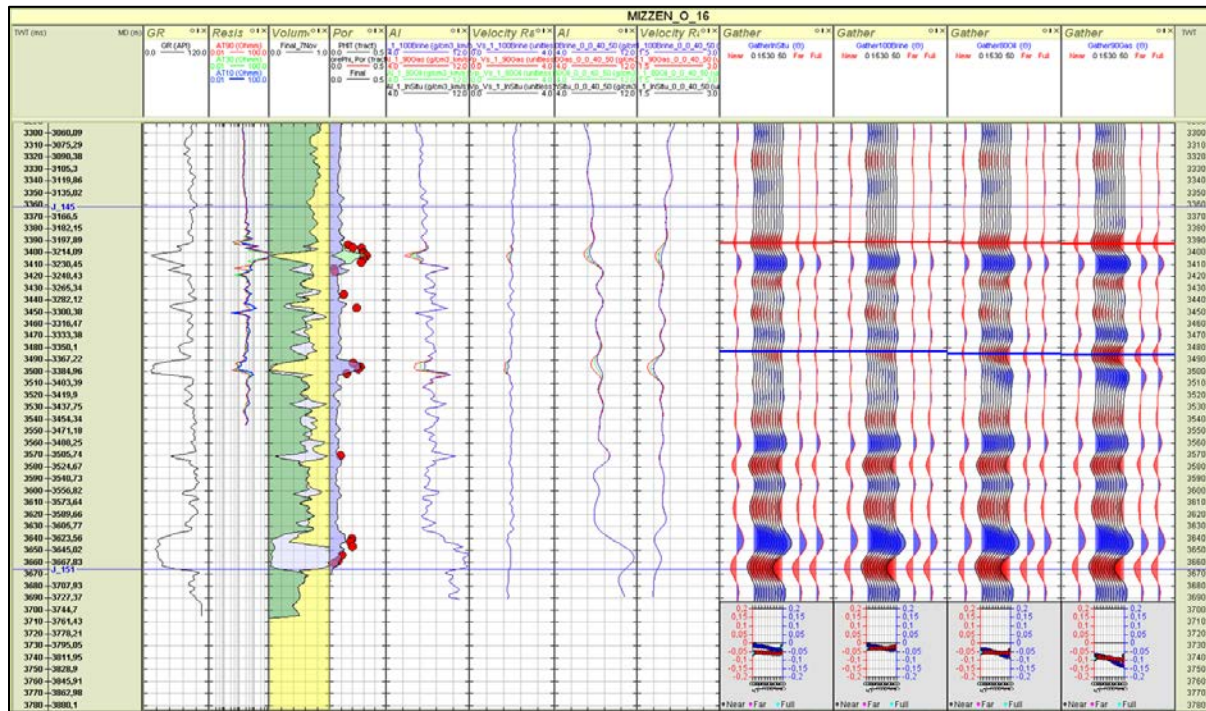


Figure 84: Isotropic synthetic seismic for Mizzen O-16, showing the ZOI only. In-situ case is oil-bearing. Tracks from left to right: GR, resistivity, lithology, porosity, acoustic impedance (coloured by fluid case; in-situ: black, blue: brine, green: oil, red: gas), up-scaled acoustic impedance (coloured by fluid case), VpVs (coloured by fluid case), up-scaled VpVs (coloured by fluid case), gather for in-situ case (brine), gather for oil case and gather for gas case. The plots below the synthetic seismic show the amplitude, extracted along the red and blue markers, vs. angle.

The fluid substitutions in Mizzen L-11 were performed in Jurassic sands (Table 17). Figure 85 and Figure 86 show the synthetic gathers for Mizzen L-11, the whole well and the zone of interest (ZOI), respectively. The red extraction is picked at the trough, which is above the sand, while the sand itself appears to be at the zero crossing. The reason for picking the red trough is that it can be more easily identified in the seismic than the zero crossing.

Depth (MD)	AVO Class – Brine	AVO Class - Oil	AVO Class - Gas
3599 – 3625 m	Class II	Class III	Class III
3742 – 3767 m	Class II	Class III	Class III

Table 17: AVO classes from isotropic synthetic seismic for the Jurassic sands in Mizzen L-11

The fluid substitutions in Mizzen F-09 were performed in Jurassic sands (Table 18). Figure 87 and Figure 88 show the synthetic gathers for Mizzen F-09, the whole well and the zone of interest (ZOI), respectively.

Depth (MD)	AVO Class – Brine	AVO Class - Oil	AVO Class - Gas
3484 – 3509 m	Class IV	Class IV	Class III
3576 – 3601 m	Class IV	Class IV	Class III

Table 18: AVO classes from isotropic synthetic seismic for the Jurassic sands in Mizzen F-09.

The fluid substitutions in Baccalieu I-78 were performed in Cretaceous sands (Table 19). Figure 89 and Figure 90 show the synthetic gathers for Baccalieu I-78, the whole well and the zone of interest (ZOI), respectively.

Depth (MD)	AVO Class – Brine	AVO Class - Oil	AVO Class - Gas
3197 – 3267 m	Class IIP	Class II/ Class III	Class III

Table 19: AVO classes from isotropic synthetic seismic for the Cretaceous sands in Baccalieu I-78.

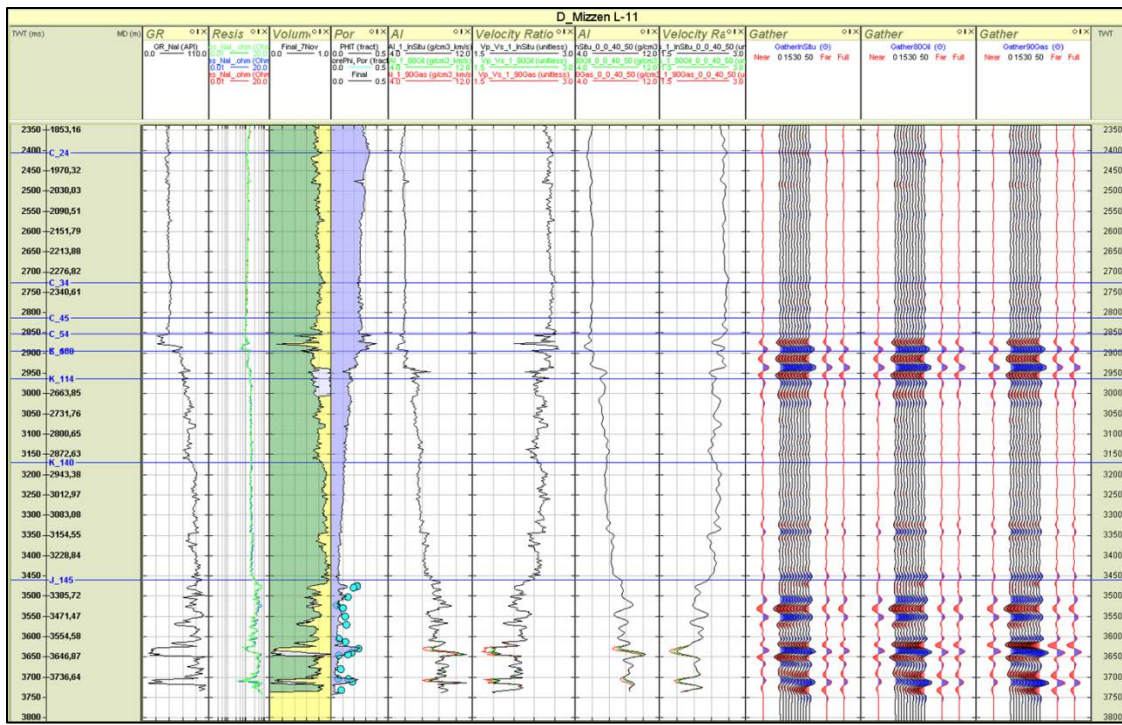


Figure 85: Isotropic synthetic seismic for Mizzen L-11, showing the whole well. In-situ case is brine. Tracks from left to right: GR, resistivity, lithology, porosity, acoustic impedance (coloured by fluid case); in-situ: black, green: oil, red: gas), up-scaled acoustic impedance (coloured by fluid case), VpVs (coloured by fluid case), up-scaled VpVs (coloured by fluid case), gather for in-situ case (brine), gather for oil case and gather for gas case.

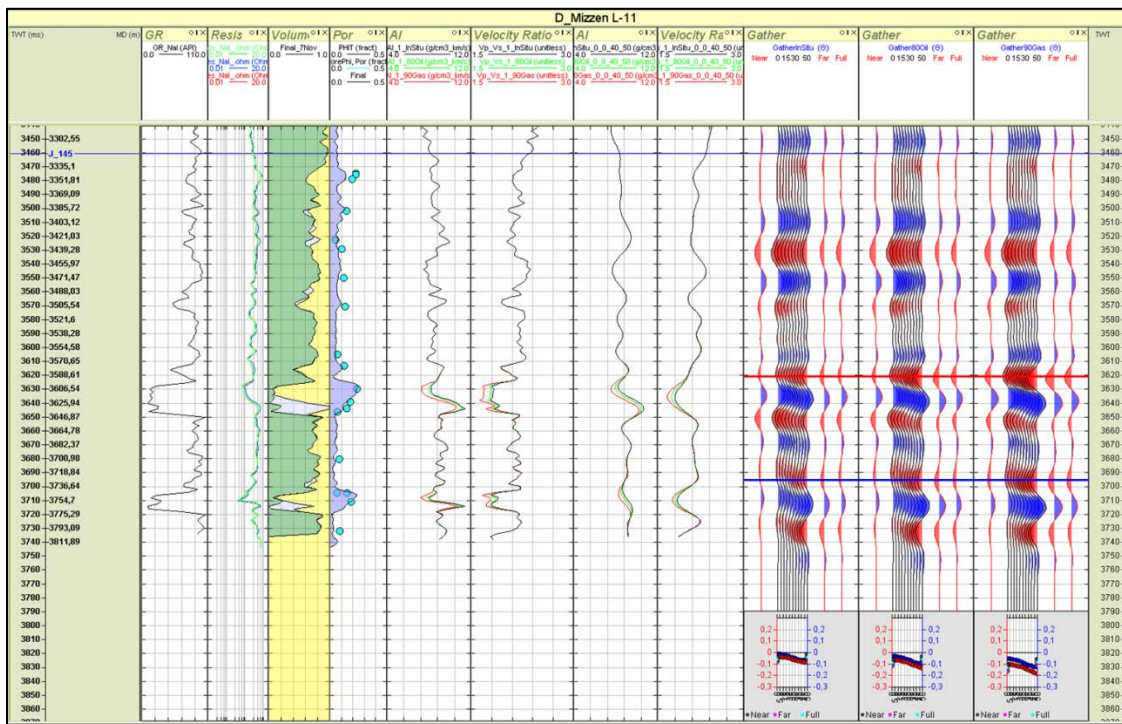


Figure 86: Isotropic synthetic seismic for Mizzen L-11, showing the ZOI only. In-situ case is brine. Tracks from left to right: GR, resistivity, lithology, porosity, acoustic impedance (coloured by fluid case); in-situ: black, green: oil, red: gas), up-scaled acoustic impedance (coloured by fluid case), VpVs (coloured by fluid case), up-scaled VpVs (coloured by fluid case), gather for in-situ case (brine), gather for oil case and gather for gas case. The plots below the synthetic seismic show the amplitude, extracted along the red and blue markers, vs. angle.

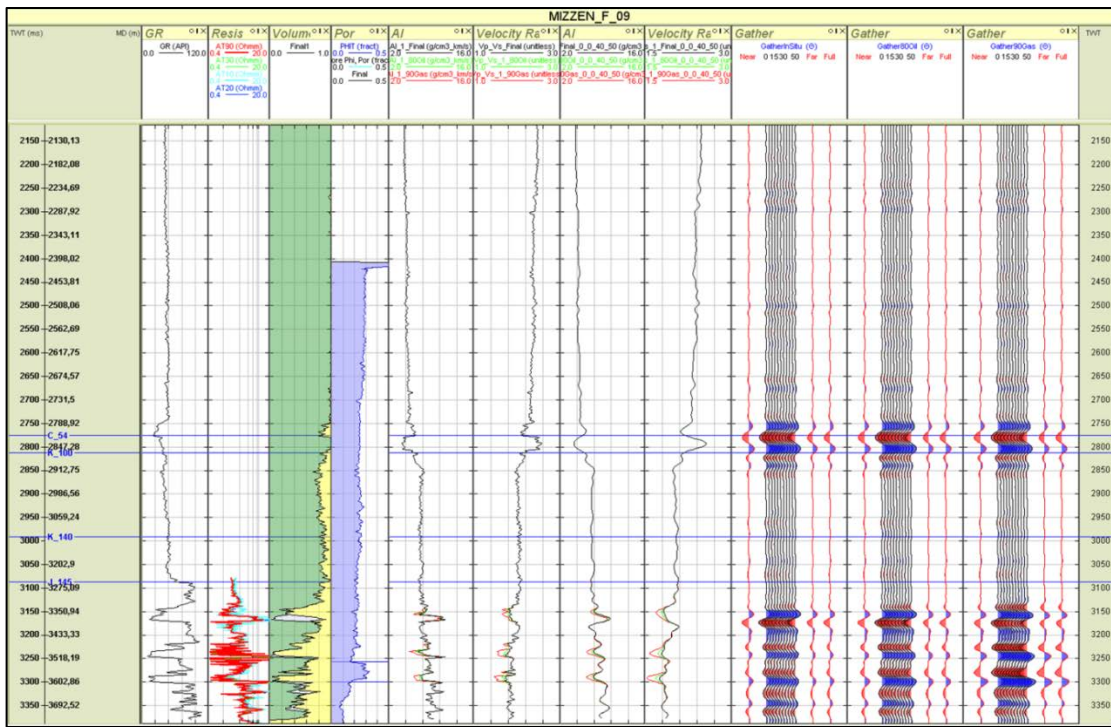


Figure 87: Isotropic synthetic seismic for Mizzen F-09, showing the whole well. In-situ case is brine. Tracks from left to right: GR, resistivity, lithology, porosity, acoustic impedance (coloured by fluid case; in-situ: black, green: oil, red: gas), up-scaled acoustic impedance (coloured by fluid case), VpVs (coloured by fluid case), up-scaled VpVs (coloured by fluid case), gather for in-situ case (brine), gather for oil case and gather for gas case.

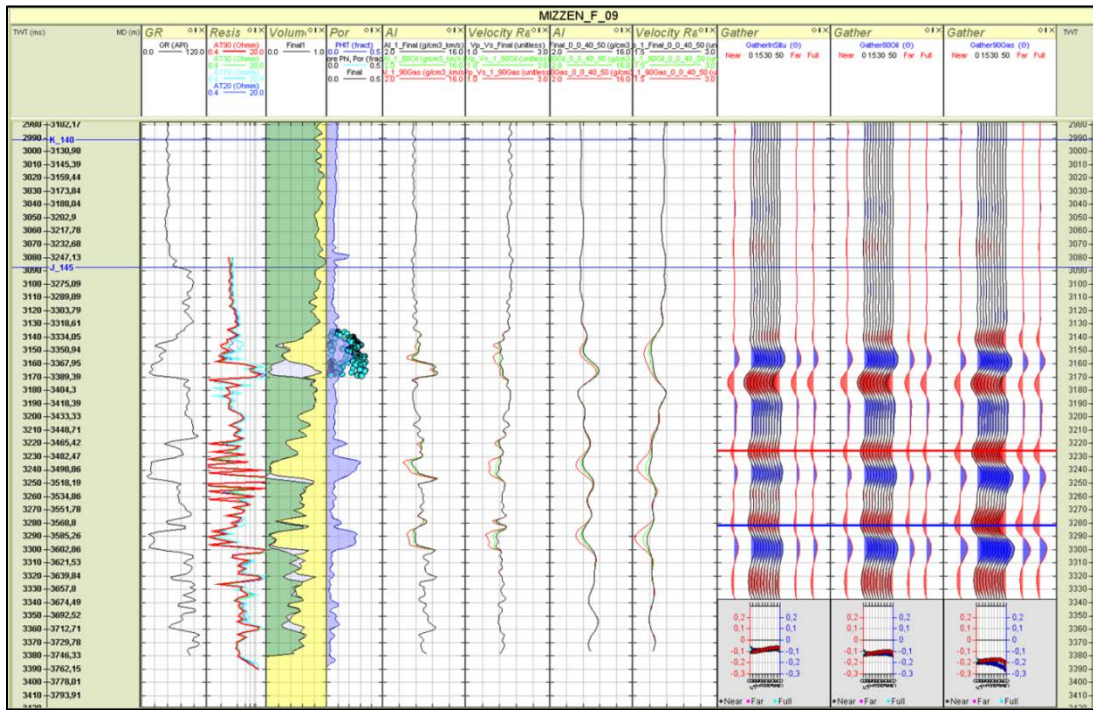


Figure 88: Isotropic synthetic seismic for Mizzen F-09, showing the ZOI only. In-situ case is brine. Tracks from left to right: GR, resistivity, lithology, porosity, acoustic impedance (coloured by fluid case; in-situ: black, green: oil, red: gas), up-scaled acoustic impedance (coloured by fluid case), VpVs (coloured by fluid case), up-scaled VpVs (coloured by fluid case), gather for in-situ case (brine), gather for oil case and gather for gas case. The plots below the synthetic seismic show the amplitude, extracted along the red and blue markers, vs. angle.

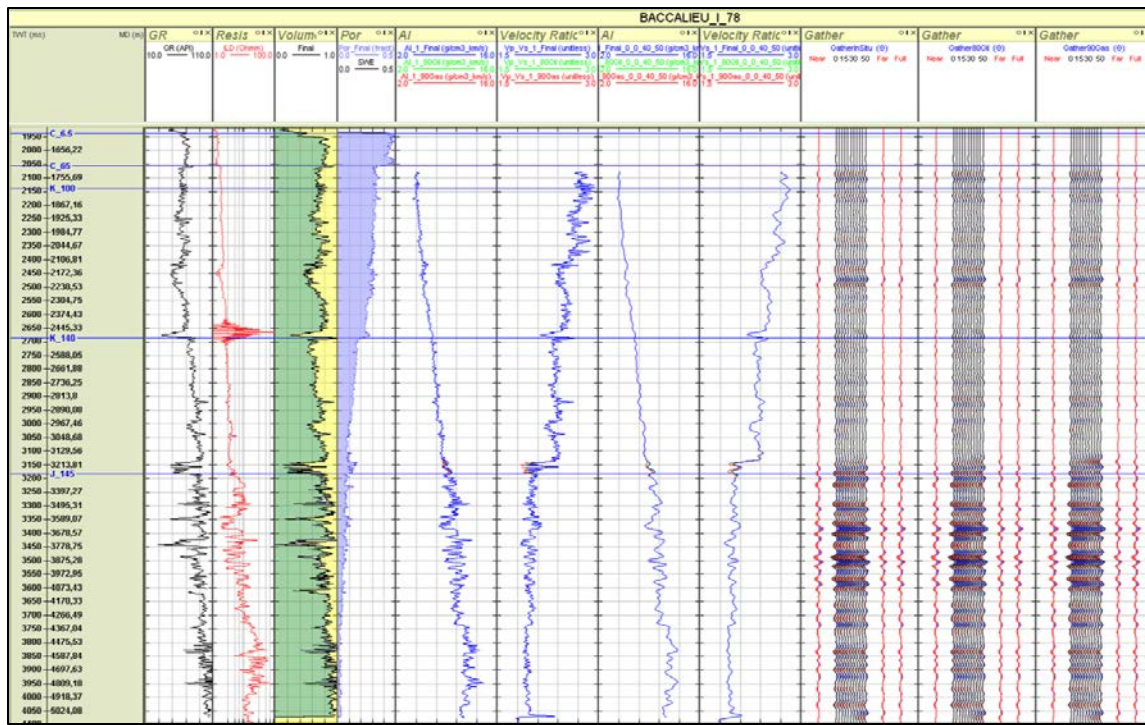


Figure 89: Isotropic synthetic seismic for Baccalieu I-78, showing the whole well. In-situ case is brine. Tracks from left to right: GR, resistivity, lithology, porosity, acoustic impedance (coloured by fluid case; in-situ: blue, green: oil, red: gas), up-scaled acoustic impedance (coloured by fluid case), VpVs (coloured by fluid case), up-scaled VpVs (coloured by fluid case), gather for in-situ case (brine), gather for oil case and gather for gas case.

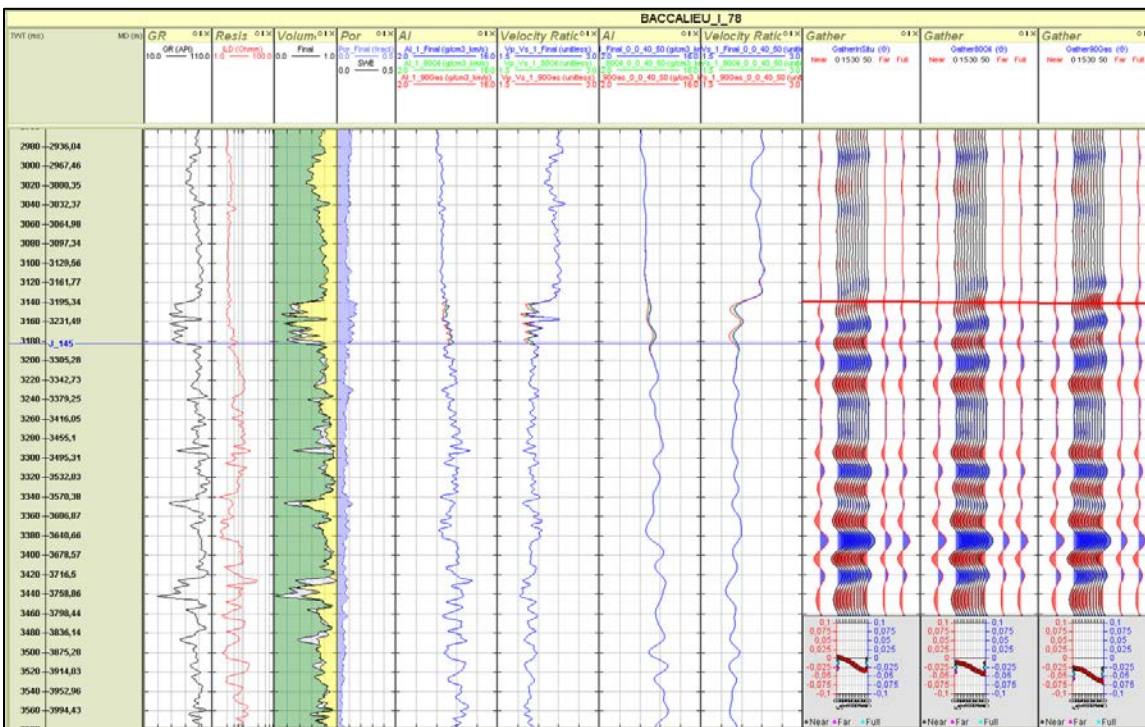


Figure 90: Isotropic synthetic seismic for Baccalieu I-78, showing the ZOI only. In-situ case is brine. Tracks from left to right: GR, resistivity, lithology, porosity, acoustic impedance (coloured by fluid case; in-situ: blue, green: oil, red: gas), up-scaled acoustic impedance (coloured by fluid case), VpVs (coloured by fluid case), up-scaled VpVs (coloured by fluid case), gather for in-situ case (brine), gather for oil case and gather for gas case. The plots below the synthetic seismic show the amplitude, extracted along the red and blue markers, vs. angle.

The fluid substitutions for Cartier D-70 were performed in the Tertiary sands (Table 20). Figure 91 and Figure 92 show Cartier D-70, the whole well and the zone of interest (ZOI), respectively.

Depth (MD)	AVO Class – Brine	AVO Class - Oil	AVO Class - Gas
1798m m	Class I	Class I/Class IIP	Class IIP
1856m (bottom ZOI)	Reverse* IIP	Reverse* III	Reverse* III

Table 20: AVO classes from isotropic synthetic seismic for the Tertiary sands in Cartier D-70. Due to the extraction at the bottom of the reservoir the classes are usually mirrored. In this case, the overburden is softer than the underburden of the reservoir, leading to different AVO characteristics of top and bottom reservoir reflections.

The fluid substitutions in Freydis B-87 were performed in Tertiary sands and Cretaceous sands (Table 21). Figure 93 and Figure 94 show Freydis B-47, the whole well and the zone of interest (ZOI), respectively.

Depth (MD)	AVO Class – Brine	AVO Class - Oil	AVO Class - Gas
1733 m - Tertiary	Class I	Class I	Class IV/Class IIP
1900 m (bottom ZOI)- Cretaceous	Class I = mirrored Class IV*	Class I = mirrored Class IV*	Class I = mirrored Class IV*

Table 21: AVO classes from isotropic synthetic seismic for the Tertiary and Cretaceous sands in Freydis B-87. *Note the distinct difference between overburden lithology and underburden lithology, if the configuration would have been reversed then top reflection would have been classified as class IV.

The fluid substitutions in Gudrid H-55 were performed in Tertiary sands (Table 22). Figure 95 and Figure 96 show Gudrid H-55, the whole well and the zone of interest (ZOI), respectively.

Depth (MD)	AVO Class – Brine	AVO Class - Oil	AVO Class - Gas
2173 m	Class II	Class III	Class III
2343 m (bottom ZOI)	Class I = mirrored Class IV*	Class I = mirrored Class IV*	Class I = mirrored Class IV*

Table 22: AVO classes from isotropic synthetic seismic for the Tertiary sands in Gudrid H-55. *Note the distinct difference between overburden lithology and underburden lithology, if the configuration would have been reversed then top reflection would have been classified as class IV.

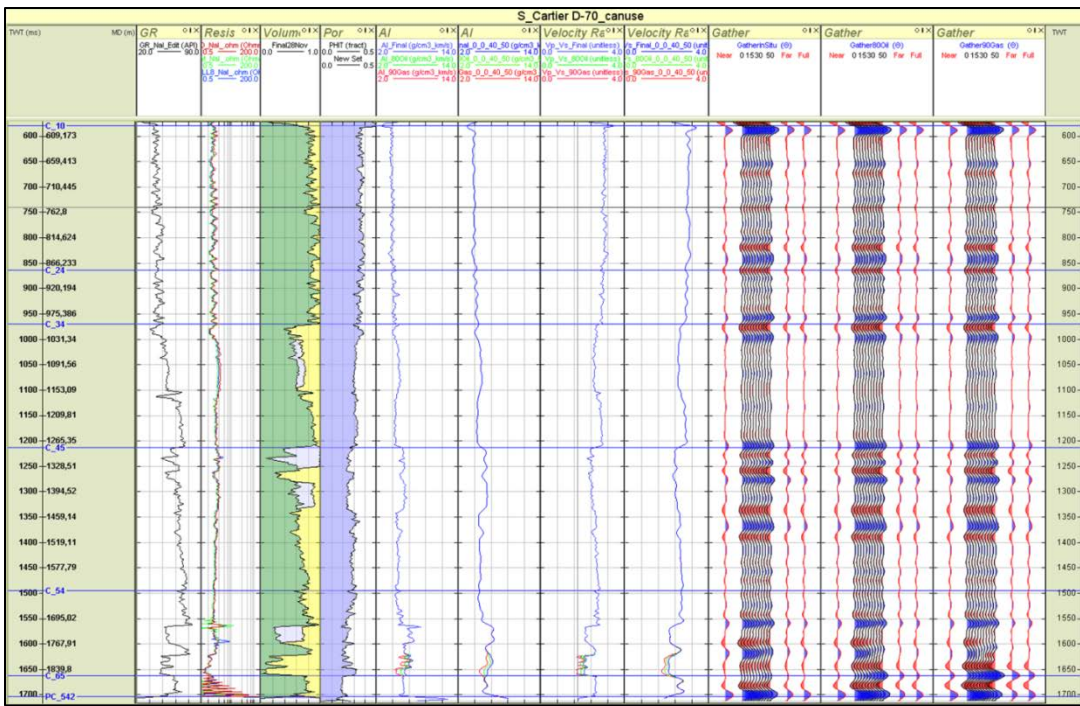


Figure 91: Isotropic synthetic seismic for Cartier D-70, showing the whole well. In-situ case is brine. Tracks from left to right: GR, resistivity, lithology, porosity, acoustic impedance (coloured by fluid case; in-situ: blue, green: oil, red: gas), up-scaled acoustic impedance (coloured by fluid case), VpVs (coloured by fluid case), up-scaled VpVs (coloured by fluid case), gather for in-situ case (brine), gather for oil case and gather for gas case.

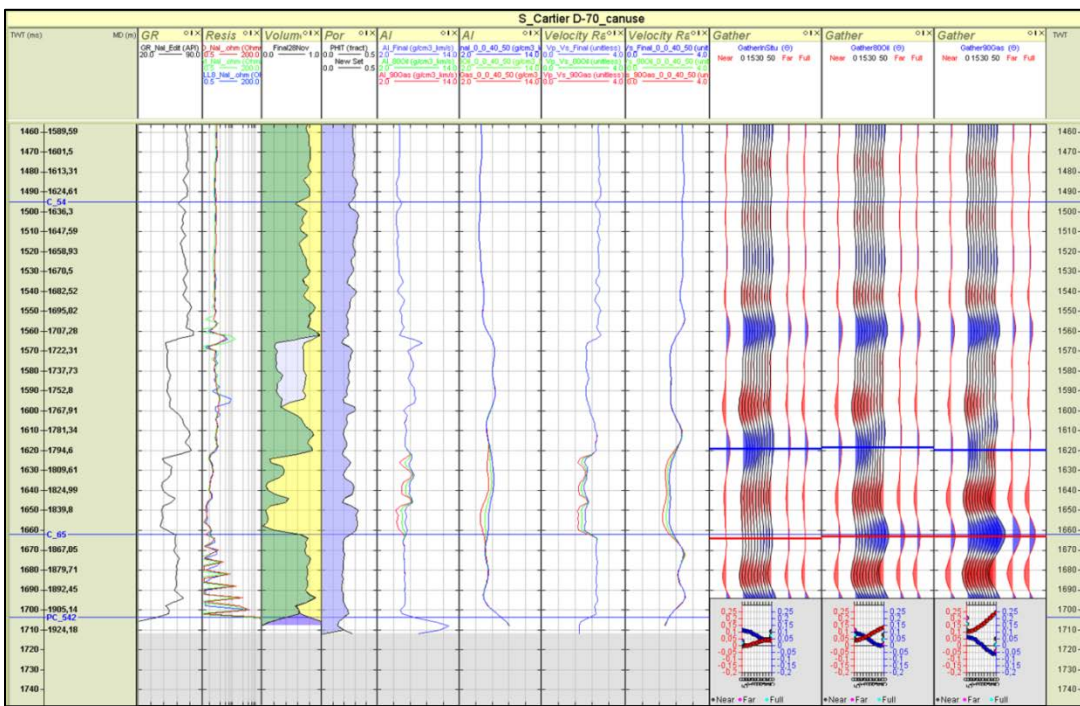


Figure 92: Isotropic synthetic seismic for Cartier D-70, showing the ZOI only. In-situ case is brine. Tracks from left to right: GR, resistivity, lithology, porosity, acoustic impedance (coloured by fluid case; in-situ: blue, green: oil, red: gas), up-scaled acoustic impedance (coloured by fluid case), VpVs (coloured by fluid case), up-scaled VpVs (coloured by fluid case), gather for in-situ case (brine), gather for oil case and gather for gas case. The plots below the synthetic seismic show the amplitude, extracted along the red and blue markers, vs. angle.

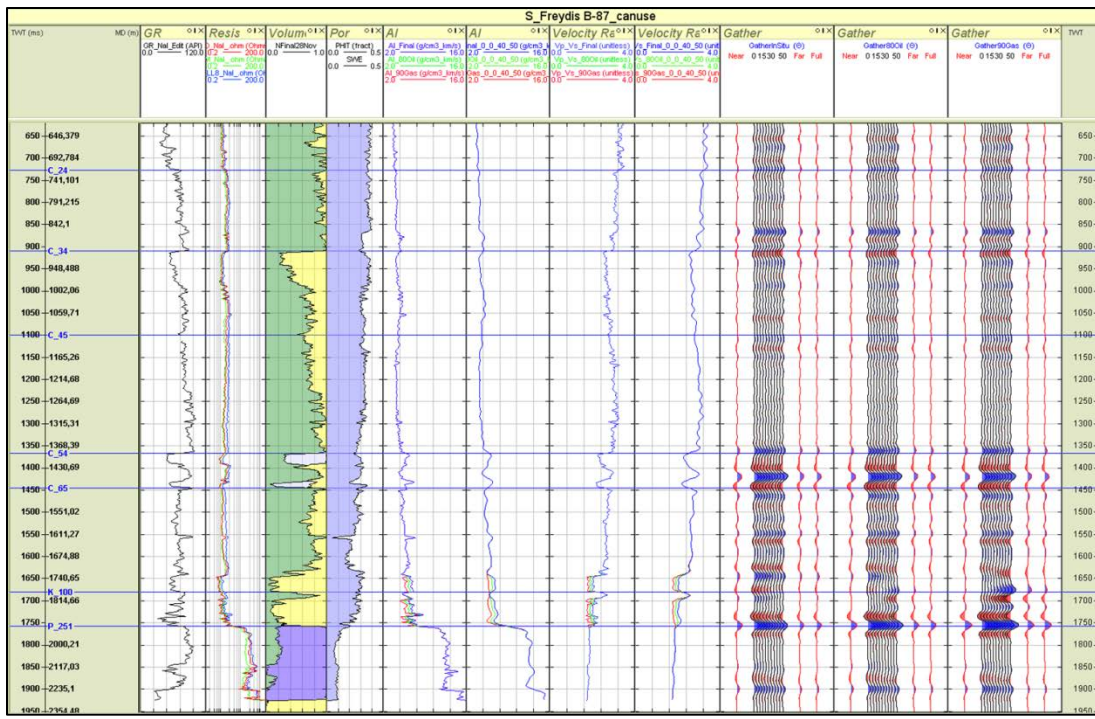


Figure 93: Isotropic synthetic seismic for Freydis B-87, showing the whole well. In-situ case is brine. Tracks from left to right: GR, resistivity, lithology, porosity, acoustic impedance (coloured by fluid case; in-situ: blue, green: oil, red: gas), up-scaled acoustic impedance (coloured by fluid case), VpVs (coloured by fluid case), up-scaled VpVs (coloured by fluid case), gather for in-situ case (brine), gather for oil case and gather for gas case.

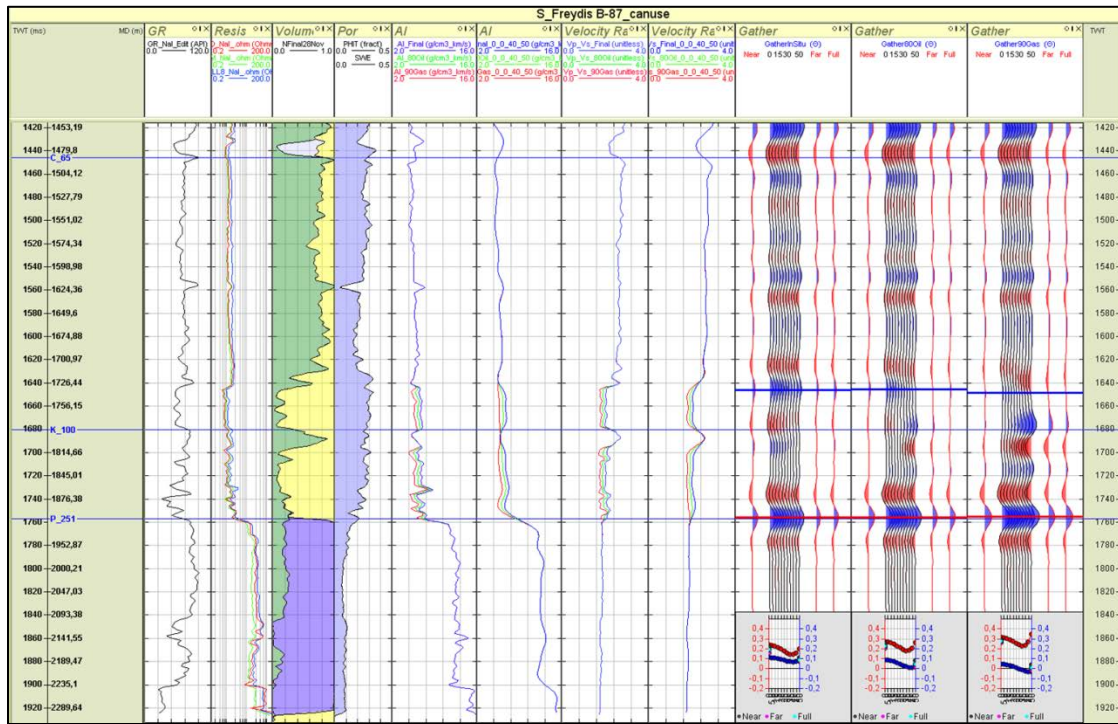


Figure 94: Isotropic synthetic seismic for Freydis B-87, showing the ZOI only. In-situ case is brine. Tracks from left to right: GR, resistivity, lithology, porosity, acoustic impedance (coloured by fluid case; in-situ: blue, green: oil, red: gas), up-scaled acoustic impedance (coloured by fluid case), VpVs (coloured by fluid case), up-scaled VpVs (coloured by fluid case), gather for in-situ case (brine), gather for oil case and gather for gas case. The plots below the synthetic seismic show the amplitude, extracted along the red and blue markers, vs. angle.

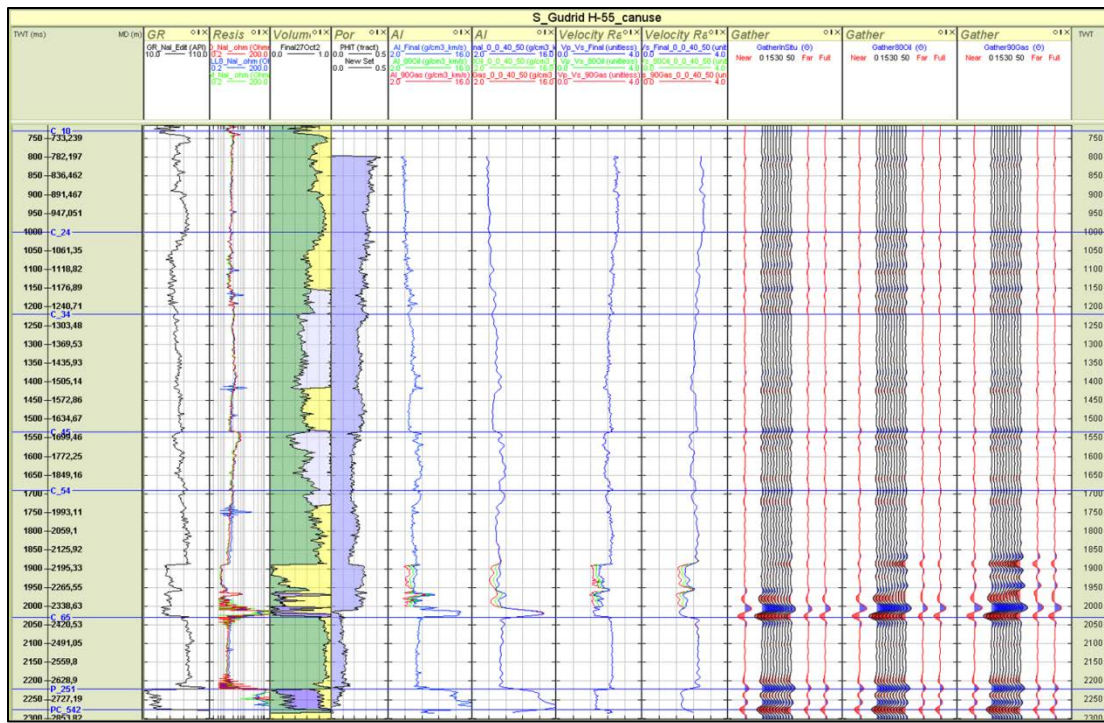


Figure 95: Isotropic synthetic seismic for Gudrid H-55, showing the whole well. In-situ case is brine. Tracks from left to right: GR, resistivity, lithology, porosity, acoustic impedance (coloured by fluid case; in-situ: blue, green: oil, red: gas), up-scaled acoustic impedance (coloured by fluid case), VpVs (coloured by fluid case), up-scaled VpVs (coloured by fluid case), gather for in-situ case (brine), gather for oil case and gather for gas case.

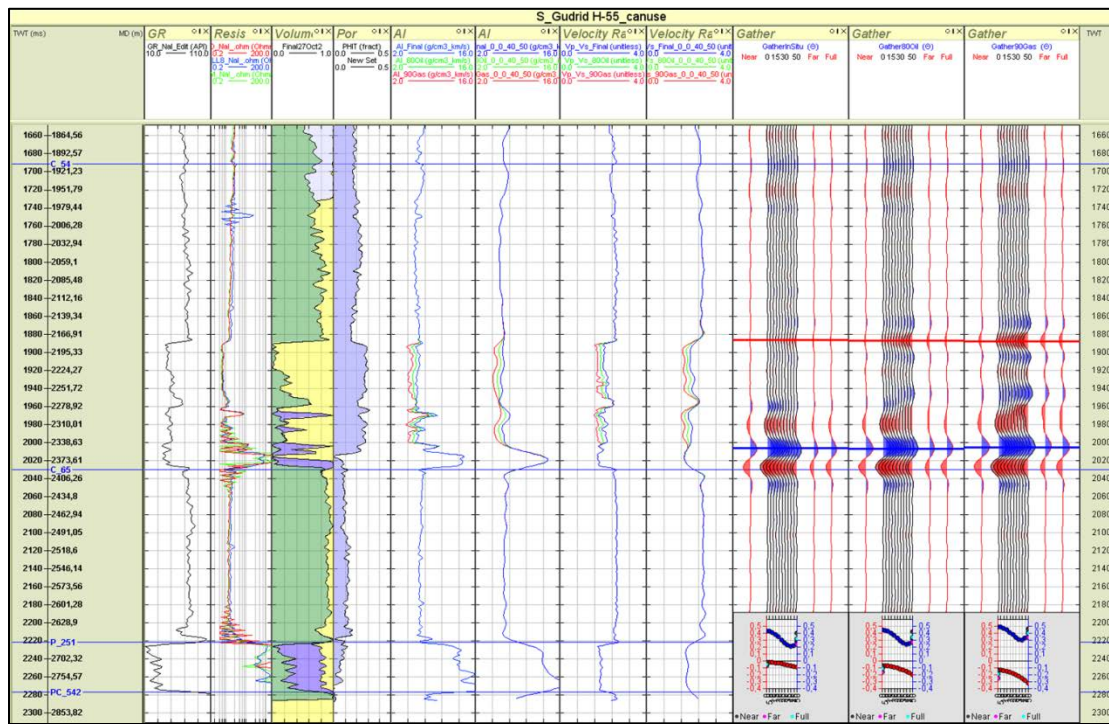


Figure 96: Isotropic synthetic seismic for Gudrid H-55, showing the ZOI only. In-situ case is brine. Tracks from left to right: GR, resistivity, lithology, porosity, acoustic impedance (coloured by fluid case; in-situ: blue, green: oil, red: gas), up-scaled acoustic impedance (coloured by fluid case), VpVs (coloured by fluid case), up-scaled VpVs (coloured by fluid case), gather for in-situ case (brine), gather for oil case and gather for gas case. The plots below the synthetic seismic show the amplitude, extracted along the red and blue markers, vs. angle.

The fluid substitutions in Roberval C-02 were performed in Tertiary sands (Table 23). Figure 97 and Figure 98 show Roberval C-02, the whole well and the zone of interest (ZOI), respectively.

Depth (MD)	AVO Class – Brine	AVO Class - Oil	AVO Class - Gas
2192 – 2416 m	Class I	Class I	Class IV/Class IIP
2416 m (bottom ZOI)	Class I = mirrored Class IV*	Class I = mirrored Class IV*	Class IIP = mirrored Class does not 'exist'.

Table 23: AVO classes from isotropic synthetic seismic for the Tertiary sands in Roberval C-02. *Note the distinct difference between overburden lithology and underburned lithology, if the configuration would have been reversed then top reflection would have been classified as class IV for brine and oil, and a exotic class for gas (soft reflection with positive gradient).

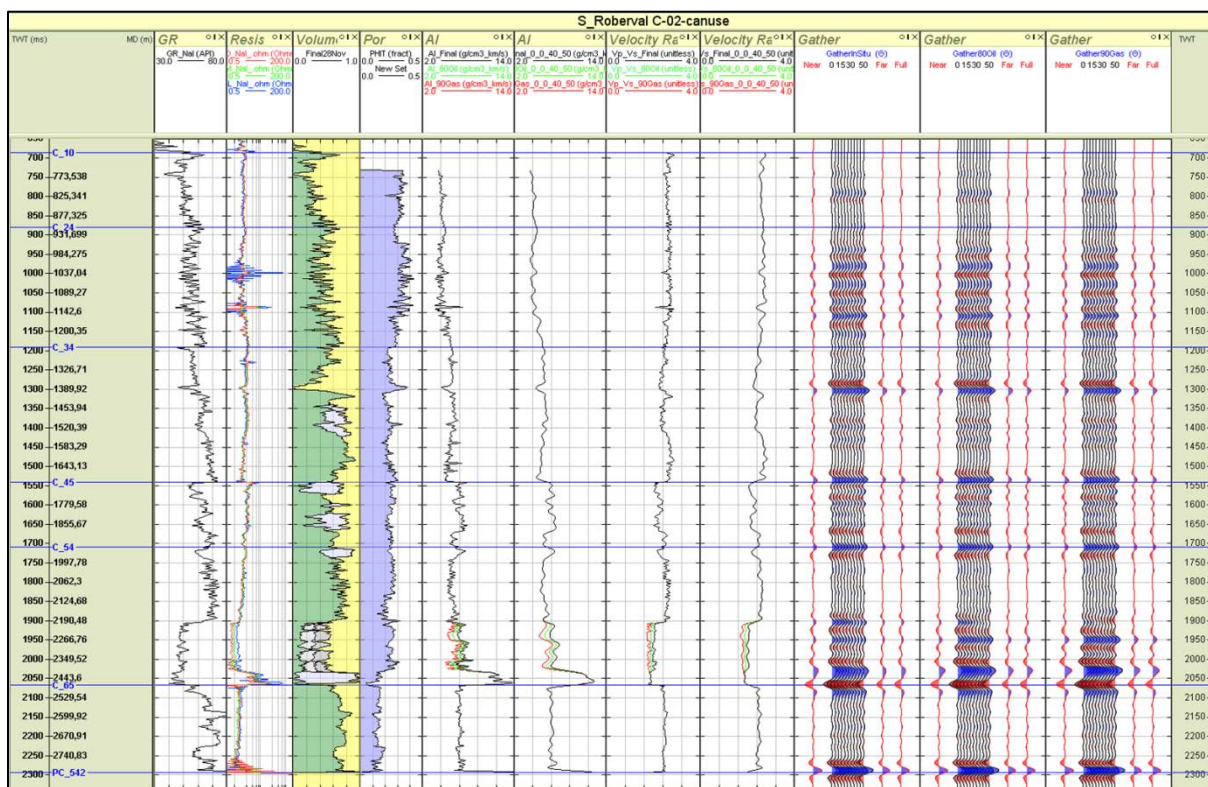


Figure 97: Isotropic synthetic seismic for Roberval C-02, showing the whole well. In-situ case is brine. Tracks from left to right: GR, resistivity, lithology, porosity, acoustic impedance (coloured by fluid case; in-situ: black, green: oil, red: gas), up-scaled acoustic impedance (coloured by fluid case), VpVs (coloured by fluid case), up-scaled VpVs (coloured by fluid case), gather for in-situ case (brine), gather for oil case and gather for gas case.

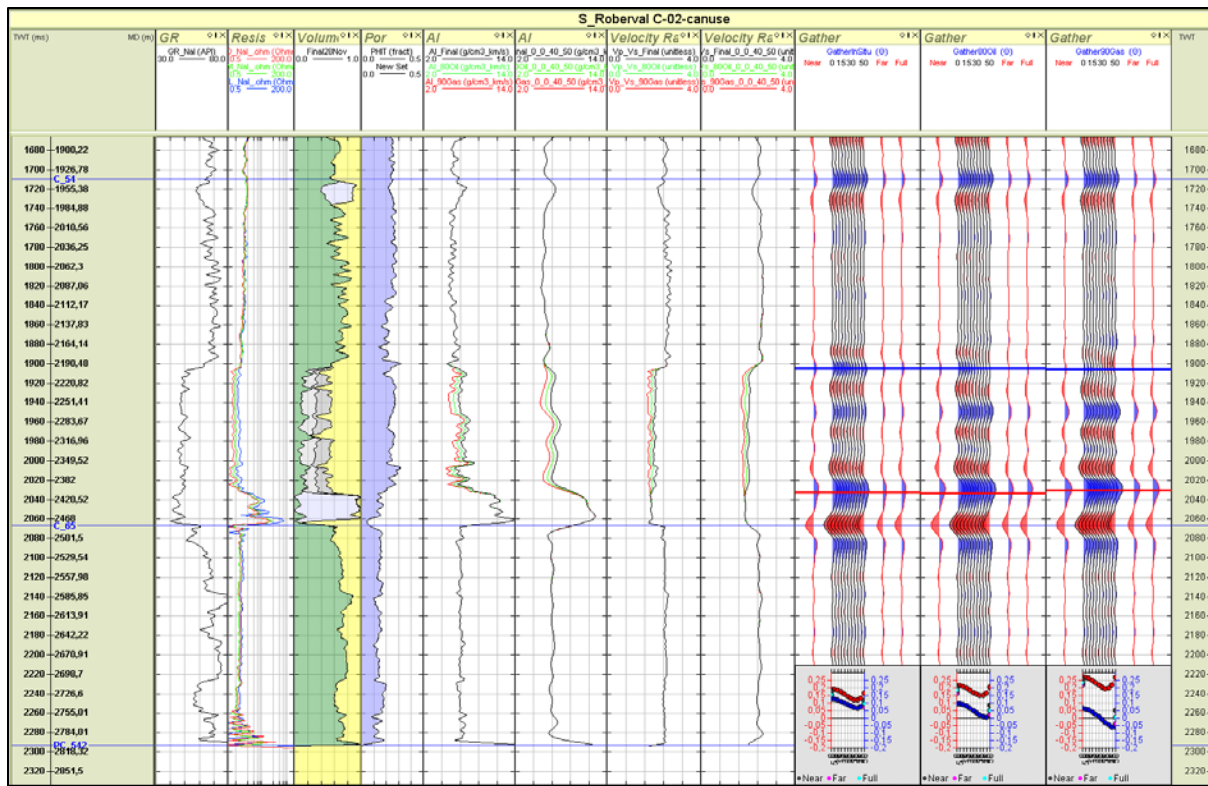


Figure 98: Isotropic synthetic seismic for Roberval C-02, showing the ZOI only. In-situ case is brine. Tracks from left to right: GR, resistivity, lithology, porosity, acoustic impedance (coloured by fluid case; in-situ: black, green: oil, red: gas), up-scaled acoustic impedance (coloured by fluid case), VpVs (coloured by fluid case), up-scaled VpVs (coloured by fluid case), gather for in-situ case (brine), gather for oil case and gather for gas case. The plots below the synthetic seismic show the amplitude, extracted along the red and blue markers, vs. angle.

4.2.2 Blocky Modelling

AVO half-space models (or blocky models) were generated (Figure 99 through Figure 112) to assess the relationship between the caprock and reservoir properties. It is often the case that interbedded lithologies or gradational interfaces can affect the synthetic seismic, resulting in an AVO response that is not entirely representative of the caprock and reservoir. Average elastic property values for the reservoir (for all fluid cases) served as the lower half-space, while elastic property average values of sediment packages 60-70 m thick above the reservoir, acting as a potential cap rock, were used as the upper half-space to create an AVO response. In many cases, there was a good agreement between the isotropic synthetic seismic response and the half-space modelling, and it is expected that heterogeneity, and tuning effects of the cap rocks and reservoir play a vital role when there are disagreements.

In summary, these half-space models are very useful for quickly understanding the expected AVO response, but further modelling must incorporate varying cap rock properties and varying thicknesses of the reservoir to address tuning effects to fully understand seismic amplitudes.

The AVO half-space models are displayed in Figure 99 to Figure 112 and a summary of the corresponding AVO responses is given in Table 24 to Table 33.

Lona O-55

Depth (MD)	AVO Class – Brine	AVO Class - Oil	AVO Class - Gas
Sand1: 4842 – 4905 m	Class IV	Class III	Class III
Sand 2: 5176 – 5208 m	Class III	Class III	Class III

Table 24: AVO classes from isotropic half-space models for the Jurassic sands in Lona O-55.

Lithology	Vp (km/s)	Vs (km/s)	RhoB (g/cc)
Shale	3.08	1.44	2.47
Brine Sand	3.12	1.58	2.19
Oil Sand	3.06	1.59	2.16
Gas Sand	2.89	1.64	2.03

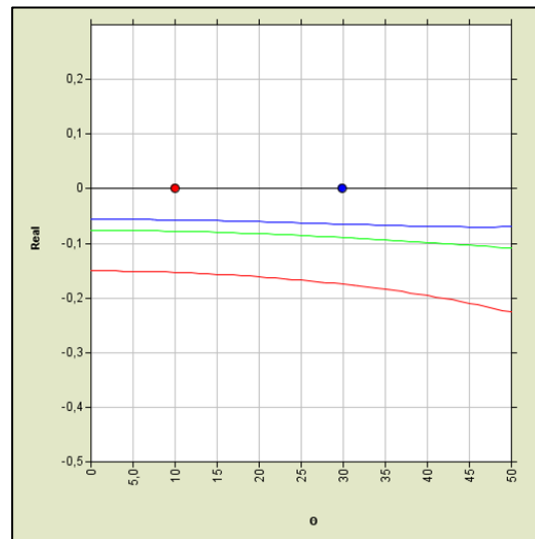


Figure 99: AVO half-space model for Sand 1 in Lona O-55. Coloured by reservoir fluid case; blue: brine, green: oil and red: gas. Overburden and reservoir properties used in the model are documented in the table.

Lithology	Vp (km/s)	Vs (km/s)	RhoB (g/cc)
Shale	3.24	1.58	2.53
Brine Sand	3.46	1.84	2.28
Oil Sand	3.38	1.85	2.25
Gas Sand	3.21	1.90	2.13

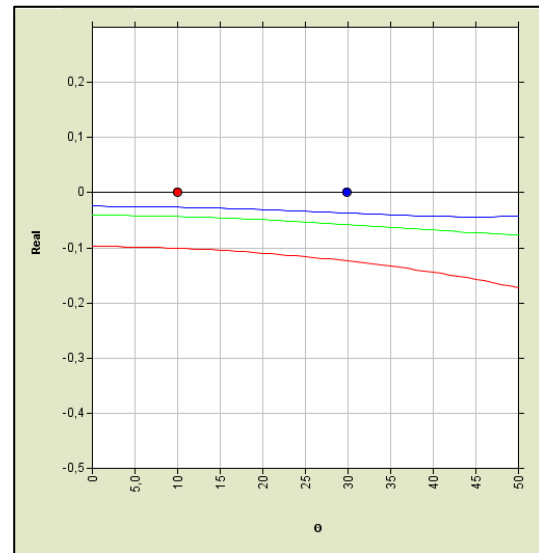


Figure 100: AVO half-space model for Sand 2 in Lona O-55. Coloured by reservoir fluid case; blue: brine, green: oil and red: gas. Overburden and reservoir properties used in the model are documented in the table.

Great Barasway F-66

Depth (MD)	AVO Class – Brine	AVO Class - Oil	AVO Class - Gas
Sand 1: 4106 – 4127 m	Class IV	Class IV/Class III	Class III

Table 25: AVO classes from isotropic half-space models for the Cretaceous sands in Great Barasway F-66. Note that the apparent Class IV AVO responses are very flat.

Lithology	Vp (km/s)	Vs (km/s)	RhoB (g/cc)
Shale	2.82	1.18	2.38
Brine Sand	2.54	1.15	2.16
Oil Sand	2.14	1.17	2.14
Gas Sand	2.07	1.21	1.20

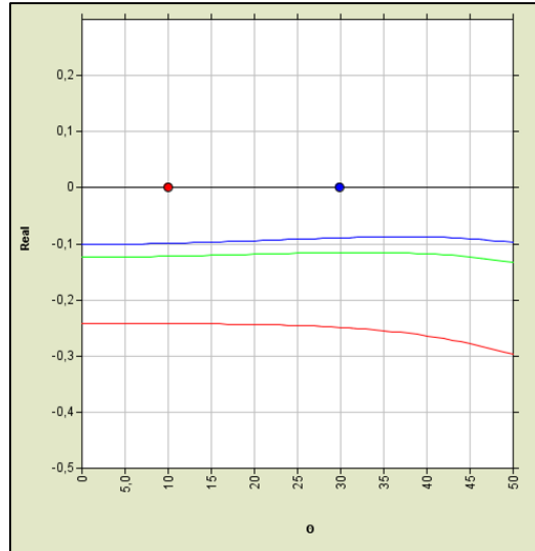


Figure 101: AVO half-space model for Sand 1 in Great Barasway F-66. Coloured by reservoir fluid case; blue: brine, green: oil and red: gas. Overburden and reservoir properties used in the model are documented in the table.

Mizzen O-16

Depth (MD)	AVO Class – Brine	AVO Class - Oil	AVO Class - Gas
Sand 1: 3213 – 3223 m	Class IV	Class IV	Class III
Sand 2: 3369 – 3386 m	Class III	Class III	Class III

Table 26: AVO classes from isotropic half-space models for the Jurassic sands in Mizzen O-16.

Lithology	Vp (km/s)	Vs (km/s)	RhoB (g/cc)
Shale	3.11	1.55	2.48
Brine Sand	3.24	1.7	2.17
Oil Sand	3.16	1.71	2.14
Gas Sand	3.05	1.77	1.99

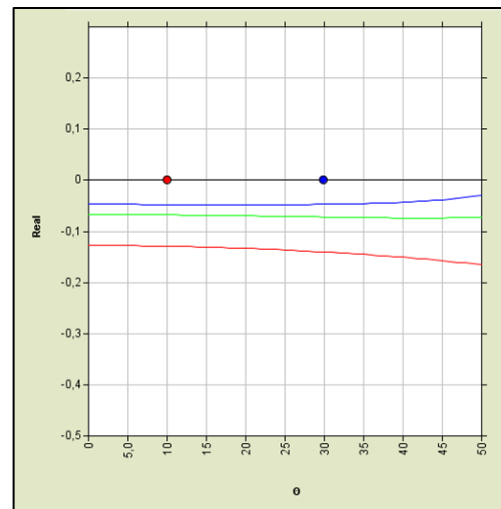


Figure 102: AVO half-space model for Sand 1 in Mizzen O-16. Coloured by reservoir fluid case; blue: brine, green: oil and red: gas. Overburden and reservoir properties used in the model are documented in the table.

Lithology	Vp (km/s)	Vs (km/s)	RhoB (g/cc)
Shale	3.36	1.74	2.51
Brine Sand	3.48	1.94	2.27
Oil Sand	3.41	1.95	2.24
Gas Sand	3.31	2.02	2.108

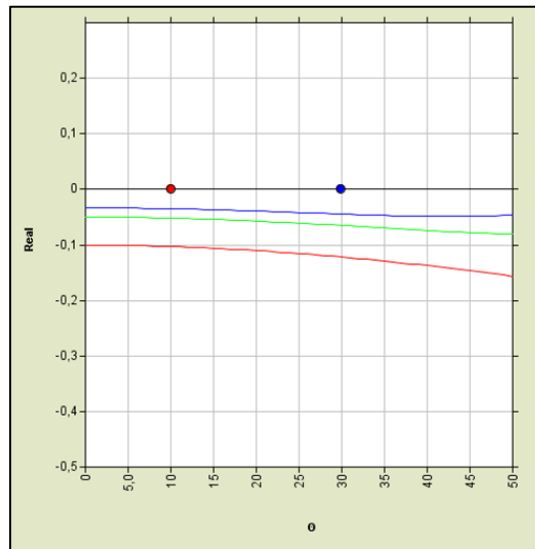


Figure 103: AVO half-space model for Sand 2 in Mizzen O-16. Coloured by reservoir fluid case; blue: brine, green: oil and red: gas. Overburden and reservoir properties used in the model are documented in the table.

Mizzen L-11

Depth (MD)	AVO Class – Brine	AVO Class - Oil	AVO Class - Gas
Sand 1: 3599 – 3625 m	Class IIP	Class II	Class III
Sand 2: 3742 – 3767 m	Class III	Class III	Class III

Table 27: AVO classes from isotropic half-space models for the Jurassic sands in Mizzen L-11.

Lithology	Vp (km/s)	Vs (km/s)	RhoB (g/cc)
Shale	3.62	1.78	2.51
Brine Sand	3.68	2.03	2.24
Oil Sand	3.63	2.04	2.22
Gas Sand	3.54	2.10	2.09

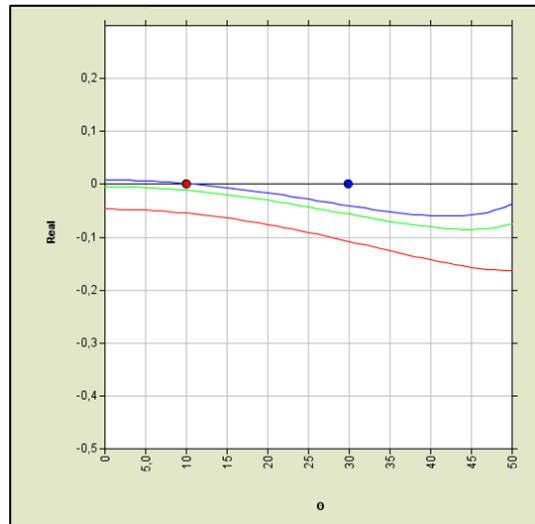


Figure 104: AVO half-space model for Sand 1 in Mizzen L-11. Coloured by reservoir fluid case; blue: brine, green: oil and red: gas. Overburden and reservoir properties used in the model are documented in the table.

Lithology	Vp (km/s)	Vs (km/s)	RhoB (g/cc)
Shale	3.50	1.65	2.57
Brine Sand	3.73	2.03	2.28
Oil Sand	3.68	2.03	2.26
Gas Sand	3.60	2.08	2.16

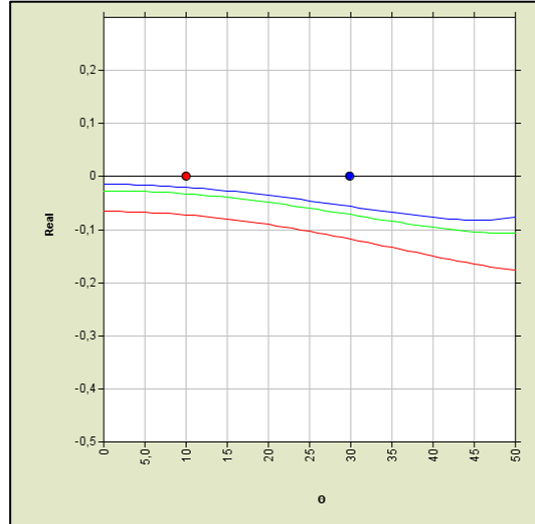


Figure 105: AVO half-space model for Sand 2 in Mizzen L-11. Coloured by reservoir fluid case; blue: brine, green: oil and red: gas. Overburden and reservoir properties used in the model are documented in the table.

Mizzen F-09

Depth (MD)	AVO Class – Brine	AVO Class - Oil	AVO Class - Gas
Sand 1: 3484 – 3509 m	Class IIP	Class II	Class III
Sand 2: 3576 – 3601 m	Class IIP	Class II	Class III

Table 28: AVO classes from isotropic half-space models for the Jurassic sands in Mizzen F-09.

Lithology	Vp (km/s)	Vs (km/s)	RhoB (g/cc)
Shale	3.40	1.84	2.54
Brine Sand	3.38	1.86	2.24
Oil Sand	3.27	1.90	2.21
Gas Sand	3.10	1.97	2.06

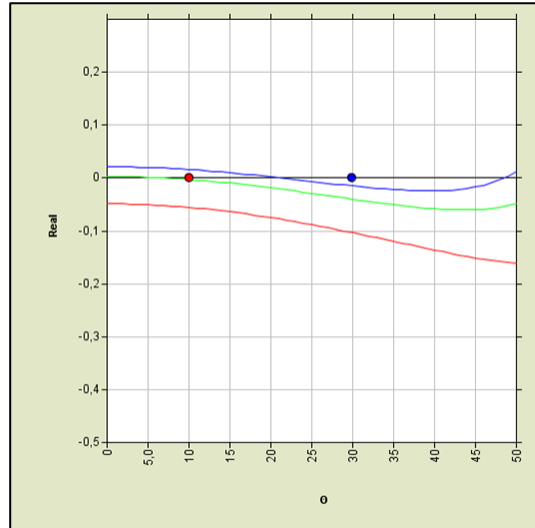


Figure 106: AVO half-space model for Sand 1 in Mizzen F-09. Coloured by reservoir fluid case; blue: brine, green: oil and red: gas. Overburden and reservoir properties used in the model are documented in the table.

Lithology	Vp (km/s)	Vs (km/s)	RhoB (g/cc)
Shale	3.05	1.60	2.56
Brine Sand	3.42	1.97	2.27
Oil Sand	3.31	2.00	2.24
Gas Sand	3.12	2.03	2.11

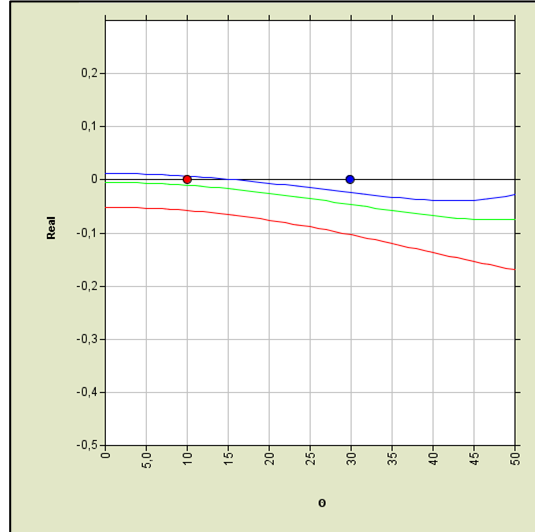


Figure 107: AVO half-space model for Sand 2 in Mizzen F-09. Coloured by reservoir fluid case; blue: brine, green: oil and red: gas. Overburden and reservoir properties used in the model are documented in the table.

Baccaieu I-78

Depth (MD)	AVO Class – Brine	AVO Class - Oil	AVO Class - Gas
Sand 1: 3197 – 3267 m	Class IIP	Class IIP	Class IIP

Table 29: AVO classes from isotropic half-space models for the Cretaceous sand in Baccaieu I-78.

Lithology	Vp (km/s)	Vs (km/s)	RhoB (g/cc)
Shale	3.28	1.38	2.58
Brine Sand	3.85	1.98	2.44
Oil Sand	3.82	1.99	2.43
Gas Sand	3.77	2.00	2.38

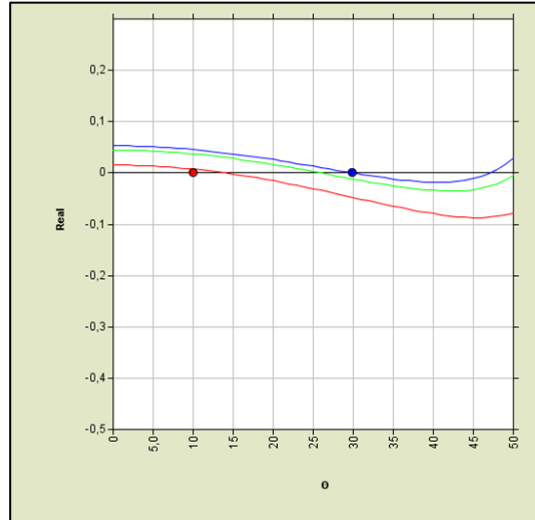


Figure 108: AVO half-space model for Sand 1 in Baccaieu I-78. Coloured by reservoir fluid case; blue: brine, green: oil and red: gas. Overburden and reservoir properties used in the model are documented in the table.

Cartier D-70

Depth (MD)	AVO Class – Brine	AVO Class - Oil	AVO Class - Gas
Sand 1: 1798 – 1856 m	Class I	Class I/Class IIP	Class IIP

Table 30: AVO classes from isotropic half-space models for the Tertiary sand in Cartier D-70.

Lithology	Vp (km/s)	Vs (km/s)	RhoB (g/cc)
Shale	2.71	1.09	2.30
Brine Sand	3.00	1.42	2.23
Oil Sand	2.90	1.43	2.20
Gas Sand	2.73	1.47	2.08

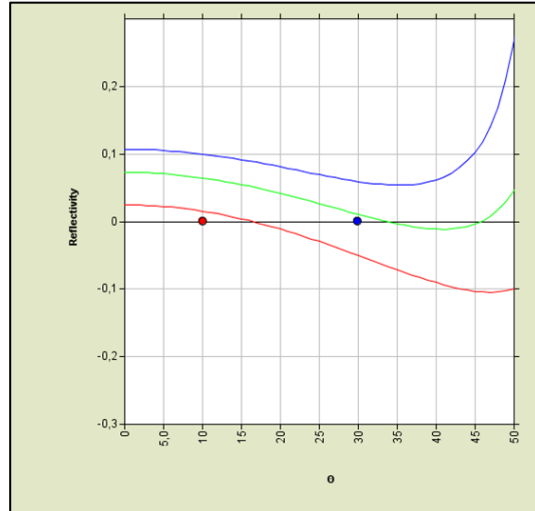


Figure 109: AVO half-space model for Sand 1 in Cartier D-70. Coloured by reservoir fluid case; blue: brine, green: oil and red: gas. Overburden and reservoir properties used in the model are documented in the table.

Freydis B-87

Depth (MD)	AVO Class – Brine	AVO Class - Oil	AVO Class - Gas
Sand 1: 1733 – 1900 m	Class I	Class IIP	Class II/Class III

Table 31: AVO classes from isotropic half-space models for the Tertiary sand in Freydis B-87.

Lithology	Vp (km/s)	Vs (km/s)	RhoB (g/cc)
Shale	2.55	0.97	2.34
Brine Sand	3.07	1.50	2.22
Oil Sand	2.92	1.51	2.17
Gas Sand	2.80	1.55	2.06

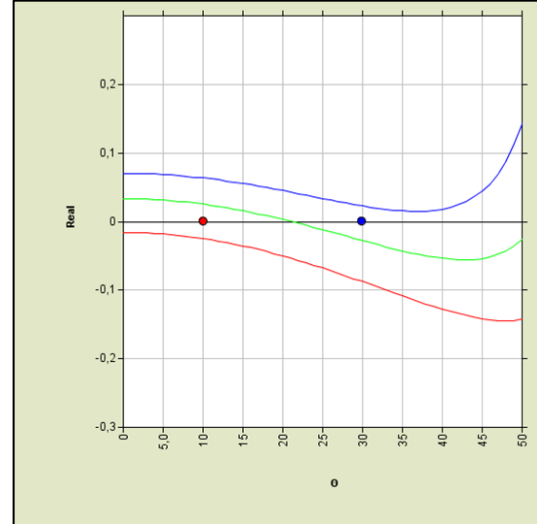


Figure 110: AVO half-space model for Sand 1 in Freydis B-87. Coloured by reservoir fluid case; blue: brine, green: oil and red: gas. Overburden and reservoir properties used in the model are documented in the table.

Gudrid H-55

Depth (MD)	AVO Class – Brine	AVO Class - Oil	AVO Class - Gas
Sand 1: 2173 – 2343 m	Class IIP	Class IIN	Class III

Table 32: AVO classes from isotropic half-space models for the Tertiary sand in Gudrid H-55.

Lithology	Vp (km/s)	Vs (km/s)	RhoB (g/cc)
Shale	2.76	1.11	2.33
Brine Sand	2.90	1.38	2.22
Oil Sand	2.71	1.40	2.17
Gas Sand	2.61	1.53	2.03

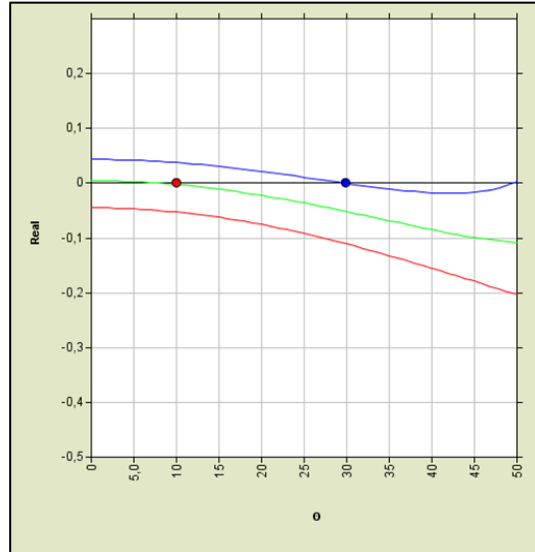


Figure 111: AVO half-space model for Sand 1 in Gudrid H-55. Coloured by reservoir fluid case; blue: brine, green: oil and red: gas. Overburden and reservoir properties used in the model are documented in the table.

Roberval C-02

Depth (MD)	AVO Class – Brine	AVO Class - Oil	AVO Class - Gas
Sand 1: 2192 – 2416 m	Class I	Class I	Class IIP

Table 33: AVO classes from isotropic half-space models for the Tertiary sand in Roberval C-02.

Lithology	Vp (km/s)	Vs (km/s)	RhoB (g/cc)
Shale	2.60	1.03	2.28
Brine Sand	3.25	1.61	2.23
Oil Sand	3.09	1.63	2.18
Gas Sand	2.99	1.67	2.08

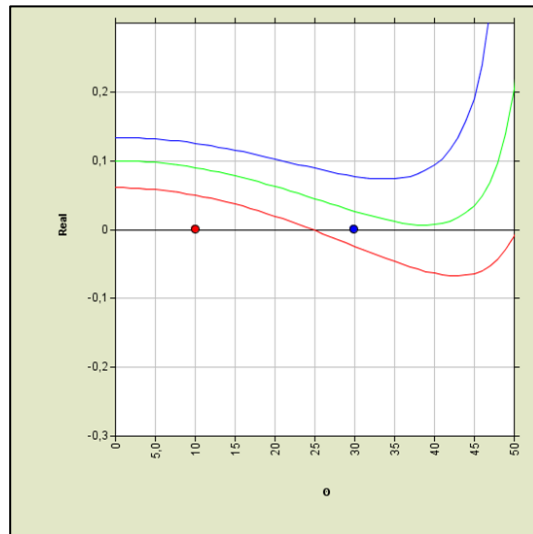


Figure 112: AVO half-space model for Sand 1 in Roberval C-02. Coloured by reservoir fluid case; blue: brine, green: oil and red: gas. Overburden and reservoir properties used in the model are documented in the table.

4.3 Summary

The shale-on-sand interfaces for most of the shallow-water wells have a positive reflectivity on the near offset traces for all fluid fills, with a mid-angle phase reversal expected for hydrocarbon in many cases (AVO Class I to AVO Class IIp).

The shale-on-sand interfaces in the deep-water wells show an AVO character that indicates negative reflectivity at the near offset traces. The negative reflectivity is highly dependent on the shale type in the immediate overburden, and the compaction state of the sandstone and its porosity. To illustrate the expected near offset trace response for sands and shales in the study, the derived Vp-TVDml and RhoB-TVDml trends are used to generate AI-TVDml trends for sands and shales, shown in Figure 113. The blue contours here are the AI depth trends for the sands, the lower lightest blue line is the unconsolidated sand line, the upper darker blue is the most cemented sand line. The normal and cemented shale trends are shown in pink and red dashed lines respectively. As can be seen at some depths the uncemented and slightly cemented sands are acoustically softer than the normal shales, whereas the cemented shales are generally acoustically harder than the sands except in the very shallow section.

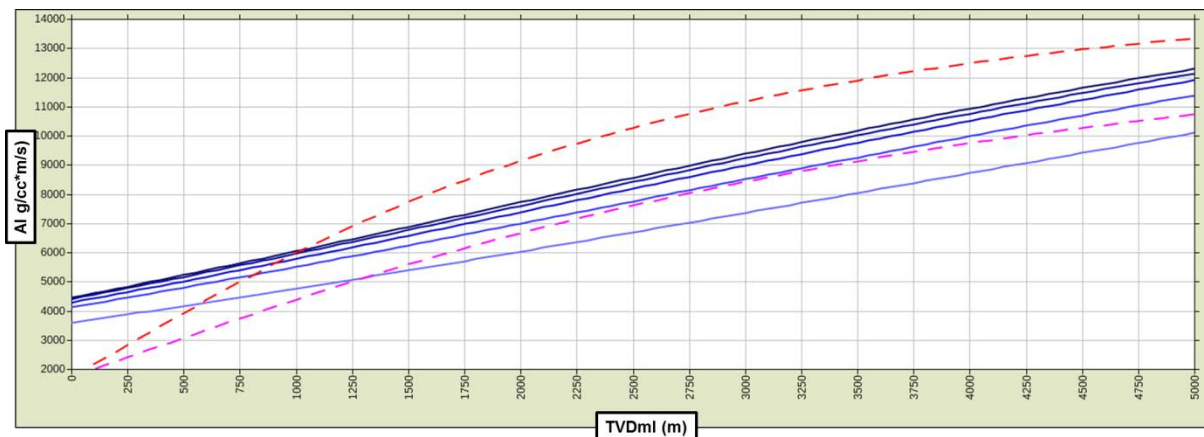


Figure 113: AI-TVDml trends derived from the Vp-TVDml and RhoB-TVDml trends from the study. The blue lines are the sandstone trends (light blue = uncemented, dark blue = cemented), the pink dashed line is the normal shale trend, and the red dashed line the cemented shale trend.

A varying gradient response is observed, with both positive gradients (AVO Class IV) and negative gradients (AVO Class II/III) being present. The gradients of some of the AVO Class IV responses are very low and are the result of modelling a mix of lithologies, rather than pure end-member sand and shale.

5 An Integrated Workflow for De-Risking in Frontier Basins

5.1 Introduction

Chapter 5 incorporates the regional rock physics work from the previous chapters into an analysis of pre-stack responses over three leads in the Flemish Pass and Orphan Basin. The framework is used to predict the elastic response of each facies at the depth (TVDml) of each lead, and the associated AVO response based on the predicted elastic properties. The framework predicts the elastic properties of each facies as a function of burial depth, sand porosity, consolidation, saturating fluid, shale lithology and Vertical Effective Stress (VES).

For the purposes of illustrating how the defined framework can be used, and for performing an initial investigation of the three leads in question, half-space, single interface models were generated that assume a simple layering geometry here. It is worth noting that the predictive framework can be expanded to incorporate more complex lithologic relationships should that be desirable to the end user.

5.2 Modelling Constraints

The following sections demonstrate how the Rock Physics and AVO workflows from the previous chapters of this report can be used to gain an understanding of geological properties via seismic amplitude analysis in the subsurface away from well control.

The workflow combines everything that has been learned so far; the calibrated rock physics models, depth trends, regional pressure profiles, vertical effective stress transforms, geological knowledge and seismic interpretation. The data and information is brought together as an integrated tool to help quantify the seismic responses resulting from a variety of geological scenarios. The data provides regional trends that can be used to build the blocky model scenarios. It should be noted that this modelling approach does not incorporate velocities derived from seismic data. It is advisable to QC the depth trend velocities with the seismically derived interval velocities to confirm consistency between the regionally derived depth trends and locally measured velocities.

The modelling is based around the facies identified in the well database. As discussed in previous chapters, log responses indicate that both unconsolidated (no grain contact cement, as

seen in the sands at the Great Barasway F-66 well) and cemented (various levels of grain contact cement) sands are encountered in the region, as well as three types of shale:

- “Normal” shale – the bulk of the shale data identified in the petrophysical interpretation. This shale is assumed to be smectite-rich, given its shallower depth of burial, and is the most likely candidate as the overburden for a shale/sand interface, given its abundance.
- “Calcareous” shale – identified during the petrophysical interpretation. There are two different trends: one for Tertiary-Cretaceous and one for the Jurassic.
- “Cemented” shale – a harder shale that appears to be present in the deep section. Given its deep depth of burial, it is assumed to be below the smectite-to-illite (S/I) transformation zone for shales, and therefore represents an illite-rich shale.

It was shown in Chapter 2 that the rock physics diagnostics procedure could successfully capture the elastic behaviour of the slightly cemented sands encountered in the deep-water wells via the use of the calibrated Constant Cement rock physics model of Avseth et al. 2000. Cementation increases with depth, so the modelling workflow will account for this by using a higher cement content for the deeper leads, based on the quartz overgrowth – TVDml trend documented in Chapter 3. The Tertiary and Cretaceous leads in this part of the study are deeper (>3000m TVDml) than most of the sands encountered by the offset wells (~2500m TVDml). The modelling framework will be run for the expected grain contact cement content, and for the unconsolidated case at each lead in order to help illustrate the effect of sand cementation on the AVO response.

The sand porosity expected at a given depth will be obtained from the sand RhoB-TVDml, with a high and low case porosity being obtained from the low and high case RhoB-TVDml trends. Using the trends above will give three porosity cases, which will be important for understanding the effect of porosity on sandstone elastic response.

Acoustic fluid properties are derived using the FLAG algorithm (**F**luid **A**pplication of **G**eophysics, University of Houston). The FLAG algorithm is an empirical calculator that relates the physical properties of the pore fluids, pressure and temperature to an acoustic response.

The fluid cases being modelled are brine, normal oil, light oil and gas. The light oil case has a high GOR and higher API than the normal oil case. The normal oil is consistent with hydrocarbon in the Mizzen discovery. The fluid properties are obtained from regional wells and are given in the table 34:

Fluid	Salinity (kppm)	API	GOR	Gas Gravity
Brine	65	-	-	-
Heavy Oil	-	22	5	0.65
Light Oil	-	35	300*	0.65
Gas	-	-	-	0.65

Table 34: Fluid properties used as inputs to the FLAG algorithms. *The GOR for light oil is reduced when modelling shallow leads, where the pressure is too low to allow a GOR of 300.

The final additional inputs for the FLAG algorithms are temperature and pressure. The regional temperature profile has been identified as 30°C/km and a regional pore pressure profile will be used for the leads. The regional pore pressure profile is hydrostatic pressure down to a fluid retention depth (FRD; Swarbrick, 2012) of 1200m TVDml, after which pressure builds out at 0.7 psi/ft. The pore pressure profile is broadly consistent with the pressures encountered in the deep-water wells and will also be used as the base case for the VES modelling. For the highly overpressured case in the VES modelling, the FRD will remain the same but the pressure will build out at 0.95 psi/ft, as documented in Chapter 3, Section 1.2.

5.3 AVO Modelling Workflow

It has been shown that a shale-on-sand interface in this area could be composed of a number of different shale overburdens (normal shale, calcareous shale or cemented shale) and a number of different sands, differentiated by their cement content and porosity. A robust workflow must therefore be designed for AVO modelling, to ensure that the different combinations are accounted for.

The workflow for AVO modelling follows a similar approach used by Gutierrez and Dvorkin (2010), and is summarised as follows:

1. Derive shale elastic properties (for normal shale, calcareous shale and cemented shale) at the prospect depth using the shale V_p , V_s and ρ_B – TVDml trends.
2. Calculate acoustic fluid properties at prospect depth using a model pore pressure profile.
3. Derive sand ρ_B at the prospect depth using the sand ρ_B – TVDml trend and convert to porosity.
4. Use the calibrated Constant Cement model to model V_p at the prospect depth for an uncemented case and an expected grain contact cement case.
5. Calculate sand V_s from the calibrated V_s - V_p trend for sands.
6. Use the RMS error for the sand ρ_B -depth trend to derive elastic properties for high and low case porosity sands.
7. Fluid substitute the sand elastic properties to the desired hydrocarbon cases.
8. Use the Vertical Effective Stress (VES) trends to investigate the effect of changing overpressure on sand porosity and shale elastic response.
9. Plot AVO half-space models for each combination of shale and sand, and generate intercept/gradient values for the models that show a match to the seismic response.
10. Make a model-seismic comparison per lead based on the AVO curves and intercept/gradient responses.

Using all combinations of sands and overburdens results in 15 models for the initial modelling and eight models for the VES modelling. Outputs from the predictive framework will be referred to as “the model” in the following analyses.

5.4 Ground Truthing at Mizzen O-16

5.4.1 Introduction

The modelling framework was run for the Mizzen oil discovery (Mizzen O-16). AVO response models were generated and compared to the well and seismic response at this location. The aim of the comparison is to verify the models against a known response, where the rocks are sampled by both well logs and seismic.

The Mizzen field is a fault-bounded horst block (Figure 114), with two Jurassic reservoir intervals encountered by the Mizzen O-16 well, at ~3400ms and 3500ms TWT. Within the fault block, only the upper reservoir sand is hydrocarbon bearing.

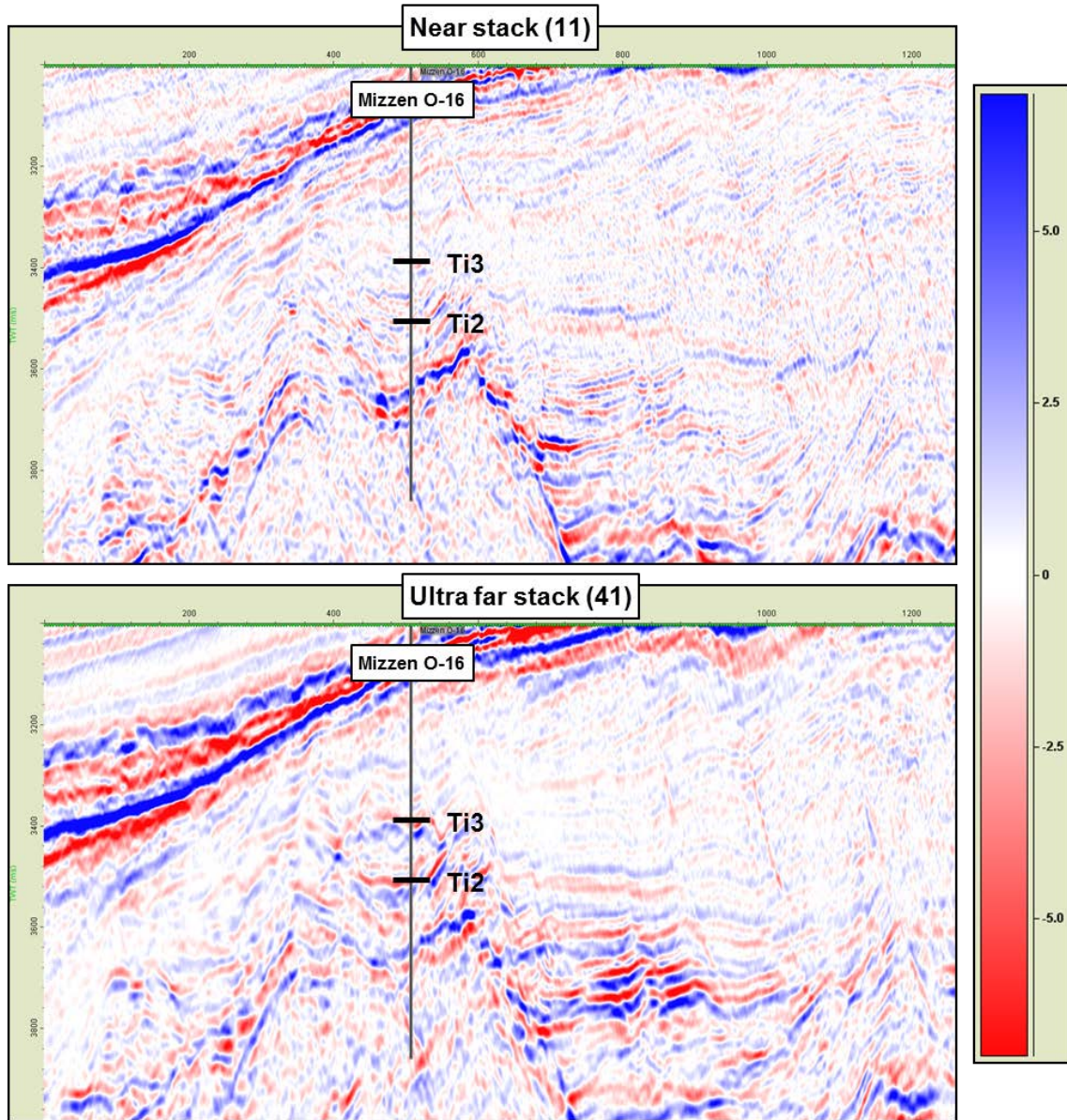


Figure 114: Angle stacks through Mizzen O-16. Upper image: near stack, lower image: ultra-far stack.

5.4.2 Angle Stack Responses

The angle stack responses at Mizzen O-16 (Figure 115) show weak amplitude events on the near stack that brighten significantly with increasing offset resulting in strong soft events on the far stack. These are class II_p/class II AVO responses.

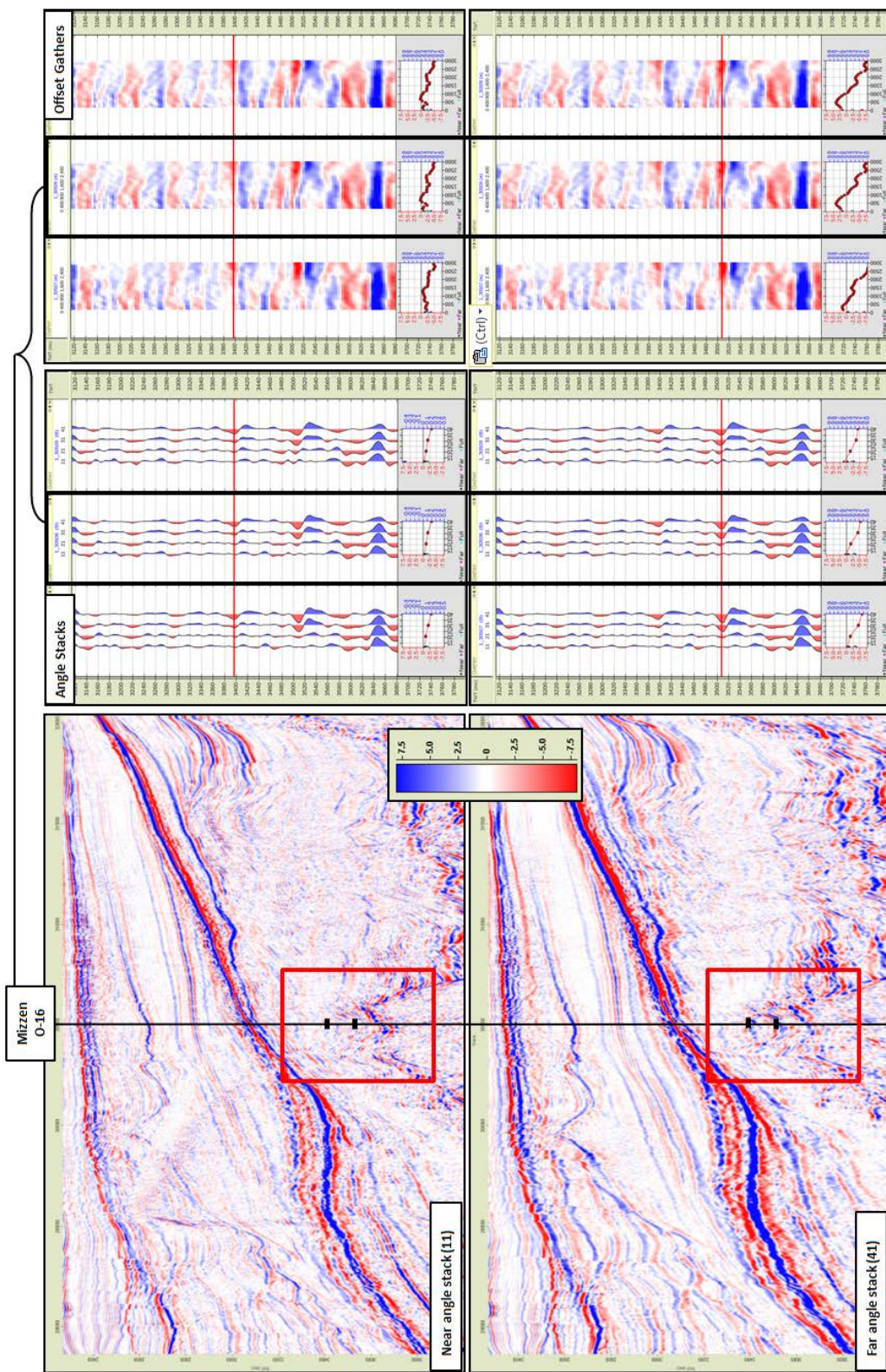


Figure 115: AVO extractions from angle stacks and far offset gathers at the Mizzen O-16 reservoir interval. SEG Normal polarity. The AVO is extracted as a single value per trace along the red bars, this is shown in the attribute plot at the base of each gather.

5.4.3 AVO Modelling

AVO half-space models were calculated for the upper and lower Jurassic sands in Mizzen O-16, there are 15 normally pressured scenarios and eight overpressured scenarios. The resulting Model Response Matrix (MRM) for the depth trends is shown in Figure 116 (upper sand) and Figure 117 (lower sand). As comparisons are being made at this stage between reflectivity from AVO half-space models and the seismic amplitudes, assessments here are only made in terms of AVO class, curve shape and the relative effect of overburden type, pore fluid fill and porosity.

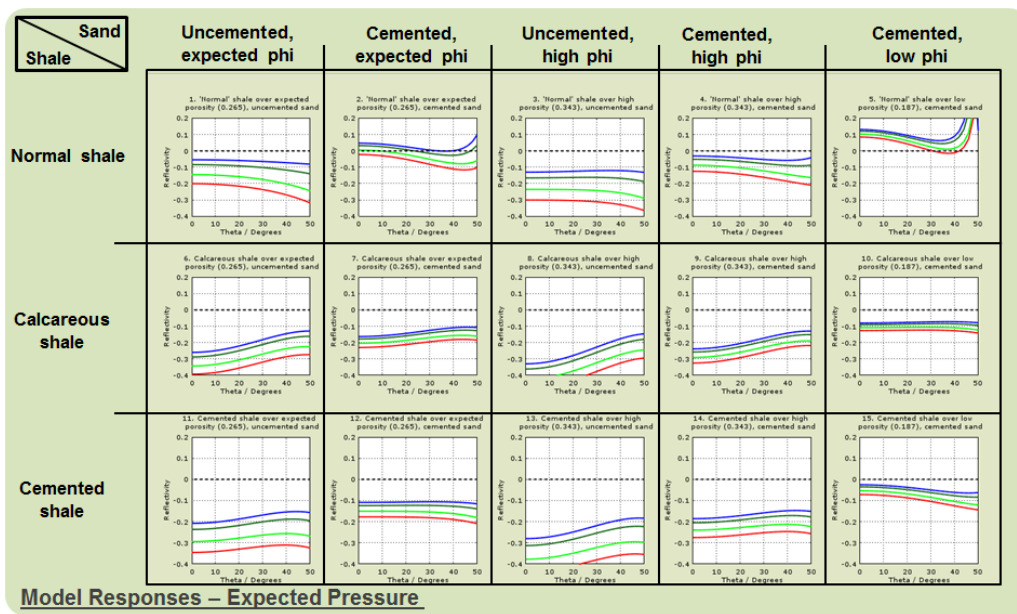


Figure 116: MRM for upper sand in Mizzen O-16.

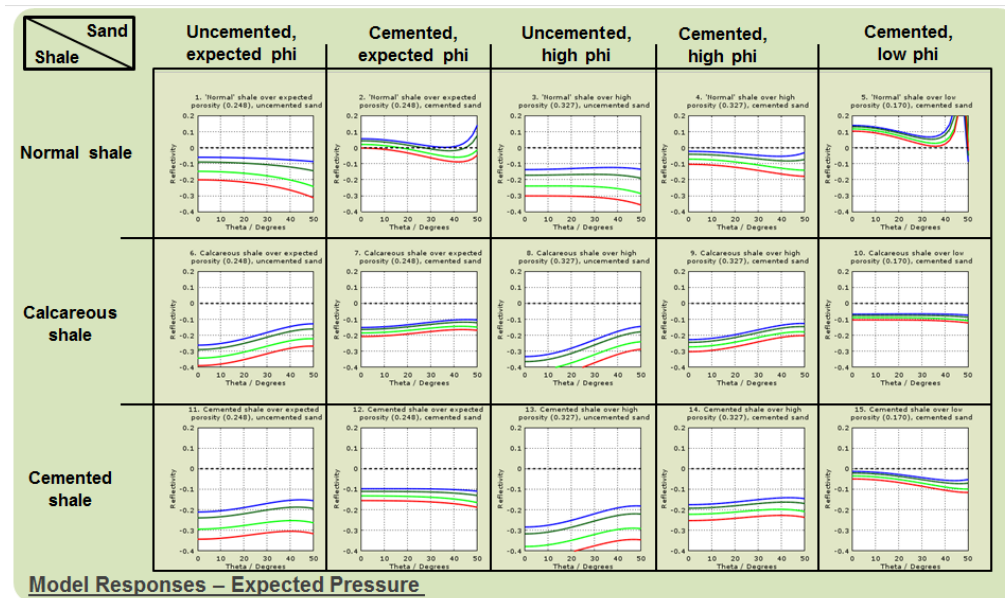


Figure 117: MRM for lower sand in Mizzen O-16.

5.4.4 Model - Well Comparisons

A comparison of half-space AVO responses between the well responses and model is shown in Figure 118. The well response is generated from average Vp, Vs and RhoB values in the sands, and immediate overburden.

For the upper sand, the porosity falls toward the high case regional trend. The model for a normal shale overlying a high porosity, cemented sand (with 4% cement) shows a good match to the well response.

For the lower sand, the porosity falls between the high and expected case regional trend, and both the high and expected porosity models are shown.

The oil in Mizzen O-16 is represented by the normal oil case, so the half-space well response in the upper sand should be compared to the darker green model response.

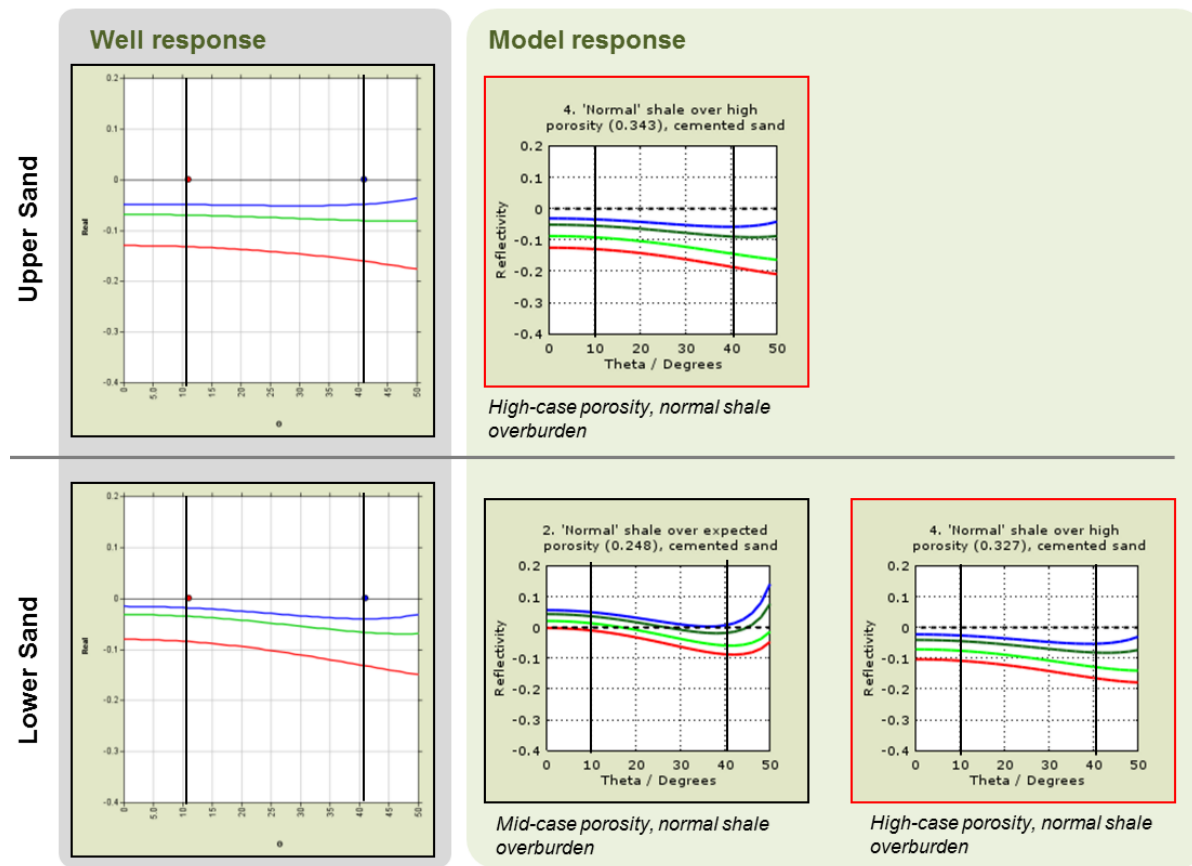


Figure 118: Comparison of half-space well and model responses for the Jurassic sands in Mizzen O-16. Brine, normal oil, light oil and gas cases shown, blue, dark green, light green, red respectively. The well log derived porosity for the lower sand is mid-way between the expected porosity and high porosity (highlighted in red) trend.

5.4.5 Model - Seismic Comparisons

The model and well responses are then compared to the seismic response for the upper sand and lower sand (Figure 119) in Mizzen O-16. Synthetic gathers are generated from the well log data (left hand well panel in Figure 119), and from the predictive framework (central well panel in Figure 119), the seismic angle stack response is also shown at the Mizzen O-16 well location (right well panel in Figure 119, gather at well highlighted). In Figure 119 the AVO for the upper and lower sand packages are extracted along the blue and red bars respectively, the amplitude per trace is then displayed at the base of each gather.

The synthetic gathers are generated using a statistically extracted wavelet from the mid angle stack over the interval of interest (3-4s), in order to generate gathers with the appropriate bandwidth for comparison to the seismic.

The AVO response for the upper sand in the seismic is generally captured by the model, with both the seismic and the model displaying a negative response at zero offset that brightens with increasing offset. However, the weak near offset response in the seismic is not observed in either the well-based or model-based synthetic gathers, where a stronger soft event is seen on the near.

There is a good match between the model, well and seismic responses for the lower sand in Mizzen O-16, although the seismic shows more brightening of the far offsets.

It is expected that tuning and offset scaling issues in the seismic are some of the main causes of mis-matches between well, model and seismic response, although an appropriate bandwidth (wavelet) has been used when generating the synthetic gathers and tuning wedge.

Specifically tuning could result in a weakening of the intercept response and steepening of the negative gradient, Figure 120 is illustrative of this effect. Here a 2D wedge model is populated with constant properties (V_p , V_s and ρ_{B}) from the Mizzen O-16 well. At each trace across the model an AVO synthetic is generated (near to far traces from right to left, per CDP). An AVO extraction is made across the apparent top of the wedge, with the extractions per trace shown in the attribute plot at the base. As can be seen the AVO is effected by thickness, where the response is tuned the AVO intercept becomes weaker, and the AVO gradient becomes steeper. The Mizzen O-16 sands are around 10ms thick, and it can be seen that this is the TWT thickness at which tuning is expected to influence AVO response.

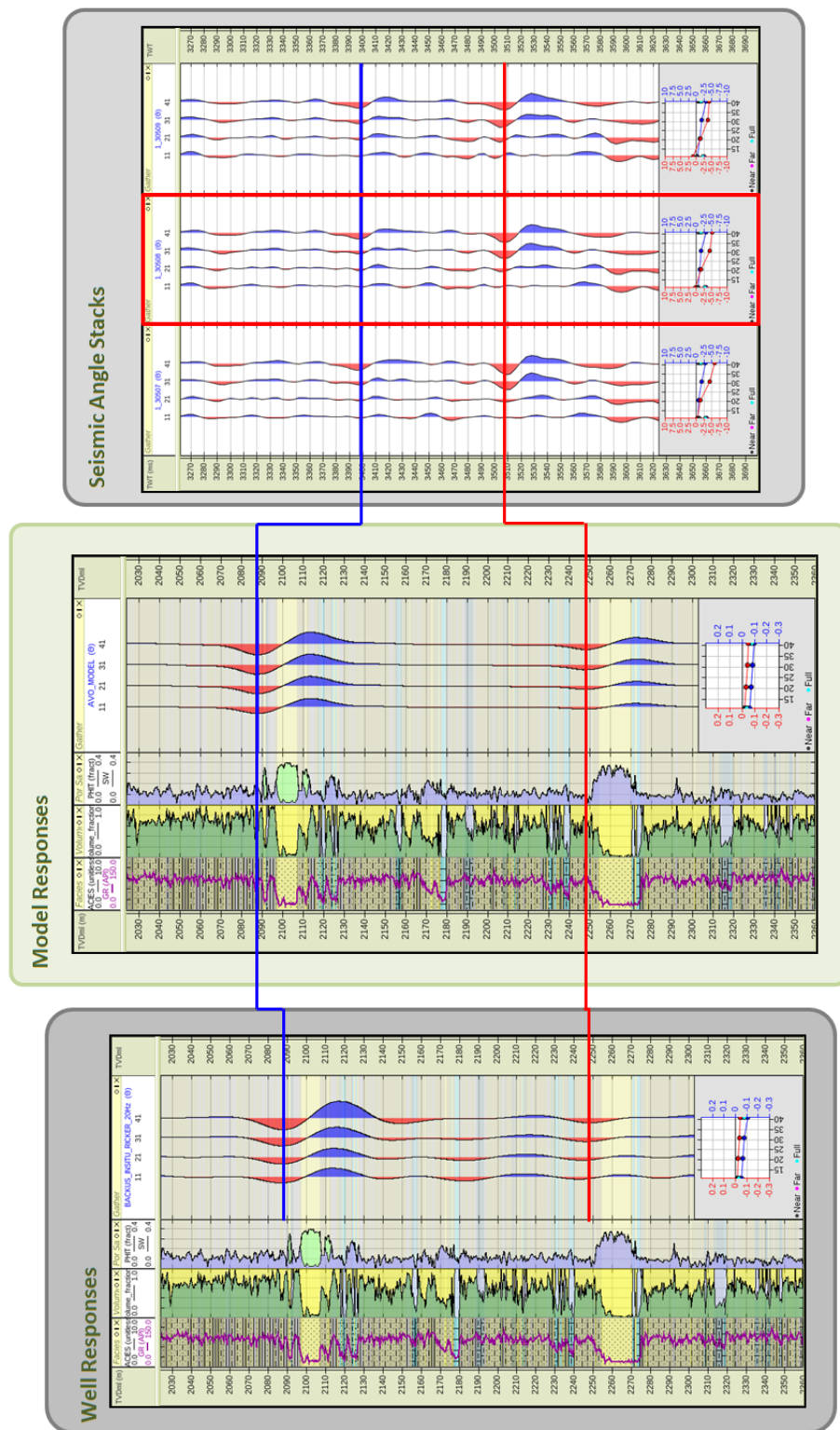
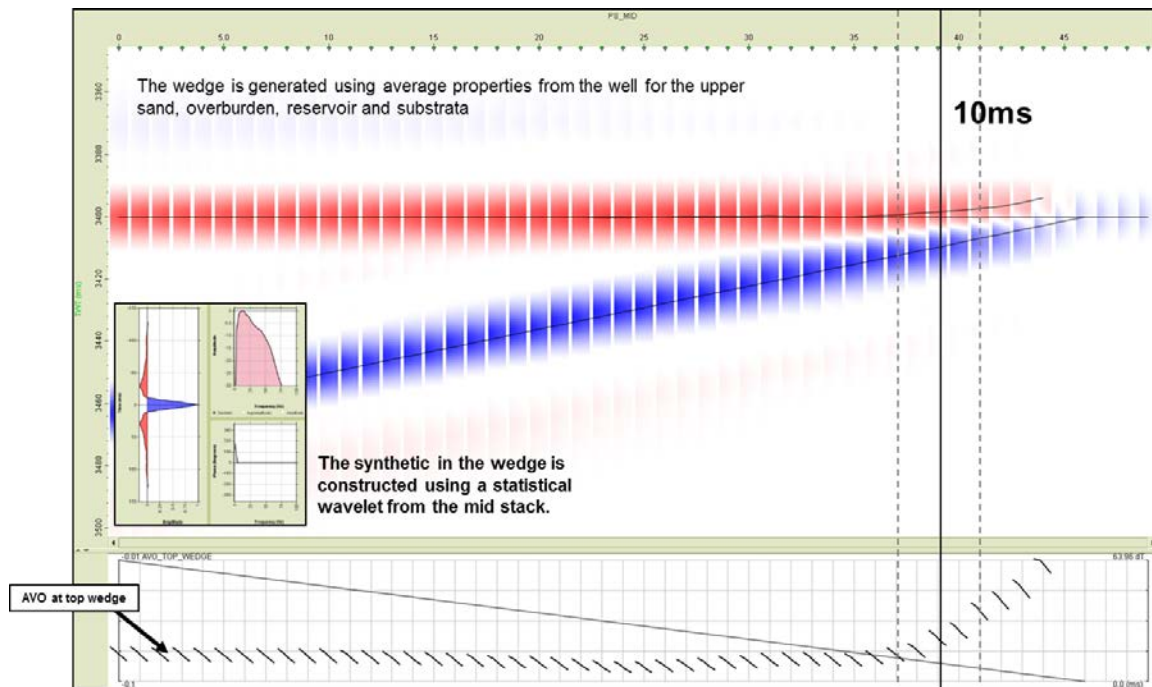


Figure 119: A comparison of well, seismic and model responses for the upper and lower sand in Mizzen O-16. The well synthetic is generated from the elastic log data (Vp, Vs and RhoB). As can be seen a good match between well and model is achieved. The seismic match is reasonable, although the near stack seismic response is weaker than the well synthetic or model in the upper sand, and the far stack brightens more in the seismic than in the well or model synthetic for the lower sand.



**The intercept becomes weaker, and the gradient steeper at tuning.
The sands at Mizzen O-16 are around 10ms thick.**

Figure 120: A tuning wedge for the upper sand in Mizzen O-16 (Mizzen sand encased in shale). At each trace in the model a synthetic AVO gather is generated, with an extraction per trace shown at the base in the attribute plot. The sands in Mizzen O-16 are approximately 10ms thick, this thickness is noted on the model.

5.4.6 Summary and Conclusions

The modelling workflow (outlined in section 1.3) has been compared to both the well response and the seismic response for the upper and lower sands in Mizzen O-16.

The goal of this section is to review the AVO responses predicted by the modelling framework for points in the subsurface where we have measured log and seismic responses.

There is a good match between the models and well response in Mizzen O-16, whilst the match between the models and seismic response shows some discrepancy most notably in the lower sand where the sand is showing a Class II_p anomaly in the angle stacks and a Class II on the models. It is important to note that the Mizzen O-16 is located approximately 700 m from the 2D line so the sand and shale properties may not be exactly the same as seen in the well.

5.5 Deploying the Model for AVO Screening

In the following sections of this chapter, the modelling framework was used to investigate three leads in the Orphan Basin / Flemish Pass. The leads are amplitude anomalies that have been identified in the 2D seismic database, the first lead is in the Tertiary section, the second in the Cretaceous section and the third in the Jurassic section. The modelling performed here serves to illustrate how the framework can be used to provide an insight into the geological properties that drive the seismic response.

The modelling framework was run for each lead based on the depth, age, expected sandstone porosity and consolidation (see Chapter 3 for details on how the expected sand porosity and consolidation is derived) and top sand AVO responses were generated for all possible sand-seal pairs from the identified facies set. The model responses which show consistent AVO responses with those observed in the seismic are extracted from the matrix of all possible model responses for each lead, and used for detailed comparison to the seismic response.

In order to ensure that the model – seismic comparison is made in the most robust manner (by including as many data points from the seismic across the lead as possible) the match will be made in terms of seismic intercept / gradient (hence referred to as I/G) extracted across the top lead interpretation. The I/G response is then computed from the modelling framework and compared to the seismic response in an I/G cross-plot.

5.5.1 Absolute Amplitude Calibration

The AVO modelling framework generates reflectivity values, and the seismic is on an arbitrary amplitude scale dictated by the processing. Therefore, an absolute scaling step is required to make the two comparable in terms of I/G responses.

Deriving an absolute scalar requires well control, as the scalar between reflectivity and amplitude must be known. For the 2D lines used in this study, well control is sparse. However, the Mizzen wells are close to a 2D line that passes through the Mizzen discovery (see Figure 121). An absolute scalar was defined based on the well reflectivity in the Mizzen wells, and the seismic amplitudes within the same TWT window along that 2D line.

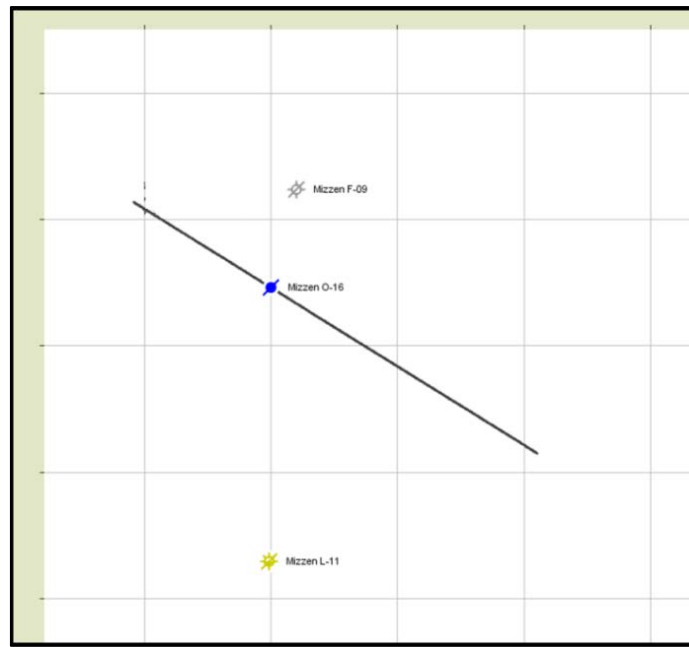


Figure 121: A 2D seismic line passes through the Mizzen discovery. The scalars for the Cretaceous and Jurassic leads are defined based on this line, and the three Mizzen wells (F-09, L-11 and O-16).

The RMS of the near stack reflectivity is taken from the three Mizzen wells over a long window (3000ms to 4200ms), and the RMS of the near stack seismic is taken over the same window along the 2D seismic line. A scalar that matches the near stack seismic trace to the near-stack reflectivity trace is then derived (shown in Table 35).

Table 35: Absolute scalar calculated for the near stack based on the seismic amplitudes and well log reflectivity at Mizzen. This scalar is used for the Cretaceous and Jurassic leads.

$$\begin{array}{c|c} \text{Average well-log} & \\ \hline \text{Angle} & \text{RMS} \\ \hline 11 & 0.033 \end{array} / \begin{array}{c|c} \text{Average seismic} & \\ \hline \text{Angle} & \text{RMS} \\ \hline 11 & 1.48 \end{array} = \begin{array}{c|c} \text{Angle} & \text{Ratio} \\ \hline 11 & 0.0223 \end{array}$$

The scalar is calculated for the near stack, and applied to all four angle stacks. It is considered that the absolute scaling across the line is reasonably uniform, and that any minor differences will not significantly detract from the matching process (in practice any differences in absolute scaling will manifest themselves as differences in the absolute value of intercept and gradient between model and seismic, but the trend of the responses will be equivalent). Differences in absolute scaling are therefore considered a known uncertainty, and the comparisons between model and seismic made with this in mind.

A smaller scalar is used for the Tertiary lead, this is further from the Mizzen area, and in rocks of younger age. The difference between seismic amplitude and reflectivity are noted to be greater

here, and the scalar is adjusted accordingly (shown in Table 36). The scalar is calculated in the same manner as that described above, but with the seismic RMS extracted over the Tertiary lead rather than from the Mizzen seismic line. It should be understood that there are greater uncertainties attached with the absolute amplitude calibration at the Tertiary lead versus the Cretaceous and Jurassic leads as no well log reflectivity for the geographic location, TWT or age of rocks is available for the Tertiary lead.

Table 36: Absolute scalar calculated for the near stack based on the seismic amplitudes at the Tertiary lead and well log reflectivity at Mizzen. This scalar is used for the Tertiary lead.

Average well-log		Average seismic		=	Angle	Ratio
Angle	RMS	Angle	RMS		11	0.014
11	0.033	11	2.3			

5.6 Cretaceous Lead

5.6.1 Introduction

The Cretaceous lead is located in the Orphan Basin, approximately 50km from the Mizzen area, and has been interpreted to be a fan system. The lead is at approximately 5500ms to 6000ms TWT in the seismic data.

The observed amplitude anomaly is predominantly seen on the ultra-far (41) angle stack. Brightening of intra-anomaly events on both the near and far stack are noted up-dip of ~6000ms TWT (see Figure 122). It is obvious that the geometry and internal layering of the fan system are important here, with many intra-anomaly events on the near and far stack, some of these events show strong brightening on the far stack. It is also clear that the ultra-far stack has a lower dominant frequency than the near stack, with fewer events on the ultra-far angle traces. There is also some evidence for an apparent flat spot at around 6000ms TWT.

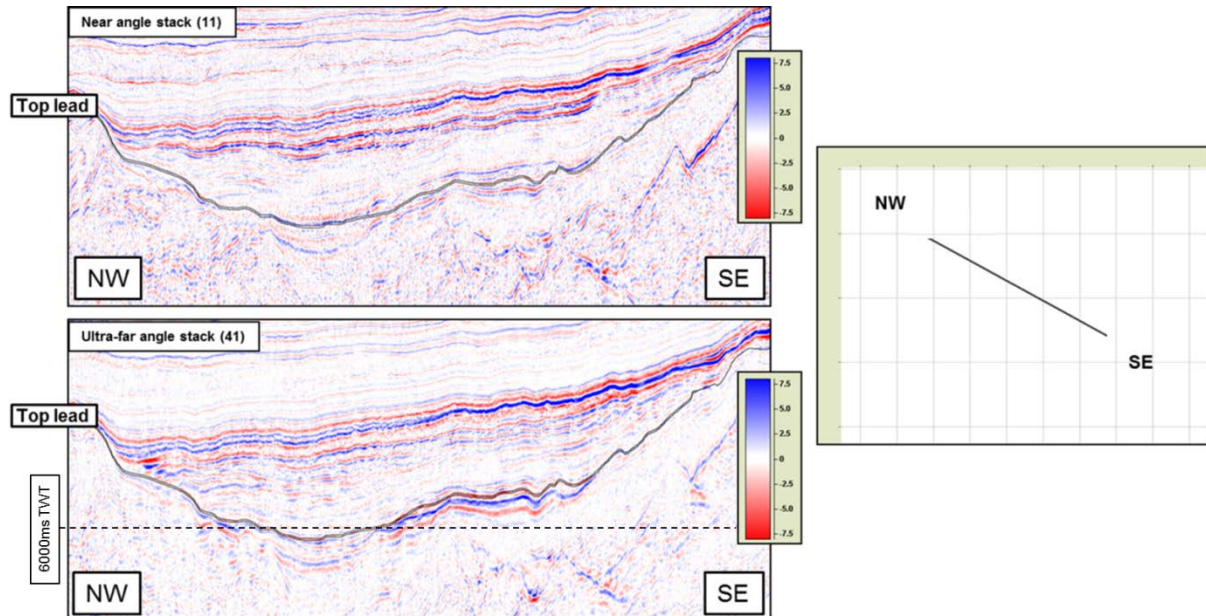


Figure 122: The Cretaceous lead is identified as bright amplitudes on the far stack (lower image above).

5.6.2 AVO Modelling

The AVO half-space models were calculated for the Cretaceous fan lead using the inputs in Table 37. The resulting Model Response Matrix (MRM) for the depth trends are shown in Figure 123. The vertical lines on the model response plots correspond to angle plot range for the near stack (11 degrees) and the ultra-far stack (41 degrees). The porosity and elastic property values (V_p , V_s , ρ_B , A_I and V_p/V_s ratio) predicted by the model for this lead are documented in the appendix for this chapter.

The MRM for the VES modelling is shown in Figure 124, where the expected porosity model from VES (highlighted in blue) is directly comparable to the expected porosity, expected cement content case in the MRM for the depth trends (model 2 in the depth trends MRM). This model is the response at the expected VES as predicted by the VES trends (that are based on the well data), so it should be a close match to the response from the depth trends and RPM, which is also calibrated to the well data.

The models in red are of interest in the VES modelling; they are the highly overpressured sand (1), the highly overpressured shale (2) and the highly overpressured shale and sand models (3). These models can be compared to the seismic as an increased overpressure case.

For the Cretaceous lead, Nalcor requested that Ikon model a “mid-high” overpressure case, to capture the elastic properties if the pore pressure was between the expected and high case. This pressure was used as part of the inputs to the AVO half-space model in Figure 125.

Variable	Value
Lead depth (TVD _m , m)	3905
Expected porosity at lead (%)	12
High case porosity at lead (%)	20
Expected VES at lead (MPa)	28.965
Low case VES at lead (MPa)	13.667
Porosity at low VES case (%)	34.7
Expected sand cement content (%)	8
VES for “Mid-High” Overpressure (MPa)	21.316

Table 37: AVO modelling inputs for the Cretaceous lead.

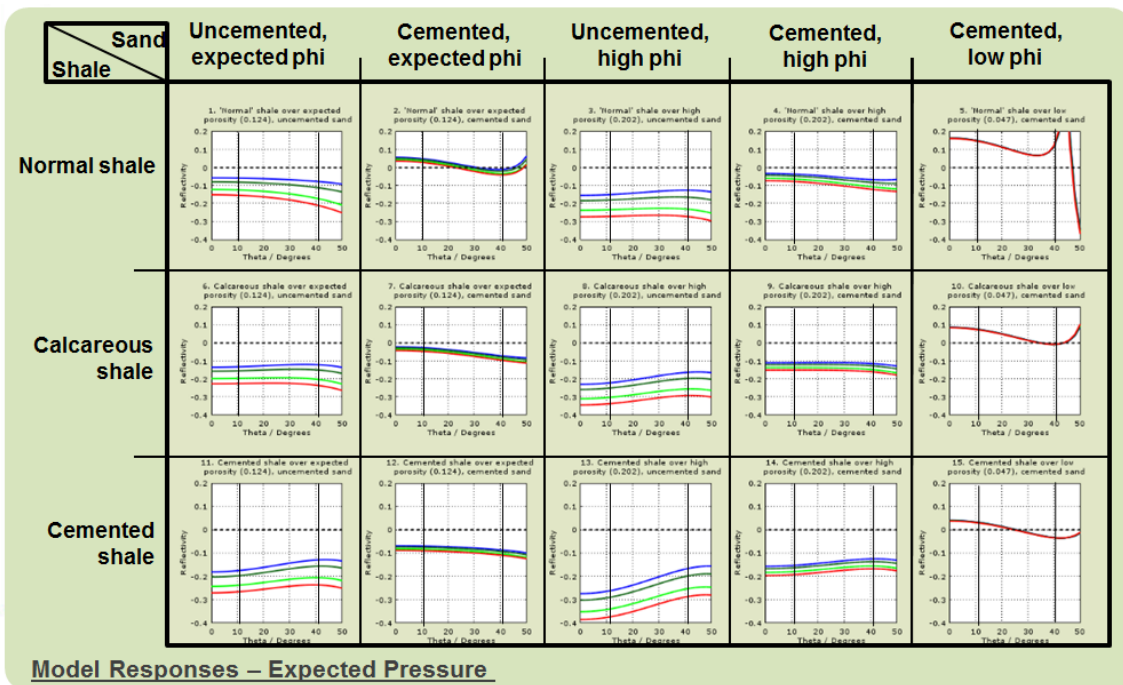


Figure 123: Model Response Matrix for the Cretaceous Lead, from depth trends.

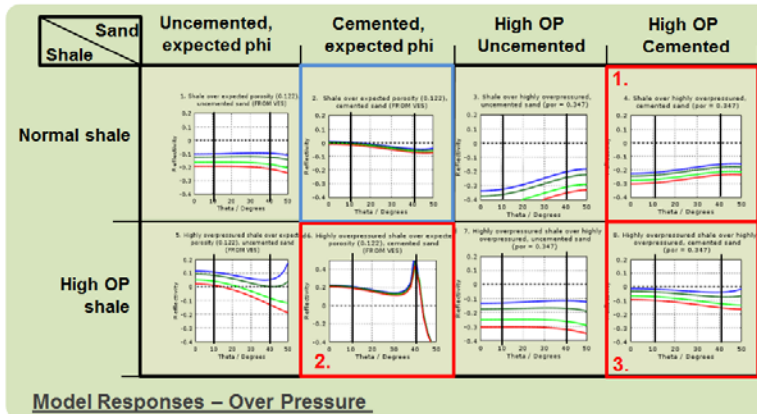


Figure 124: Model Response Matrix for the Cretaceous Lead, from VES modelling. The highlighted models are as explained in the text:
 1. = Highly overpressured sand with a normally pressured shale overburden, 2. Highly overpressured shale overburden with a normally pressured sand, 3. highly overpressured shale above a highly overpressured sand.

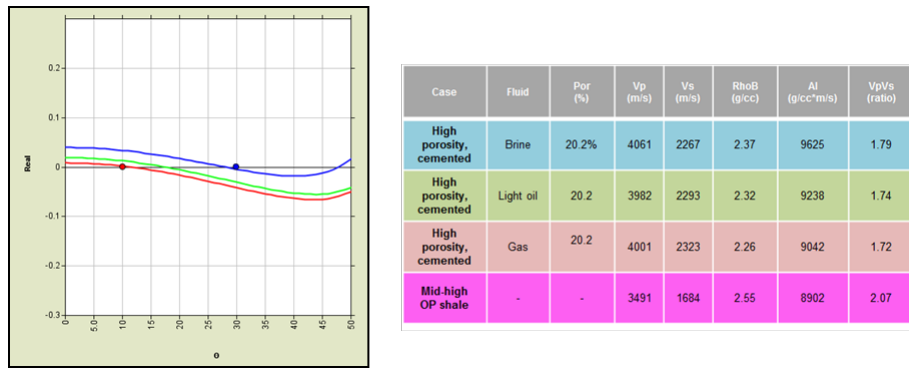


Figure 125: An alternate model has been generated for the Cretaceous lead, that has elevated overpressure in the overburden shales, but this is not as high as the high-case overpressure case from the VES modelling. The sand corresponds to the normally pressured expected cement (8%) case.

5.6.3 Cretaceous Lead Seismic Responses

The seismic response across the lead is reviewed first, with a subsequent comparison to the model outputs for this lead. The seismic-model comparison is made with reference to I/G responses. I/G values are extracted from the seismic using a linear fit to the seismic angle stack data. Therefore the first step is to review the seismic I/G response across the amplitude anomaly.

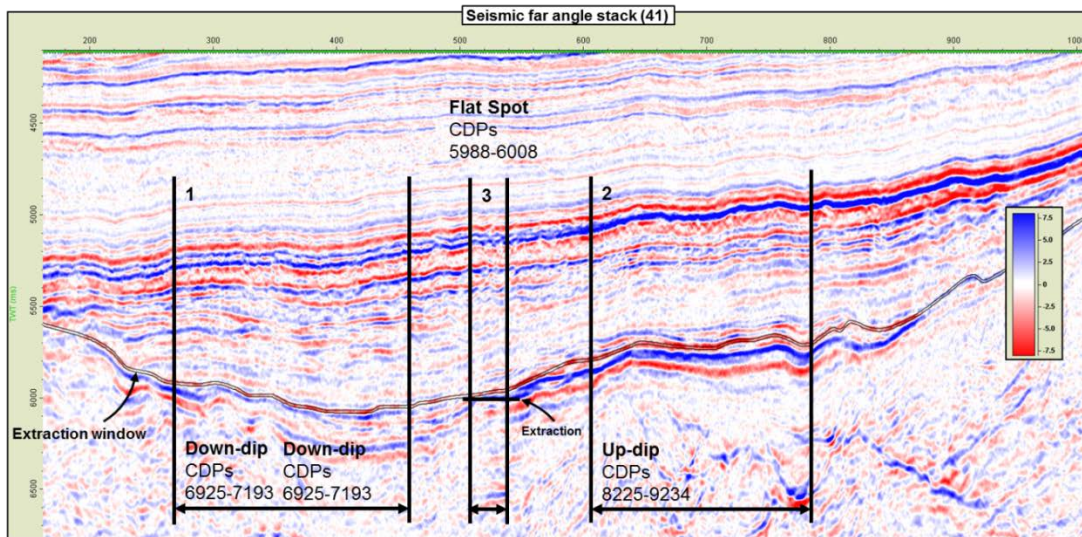


Figure 126: The seismic response at the lead is divided into three segments for the analysis, an up-dip (2), down-dip (1) and apparent flat spot (3) location.

The lead is divided into three segments based on the amplitudes seen in the seismic. Segment #1 is in the down-dip location, segment #2 in the up-dip location and segment #3 captures the apparent flat spot. The CDPs that make up each segment are indicated in Figure 126. In Figure

126 the top lead interpretation is shown, this is designed to capture the strongest apparent top responses as seen on the far stack seismic response, and follows the strongest soft events tracked from the up-dip location across the line.

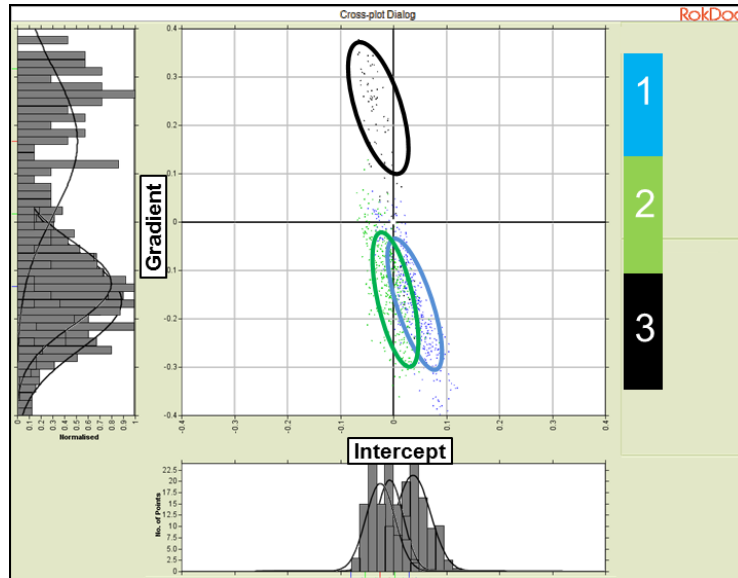


Figure 127: Seismic I/G responses across the Cretaceous lead. The blue points are extracted from the down-dip segment, the green points from the up-dip segment, and the black points from an apparent flat spot between the two.

The seismic I/G responses extracted across the top lead interpretation are shown in Figure 127. The I/G responses here are generated after the application of the absolute scalar, so should now be comparable with the model reflectivity output.

The responses in segments #1 and #2 show a distinct shift in I/G response, from class I responses in segment #1 to class II_p responses in segment #2

The responses in segment #3 show strong positive gradients and weak negative intercepts, these are class V_p AVO responses (a soft intercept associated with a positive gradient and hard events on the far angle).

5.6.4 Cretaceous Lead Model Responses

The model scenario that shows responses that are consistent with the seismic response are extracted from the MRM (shown in Figure 123 and Figure 124) and used in the comparison. Here two models are chosen, shown in Figure 128;

- The first (model #1) is the expected porosity, expected grain contact cement content sand with a normal shale overburden.

- The second (model #2) is high porosity, expected grain contact cement content sand with a slightly overpressured shale overburden.

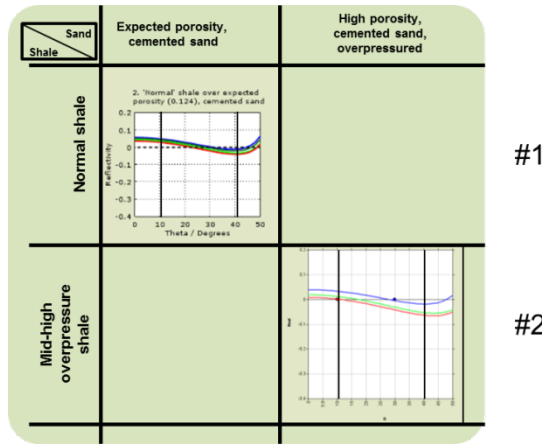


Figure 128: Top sand models selected from the model response matrix based on their match to the observed seismic responses, these models will be compared to the seismic response via the generation of I/G from the model.

Model #2 represents a slight increase in the shale overpressure mid-way between the expected case (based on the direct measurements in the study wells) and the high case (from the pressure study).

5.6.5 Cretaceous Lead Model – Seismic Comparison

The seismic I/G extracted from each of the three segments is now compared to the selected model I/G responses.

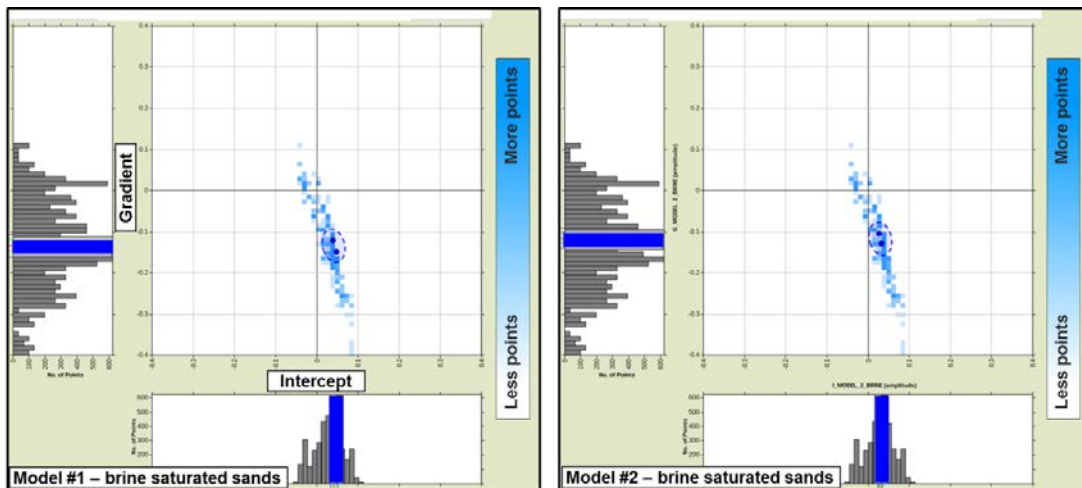


Figure 129: Seismic and model comparison for segment #1. The I/G responses for model #1 are shown on the left, and those for model #2 are shown on the right. Point densities are plotted above, these are the number of points that fall into each histogram bin, and allow visualisation of the centre of the data cloud.

Figure 129 shows the seismic I/G extractions for segment #1, in the figure these are the cloud of data for the CDPs within segment #1. The model responses for models #1 and #2 (see Figure 128) with a brine saturated sand are shown as the dots and circles in each plot. As can be seen there is a good correspondence between the brine saturated sand model I/G and the seismic I/G at this location for both models. Model #2 is seen to be marginally closer to the centre of the seismic I/G trend.

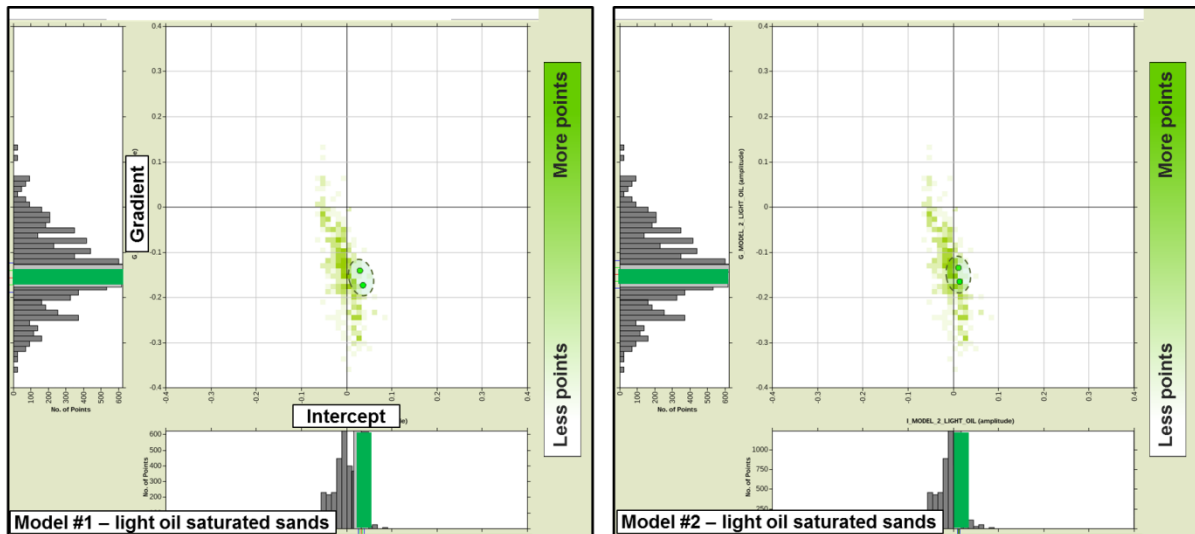


Figure 130: Seismic and model comparison for segment #2. The I/G responses for model #1 are shown on the left, and those for model #2 are shown on the right. Point densities are plotted above, these are the number of points that fall into each histogram bin, and allow visualisation of the centre of the data cloud.

Figure 130 shows the seismic data for segment #2, which is in the up-dip location where bright responses are noted on the far stack. The models are shown again as circled dots in this figure, here the sands in the model are saturated with light oil. As noted in Figure 127 there is a shift or rotation from segment #1 to segment #2, where the intercept becomes weaker, and the gradient slightly stronger in the up-dip location. The light oil model scenario (for both models #1 and #2) capture this change in I/G behaviour, although the change is not as significant as seen in the seismic (i.e. a larger shift is noted in the seismic I/G response).

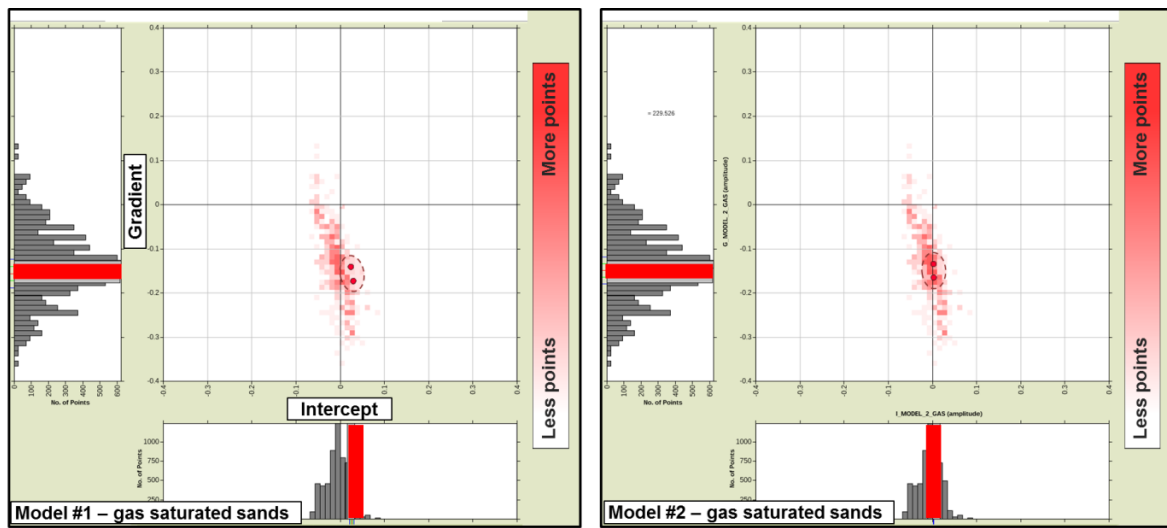


Figure 131: Seismic and model comparison for segment #2. The I/G responses for model #1 are shown on the left, and those for model #2 are shown on the right. Point densities are plotted above, these are the number of points that fall into each histogram bin, and allow visualisation of the centre of the data cloud.

Figure 131 shows the same seismic I/G points as in Figure 130, these are extracted from segment #2, in the up-dip location where there is a far stack amplitude anomaly. The models (#1 and #2) are shown here with a gas saturation in the sands. As can be seen the shift to weaker intercepts and stronger negative gradients is greater with the gas saturation, and the model response is more consistent with the seismic response. Here model #2 with a gas saturated sand shows a good match to the extracted seismic response.

Figure 132 illustrates the seismic angle stack response at segment #3, where a flat reflector is noted on the seismic data at the same depth as the far stack amplitude cut-off. Here, the angle stacks indicate a soft event on the near, and a hard event on the far with a phase reversal at mid-angles. The outputs from the modelling are specified with hydrocarbon contact and base sand geometries (i.e. the predicted elastic properties for the lead are rearranged to model non-top sand responses), and are shown in Figure 132.

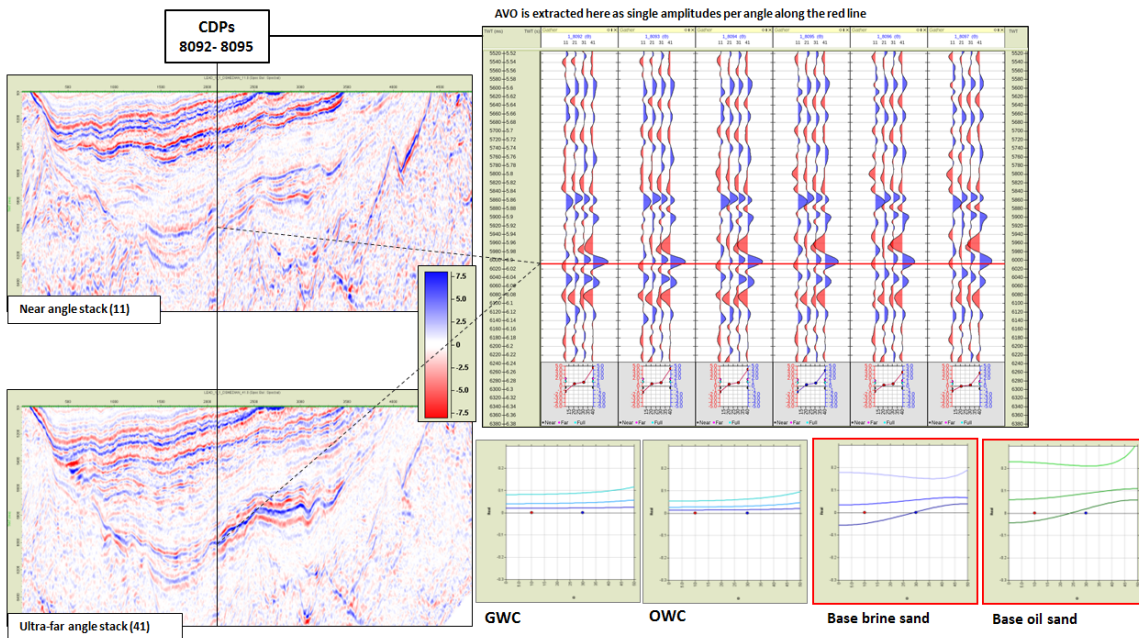


Figure 132: Alternate geometries are specified within an extra set of model scenarios that aim to investigate the apparent flat spot seen in segment #3. These are for hydrocarbon contacts and base sand responses. As can be seen the seismic shows a weak soft response on the near stack and a strong hard event on the far stack.

Figure 133 shows the seismic I/G extracted from segment #3 with the I/G response from a base sand (model #1 – left hand plot) and hydrocarbon contact (model #2 – right hand plot) scenario. The hydrocarbon contact shows hard events on all offsets, with some brightening of the hard event with increasing angle. The base sand model (right hand AVO plots in Figure 132) are considered more consistent with the angle stack seismic response in this segment.

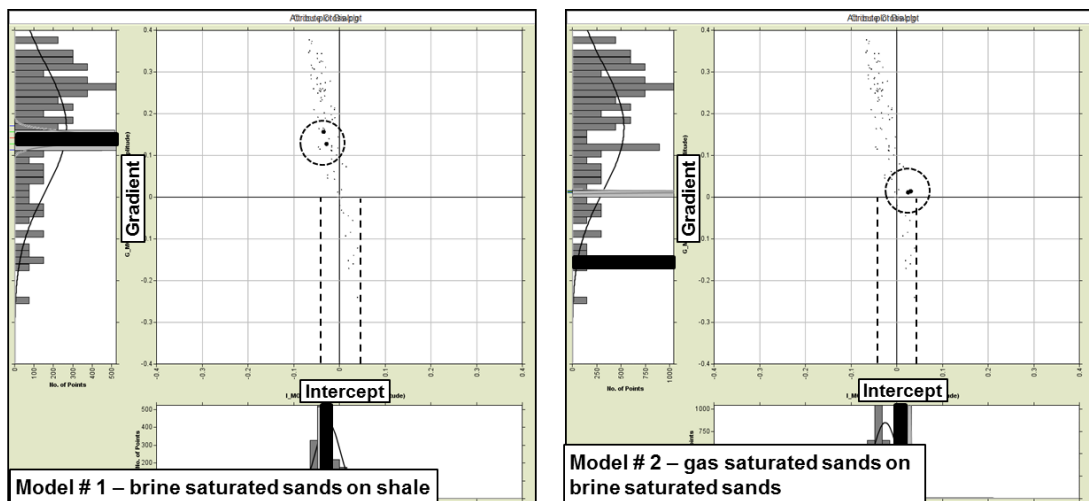


Figure 133: Seismic I/G extracted from segment #3 with the two models shown in Figure 132 also plotted as circled black dots. As the apparent flat spot is short, there are few seismic data points. Above the points themselves are plotted rather than point densities.

The interpretation of the observed flat spot as a base sand response is based on the currently available seismic data. To provide some further insight into the amplitude response here, four offset gathers for the flat spot are shown in Figure 135, these correspond to the angle stack traces shown in Figure 133. The offset gather response shows a soft event on the near and a strong hard event on the far, which is consistent with the response seen in the angle stacks. There is some ambiguity with the interpretation of the offset gather, and it is not straight forward to track the reflector from near to far offset.

Based on the currently available seismic dataset, it is concluded that the amplitudes observed in the seismic data are more consistent with a base sand response rather than a fluid contact response. However it is expected that newly acquired (3D), data could provide additional insight into the cause of the observed flat spot at this location.

It is notable that directly below the anomalous amplitude cutoff the flat reflector in question forms a doublet not seen over the western portion of the flat spot. The lower part of the doublet shows a soft response on the near offset consistent with the modelled lithologic contact however the upper portion of the doublet shows a response consistent with the modelled fluid contact. Given that the flat reflector appears to manifest itself as a lithologic contact the fluid response may be present but more subtle than as first interpreted (Figure 134). Further investigation of the Cretaceous fan complex on offsetting lines illustrate that the fan has complexities not evident on the analysed line. In particular, multiple sand lenses and faulting within the fan complex make interpretation of the amplitudes difficult. Structural conformance cannot be confirmed based on the 2D line spacing that is currently available. 3D will likely be required over this lead in order to better understand of fault relationships, amplitude conformance to structure and compartmentalization across this lead.

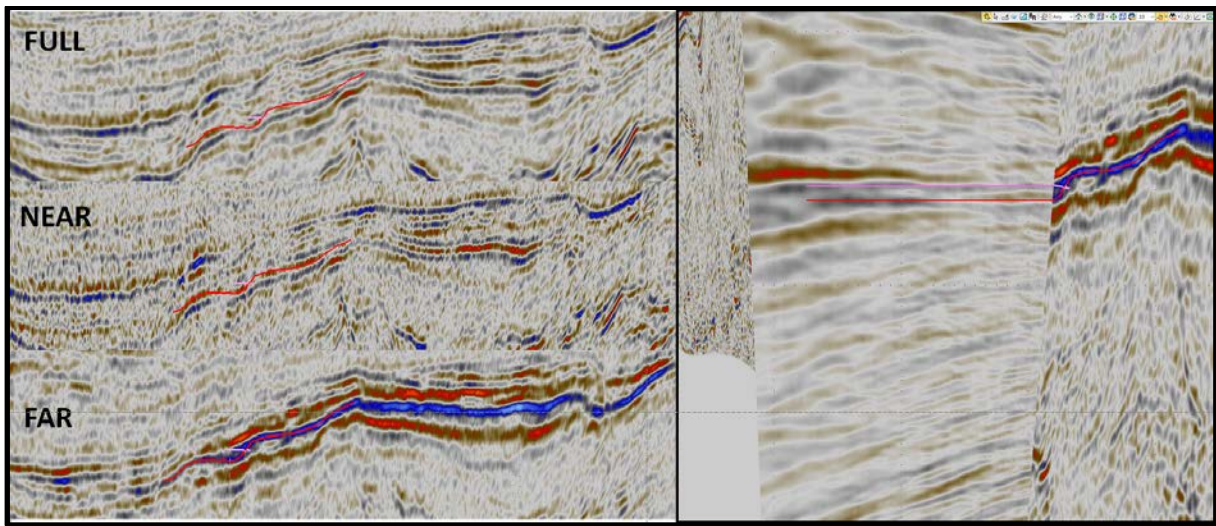


Figure 134: Images on the left show the lead full (top), near (middle) and far (lower) response, with the interpreted base of sand in shown in red. A portion of the red reflector is flat on the depth image, and was analysed as a possible fluid contact. The pink horizon is where a possible fluid contact is noted. The image to the right shows the offset gather at a trace where both horizons are mapped and illustrates the difference between the two AVO signatures.

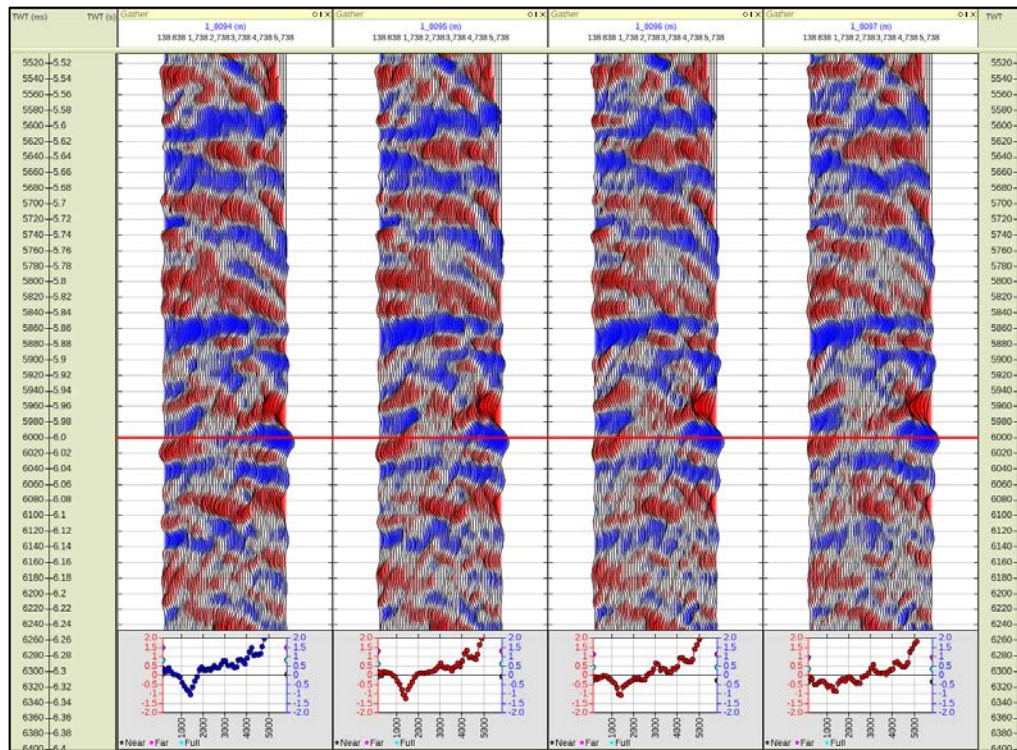


Figure 135: Offset gathers at the flat spot location. Amplitude is extracted with offset for each gather at the red line. As can be seen there is ambiguity with tracking the reflector across the offsets, but at the extraction a soft event is noted on the near with a hard on the far.

5.6.6 Summary & Conclusions

The seismic intercept / gradient response (I/G) has been extracted across the lead within three segments that cover the amplitude anomaly, with segment #1 in a down-dip location, segment #2 in an up-dip location and segment #3 at the observed flat spot.

I/G is also calculated from the modelling framework for this lead and compared to the seismic I/G response. Two model scenarios are selected from all model outputs (the previously documented 'Model Response Matrix'), as these are seen to be consistent with the seismic response at this lead.

The model – seismic comparison is then made in terms of I/G response, with the comparison being made for CDPs 'down-dip' of the amplitude anomaly, and 'up-dip' within the anomaly. A seismic-model comparison of responses at the apparent flat spot is also made. The flat spot comparison uses model responses to generate fluid contact and base sand scenarios.

Model I/G responses are seen to match the seismic response across the Cretaceous lead. The brine responses show a good match in the down-dip locations, with gas saturation in the sands showing the closest match up-dip.

A rotation in seismic I/G is noted when moving from the 'down-dip' to the 'up-dip' location, this is captured in the model by a change in the saturating fluid within the sand from brine to gas. Based on the angle and offset seismic data, the apparent flat spot is seen to be more consistent with a base sand response rather than a hydrocarbon contact however there may be a subtle fluid contact just above it to the east as noted in Figure 134.

5.7 Jurassic Lead

5.7.1 Introduction

The Jurassic lead under investigation is a rotated fault block located in the Mizzen and Baccalieu area. The top reservoir response is a weak hard on the near stack that brightens significantly on the ultra-far stack, which is a Class IIp AVO response over the up-dip section of the lead (see Figure 136). The potential of this Jurassic play-type has been proven in the area with the discovery of oil in Mizzen O-16, and this lead is at a similar depth and within 50km of the Mizzen discovery (see Figure 137). The lead is at around 3500ms TWT.

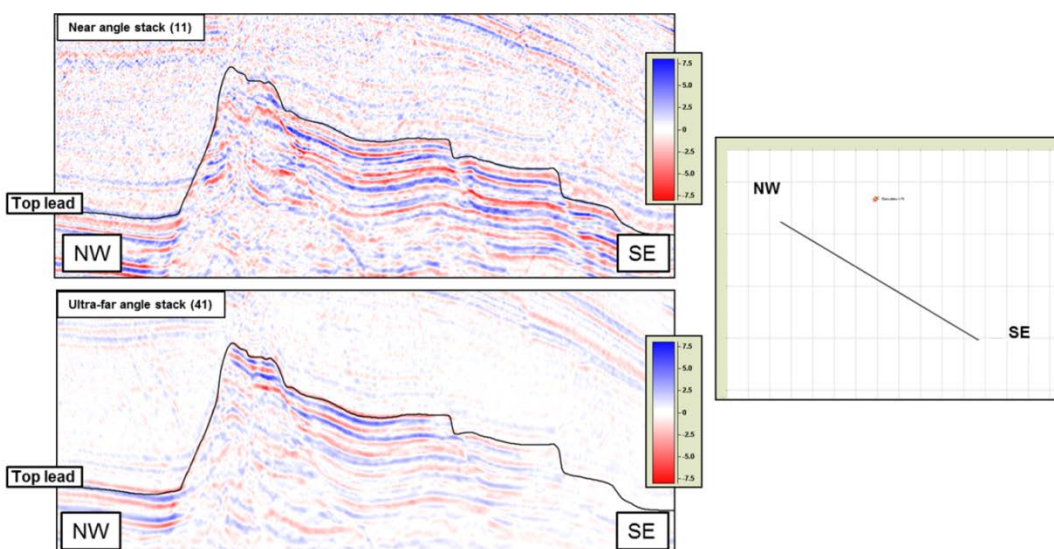


Figure 136: Angle stack responses for the Jurassic lead. A near stack weak event is associated with a far stack soft event over the structural high.

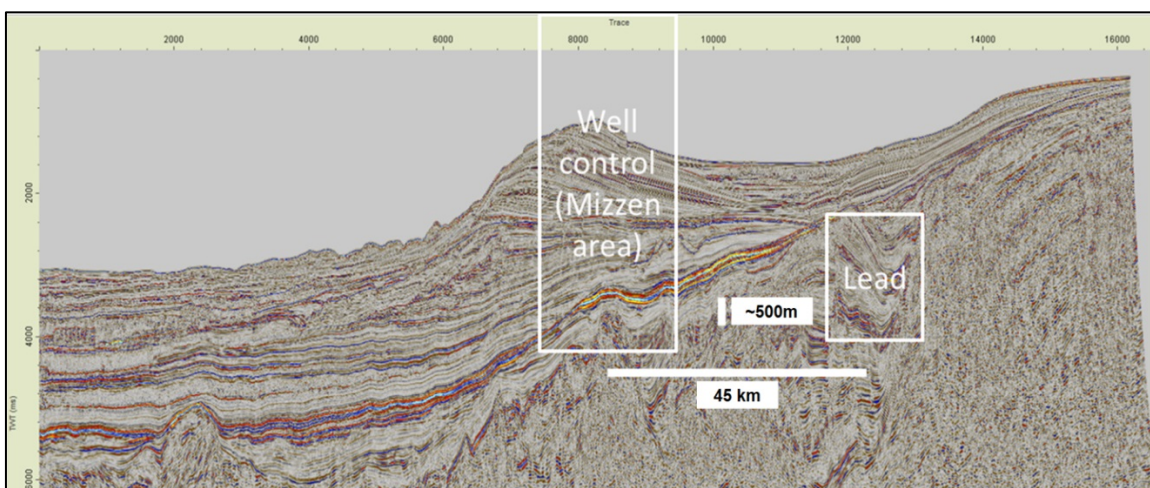


Figure 137: The Jurassic lead is close to the Mizzen discovery both geographically and in depth.

5.7.2 AVO Modelling

The AVO half-space models were calculated for the Jurassic lead using the inputs in Table 38. The resulting Model Response Matrix (MRM) for the depth trends are shown in Figure 138. The vertical lines on the model response plots correspond to angle plot range for the near stack (11 degrees) and the ultra-far stack (41 degrees). The porosity and elastic property values (V_p , V_s , ρ_B , A_I and V_p/V_s ratio) predicted by the model for this lead are documented in the appendix for this chapter.

The MRM for the VES modelling is shown in Figure 139, where the expected porosity model from VES (highlighted in blue) is directly comparable to the expected porosity, expected cement content case in the MRM for the depth trends (model 2 in the depth trends MRM). The response above is the response at the expected VES as predicted by the VES trends (that are based on the well data), so should be a close match to the response from the depth trends and RPM, which are also calibrated to the well data.

The models in red are of interest in the VES modelling; they are the highly overpressured sand (1), the highly overpressured shale (2) and the highly overpressured shale and sand models (3). These models can be compared to the seismic data as an increased overpressure case.

Variable	Value
Lead depth (TVDml, m)	2830
Expected porosity at lead (%)	19.7
High case porosity at lead (%)	27.5
Expected VES at lead (MPa)	22.885
Low case VES at lead (MPa)	13.667
Porosity at low VES case (%)	34.9
Expected sand cement content (%)	6

Table 38: Inputs for AVO modelling in the Jurassic Lead.

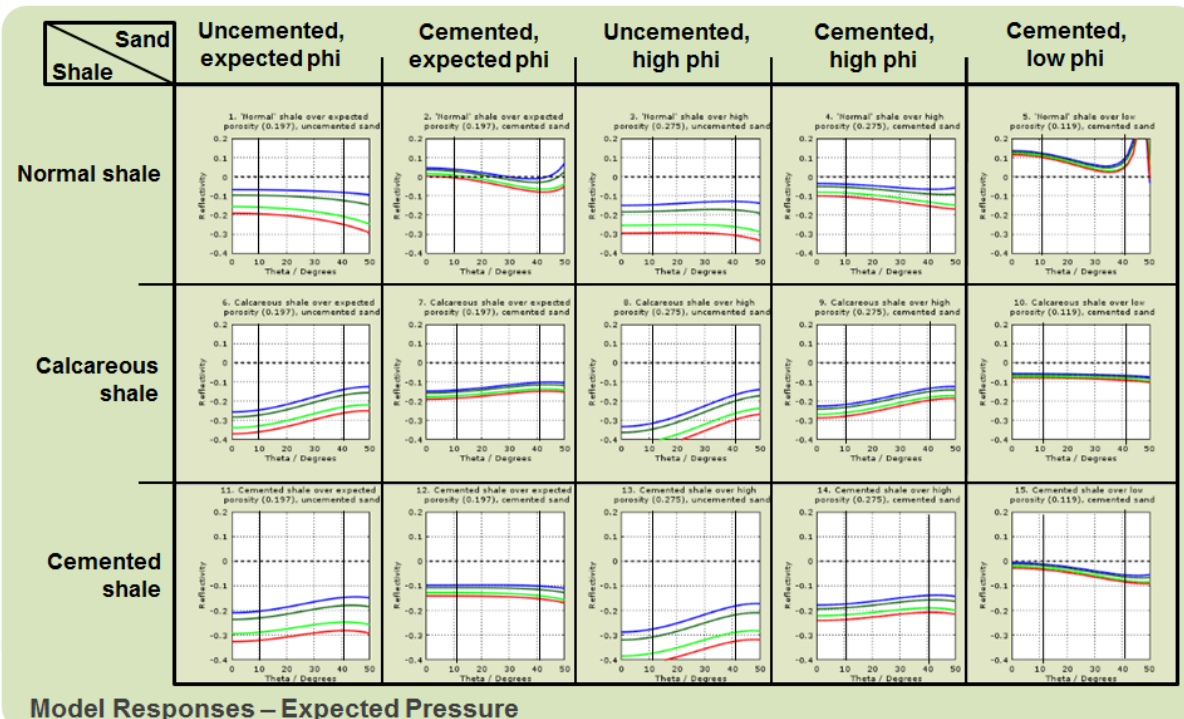


Figure 138: Model Response Matrix for the Jurassic lead, from depth trends.

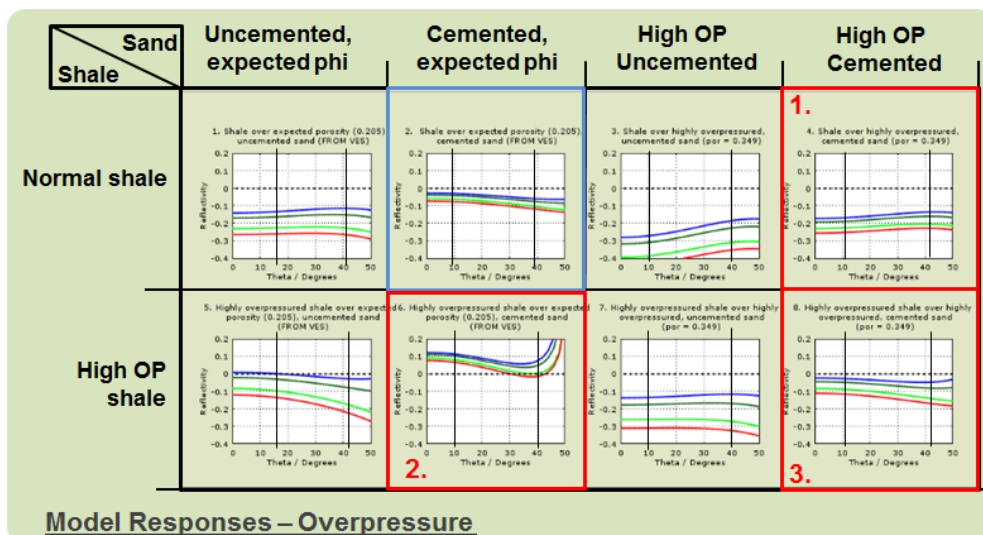


Figure 139: Model Response Matrix for the Jurassic lead, from VES modelling. The highlighted models are as explained in the text: 1. = Highly overpressured sand with a normally pressured shale overburden, 2. Highly overpressured shale overburden with a normally pressured sand, 3. highly overpressured shale above a highly overpressured sand.

5.7.3 Jurassic Lead Seismic Responses

The seismic response across the lead was reviewed and subsequently compared to the model outputs. The seismic-model comparison is made with reference to I/G responses. I/G values were generated from the seismic using a linear fit to the seismic angle stack data.

The lead is divided into 4 segments, indicated in Figure 140. These segments are defined based on the observed seismic response and structural elements of the lead. Segments #1 and #2 encompass far stack bright anomalies, segments #3 and #4 are located in a down-dip location, where the far stack is of lower amplitude.

A top lead pick was interpreted, and is shown in Figure 140, it was picked based on both the far stack and near stack amplitude responses.

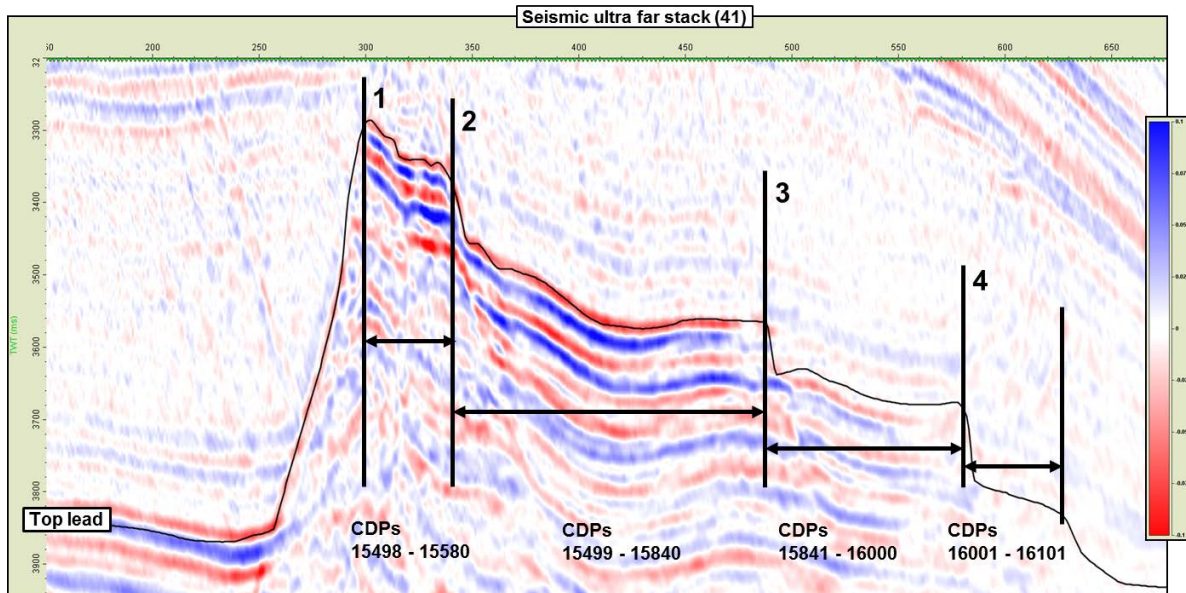


Figure 140: The Jurassic lead is divided into four segments, with segments #1, #2 and #3 in an up-dip location where far stack bright events are noted, and segment #4 in a down-dip location where far stack bright anomalies are not seen.

The seismic I/G responses extracted across the top lead interpretation are shown in Figure 141. The I/G responses here are generated after the application of the absolute scalar, so should now be comparable with the model reflectivity output.

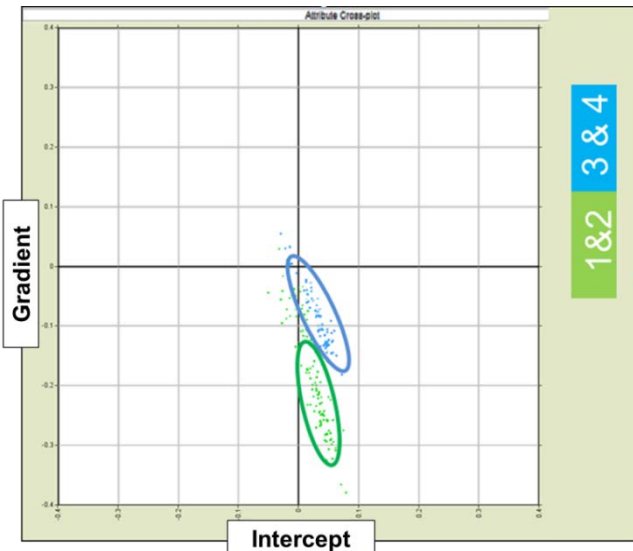


Figure 141: Seismic I/G responses for the Jurassic lead. The blue points come from segments #3 and #4, the green points come from segments #1 and #2.

The seismic responses in segments #1 and #2 show a distinct shift or rotation in I/G response versus segments #3 and #4. The seismic response shifts from a class I response, where positive intercepts are associated with weak negative gradients, to class II_p responses where the intercept responses are weaker, and the negative gradient is stronger.

5.7.4 Jurassic Lead Model Responses

The model scenario that shows responses that are consistent with the seismic response are extracted from the MRM (shown in Figure 138 and Figure 139) and used in the comparison to the seismic response. Here a single model shows responses that are consistent with the seismic, this model is the expected porosity, expected grain contact cement content sand with a normal shale overburden.

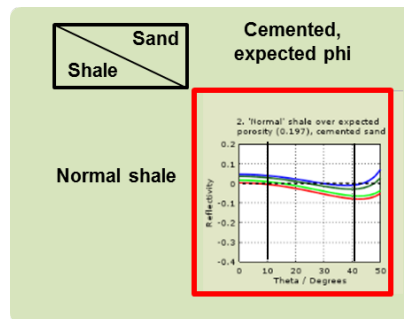


Figure 142: The expected cement, expected porosity sand with normal shale overburden is selected from the MRM, as this model scenario shows responses consistent with those observed in the seismic angle stacks.

5.7.5 Jurassic Lead Model – Seismic Comparison

The seismic I/G extracted from each of the three segments is now compared to the selected model I/G responses for the Jurassic lead.

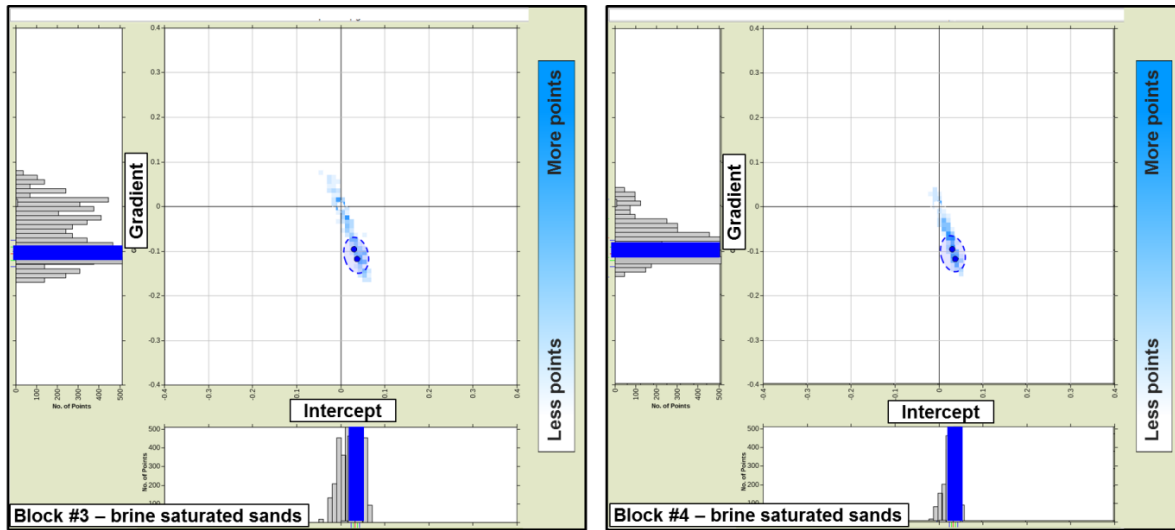


Figure 143: Seismic intercept / gradient extracted over segments #3 (left) and #4 (right). The model response for brine saturated sands with a normal shale overburden are plotted as circled blue dots. Point densities are plotted above, these are the number of points that fall into each histogram bin, and allow visualisation of the centre of the data cloud.

Figure 143 shows the seismic I/G extracted across the top lead for the down-dip segments (#3 and #4). The model responses are shown as circled dots in blue, where the sands are saturated with brine. As can be seen the model I/G responses match closely with the seismic I/G responses over this segment of the seismic.

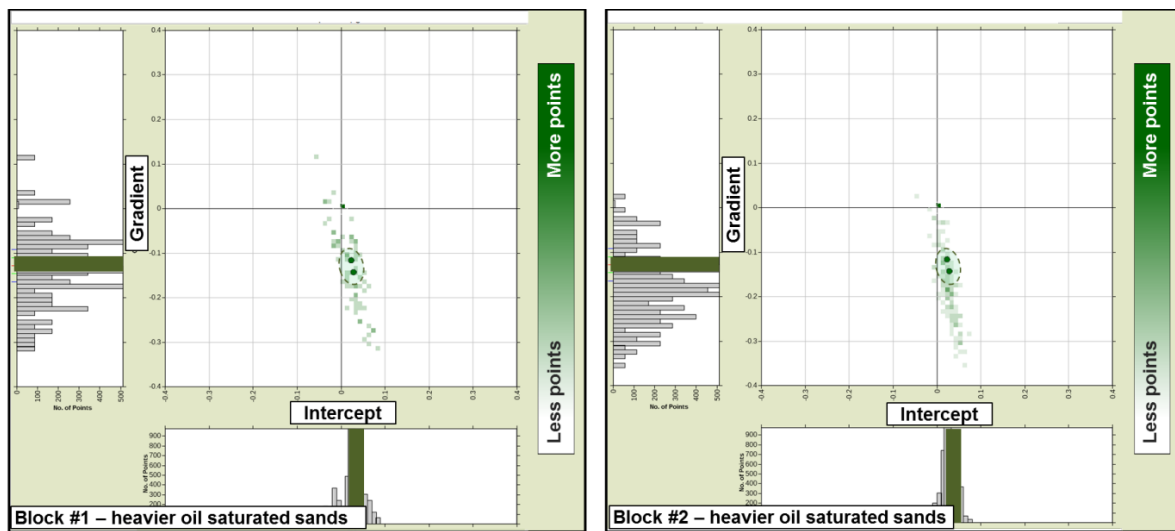


Figure 144: Seismic intercept / gradient extracted over segments #1 (left) and #2 (right). The model response for heavier oil saturated sands with a normal shale overburden are plotted as circled green dots. Point densities are plotted above, these are the number of points that fall into each histogram bin, and allow visualisation of the centre of the data cloud.

Figure 144 shows the seismic I/G responses extracted over segments #1 and #2, in these segments a distinct shift in I/G response is noted, where the intercept is weakened and the gradient slightly strengthened. The model responses are again shown as circled dots, here the saturating fluid in the sand is the normal oil. As can be seen the oil saturated sand model captures the trend of the seismic I/G response in these up-dip segments. The oil case at the lead has the same properties as the oil at the nearby Mizzen discovery.

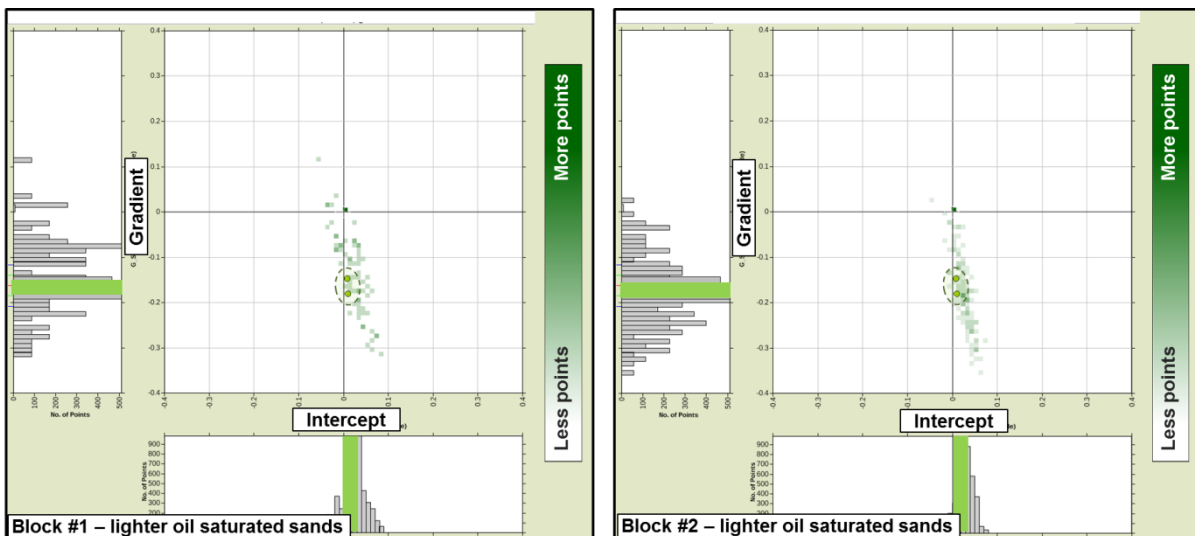


Figure 145: Seismic intercept / gradient extracted over segments #1 (left) and #2 (right). The model response for lighter oil saturated sands with a normal shale overburden are plotted as circled green dots. Point densities are plotted above, these are the number of points that fall into each histogram bin, and allow visualisation of the centre of the data cloud.

Figure 145 shows the same seismic I/G extractions (from segments #1 and #2), now the model has a lighter oil as the saturating fluids in the sands. As can be seen, the model I/G responses are further shifted, or rotated, however the shift is larger than that observed in the seismic. Introducing oil saturation to the model captures the change in I/G response observed in the seismic from segments #3 and #4 to segments #1 and #2, but the heavier oil saturation gives a closer match to the observed seismic response.

5.7.6 Jurassic Lead Model-Seismic Comparison – 2D modelling

As a further illustration of how the predictive framework can be deployed, an additional model has been defined and populated here, this is in the form of a 2D model.

The idea was to provide a further investigation of the seismic response using the modelling framework output, but also illustrate how the outputs of the modelling framework might be used. The outputs of the model shown in Figure 142 are used to construct a 2D model, the V_p , V_s and ρ_B values inferred by the model for this lead are documented in Table 39.

Table 39: Vp, Vs, RhoB values predicted for lead 4.

Facies	Vp	Vs	RhoB
Normal shale	3.172	1.461	2.57
Expected porosity, cemented sand, brine	3.838	2.105	2.33
Expected porosity, cemented sand, light oil	3.721	2.136	2.26
Expected porosity, cemented sand, heavy oil	3.793	2.115	2.31

2D interpretations are made based on the seismic response along the 2D line that crosses the lead, these are used to provide the 2D model framework which is populated with the values in Table 39. Once the framework has been built and populated with elastic properties synthetic angle stacks are generated based on the reflectivity implied by the modelling and a statistical wavelet extracted from the 2D seismic over the interval of the lead (3000ms to 4000ms), this is shown in Figure 146. The model is built using brine bearing sand properties in segments #3 and #4 and heavier oil (oil equivalent to that at Mizzen) in segments #1 and #2. The overburden is kept consistent as the normal shale facies.

Synthetic near and far stacks are generated and compared to the seismic angle stacks.

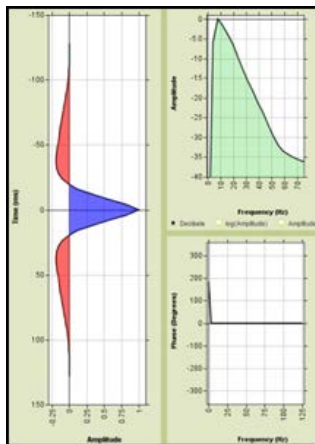


Figure 146: Statistical wavelet extracted from the 2D seismic that crosses lead 4 (line 4281). This is used to generate synthetic angle stacks across the 2D model.

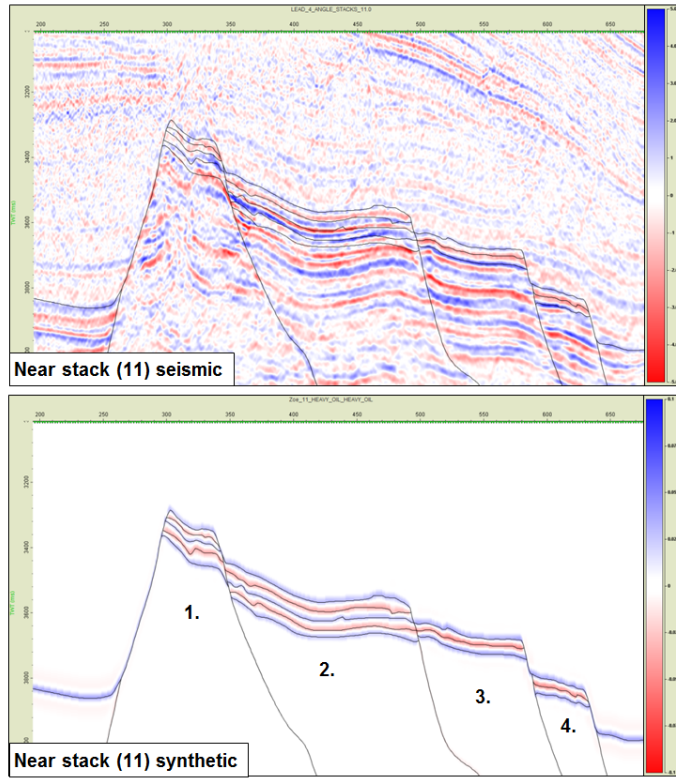


Figure 147: Synthetic near stack from the 2D model (lower image) compared to the near stack seismic (upper image).

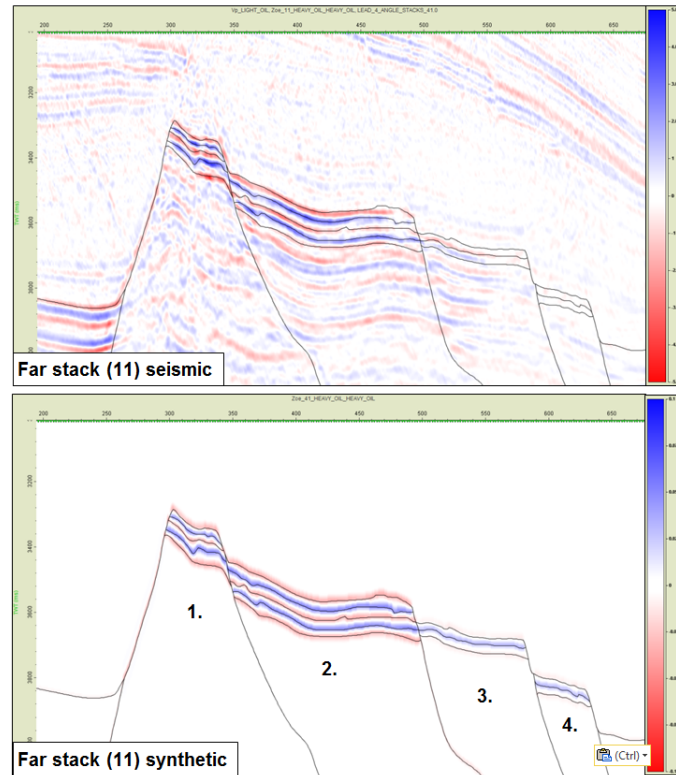


Figure 148: Synthetic far stack from the 2D model (lower image) compared to the far stack seismic (upper image).

Figure 147 and Figure 148 shows comparisons between the near stack and far stack synthetic from the 2D model and the seismic angle stacks. Qualitatively a good visual match is noted for both the near and far stack when the model is specified as being brine bearing in segments #3 and #4 and oil (heavier oil case) in segments #1 and #2. The synthetic match backs up the quantitative comparison made in terms of I/G response comparison.

5.7.7 Summary & Conclusions

A comparison has been made between the model output and the seismic angle stack response for this lead. The lead was analysed in terms of the intercept / gradient response, and via synthetics generated across a 2D model.

The amplitudes at the top of the Jurassic rotated fault block are identified predominantly as Class IIp AVO responses, these are weak hard events on the near stack, and brighter soft events on the far stack.

The modelling indicates Class IIp AVO responses with oil and gas bearing sands, when the expected porosity and cement content have ‘normal’ shale as the overburden. In this model the sands have a Class I AVO response when brine-bearing. A good match between model and seismic is observed when the sands in the model are saturated with brine in the down-dip location, and oil in the up-dip locations. The overburden is consistently specified as the normal shale facies.

Although the fluid effect is modest at this depth, there is a potential for a change in AVO class from brine to oil saturation in the sands based on this model. Down-dip to the south-east, the top structure reflector is a Class I AVO response; this turns into a Class IIp in the up-dip location.

In addition a 2D model has been generated at this depth based on the selected model scenario, and this is seen to give a good match to both the near and far seismic angle stacks for this lead.

5.8 Tertiary Lead

5.8.1 Introduction

The Tertiary lead is a turbidite observed at approximately 4600ms TWT on one of the study 2D seismic lines. The amplitude anomaly shows significant brightening in the far and ultra-far stacks. The near stack response is very dim, showing a variation between a weak hard and a weak soft. There is a subtle dimming of the near stack response in the up-dip location associated with significant ultra-far stack brightening (see Figure 149).

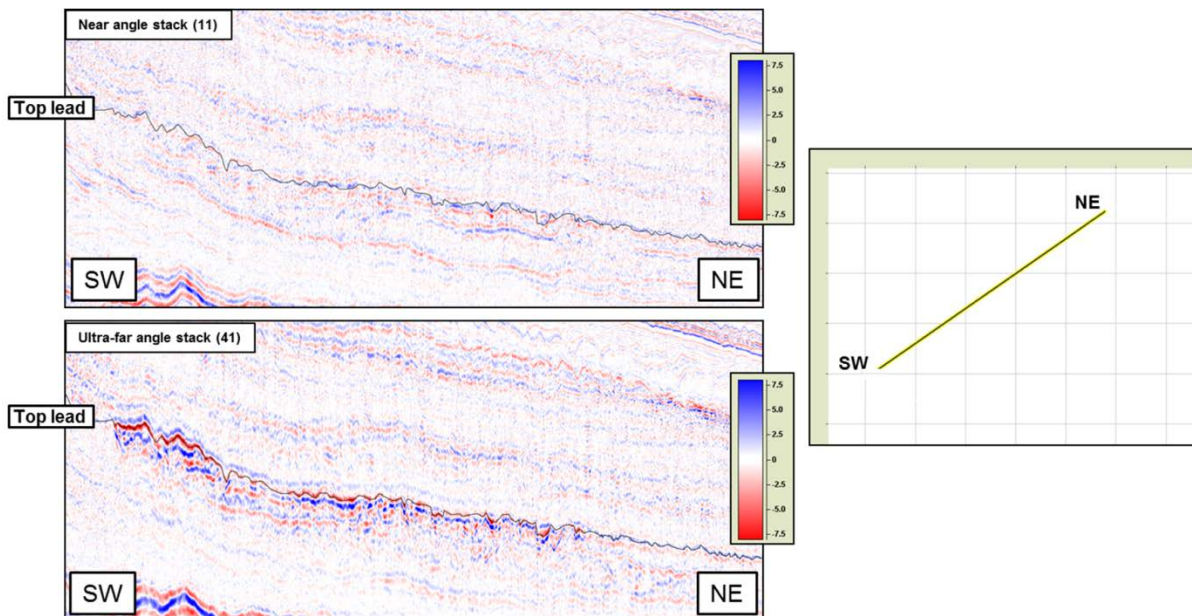


Figure 149: Angle stacks showing the Tertiary lead. Upper image: near stack, lower image: ultra-far stack.

5.8.2 AVO Modelling

The AVO half-space models were calculated for the Tertiary lead using the inputs shown in Table 40. As per Chapter 3, the modelling framework allows for a number of alternate possible overburden lithologies, different grain contact cement contents, porosities and saturating fluids in the sands, different saturations in the sands, as well as the potential for elevated pore pressure within the sands and shales. The porosity and elastic property values (V_p , V_s , ρ_B , A_I and V_p/V_s ratio) predicted by the model for this lead are documented in the appendix for this chapter.

All the modelled responses are documented in the Model Response Matrix (MRM), shown in Figure 150. The MRM displays AVO responses for reservoir-seal pairs modelled, the vertical lines on the

model AVO plots correspond to angle plot range for the near stack (11 degrees) and the ultra-far stack (41 degrees). The MRM for the VES modelling is shown in Figure 151, where the expected porosity model from VES (highlighted in blue) is directly comparable to the expected porosity, expected cement content case in the MRM for the depth trends. This is the response at the expected VES as predicted by the VES trends (that are based on the well data), so it should be a close match to the response from the depth trends and rock physics model, which is also calibrated to the well data. The models in red are of interest in the VES modelling; they are the highly overpressured sand (1), the highly overpressured shale (2) and the highly overpressured shale and sand models (3). These responses can be compared to the seismic data as an increased overpressure case.

Variable	Value
Lead depth (TVDss, m)	5200
Lead depth (TVDml, m)	3200
Water depth (m)	2000
Age	Tertiary
Expected porosity at lead (%)	16.9
High case porosity at lead (%)	24.7
Expected VES at lead (MPa)	28.965
Low case VES at lead (MPa)	13.667
Porosity at low VES case (%)	34.9%
Expected sand cement content (%)	6

Table 40: Inputs for AVO modelling in the Tertiary Lead.

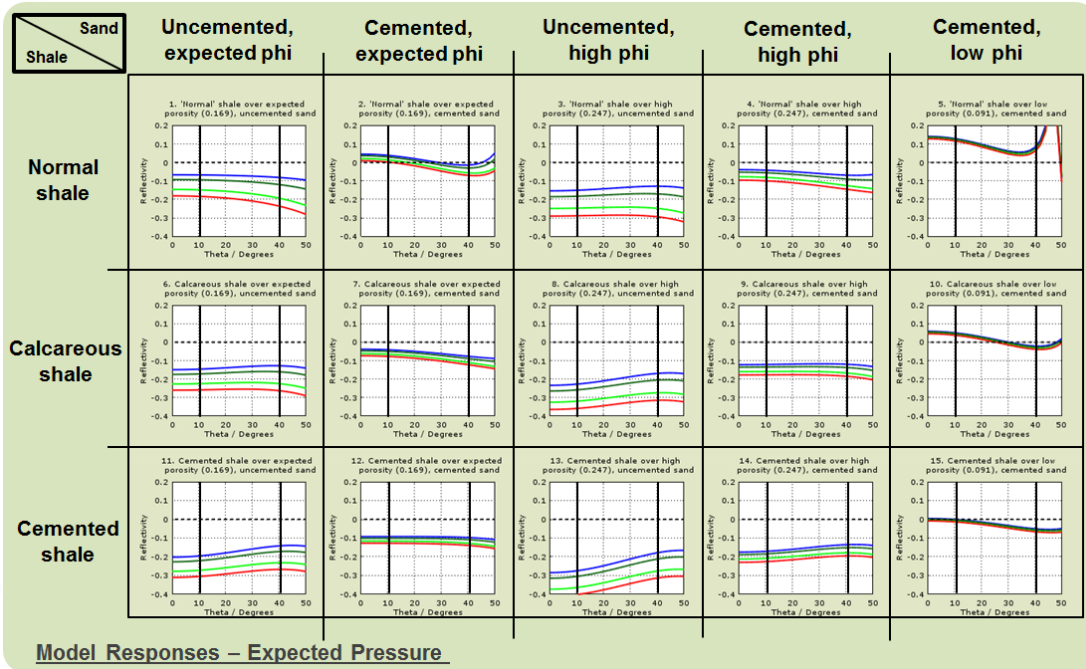


Figure 150: Model Response Matrix for the Tertiary Lead, from depth trends.

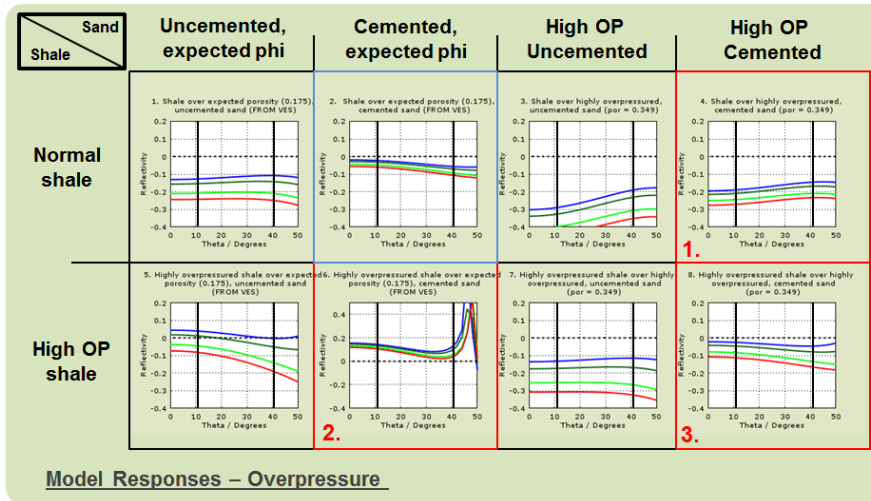


Figure 151: Model Response Matrix for the Tertiary Lead, from the VES modelling. The highlighted models are as explained in the text:
 1. Highly overpressured sand with a normally pressured shale overburden, 2. Highly overpressured shale overburden with a normally pressured sand, 3. Highly overpressured shale above a highly overpressured sand.

5.8.3 Tertiary Lead Seismic Responses

The seismic response across the lead is first reviewed, with a subsequent comparison to the model outputs for this lead. The seismic-model comparison is made with reference to I/G responses, I/G values are generated from the seismic using a linear fit to the seismic angle stack data. Therefore the first step is to review the seismic I/G response across the amplitude anomaly.

The lead is divided into five segments based on the amplitudes seen in the seismic. Segment #1 is in the up-dip location, and segment #5 is in the down-dip location. The CDPs that make up each segment are indicated in Figure 152, along with the colour assigned to each segment for reference in the analysis. In Figure 152 the top lead interpretation is shown, this follows the far stack soft event that is considered the top of the lead, and is the event at which the seismic response will be extracted.

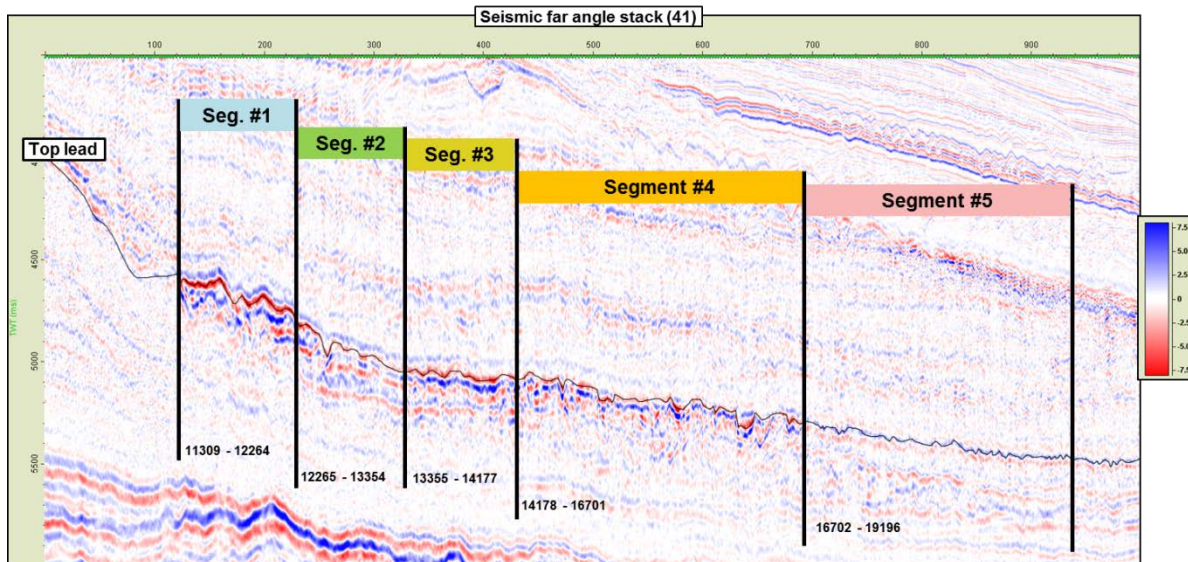


Figure 152: The lead is divided into five segments, for AVO analysis.

The seismic I/G responses extracted across the top lead interpretation are shown in Figure 153, the points are coloured in a consistent manner with Figure 152. The I/G responses here are computed from the angle stack seismic data after the application of the absolute scalar, so should now be comparable with the model reflectivity output.

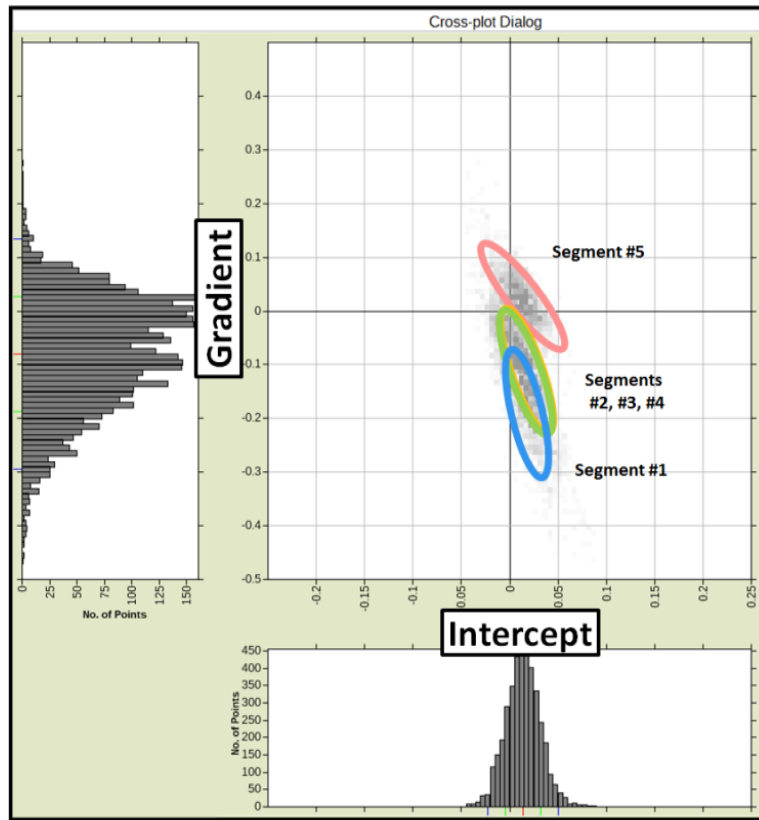


Figure 153: The seismic I/G responses extracted from the top of the lead are shown here, the segments numbers and colours used for the ellipses are the same as in Figure 152.

The responses across the Tertiary lead can be summarised as:

- **Segment #1** – weak positive intercepts, and strong negative gradients (class IIp/II AVO responses).
- **Segments #2, #3, #4** – stronger positive intercepts, weaker negative gradients. These are class IIp AVO responses.
- **Segment #5** – weak seismic I/G responses that group close to the centre of the I/G plot, the centre point of this group is a weak positive intercept, and weak positive gradient (weak class IV).

5.8.4 Tertiary Lead Model Responses

The model scenario that shows responses that are consistent with the seismic response are extracted from the MRM (shown in Figure 150 and Figure 151) and used in the comparison. Here two models are chosen, shown in Figure 154;

- The first (model #1) is the expected porosity, expected grain contact cement content sand with a normal shale overburden.
- The second (model #2) is a shale-shale interface.

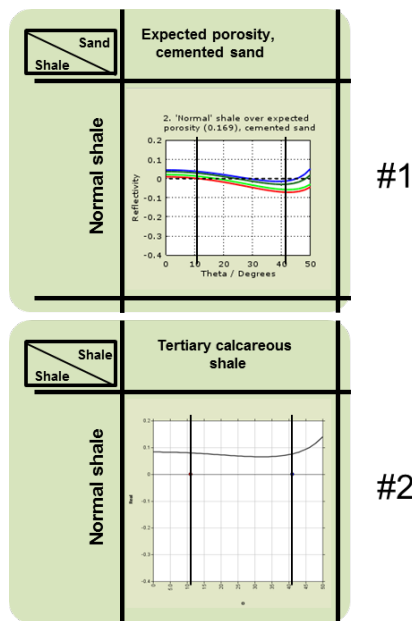


Figure 154: Model scenarios selected for comparison to the tertiary lead response.

Model #2 represents an interface where the normal shale rests on a calcareous Tertiary shale (the two shale types identified in the Tertiary), with the aim to include non-reservoir responses that could be present in the down-dip location for this lead.

5.8.5 Tertiary Lead Model – Seismic Comparison

The seismic I/G extracted from the top lead in segments 1, 2, 3 and 4 are shown in Figure 155, these are the responses noted where there is a far stack amplitude anomaly.

For each segment the I/G response is extracted across the CDPs within that segment as indicated in Figure 152, the result is a cloud of data from the seismic with I/G values also indicated in the histograms. The plots are coloured by bin count (number of data points within each axis histogram bin), stronger colours indicate more points.

The model responses are also included in these plots, these are represented by the circled dots and the coloured bars in the histograms. Here the model responses are from model #1. For segment #1 the sand is specified as being gas bearing in the model, for segments #2, #3 and #4 the sand is specified as being oil bearing.

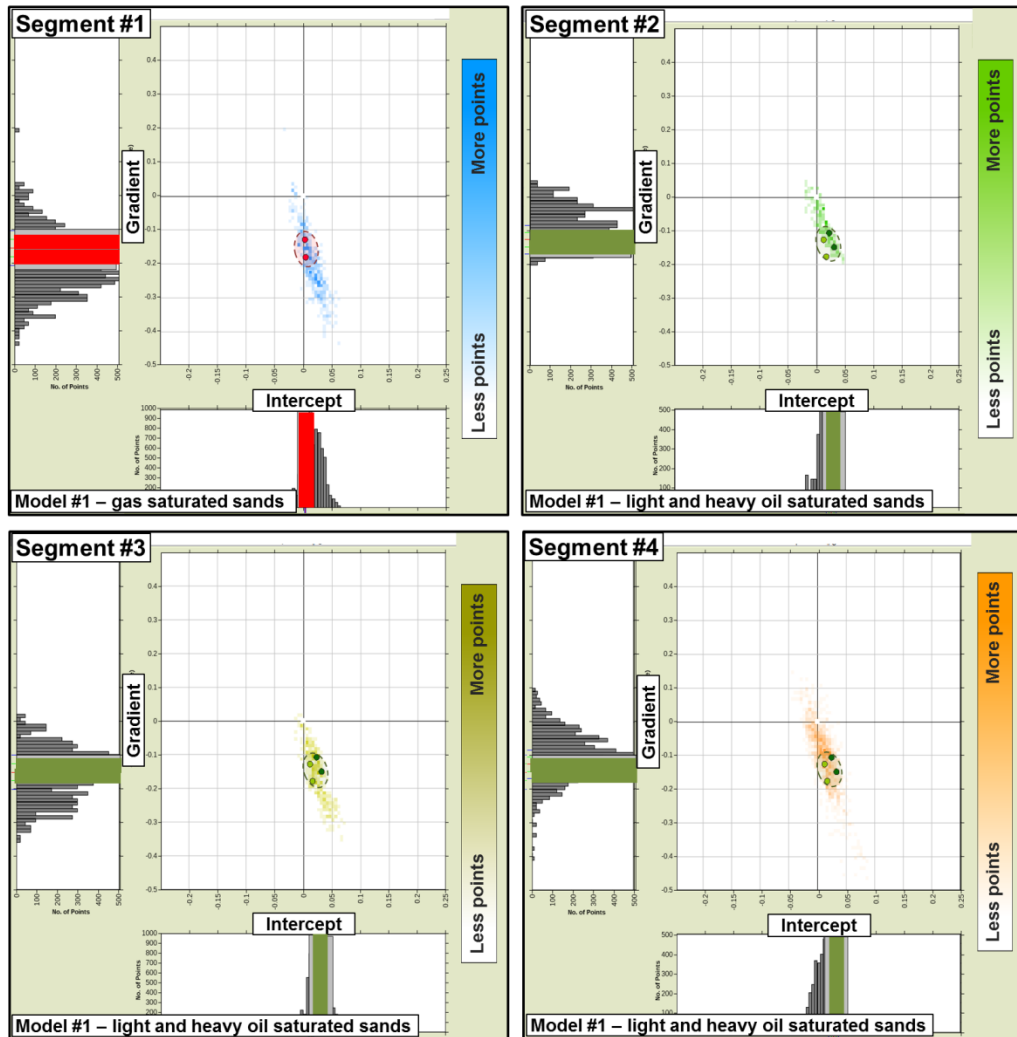


Figure 155: Here the seismic I/G is compared to the model I/G across the first four segments (#1 to #4), these locations are within the far stack amplitude anomaly. Point densities are plotted above, these are the number of points that fall into each histogram bin, and allow visualisation of the centre of the data cloud.

The seismic I/G behaviour is notably different in segment #1 versus segments #2, #3 and #4. The segment #1 behaviour shows weak intercept responses, and strong negative gradients (these are AVO class II/IIP responses), segments #2, #3 and #4 show stronger positive intercept responses, and slightly weaker negative gradient responses (these are class IIP responses). There is a shift or rotation of the top lead responses from segments #2, #3 and #4 to segment #1, this is most evident on Figure 153.

The model I/G response matches this behaviour when gas saturates the sands in segment #1 and oil saturates the sands in segments #2, #3 and #4. While the absolute amplitudes are not exactly matched the trend of the seismic I/G data is captured by the model when a gas over oil fluid scenario is specified in the sand, and the overburden shale is kept constant.

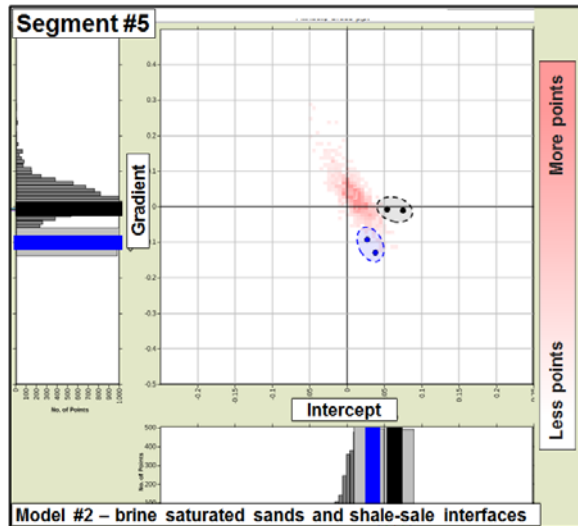


Figure 156: The seismic responses in the down-dip segment of the lead are shown above (in pink), the brine saturated sand model is shown as circled blue dots, and the shale-shale interface (normal shales on calcareous shales) shown as circled black dots. Point densities are plotted above, these are the number of points that fall into each histogram bin, and allow visualisation of the centre of the data cloud.

Segment #5 is located in the down-dip location where no far stack amplitude anomaly is seen. Here the seismic shows weak AVO, with hard intercept responses and weak positive gradients (class VI AVO), these responses are not typical of a top sand response.

Figure 156 shows a comparison between the seismic I/G response in segment #5 (points plotted in pink) and the brine bearing model #1 response (normal shale on brine sand) shown in blue, and the model #2 response (normal shale on calcareous shale) shown in black.

The brine bearing model shows a class I AVO response, where a hard event dims with increasing offset. This model sits on the edge of the cloud of seismic data.

The normal shale on calcareous shale model is included to illustrate the responses that might be expected for a non-reservoir interface. Here a flat hard event is expected, and this lies closer to the seismic I/G response.

Shale on brine sand interfaces could therefore be present in the down-dip location, but the AVO class also indicates a non-reservoir interface (e.g. shale-shale), where there are minor changes in shale properties.

5.8.5.1 Alternative Scenarios

The seismic Gradient (G) response is observed to be very large at this lead, particularly in segment #1 where the model used in the comparison in Figure 155 does not achieve a match in terms of the absolute gradient magnitude.

While there are uncertainties here associated with the absolute scalar used for this lead, other model scenarios must be considered. In particular when referring to Figure 151 it can be seen that an overpressured shale above the sand could provide the stronger gradient responses noted in the seismic. It may be the case that the Tertiary lead falls between the end-member scenarios output from the predictive framework in this work, and it should be recognised that the elastic responses per facies that are predicted by the modelling framework can be used to populate any number of model scenarios. Given that the shales have fairly low AI's for the given depth below mudline as indicated by the anomalously low interval velocities from seismic, the sands must also have low AI properties due to the lack of near stack reflectivity. In addition, the high gradient responses in the far stack whose large changes in gradient are likely due to fluid from mapping makes it plausible that the sands may not be as cemented as depth trends would suggest at this location. The AVO response of uncemented/slightly cemented sands are more sensitive to fluids so lower cemented scenarios in this case should be investigated. This is a good example of a case where care needs to be taken when predicting models based on regional trends as local geological processes may cause scenarios where perturbations from established trends are required to honour the data.

5.8.6 Recent Analysis with New 3D Seismic Data

Using recently acquired 3D seismic data which was not available at the time of this study, new models were created using detailed interval velocities from the seismic dataset. Slightly cemented rock physics models (2.5%) show a better match to the data for the oil case vs the gas case in the updip/proximal part of the fan (Segment #1). The results of the modeling for segment #1 are displayed in Intercept/Gradient space (Figure 157). A gas case under these modeled conditions would likely manifest itself as a Class III AVO response. The interval velocity volumes from 3D indicate overpressure that retards velocities in the bounding shales more than the overpressure case predicted from the VES trends. This particular lead analysis illustrates why it is important to incorporate evidence of local geological complexities into the modelled scenarios.

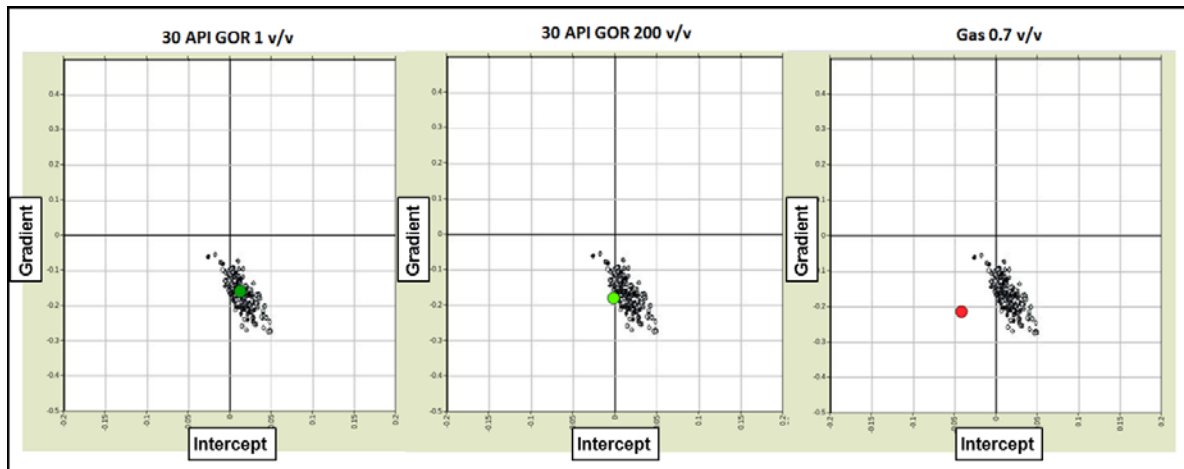


Figure 157: Segment #1 from 3D Seismic showing Intercept Gradient match to multiple fluid cases under slightly cemented conditions.

5.8.7 Summary & Conclusions

The I/G responses have been extracted across the lead within five segments that cover the amplitude anomaly from segment #1 in an up-dip location to segment #5 in a down-dip location outside of the amplitude anomaly. From the matrix of all modelled responses two models have been selected that show consistent AVO trends with the seismic. These models are the expected porosity, expected grain contact cement model with normal shale overburden, and a normal shale – calcareous shale non-reservoir scenario.

The seismic I/G response shows a systematic change across the lead, with a change from weak AVO responses in the down-dip location to increasingly strong class II_{lp} and class II in the up-dip location. The absolute amplitude of these responses varies, with a drop in terms of absolute amplitude noted in segment #2 versus segments #1 and #3, however the trend of the seismic I/G response shows a systematic shift from segment #5 to segments #4, #3 and #2 to segment #1.

The derived modelling workflow suggests that a gas over oil interpretation is a plausible outcome using regional depth trends for porosity, and grain contact cement content with a normal shale as a bounding lithology (segments #1, #2, #3, #4) as it shows a fairly good match between seismic and model I/G in these locations. However, once evidence of local variability in the form of interval velocities, local cementation information, 3D seismic interpretations, and basin modelling are incorporated into the workflow, updated models that fit the seismic and better reflect the local geologic conditions suggest a preferred interpretation of oil over brine as references in Section 5.8.6 Recent Analysis with New 3D Seismic Data.

The seismic responses in the down dip location (segment #5) are not typical of a top sand response, here weak responses are noted, with some weak class VI AVO responses (positive intercept and positive gradient). The best match between the model and seismic I/G response is noted for the shale-shale interface. The down-dip location is probably therefore a non-reservoir interface, and could be the result of changes in shale properties.

5.9 Summary & Conclusions

The defined modelling framework has been used to investigate three leads in the study area. The goal of this analysis is to demonstrate how the predictive modelling framework can be deployed to model AVO response, and to gain an insight into the geological properties that may be driving the observed amplitudes at these three leads.

The outputs from the modelling have been compared to the seismic response in terms of intercept / gradient. The modelling is run for each lead by specifying the burial depth, expected porosity (high, mid and low case), expected grain contact cement content and saturating fluid in the sands, overburden shale lithology and stress.

In this analysis the models are specified as single interface models, where a overburden and reservoir facies is specified. Top sand AVO curves are generated for each possible scenario

It has been shown that the modelling framework produces responses that are consistent with the seismic at these leads, and the models have been used to make interpretations as to the geological properties driving the seismic response.

The work on the leads is designed to provide a workflow which can be used to screen potential leads and prospects, with the aim being to high-grade the most promising for further analysis.

Appendix – model elastic property predictions

Fluid	Lithology	Vp (km/s)	Vs (km/s)	RhoB (g/cc)	Por (fract.)	AI (g/cm*km/s)	Vp/Vs (ratio)
Brine	Expected Porosity, Uncemented	3.207	1.649	2.38	0.17	7.62	1.95
Brine	Expected Porosity, Cemented	4.012	2.232	2.38	0.17	9.53	1.8
Brine	High Porosity, Uncemented	2.838	1.381	2.25	0.25	6.39	2.05
Brine	High Porosity, Cemented	3.576	1.916	2.25	0.25	8.06	1.87
Brine	Low Porosity, Cemented	4.63	2.679	2.5	0.09	11.58	1.73
Heavy Oil	Expected Porosity, Uncemented	3.068	1.655	2.36	0.17	7.24	1.85
Heavy Oil	Expected Porosity, Cemented	3.974	2.24	2.36	0.17	9.37	1.77
Heavy Oil	High Porosity, Uncemented	2.689	1.389	2.23	0.25	5.99	1.94
Heavy Oil	High Porosity, Cemented	3.521	1.927	2.23	0.25	7.84	1.83
Heavy Oil	Low Porosity, Cemented	4.62	2.684	2.49	0.09	11.51	1.72
Light Oil	Expected Porosity, Uncemented	2.797	1.668	2.32	0.17	6.49	1.68
Light Oil	Expected Porosity, Cemented	3.917	2.258	2.32	0.17	9.09	1.73
Light Oil	High Porosity, Uncemented	2.412	1.406	2.17	0.25	5.24	1.72
Light Oil	High Porosity, Cemented	3.436	1.951	2.17	0.25	7.46	1.76
Light Oil	Low Porosity, Cemented	4.608	2.695	2.47	0.09	11.38	1.71
Gas	Expected Porosity, Uncemented	2.671	1.689	2.26	0.17	6.04	1.58
Gas	Expected Porosity, Cemented	3.924	2.287	2.26	0.17	8.88	1.72
Gas	High Porosity, Uncemented	2.296	1.435	2.09	0.25	4.79	1.6
Gas	High Porosity, Cemented	3.444	1.99	2.09	0.25	7.19	1.73
Gas	Low Porosity, Cemented	4.623	2.713	2.44	0.09	11.28	1.7
-	"Normal" Shale	3.344	1.573	2.6	-	8.71	2.13
-	Tertiary/Cret. Calc. Shale	3.905	1.907	2.63	-	10.29	2.05
-	Jurassic Cemented Shale	4.225	2.147	2.72	-	11.48	1.97
Brine	Expected Porosity, Uncemented	3.507	1.866	2.45	0.12	8.58	1.88
Brine	Expected Porosity, Cemented	4.404	2.515	2.45	0.12	10.78	1.75
Brine	High Porosity, Uncemented	3.035	1.524	2.32	0.2	7.05	1.99
Brine	High Porosity, Cemented	3.879	2.135	2.32	0.2	9.02	1.82
Brine	Low Porosity, Cemented	5.216	3.103	2.57	0.05	13.41	1.68
Heavy Oil	Expected Porosity, Uncemented	3.372	1.87	2.43	0.12	8.21	1.8
Heavy Oil	Expected Porosity, Cemented	4.383	2.522	2.43	0.12	10.67	1.74
Heavy Oil	High Porosity, Uncemented	2.882	1.53	2.3	0.2	6.64	1.88
Heavy Oil	High Porosity, Cemented	3.835	2.145	2.3	0.2	8.84	1.79
Heavy Oil	Low Porosity, Cemented	5.22	3.106	2.57	0.05	13.4	1.68
Light Oil	Expected Porosity, Uncemented	3.131	1.881	2.41	0.12	7.54	1.66
Light Oil	Expected Porosity, Cemented	4.361	2.536	2.41	0.12	10.5	1.72
Light Oil	High Porosity, Uncemented	2.627	1.545	2.26	0.2	5.94	1.7
Light Oil	High Porosity, Cemented	3.78	2.165	2.26	0.2	8.55	1.75
Light Oil	Low Porosity, Cemented	5.231	3.112	2.56	0.05	13.38	1.68
Gas	Expected Porosity, Uncemented	3.003	1.898	2.37	0.12	7.11	1.58
Gas	Expected Porosity, Cemented	4.376	2.558	2.37	0.12	10.35	1.71
Gas	High Porosity, Uncemented	2.506	1.569	2.19	0.2	5.49	1.6
Gas	High Porosity, Cemented	3.793	2.199	2.19	0.2	8.32	1.73
Gas	Low Porosity, Cemented	5.247	3.122	2.54	0.05	13.33	1.68
-	"Normal" Shale	3.633	1.761	2.65	-	9.62	2.06
-	Tertiary/Cret. Calc. Shale	4.219	2.103	2.67	-	11.26	2.01
-	Jurassic Cemented Shale	4.525	2.342	2.73	-	12.37	1.93
Brine	Expected Porosity, Uncemented	3.055	1.538	2.33	0.2	7.12	1.99
Brine	Expected Porosity, Cemented	3.838	2.105	2.33	0.2	8.95	1.82
Brine	High Porosity, Uncemented	2.73	1.303	2.21	0.28	6.03	2.1
Brine	High Porosity, Cemented	3.441	1.818	2.21	0.28	7.6	1.89
Brine	Low Porosity, Cemented	4.374	2.494	2.46	0.12	10.74	1.75
Heavy Oil	Expected Porosity, Uncemented	2.912	1.546	2.31	0.2	6.72	1.88
Heavy Oil	Expected Porosity, Cemented	3.793	2.115	2.31	0.2	8.76	1.79
Heavy Oil	High Porosity, Uncemented	2.58	1.312	2.18	0.28	5.62	1.97
Heavy Oil	High Porosity, Cemented	3.382	1.831	2.18	0.28	7.36	1.85
Heavy Oil	Low Porosity, Cemented	4.353	2.5	2.44	0.12	10.63	1.74
Light Oil	Expected Porosity, Uncemented	2.625	1.561	2.26	0.2	5.94	1.68
Light Oil	Expected Porosity, Cemented	3.721	2.136	2.26	0.2	8.42	1.74
Light Oil	High Porosity, Uncemented	2.289	1.332	2.11	0.28	4.84	1.72
Light Oil	High Porosity, Cemented	3.285	1.858	2.11	0.28	6.94	1.77
Light Oil	Low Porosity, Cemented	4.32	2.515	2.41	0.12	10.43	1.72
Gas	Expected Porosity, Uncemented	2.524	1.586	2.19	0.2	5.54	1.59
Gas	Expected Porosity, Cemented	3.737	2.17	2.19	0.2	8.2	1.72
Gas	High Porosity, Uncemented	2.198	1.364	2.02	0.28	4.43	1.61
Gas	High Porosity, Cemented	3.306	1.902	2.02	0.28	6.66	1.74
Gas	Low Porosity, Cemented	4.335	2.537	2.37	0.12	10.28	1.71
-	"Normal" Shale	3.172	1.461	2.57	-	8.15	2.17
-	Tertiary/Cret. Calc. Shale	3.712	1.785	2.61	-	9.67	2.08
-	Jurassic Calcareous Shale	4.485	2.387	2.68	-	12.03	1.88
-	Jurassic Cemented Shale	4.033	2.022	2.7	-	10.88	1.99

6 Glossary of Terms

Acoustic impedance (AI)

$$AI = V_p * \rho$$

The interval property whose change determines reflection coefficients at normal incidence. It is calculated as the seismic P-wave velocity multiplied by density. Because reflection coefficients change with angle, the term elastic impedance is sometimes used when referring to non-normal incidence situations.

Aki Richards (PP) approximation

A linearization of the full Zoeppritz equations, accurate for small contrasts in the interval properties across the interface.

$$R_{pp}(\theta) = A + B \sin^2 \theta + C \sin^2 \theta \tan^2 \theta$$

$$A = \frac{1}{2} \left(\frac{\Delta V_p}{V_p} + \frac{\Delta \rho}{\rho} \right) \quad B = \frac{1}{2} \frac{\Delta V_p}{V_p} - 2 \left(\frac{V_s}{V_p} \right)^2 \left(\frac{\Delta \rho}{\rho} + \frac{2 \Delta V_s}{V_s} \right) \quad C = \frac{1}{2} \frac{\Delta V_p}{V_p}$$

Where:

$R_{pp}(\Theta)$ = P-wave reflection coefficient at given incidence angle (Θ)

V_p = Average P-wave velocity (average of V_{p_1} and V_{p_2})

V_s = Average S-wave velocity (average of V_{s_1} and V_{s_2})

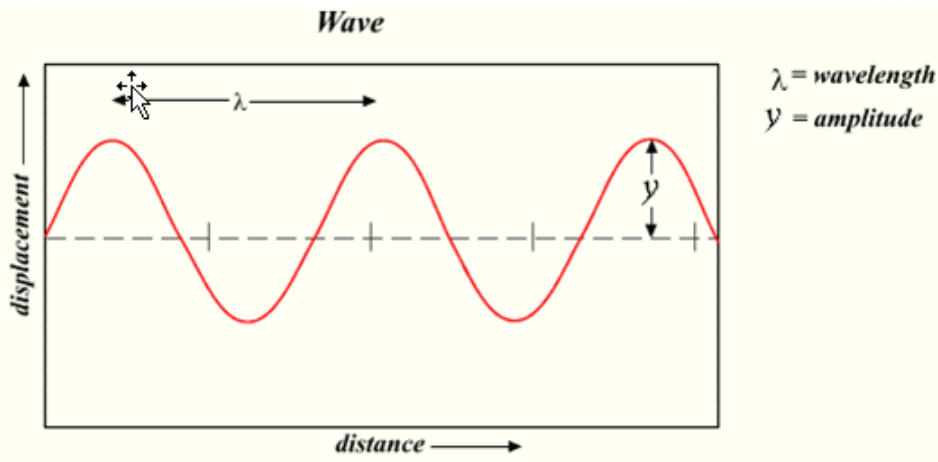
ρ = Average density (average of ρ_1 and ρ_2)

Θ = Angle of incidence

$\Delta V_p = V_{p_2} - V_{p_1}$

Amplitude

Amplitude is a measure of a wave's magnitude of oscillation, that is, the maximum departure of a wave from its average value.



Angle of incidence

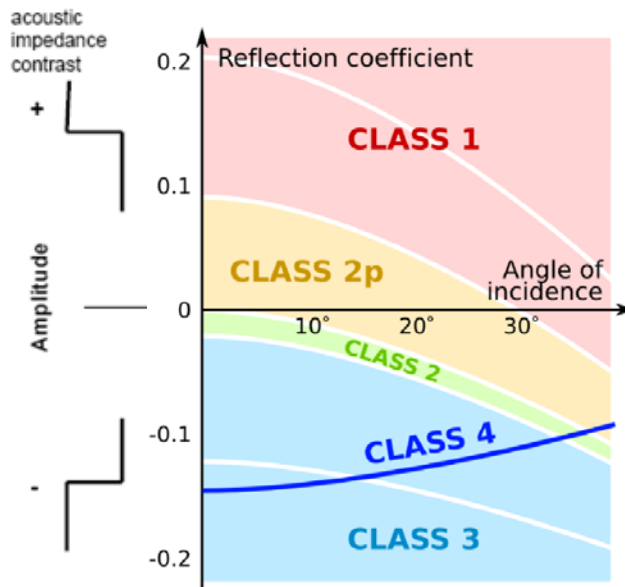
The angle that a raypath makes with the normal to an interface. This is the same angle that an approaching wave-front makes with the interface in an isotropic medium.

AVO (or AVA)

Amplitude Variation with Offset (or Amplitude Variation with Angle). This is a description of how the seismic reflections amplitudes change as a function of the source-to-receiver offset, or, angle of incidence.

AVO (or AVA) Classes

This project follows the AVO classification scheme by Agile Geoscience, which is explained in the schematic below.

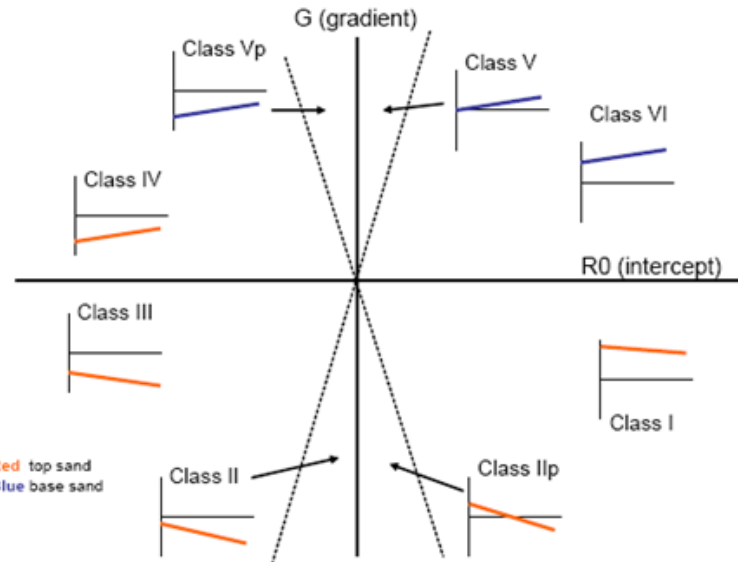


- AVO Class I:
A positive reflection that dims by with increasing incidence angle.
At normal incidence (0 degrees), the magnitude of the reflectivity is larger than 0.1.
The reflectivity remains positive to an incidence angle of at least 30 degrees.
The reflectivity changes/dims by more than 0.05 between 0-40 degrees.
- AVO Class IIp:
A positive reflection event that dims with increasing incidence angle.
At normal incidence (0 degrees), the magnitude of the reflectivity is smaller than 0.1.
The reflectivity becomes negative at an incidence angle <30 degree.
- AVO Class II:
A weak negative reflection that brightens with increasing incidence angle.
At normal incidence (0 degrees), the magnitude of the reflectivity is smaller than -0.02.
The reflectivity changes/brightens by more than 0.05 between 0-40 degrees.
- AVO Class III:
A negative reflection that brightens with increasing incidence angles.
At normal incidence (0 degrees), the magnitude of the reflectivity is greater than -0.02.
The reflectivity changes/brightens by more than 0.05 between 0-40 degrees.

- AVO Class IV:

A negative reflection that dims with increasing incidence angles. The reflectivity changes/dims by more than 0.05 between 0-40 degrees

These responses translate to points in intercept-gradient space, and can be visualized as follows:



Bortfeld PP approximation to Zoeppritz

A linearization of the full Zoeppritz equations, accurate for small contrasts in the interval properties across the interface.

$$R_{PP}(\theta) = \frac{1}{2} \ln \left(\frac{Vp_2 \rho_2 \cos \theta_1}{Vp_1 \rho_1 \cos \theta_2} \right) + \left(\frac{\sin \theta_1}{Vp_1} \right)^2 \left(Vs_1^2 - Vs_2^2 \right) \left[2 + \frac{\ln \left(\frac{\rho_2}{\rho_1} \right)}{\ln \left(\frac{Vp_2}{Vp_1} \right)} \right]$$

Bulk Modulus (K)

The bulk modulus describes the change in a material's volume that results from a change in the stress acting on it. It is therefore a measure of how stiff a material is.

$$K = Vp^2 \rho - \frac{4Vs^2 \rho}{3}$$

Density (ρ)

Mass per unit volume. Density is typically reported in g/cm³ (solid materials) or pounds per gallon (drilling mud) in the oil field.

Elastic Impedance (EI)

The interval property whose change determines reflection coefficients at angles of incidence. The equation below was derived from a linearization of the Zoeppritz equations, so it is valid for small contrasts in interval properties (Connolly, 1999).

$$EI = Vp_0 \rho_0 \left[\left(\frac{Vp}{Vp_0} \right)^{1+\sin^2\theta} \left(\frac{Vs}{Vs_0} \right)^{-8K \sin^2\theta} \left(\frac{\rho}{\rho_0} \right)^{1-4K \sin^2\theta} \right]$$

Where:

θ is the incidence angle

Vp is the P-wave velocity

Vs is the S-wave velocity ρ is the density, and

$$K = Vs^2/Vp^2$$

Vp_0 , Vs_0 and ρ_0 are the averages of Vp , Vs and density, respectively.

Gardner's Equation

An empirical relationship that computes density from sonic data.

$$\rho = dVp^f$$

where Vp is in km/s and d and f are constants that vary with rock type.

Gas Oil Ratio (GOR)

The ratio of produced gas to produced oil.

Gamma Ray log (GR)

A well log that records natural radioactivity. Gamma ray logs are particularly helpful in sediments, mainly reflecting the shale content since the radioactive minerals tend to concentrate in clays and shales.

Gassmann Equation

An equation used to estimate the properties of a rock saturated with one fluid from the properties of a rock saturated with a different fluid (Gassmann, 1951).

(i) from in situ saturation to dry rock

$$K_{dry} = \frac{K_{sat} \left(\frac{\phi K_0}{K_{fl}} + 1 - \phi \right) - K_0}{\frac{\phi K_0}{K_{fl}} + \frac{K_{sat}}{K_0} - 1 - \phi}$$

(ii) dry rock to fluid substitution case

$$K_{sat} = K_{dry} + \frac{\left(1 - \frac{K_{dry}}{K_0} \right)^2}{\frac{\phi}{K_{fl}} + \frac{1-\phi}{K_0} - \frac{K_{dry}}{K_0^2}}$$

Where:

K_{fl} , K_{dry} , K_0 are the bulk moduli of pore fluid, rock frame, mineral matrix, respectively.

Gassmann (Linear)

Using the critical porosity concept, the ratio of the saturated fluid and mineral moduli are used to estimate the change in bulk modulus due to fluid substitution at a given porosity (after Mavko et al (1997)). Using this information, the hydrocarbon saturation effect can be removed from V_p and Density in a method independent from V_s .

- $\Delta M_{Gassmann}(\phi) = \Delta K_{Gassmann}(\phi) \approx \frac{\phi}{\phi R^2} \Delta K_{fluid}$

Where:

$\Delta M_{Gassmann}(\phi)$ = change in p-wave modulus due to fluid effect at a given porosity

$\Delta K_{Gassmann}(\phi)$ = change in bulk modulus due to fluid effect at a given porosity

ϕ = porosity

ϕR = critical porosity

ΔK_{fluid} = change in bulk modulus due to fluid effect

Gradient (AVO)

The rate of change of reflection amplitude as a function of the sin-squared of the incidence angle.

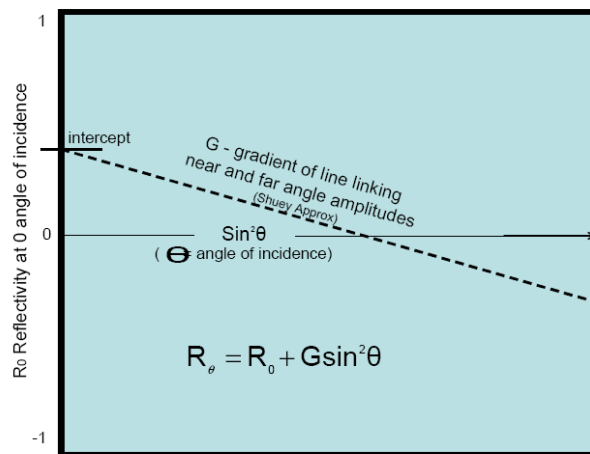
$$R_\theta = R_0 + G \sin^2 \theta$$

Where:

R_θ is the seismic reflection amplitude at incidence angle, θ .

R_0 is the seismic reflection amplitude at zero incidence angle (known as the AVO intercept).

G is the AVO gradient.



Greenberg-Castagna

An empirical relationship, derived from Gulf of Mexico data, for computing shear-velocity (V_s) from compressional-velocity (V_p) in a water saturated environment. Castagna et al. (1993) give a review of the subject.

Hydrostatic Pressure (Phydro)

The force per unit area exerted by a column of fresh water measured from the surface down to a given depth. Abnormally low pressure might occur in areas where fluids have been drained, such as a depleted hydrocarbon reservoir. Abnormally high pressure might occur in areas where the burial of sediments has occurred at such a rate that the dewatering process has not reached equilibrium.

Intercept (AVO)

An attribute describing the reflectivity at zero angles of incidence. See schematic under 'Gradient (AVO)'.

Lambda (λ)

Lambda is one of two Lamé parameters - the other being Mu. Lambda is sometimes called the fluid incompressibility parameter. Lambda can be defined in terms of V_p , V_s and Rho as follows:

$$\lambda = V_p^2 (\rho - 2V_s^2)\rho$$

Lithology

The macroscopic nature of the mineral content, grain size, texture and colour of rocks.

MD / AHD

Measured Depth / Along Hole Depth – the depth measured along the well-bore, below the Kelly Bushing (see schematic under TWT).

MSL

Mean sea-level.

Permeability

A tensor describing a material's ability to transmit fluids, for geological materials this quantity is typically measured in Darcie's and may span many orders of magnitude.

Porosity (ϕ)

The amount of void-volume, per unit gross volume, of a rock. Porosity can be composed of fracture-voids and pores, and may be expressed as a percentage, decimal or fraction. Total porosity describes the void-volume of the whole rock volume, including isolated pores and mineral-bound fluid. Effective porosity describes only the void-volume component which may contribute to fluid flow.

Poisson's Ratio (σ)

The ratio of the transverse contractional strain to longitudinal extensional strain that results from an applied stress. A perfectly elastic and isotropic material has a Poisson's ratio of 0.5.

$$\sigma = \frac{V_p^2 - 2V_s^2}{2(V_p^2 - V_s^2)} \quad \sigma = \frac{3k - 2\mu}{2\mu + 6k}$$

Pressure Gradient

The change in pressure per unit of depth, typically expressed in units of psi/ft or KPa/m. Pressure increases predictably with depth in areas of normal pressure. The normal hydrostatic pressure gradient for freshwater is approximately 0.433 psi/ft and 0.465 psi/ft for water with 100,000 ppm total dissolved solids (a typical Gulf Coast water).

P-wave or compressional wave velocity (V_p)

A P-wave is an elastic body wave in which particles oscillate in the direction of wave propagation. P-waves are studied in conventional seismic reflectivity data. P-waves incident on an interface, at any angle other than at normal incidence, can produce reflected and transmitted S-waves, which are known as converted waves.

$$V_p = \sqrt{\frac{K + \left(\frac{4\mu}{3}\right)}{\rho}}$$

Saturation (Sat)

The relative amount of water, oil and gas in the pores of a rock, usually expressed as a percentage, or fraction, of the available pore-volume.

Shear Modulus (μ)

An elastic constant for the ratio of shear stress to shear strain. The shear modulus is one of the Lamé constants – the other being Lambda, and sometimes is referred to as the modulus of rigidity.

$$\mu = V_s^2 \rho$$

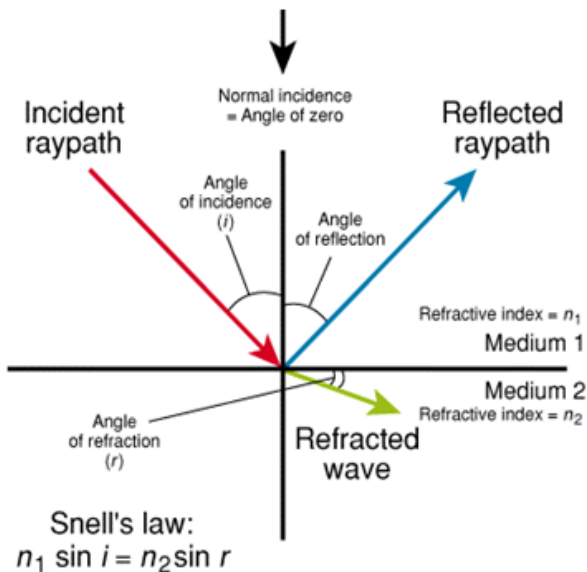
Shear Impedance (SI)

The product of s-wave velocity and density.

$$SI = Vs \cdot \rho$$

Snell's law

Snell's law describes the relationship between the angle of incidence and the angle of refraction of a wave or ray at an interface between two media.



S-wave or shear wave velocity (Vs)

The velocity of a wave whose particle motion is orthogonal to the direction of travel.

$$V_s = \sqrt{\frac{\mu}{\rho}}$$

TVDkb

True Vertical Depth referenced to the Kelly Bushing (see schematic under TWT).

TVDml

True Vertical Depth referenced to the mud line (see schematic under TWT).

TVDml_uplift

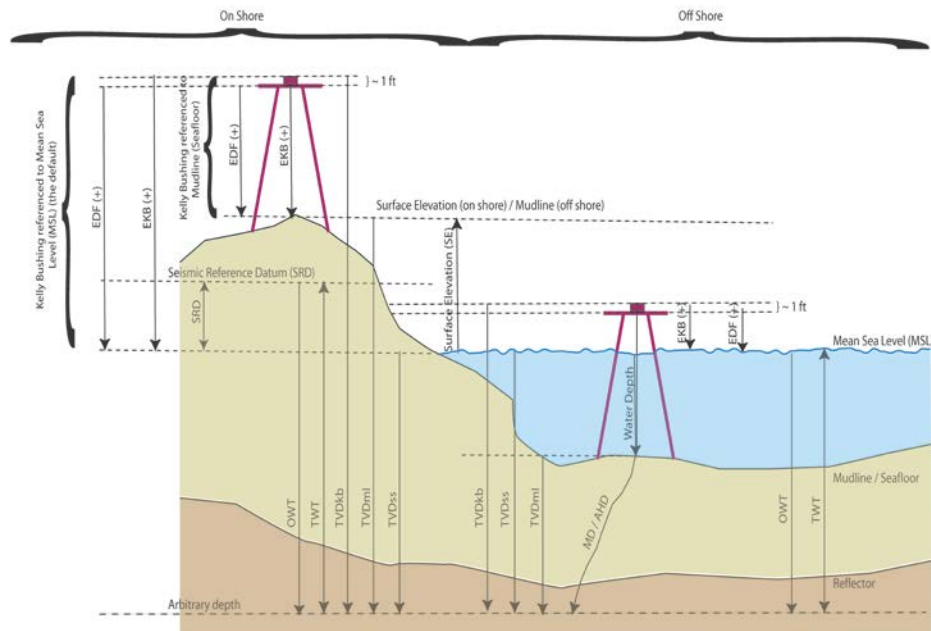
True Vertical Depth mud line corrected for relevant uplift

TVDss

True Vertical Depth referenced to the Mean Sea Level (see schematic under TWT).

TWT (Two way time)

The travel-time measured below the Seismic Reference Datum.



Zoeppritz equation

Equation that expresses the partition of energy when a plane wave impinges on interface between two media. In the general case for an interface between two solids when the incident angle is non-zero, four waves are generated: reflected P-wave and S-wave and transmitted P-wave and S-wave.

7 References

- Archie, G. E., 1942. **The electrical resistivity log as an aid in determining some reservoir characteristics.** Transactions of the AIME, 146(01), 54-62.
- Avseth, P., Dræge, A., van Wijngaarden, A., Johansen, T. and Jørstad, A. 2008. **Shale rock physics and implications for AVO analysis: A North Sea demonstration.** The Leading Edge, 22 (10), 170-173.
- Avseth, P., Dvorkin, J., Mavko, G. and Rykkje, J., 2000. **Rock physics diagnostic of North Sea sands: Link between microstructure and seismic properties,** Geophysics. Res. Lett., 27, 2761-2764.
- Avseth, P., Flesche, H., and Van Wijngaarden, A. J., 2003. **AVO classification of lithology and pore fluids constrained by rock physics depth trends.** The Leading Edge, 22(10), 1004-1011.

Avseth, P., Jorstad, A., van Wijngaarden, A. J., and Mavko, G., 2009. **Rock physics estimation of cementation, sorting and net-to-gross in North Sea sandstones**, The Leading Edge, 28, 98-109.

Avseth, P., Mukerji, T., Mavko, G. and Dvorkin, J., 2010. **Rock-physics diagnostics of depositional texture, diagenetic alterations, and reservoir heterogeneity in high-porosity siliciclastic sediments and rocks – A review of selected models and suggested work flows**. Geophysics 75, 7531–47.

Avseth, P., Mukerji, T., Mavko, G., and Tyssekvam, J., 2001. **Rock physics and AVO analysis for lithofacies and pore fluid prediction in a North Sea oil field**, The Leading Edge, 20, 429-434.

Avseth, P., Skjei, N., and Mavko, G., 2012. **Rock physics modeling of stress sensitivity in patchy cemented sandstones**. EAGE Expanded Abstract, 74th EAGE conference, Copenhagen, June 2012

Bachrach, N. M., Mow, V. C., and Guilak, F., 1998. **Incompressibility of the solid matrix of articular cartilage under high hydrostatic pressures**. Journal of biomechanics, 31(5), 445-451.

Bachrach, R. and Avseth, P., 2008. **Rock physics modelling of unconsolidated sands: accounting for non-uniform contacts and heterogeneous stress fields in the effective media approximation with applications to hydrocarbon exploration**, Geophysics, Vol. 73, No. 6.

Bachrach, R., 2011. **Elastic and resistivity anisotropy of shale during compaction and diagenesis: Joint effective medium modeling and field observations**. Geophysics, 76(6), E175-E186.

Bakulin, A., Kets, F., Vines, R., Wieseneck, J., and Hauser, M., 2008. **Influence of horizontal and vertical Stresses on Vp-Vs trends**. In 2008 SEG Annual Meeting. Society of Exploration Geophysicists.

Balkwill, H.R., McMillan, N. J., MacLean, B., Williams, G. L., and Srivastava, S. P., 1990. **Geology of the Labrador Shelf, Baffin Bay, and David Strait**, in Geology of the Continental Margin of East Canada, Geol. Of Can., v.2.

Banik, N. C., 1987. **An effective anisotropy parameter in transversely isotropic media**: Geophysics, 52, 1654–1664.

Bell, J.S., Howie, R.D., McMillan, N.J., Hawkins, C.M., and Bates, J.L., 1989. **Labrador Sea, East Coast Basin Atlas series**. Geological Survey of Canada, Canada.

Berryman, J. G., 1985. **Measurement of spatial correlation functions using image processing techniques**. Journal of Applied Physics, 57(7), 2374-2384.

Biot, M.A., 1956. **Theory of Propagation of Elastic Waves in a Fluid-Saturated Porous Solid: I Low Frequency Range**, Journal of the Acoustical Society of America 28, 168-178.

Biot, M.A., 1956. **Theory of Propagation of Elastic Waves in a Fluid-Saturated Porous Solid: II Higher Frequency Range**, Journal of the Acoustical Society of America 28, 179-191.

Bjørkum, P. A., and Walderhaug, O., 1990. **Geometrical arrangement of calcite cementation within shallow marine sandstones**. Earth-Science Reviews, 29(1), 145-161.

Bjørlykke, K. 1999. **Principal aspects of compaction and fluid flow in mudstones**. Geological Society, London, Special Publications, 158(1), 73-78.

Bosl, W. J., Dvorkin, J. and Nur, A., 1998. **A study of porosity and permeability using a lattice Boltzmann simulation**, Geophy. Res. Lett., 25 (9), p. 1475–1478.

Box, G. E. P. and Draper, N. R., 1987. **Empirical Model Building and Response Surfaces**, John Wiley and Sons, New York, NY.

Brevik, I., Ahmadi, G. R., Hatteland, T. and Rojas, M. A., 2007. **Documentation and quantification of velocity anisotropy in shales using wireline log measurements**. The Leading Edge, 26, 272–277.

Chalmers, J. A. and Pulvertaft, T. C. R., 2001. Development of the continental margins of the Labrador Sea: a review. *Geological Society, London, Special Publications*, 187(1), 77-105.

Chalmers, J.A., 1991. **New evidence on the structure of the Labrador Sea/Greenland continental margin**. Journal of the Geological Society of London, 148, 899-908.

Chalmers, J.A., Pulvertaft, T.C.R., Christiansen, F.G., Larsen, H.C., Laursen, K.H. Ottesen, T.G., 1993. **The southern West Greenland continental margin: rifting history, basin development, and petroleum potential**. In: Parker, J.R. (ed), Petroleum Geology of Northwest Europe: Proceedings of the 4th Conference, The Geological Society of London, 915-931.

Dafoe, L. T., Keen, C. E., Dickie, K., and Williams, G. L. 2015. **Regional stratigraphy and subsidence of Orphan Basin near the time of breakup and implications for rifting processes**. Basin Research.

Dafoe, L. T., Keen, C. E., Williams, G. L., and Dehler, S. A., 2013. **A tectonostratigraphic history of Orphan Basin, offshore Newfoundland, Canada.** Canadian Society of Petroleum Geologists, GeoConvention.

Dejtrakulwong, P., 2012. **Rock Physics and Seismic Signatures of Sub-resolution Sand shale Systems.** (Doctoral dissertation, Stanford University).

DeSilva, N.R., 1999. **Sedimentary basins and petroleum systems offshore Newfoundland and Labrador.** In: Fleet, A.J. and Boldy, S.A.R. (eds.), Petroleum Geology of Northwest Europe: Proceedings of the 5th Conference, The Geological Society of London, 501-515.

Digby, P.J., 1981. **The effective elastic moduli of porous granular rocks**, Journal of Applied Mathematics, v. 48, p. 803-808.

Draege, A., Jakobsen, M., and Johansen, T. A., 2006. **Rock physics modelling of shale diagenesis.** Petroleum Geoscience, 12(1), 49-57.

Duffaut K., 2011. **Stress sensitivity of elastic wave velocities in granular media.** Thesis for the degree of Philosophy Doctor. Norwegian University of Science and Technology

Dutta, T., Mavko, G., Mukerji, T., and Lane, T., 2009. **Compaction trends for shale and clean sandstone in shallow sediments.** Gulf of Mexico. The Leading Edge, 28(5), 590-596.

Dutta, T., Mukerji, T., and Mavko, G. 2008. **How does carbonate cementation in sandstones affect seismic response?**. In 2008 SEG Annual Meeting. Society of Exploration Geophysicists.

Dvorkin, J. and Brevik, I., 1999. **Diagnosing high-porosity sandstones: strength and permeability from porosity and velocity**, Geophysics, v. 64, p. 795-799.

Dvorkin, J. and Gutierrez, M.A., 2002. **Grain Sorting, Porosity, and Elasticity:** Petrophysics, 43(3), a3.

Dvorkin, J. and Nur, A., 1996. **Elasticity of high-porosity sandstones: Theory for two North Sea data sets**, Geophysics, v. 61, p 1363-1370.

Dvorkin, J., and Brevik, I., 1999. **Diagnosing high-porosity sandstones: Strength and permeability from porosity and velocity**. Geophysics, 64(3), 795-799.

Dvorkin, J., and Gutierrez, M. A., 2001. **Textural sorting effect on elastic velocities, part II: elasticity of a bimodal grain mixture.** In 2001 SEG Annual Meeting. Society of Exploration Geophysicists.

Dvorkin, J., and Nur, A., 1996. **Elasticity of high-porosity sandstones: Theory for two North Sea data sets.** Geophysics, 61(5), 1363-1370.

Dvorkin, J., Nur, A., and Yin, H., 1994. **Effective properties of cemented granular materials. Mechanics of materials**, 18(4), 351-366.

Eberhart-Phillips D., Han D. H, Zoback M. D., 1989. **Empirical relationships among seismic velocity, effective pressure, porosity and clay content in sandstone.** Geophysics 54:82–89.

Edwards, A., O'Connor, S., Waters, K. and Selnes, A. 2014. **Identifying the presence of secondary overpressure generating mechanisms in Jurassic shales, UK-Sector, Central North Sea.** Abstract, EAGE, Amsterdam, Holland.

Edwards, A., Selnes, A., Cameron, D., Welford, J. K., Wright, R., Atkinson, I., Green, S., Busutil, W., and O'Connor, S, 2015. **Cemented Shales and their Impact on Exploration, Offshore Newfoundland and Labrador-Identification and Implications.** In 77th EAGE Conference and Exhibition 2015.

Ermanovics, I.F. and Ryan, B., 1990. **Early Proterozoic orogenic activity adjacent to the Hopedale block of southern Nain Province,** Geoscience Canada, V. 17, p. 293-297.

Fabricius, I.L. 2003. **How burial diagenesis of chalk sediments controls sonic velocity and porosity.** American Association of Petroleum Geologists Bulletin, 87, 1755–1778.

Flostad, K., Witney,J., Borsato,R., Carter,J.,Wright,R. and Neugebauer,T., 2013. **Deep-Water Hydrocarbon Potential beneath the Labrador Sea, Offshore Newfoundland and Labrador, Canada.** GeoConvention 2013

Florez, J. M. 2005. **Integrating geology, rock physics, and seismology for reservoir quality prediction.** Doctoral dissertation, Ph. D. dissertation, Stanford University.

Folk, R.L., 1974. **Petrology of sedimentary rocks.** Austin, Texas, Hemphill Publishing, 184 p.

Freed R.L and Peacor D. R., 1989. **Variability in temperature of the smectite/illite reaction on Gulf Coast sediments.** Clay Miner 24:171-180.

Gardner, G.H.F., Gardner, L.W. and Gregory, A.R., 1974. **Formation velocity and density - the diagnostic basics for stratigraphic traps,** Geophysics 39: 770–780

Gardner, G.H.F., Gardner, L.W., and Gregory, A.R., 1974. **Formation velocity and density – the diagnostic basics for stratigraphic traps.** Geophysics, 39, 770-780.

- Gassmann, F., 1951. **Elastic waves through a packing of spheres**. Geophysics, 16, 673–685.
- Gist, G., A. Ciucivara, R. Houck, M. Rainwater, D. Willen, and J. J. Zhou, 2013. **Case study of a CSEM false positive, Orphan Basin, Canada**: 83rd Annual International Meeting, SEG, Extended Abstracts, 805–809.
- Greenberg, M.L. and Castagna, J.P., 1992. **Shear-wave velocity estimation in porous rocks: theoretical formulation, preliminary verification and applications**. Geophysical Prospecting, Volume 40, pp 195-209.
- Gutierrez, M. A. and Dvorkin J., 2010. **Rock physics workflows for exploration in frontier basins**. SEG Technical Program Expanded Abstracts 2010: pp. 2441-2446.
- Han, D., 1986. **Effects of Porosity and Clay Content on Acoustic Properties of Sandstones and Unconsolidated Sediments**. Ph.D. dissertation, Stanford University.
- Hashin, Z, and Shtrikman, S, 1963. **A variational approach to the elastic behavior of multiphase minerals**, Journal of the Mechanics and Physics of Solids, 11 (2), 127-140.
- Helgerud, M.B., 2001. **Wave speeds in gas hydrate and sediments containing gas hydrate: A laboratory and modeling study**, Palo Alto, California, Stanford University, Ph.D. dissertation, 248 p.
- Holt, R. M., Bhuiyan, M. H., Kolstø, M. I., Bakk, A., Stenebraten, J. F., and Fjær, E., 2011. **Stress-induced versus lithological anisotropy in compacted claystones and soft shales**. The Leading Edge, 30(3), 312-317.
- Hubbert, M. K. and Rubey, W. W., 1959. **Role of fluid pressure in mechanics of overthrust faulting I. Mechanics of fluid-filled porous solids and its application to overthrust faulting**. Geological Society of America Bulletin, 70(2), 115-166.
- Ikon Science, 2014. **Labrador Shelf Pressure Study: Unlocking the Shelf-to-Deep Transition**, Durham, U.K.
- Japsen, P., Green, P.F., and Chalmers, J.A., 2005. **Separating Palaeogene and Neogene uplift on Nuussuaq, West Greenland**. Journal of the Geological Society of London, 162, 299-314.
- Katahara, K. W., 2006. **Overpressure And Shale Properties: Stress Unloading Or Smectite-illite Transformation?** 76th SEG Annual Meeting, Expanded Abstracts, pp. 11520-1524.

Katahara, K., 2004. **Fluid substitution in laminated shaly sands.** In **2004 SEG Annual Meeting.** Society of Exploration Geophysicists.

Lander, R. H. and Walderhaug, O., 1999. **Predicting porosity through simulating sandstone compaction and quartz cementation,** AAPG Bulletin, 83,433-449.

Li, Y., Pickford, S., and Downton, J., 2000. **The applications of amplitude versus offset in carbonate reservoirs: re-examining the potential.** gas, 1, 1-44.

Li, Y., 2006. **An empirical method for estimation of anisotropic parameters in clastic rocks.** The Leading Edge, June, 2006.

Li Y., Biondo B., Nichols, D., Mavko, G., and Clapp R., 2012. **Stochastic rock physics modelling for seismic anisotropy,** SEP report - 149, Stanford University.

Marion D., Nur A., Yin H. and Han D., 1992. **Compressional velocity and porosity in sand-clay mixtures.** Geophysics 57, 554-563.

Martin, M., 2007. **Seismic Stratigraphy and Tectono-structural framework of the Bjarni Area, Hopedale Basin, Labrador Sea.** MSc Thesis (Geophysics), Memorial University of Newfoundland, St. John's, NL

Mavko, G., and Jizba, D., 1991. **Estimating grain-scale fluid effects on velocity dispersion in rocks.** Geophysics, 56(12), 1940-1949.

Mavko, G., T. Mukerji, and Dvorkin J., 2009. **The rock physics handbook.** 2nd ed.: Cambridge University Press.

McWhae, J.R.H. and Michel, W.F.E., 1975. **Stratigraphy of Bjarni H-81 and Leif M-48, Labrador shelf.** Bulletin of Canadian Petroleum Geology, 23, p. 361-382.

McWhae, J.R.H., Elie, R., Laughton, D.C. and Gunther, P.R., 1980. **Stratigraphy and petroleum prospects of the Labrador shelf.** Bulletin of Canadian Petroleum Geology, 28, p. 460-488.

McWhae, J.R.H., 1981. **Structure and Spreading History of the Northwestern Atlantic Region from the Scotian Shelf to Baffin Bay in Geology of the North Atlantic Borderlands.** Canadian Society of Petroleum Geology, Memoir. Vol. 7, p.299-332.

Mindlin, R.D., 1949. **Compliance of elastic bodies in contact,** Trans. ASME, 71, A-259

Mukerji, T., Jørstad, A., Avseth, P., Mavko, G. and Granli, J. R., 2001. **Mapping lithofacies and pore-fluid probabilities in a North Sea reservoir: Seismic inversions and statistical rock physics**: Geophysics, 66, 988–100.

Murphy III, W. F., 1982. **Effects of partial water saturation on attenuation in Massilon sandstone and Vycor porous glass**. The Journal of the Acoustical Society of America, 71(6), 1458-1468.

Naylor, P.H., Bell, B.R., Jolley, D.W., Durnall, P. and Fredstead, R., 1999. **Paleogene magmatism in the Faroe-Shetland Basin: Influences on uplift history and sedimentation**, Petroleum Geology of Northwest Europe: Proceedings of the 5th Conference: Geological Society, London. P. 545-558.

Norris, A. N., 1985. **A differential scheme for the effective moduli of composites**. Mechanics of materials, 4(1), 1-16.

Peltonen, C., Marcussen, Ø., Bjørlykke, K., and Jahren, J., 2009. **Clay mineral diagenesis and quartz cementation in mudstones: The effects of smectite to illite reaction on rock properties**: Marine and Petroleum Geology, v. 26, no. 6, p. 887-898.

Pickett, G. R., 1966. **A review of current techniques for determination of water saturation from logs**. Journal of Petroleum Technology, 18(11), 1-425.

Poupon, A., and Leveaux, J., 1971. **Evaluation of water saturation in shaly formations**. In **SPWLA 12th Annual Logging Symposium**. Society of Petrophysicists and Well-Log Analysts.

Ramm, M., Bjørlykke, K., 1994. **Porosity/depth trends in reservoir sandstones: Assessing the quantitative effects of varying pore-pressure, temperature history and mineralogy, Norwegian Shelf data**, Clay minerals, v. 294, London Mineralogical Society, p. 475-490.

Rauch, M., and Collins, E., 1998. **The Greenshank anomaly- an AVO case history**. Exploration Geophysics, 29(3/4), 565-569.

Roberts, D. G., and Bally, A. W., 2012. **Some remarks on basins and basin classification and tectonostratigraphic megassequences**. Regional Geology and Tectonics: Principles of Geologic Analysis. Elsevier, 7.

Ruger, A., 1998. **Variation of P-wave reflectivity with offset and azimuth in anisotropic media**. Geophysics, 63, No. 3, 935–947.

- Russell, B., Ross, C. and Lines, L., 2002. **Neural networks and AVO**, The Leading Edge 21, 268.
- Rutherford, S. R., and Williams, R. H., 1989. **Amplitude-versus-offset variations in gas sands**, Geophysics, Volume 54. pp 680 – 688.
- Ryan-Grigor, S., 1998. **Empirical relationships between anellipticity and Vp/Vs in shales: Potential applications to AVO studies and anisotropic seismic processing**. Society of Exploration Geophysics Expanded Abstracts. 17, pp.208-211
- Sayers, C. M., 1999. **Stress-dependent seismic anisotropy of shales**. Geophysics, 64(1), 93-98.
- Sayers, C. M., 2008. **The effect of low aspect ratio pores on the seismic anisotropy of shales**. In 2008 SEG Annual Meeting. Society of Exploration Geophysicists.
- Schwartz, S., 2008. **Diagenesis and porosity evolution of the lower Palaeozoic carbonate and Cretaceous-Tertiary siliciclastic reservoir intervals, Labrador shelf**. MSc (Geology), Memorial University of Newfoundland, St. John's, NL.
- Selnes, A., Strommen, J., Lubbe, R., Waters, K., and Dvorkin, J., 2013. **Flat Spots-True DHIs or False Positives?**. In 75th EAGE Conference and Exhibition incorporating SPE EUROPEC 2013.
- Simm, R., Bacon, M. 2014. **Seismic Amplitude Interpretation: An Interpreter's Handbook**. Cambridge University Press.
- Skelt, C., 2004. **Fluid substitution in laminated sands**. The Leading Edge, 23(5), 485-493.
- Small, J.S., 1994. **Fluid Composition, mineralogy and morphological changes associated with the smectite-to-illite reaction: an experimental investigation of the effect of organic acid anions**: Clay Minerals, v. 29, no. 4, p. 539- 554.
- Sondergeld, C. H., and Rai, C. S., 2011. **Elastic anisotropy of shales**. The Leading Edge, 30(3), 324-331.
- Sondergeld, C. H., Rai C. S., Margesson R. W., and Whidden K. J., 2000. **Ultrasonic measurement of anisotropy on the Kimmeridge shale**: 70th Annual International Meeting, SEG, Expanded Abstracts, 1858–1861.
- Thomas, E.C., and Stieber, S.J., 1975. **The Distribution of shale in sandstones and its effect upon porosity**. In SPWLA 16th annual logging symposium. Society of Petrophysicists and Well-Log Analysts.

- Thomsen, L., 1986. **Weak elastic anisotropy**: Geophysics, 51, 1954–1966.
- Thyberg, B., Jahren, J., Winje, T., Bjørlykke, K., and Faleide, J. I., 2009. **From mud to shale: rock stiffening by micro-quartz cementation**. First Break, 27(2).
- Tsuneyama, F. and Mavko G., 2005. **Velocity anisotropy estimation for brine-saturated sandstone and shale**, The Leading Edge 24, pp. 882-888.
- Van der Kamp, P.C., 2008. **Silica diagenesis, I. Solubility controls**. Journal of Sedimentary Petrology, 55, pp. 301-311.
- Vanorio, T., C. Scotellaro, and G. Mavko, 2008. **The effect of chemical and physical processes on the acoustic properties of carbonate rocks**: The Leading Edge, 27, 1040–1048,
- Vega, S., Mavko, G., Nur, A. and Prasad, M., 2006. **Detection of stress induced velocity anisotropy in unconsolidated sands**. The Leading Edge, 25, 252–256.
- Verm, R. and Hilterman, F., 1995. **Lithology color-coded seismic sections: the calibration of AVO crossplotting to rock properties**, The Leading Edge, 14, 8, pg 847-853.
- Vernik, L. and Liu, X., 1997. **Velocity anisotropy in shales: A petrophysical study**. Geophysics, 62, 521–532.
- Vernik, L. and Nur A., 1992. **Ultrasonic velocity and anisotropy of hydrocarbon source rocks**: Geophysics, 57, 727–735.
- Voltolini, M., Wenk, H. R., Mondol, N. H., Bjørlykke, K., and Jahren, J., 2008. **Anisotropy of experimentally compressed kaolinite-illite-quartz mixtures**. Geophysics, 74(1), D13-D23.
- Walton, K., 1987. **The effective elastic moduli of a random packing of spheres**, Journal of the Mechanics and Physics of Solids, v. 35, p. 213-226.
- Wentworth, C. K., 1922. **A scale of grade and class terms for clastic sediments**. The Journal of Geology, 377-392.
- White, R. E., 1980. **Partial coherence matching of synthetic seismograms with seismic traces**. Geophysical Prospecting, 28(3), 333-358.
- Yin, H., Nur, A. and Mavko, G. , 1993. **Critical Porosity - a physical boundary in poroelasticity**, Pergamon-Elsevier Science Ltd, 805-808.

Zimmer, M., 2003. **Controls on the seismic velocities of unconsolidated sands: Measurements of pressure, porosity and compaction effects**. Doctoral dissertation, Ph. D. Thesis, Stanford University.

Zimmer, M., Prasad, M., Mavko G. and Nur A., 2007. **Seismic velocities of unconsolidated sands: Part 1-Pressure trends from 0.1 to 20 MPa**: Geophysics, 72, E1–E13.

Zoeppritz, K., 1919. Erdbebenwellen VIIIB. **On the reflection and propagation of seismic waves**, Gottinger Nachrichten, I. pp 66-84.